MICROSCALE PRESSURE FLUCTUATIONS MEASURED WITHIN THE LOWER ATMOSPHERIC BOUNDARY LAYER

by

JAMES ARTHUR ELLIOTT

B.Sc., University of Saskatchewan, 1962
M.Sc., University of British Columbia, 1965

A THESIS SUBMITTED IN PARTIAL FULFILMENT OF

THE REQUIREMENTS FOR THE DEGREE OF

DOCTOR OF PHILOSOPHY

in the Department

of

Physics

Institute of Oceanography

We accept this thesis as conforming to the
required standard

THE UNIVERSITY OF BRITISH COLUMBIA

September, 1970

In presenting this thesis in partial fulfilment of the requirements for an advanced degree at the University of British Columbia, I agree that the Library shall make it freely available for reference and study. I further agree that permission for extensive copying of this thesis for scholarly purposes may be granted by the Head of my Department or by his representatives. It is understood that copying or publication of this thesis for financial gain shall not be allowed without my written permission.

Department of Physics

Institute of Oceanography,
The University of British Columbia
Vancouver 8, Canada

Date Sept 29/70

ABSTRACT

An instrument was developed to measure the static pressure fluctuations within the turbulent flow of the atmospheric boundary layer. This instrument was used to measure some of the properties of pressure fluctuations over a flat boundary and over water waves and has provided the first reliable pressure data within a turbulent boundary layer.

For all observations over a flat boundary the root-mean-square pressure produced by the boundary layer turbulence was about 2.6 times the mean stress. The spectra had a power law behaviour with a mean slope of -1.7 for scales above the peak of the vertical velocity spectrum. Pressure fluctuations were approximately spherical in shape, and propagated downstream at a rate equal to the 'local' mean wind. Above the boundary, the large scale pressure fluctuations were approximately in phase with the downstream velocity fluctuations; at small scales there was a large phase difference ($\simeq 135°$). These phase differences were interpreted to be the result of the large pressure producing scales interacting with the earth's surface, while the small scales were 'free' of the surface. Pressure forces resulted in an energy flux out of the downstream velocity fluctuations of about 0.45 of the total energy source for the turbulence within the band of $0.05 < kz < 20$. The pressure term in the net energy budget was found to be about 1/10 of the energy feeding term.

Pressure measurements near wind generated waves showed a large spectral hump at the wave frequencies. The amplitude of this hump increased, and its vertical rate of decay decreased, as the mean wind speed increased. The phase difference between pressure and waves during active generation was found to be about 135°, pressure lagging waves. This did not change vertically.

TABLE OF CONTENTS

LIST OF TABLES

LIST OF FIGURES

Figure page

Figure page

Figure page

Figure page

Figure page

ACKNOWLEDGMENTS

This work was done as part of the Air-Sea Interaction program at the Institute of Oceanography, University of British Columbia. The research has been supported principally by the United States Office of Naval Research under Contract N00014-16-C-0047. Addtional support came from the National Research Council of Canada, Defence Research Board, and Department of Transport (Meteorological Branch). I have been personally supported with a National Research Council Studentship and a MacMillan Family Fellowship, while on educational leave from the Atlantic Oceanographic Laboratory, Bedford Institute, Department of Energy, Mines and Resources.

I wish to thank Dr. R.W. Stewart, Dr. R.W. Burling, and Dr. M. Miyake for their guidance during the course of this work. I also wish to thank all others who have assisted with this project: the graduate students, in particular G.H. Elliott, F.W. Dobson, G.A. McBean and J.R. Wilson, and the technicians of this institute.

Finally I thank my wife Gillian for her part in the preparation of this report.

INTRODUCTION

This study was centered around the Eulerian measurement of turbulent static pressure fluctuations within the atmospheric boundary layer. The 'static' pressure is the normal stress associated with motions within the fluid (Hinze, 1959, p.27). Increased knowledge of the role of static pressure fluctuations within turbulent fluid flow is of great interest to many engineering and geophysical studies. There is a lack of available information, not from a lack of effort but rather a lack of ability to measure this variable reliably within the body of the fluid.

The importance of this measurement is evident from the following postulated properties of the static pressure fluctuations. Pressure fluctuations are credited with being the 'isotropy producing' force; that is, they are expected to transfer energy among velocity components (directions). Or, as has been stated by Batchelor (1960, p.88), "... the pressure is nondirectional and the probable consequence is that it builds up the weaker velocity component at the expense of the stronger." There was little known of the detail of this process whereby anisotropic turbulence, the form initially generated in most turbulent flows, was transformed toward the much studied 'isotropic turbulence' further down the energy cascade. The pressure-vertical velocity correlation, which enters as a flux divergence term in the net energy budget of a boundary layer, had not been measured either. This term was usually assumed to be small (Lumley and Panofsky, 1964, p.121); a recent numerical study, (Deardorff, 1970) agreed with this assumption. Experimental verification was required. The study of wave generation is another example of an active area of research in which pressure fluctuations play an important part in energy transfer. Knowledge of the static pressure

distribution over waves would further our understanding of the wave generation process. In all these examples, direct measurement of the static pressure within the flow was required. Accordingly, in this present study, static pressure measurements were made and the above aspects were investigated.

Most of the present theoretical knowledge on turbulent pressure fluctuations is for isotropic turbulence. Some of the important predictions are Batchelor's estimate of the intensity and Obukhov's dimensional argument for the spectral slope (Batchelor, 1960).

In contrast Kraichnan (1956) has shown theoretically that for nonisotropic turbulent boundary layer flow the primary contribution to pressure fluctuations near the surface results from interaction between the turbulence and the mean shear. He estimated, using experimental velocity data, that the magnitude of the rms pressure fluctuations was greater than, but of the order of, the wall shear stress.

Previous experimental observations of boundary layer pressure fluctuations have been mainly confined to the measurement of these fluctuations at the surface, either of the earth or of a wind tunnel. Two Russian authors, Golitsyn (1964) and Gorshkov (1967, 1968) have analysed atmospheric spectra and some pressure velocity cross-spectra from such surface observations. Gossard (1960) showed atmospheric pressure spectra for a wide frequency range. He had a few examples of microscale spectra that were obtained from an 'instrument' located on a tower. For the microscale region, these studies found a mean slope of about -2 for a plot of spectral density $((\text{dynes/cm}^2)^2/\text{Hz})$ against frequency. The pressure spectra shown by Gossard did not exhibit the mid-frequency minimum found in velocity spectra as reported by Van der Hoven (see Lumley and Panofsky, 1964, p.43) but generally decreased continuously in intensity from the low frequency synoptic pressure fluctuations to the higher

frequency pressure fluctuations associated with the boundary layer turbulence. This mid-frequency 'filling-in' is thought to be due to mesoscale phenomena which do not directly produce velocity fluctuations at the earth's surface; for example, internal gravity waves at higher elevations (Herron *et al*, 1969). This suggests that microscale pressure observations near the surface may include some low frequency energy that is not associated with the local turbulent velocities.

There have been attempts to evaluate the properties of the static pressure within the fluid by relating it to the velocity (Hinze, 1959, p.239). Because the static pressure fluctuations in a turbulent flow are, generally speaking, the result of the air motions interacting with each other, they are not an independent quantity but are directly related to a field of velocity. Investigations of this relationship have so far been restricted to the consideration of simple properties such as the rms pressure in isotropic turbulence, because a general consideration of the relationship requires complicated velocity measurements.

Willmarth and Wooldridge (1962) give a thorough summary of, as well as new, data from observations obtained to that date in wind tunnel studies of surface pressure fluctuations. Conclusions drawn from their paper are 1) that the measured rms wall pressure is fairly well established at about 2.5 times the wall shear stress, 2) that the advection speed of the pressure fluctuations is about 0.6 to 0.85 times the stream speed, 3) that the pressure-producing eddies of wavelength λ decay after travelling a distance of a few λ, and 4) that the transverse scales and longitudinal scales of pressure fluctuations measured at the wall are approximately the same size.

Previous to this present study reliable experimental knowledge of turbulent static pressure fluctuations was limited to such observations made

at the surface.

It was decided to concentrate on the measurement of pressure fluctuations with scales equal to the velocity scales that carry the turbulent momentum flux. It is in this range that important energy transfers by pressure forces are expected (see Background). Instrumentation that could measure the static pressure fluctuations in the body of the fluid had to be developed and tested (see Pressure Instrument and *In Situ* Calibrations of the Pressure Instrument). This instrumentation was then used to obtain data related to the 'description' of the measured pressure fluctuations as well as to obtain estimates of some of the energy fluxes by the pressure forces (see Microscale Pressure Fluctuations over a Flat Boundary). Observations taken over wind generated waves are used to describe some of the properties of the pressure fluctuations associated with wave generation (see Microscale Pressure Fluctuations over Wind Generated Waves). The data analysed was collected at both land and over-water sites near the Institute of Oceanography, U.B.C. (I.O.U.B.C.). In making observations, other variables, such as, fluctuating wind and wave height, were obtained using instruments developed for atmospheric boundary layer research. In some cases these had been developed at I.O.U.B.C. A description of the sites and the equipment used, other than the pressure measuring instrument, is given in Appendix A. Since most of the data presented are put into nondimensional form the actual operating conditions (surface stress, mean wind) may not be given explicitly in the text but are included in a table in Appendix C. All the data are permanently labelled with a 'Run' number (e.g. 120/1). The data were analysed digitally; details on the analysis methods are given in Appendix B.

BACKGROUND

It is the purpose of this section to present for later use some aspects of a turbulent boundary layer, especially static pressure fluctuations, that can be predicted from physical arguments.

Many of the predictions are based on the Navier-Stokes equation. In the usual manner (cf. Hinze, 1959), equations can be written to represent the momentum balance for the mean and for the fluctuating part of the flow. The equation for the fluctuating components in an incompressible, viscous, constant density fluid, written in Cartesian tensor notation is

$$\frac{\partial u_i}{\partial t} + u_j \frac{\partial U_i}{\partial x_j} + U_j \frac{\partial u_i}{\partial x_j} + u_j \frac{\partial u_i}{\partial x_j} - \overline{u_j \frac{\partial u_i}{\partial x_j}} = -\frac{1}{\rho} \frac{\partial p}{\partial x_i} + \nu \frac{\partial^2 u_i}{\partial x_j \partial x_j} \qquad (1)$$

where U_i and u_i are the i^{th} components of the mean and fluctuating fluid velocity respectively, p is the fluctuating pressure, ρ is the mean density, and ν is the kinematic viscosity. The bar over a variable indicates an ensemble average; u_i and p have zero averages. When analysing observations, it is assumed that the data are measurements of a stationary, random process, and thus that the time averages used are ensemble averages (Batchelor, 1960, p.17).

The right-handed Cartesian coordinate system to be used has x_1 positive in the direction of the mean motion in the boundary layer, and x_3 vertically upward. The notation x_1, x_2, x_3; u_1, u_2, u_3; U_1 is used interchangeably with x, y, z; u, v, w; U respectively.

The close relationship between the pressure and velocity fluctuations can be seen by taking the divergence of equation (1). This gives

$$-\frac{1}{\rho}\frac{\partial^2 p}{\partial x_i \partial x_i} = -\frac{\partial}{\partial x_i}\frac{\partial}{\partial x_j}\left(\overline{u_i u_j} - u_i u_j - U_i u_j - u_i U_j\right) \qquad (2)$$

Thus the pressure is determined by the velocity field and is not an independent variable. Taking the integral of (2) over all space (e.g., Townsend, 1955, p.27) gives the pressure at a point in terms of velocity.

$$p = -\frac{1}{4\pi}\int \frac{\partial^2}{\partial x_i' \partial x_j'}\left(\overline{u_i' u_j'} - u_i' u_j' - U_i' u_j' - u_i' U_j'\right)\frac{1}{|\underset{\sim}{\chi}|}\, d\gamma \qquad (3)$$

where $\chi = x' - x$; p is measured at x and the velocities at x'. This shows that the pressure at a point can be expressed in terms of the appropriately weighted velocity gradient products from the surrounding fluid and not just at the measurement point itself. This is sometimes called the 'integral effect'.

The 'isotropy producing' characteristic of the pressure forces can be seen in the energy budget of the individual velocity components. These equations can be obtained by multiplying the i^{th} form of equation (1) by u_j, and adding to it the j^{th} form of equation (1) multiplied by u_i, and then averaging. A suitable approximation to these equations which would apply to an atmospheric boundary layer (Lumley and Panofsky, 1964, p.71) is obtained by assuming the flow is steady state and two-dimensional, with variation of mean quantities in the x_3 direction only. With these approximations the energy budgets for the individual velocity components are

$$\frac{1}{2}\frac{\partial \overline{u^2}}{\partial t} = 0 = -\overline{uw}\frac{\partial U}{\partial z} - \frac{1}{2}\frac{\partial}{\partial z}\overline{u^2 w} - \frac{1}{\rho}\overline{u\frac{\partial p}{\partial x}} + \nu\,\overline{u\nabla^2 u} \qquad (4a)$$

$$\frac{1}{2}\frac{\partial \overline{w^2}}{\partial t} = 0 = 0 - \frac{1}{2}\frac{\partial}{\partial z}\overline{w^3} - \frac{1}{\rho}\overline{w\frac{\partial p}{\partial z}} + \nu\,\overline{w\nabla^2 w} \qquad (4b)$$

$$\frac{1}{2}\frac{\partial \overline{v^2}}{\partial t} = 0 = 0 - \frac{1}{2}\frac{\partial}{\partial z}\overline{v^2 w} - \frac{1}{\rho}\overline{v\frac{\partial p}{\partial z}} + \nu\,\overline{v\nabla^2 v} \qquad (4c)$$

where the first term on the right hand side, which is non-zero only in the $\overline{u^2}/2$ equation, is the 'energy feeding' term representing extraction of energy from the mean flow and putting it into the downwind component of the turbulence; the second term represents the transfer of turbulent energy by the turbulent velocities, the third term represents the transfer of energy by the pressure gradient-velocity correlation, and the final term the total viscous effect on energy transfer which is assumed to be entirely dissipation 'ε'. The integral of the sum of these pressure terms over all space is zero, thus the pressure acts to transfer energy between components and is not a net source or sink. Since it is expected that the net viscous effect is to dissipate energy and since turbulent advection cannot produce a net transfer of energy between components (Lumley and Panofsky, 1964, p.67) the only terms remaining to transfer the energy being fed into the u-component (in equation 4a) into the other two velocity components are the pressure terms. Energy transfer by these terms had not been measured previous to this study and thus ideas about the properties of this transfer were only speculative.

Though the pressure can transfer energy between the different velocity components, it does not transfer energy between different Fourier components (wave numbers). This can be seen in the spectral energy transfer equations (Batchelor, 1960, p.87) where the pressure term drops out as a result of the

incompressibility condition. Thus any energy transferred from a velocity component via the pressure term must appear in another velocity component at the same wave number.

The total energy budget for the boundary layer can be represented by the sum of the individual equations (4); this gives

$$0 = -\overline{u_1 u_3}\frac{\partial U_1}{\partial x_3} - \frac{1}{2}\frac{\partial}{\partial x_3}\left(\overline{u_i u_i u_3}\right) - \frac{1}{\rho}\frac{\partial}{\partial x_3}\overline{pu_3} + \nu\,\overline{u_i \nabla^2 u_i} \qquad (5)$$

Three of these terms (all except the pressure term) had previously been measured for the atmospheric boundary layer (Lumley and Panofsky, 1964, p.119 ff.). For most cases it had been found that the energy feeding term was approximately balanced locally by the viscous dissipation and that the turbulent transfer term was small. Because of the approximate balance between local production and dissipation, speculation had been that the flux divergence by the pressure forces was also small. However the inaccuracy of such observations makes this method of approximating the flux divergence unsatisfactory and direct measurement is desirable. The measurements required to evaluate the relative importance of the terms in this equation can be simplified by comparing the terms in modified form. If equation (5) is integrated from z_1 to z, where z_1 is a lower level fixed near the 'transition region' (see Hinze, 1959, p.465) where the turbulence is influenced by the viscous effects of the surface, this gives

$$-\overline{u_1 u_3}\left(U|_z - U|_{z_1}\right) - \frac{1}{2}\left(\overline{u_i u_i u_3}|_z - \overline{u_i u_i u_3}|_{z_1}\right)$$

$$-\frac{1}{\rho}\left(\overline{pu_3}|_z - \overline{pu_3}|_{z_1}\right) + \int_{z_1}^{z} \nu\,\overline{u_i \nabla^2 u_i}\,dz = 0 \qquad (6)$$

The notation $U|_z$ means the wind at the level z. It is assumed that the 'transition region' is thin, and there is negligible turbulent energy flux through it, the stress being carried by viscous forces. This assumption would only be applicable to observations over a solid surface and not over water when waves are being generated. The approximations are that the terms evaluated at z_1 are small compared with those evaluated at z. These assumptions give

$$- \overline{u_1 u_3 U_1}|_z ; - \frac{1}{2} \overline{u_i u_i u_3}|_z ; - \frac{1}{\rho} \overline{p u_3}|_z$$

as approximations for the first three terms which are terms in the budget of turbulent kinetic energy in the space between the boundary and height z. The first term represents the net rate of working per unit area on the surface z by the Reynolds stress, $- \overline{u_1 u_3}$, the second the upwards flux of turbulent energy and the third the rate of working per unit area by the pressure force. A comparison of these three terms would indicate the relative importance of each as a net energy source of turbulent kinetic energy per unit area for the air below the level z.

Dimensional arguments, identical to those used to predict the -5/3 region for the velocity spectrum in the inertial subrange, have been used by Obukhov to predict the shape of the pressure spectrum, $\Pi(n)$ (see Lumley and Panofsky, 1964, p.84). For this restricted scale range with no production and no dissipation, he obtained

$$\Pi(k) = K_p \rho^2 \varepsilon^{4/3} k^{-7/3} \qquad (7)$$

where K_p is some universal constant. The predicted power law was for a

condition of 'local isotropy'. Batchelor evaluated the expected rms pressure for this condition of isotropy. His calculation, which used measurements of the velocity autocorrelation (see Batchelor, 1960, p.182), gave

$$\sqrt{\overline{p^2}} = 0.58\ \rho\ \overline{u^2} \qquad (8).$$

Since it is not certain that a condition of local isotropy occurs at any level in the lower few meters of the atmospheric boundary layer (Stewart, 1969), it is doubtful whether these results can be compared with measured values, even though velocity spectra have a -5/3 region.

The mean wind profile is assumed, for all calculations, to have the 'predicted' logarithmic form

$$U|_z = \frac{u_*}{\kappa} \ln \frac{z}{z_o} \qquad (9)$$

where $u_* = \sqrt{-\overline{uw}}$, κ is von Karman's constant (0.4) and z_o is the virtual height where the mean velocity goes to zero. The use of the logarithmic profile assumes neutral stability, a point to be discussed later. Typical winds at the experimental sites were 3 to 10 m sec^{-1}. For comparison purposes, this corresponds to a Reynolds number $Re = \frac{5m\ U|_5}{\nu}$ of order 10^6.

When nondimensionalizing the data presented below, two parameters are often used. One, the surface stress, $\tau = -\rho\overline{uw} = \rho u_*^2$, is evaluated in one of three different ways: direct measurements of $-\overline{uw}$, using the 'Φ_{11} method' or from the mean wind speed using a drag coefficient. Details on these methods are contained in Appendix B. The method used for a particular Run is given in the Data Summary in Appendix C. The other parameter is the turbulent 'energy feeding' term

$-\overline{uw}\frac{\partial U}{\partial z}$. It is evaluated in the form $\frac{u_*^3}{\kappa z}$, where this last step assumes a logarithmic profile (equation 9) for U.

It was decided to take observations of pressure over the range of scales contributing significantly to the total shear stress. For observations below 5 meters, this occurs for the range of nondimensional frequencies, $f = \frac{nz}{U}$, from approximately 10^{-2} to 10^{0} (McBean, 1970). Thus the frequency range required in the observations is from about 3×10^{-3} to 10 Hz.

Another important frequency is that at the peak of the w spectrum. When plotted in integrable logarithmic form, the peak occurs at about $f = 4 \times 10^{-1}$. At frequencies above this value, all spectra of the velocity components have approximately equal intensity and shortly thereafter a -5/3 slope.

The observational technique used was to obtain observations at a fixed level above the surface. In the usual manner, the 'frozen field' (Taylor's) hypothesis is assumed. This gives the relationship between frequency n and wave number k as

$$k = \frac{2\pi n}{U} \tag{10}$$

where U is the mean advection wind. The same assumption allows phase shift corrections to be made and horizontal gradients to be calculated from the relation

$$\frac{\partial}{\partial x} = \frac{1}{U}\frac{\partial}{\partial t} \tag{11}$$

An attempt was made to take observations only for a steady mean wind speed and direction, neutral stability and a homogeneous, flat terrain, since these are the assumptions used in analysing the data.

PRESSURE INSTRUMENT

Since no suitable technique existed for measuring the static pressure fluctuations in a turbulent boundary layer, instrumentation was developed. The main difficulty associated with this measurement is in eliminating the effects of dynamic pressure; dynamic pressure is the normal stress associated with deflecting flow around a solid body, in this case a sensor. As the air velocity fluctuates, so does the dynamic pressure. When measuring the static pressure fluctuations such dynamic pressure fluctuations are noise. A probe was specially designed to reduce the dynamic pressure variation to an acceptable level. Pressure fluctuations sampled by the probe were converted into an electrical signal by a transducer. Through the use of pneumatic filtering, only the frequency range of interest was retained. Figure 1 shows the assembled instrument package.

Probe

Since it is not possible to predict the dynamic pressure distribution over a streamlined body with sufficient accuracy, the shape of the probe was developed empirically. Testing was done in a wind tunnel.

It was considered desirable to design the probe such that the signal to noise ratio was about 10:1. The anticipated fluctuating signal level was taken to be ρu_*^2 (later found to be a good guess). Thus for a 5 m sec^{-1} wind over water, the signal would be approximately 0.3 dynes cm^{-2} and the desired maximum noise level would be 0.03 dynes cm^{-2}. This noise can be given in terms of a fraction of the stagnation pressure $\frac{1}{2} \rho U^2$ where ρ is the density

of air and U is the mean wind speed. The desired noise level is 0.001 of the of the stagnation pressure. Thus the task was to construct a pressure sampling probe which could operate at the various angles of incidence of flow that would be expected in the atmospheric boundary layer, and have a maximum dynamic pressure variation of only 0.001 of the stagnation pressure.

A suitable probe would be a shaped streamlined body, small with respect to the scales of interest, which has some point on its surface where there is sufficiently small variation in the dynamic pressure; the sampling port would be located at that point. The mean dynamic pressure at some position away from the stagnation point is minimized when the distortion of the natural flow as it passes a probe is minimized. W.W. Willmarth (personal communication to R.W. Stewart) suggested that a thin streamlined disk with a dipping in the central region might be a suitable method for flattening the streamlines. A few hundred different shapes, variations on streamlined disks similar to a planetary ellipsoid, had to be tested before a promising one was found.

The final probe was a thin, circular, streamlined disk attached to a long, thin tubular stem. The disk was slightly dipped in the middle, with two sampling ports located one on each side at the center, Figure 2. This probe was designed to be used with the plane of the disk in the horizontal. The thinness and central depression were designed such that the dynamic pressure at each of the two ports is close to zero for the wind speeds of interest. This helped eliminate pressure variations from arising from 'u', the downstream velocity fluctuations. Circular symmetry was maintained in order to eliminate 'v', the crossstream effects. Elimination of dynamic pressure changes due to 'w', the vertical wind fluctuations, was more difficult. For this the shape of the cross-section of the disk was most important. The profile was such that 'w' caused equal changes of opposite sign in the dynamic

pressure at the two ports. By connecting the ports, one on each side of the disk, to a single small nearly rectangular channel coiled in the disk, cancelling was obtained at the mid-point along the channel. The pressure signal was sampled from this mid-point. Because the requirements for eliminating the 'u' and 'w' effects conflicted, a compromise was necessary in order to keep the stalling angle as large as possible. For the shapes developed, the stalling angle was about 10°. This angle was considered large enough for the expected 'w'. If the wind came from a direction greater than the stall angle, the measured dynamic pressure jumped by an order of magnitude.

The disk part of the probe was constructed of brass. Initially it consisted of two halves (Figure 2), each 0.050 inches[1] thick and about $1\frac{3}{4}$ inches in diameter. In each of the halves a 0.031 inch wide, 0.020 inch deep slot was milled to provide the channeling between the ports and for the exit tubing. It was necessary that the two ends of the channel not intersect, but be close to the center of the disk for connection to the ports. To accomplish this, the ends of the channel were staggered to leave 0.0175 inches between the wall of the channel and the center. A 0.020 inch port was drilled at an angle from the center of the outer surface of each half, to intersect with an end of the channel. When the two halves were put together, this formed a 1.50 inch long channel (0.031 inches wide, 0.040 inches deep) connecting the two ports. The two halves and a 3/4 inch (2 cm) length of stainless steel stem (0.032 inch internal diameter) were glued together with epoxy to form the initial stage of the disk.

This disk unit was then shaped on a lathe and tested for performance in a wind tunnel. Further shaping and testing either produced a failure or a

---

1 standard engineering units

disk which had the desired qualities. The principal reason for a failure was inability to match the two sides of the disk; this was necessary for eliminating w effects. The shapes (measured with a micrometer) of suitable disks are shown in Figure 3. Table I, pages 16 and 17, contains the values used to plot these curves. It appears that it is necessary to keep the maximum and minimum thicknesses in the cross-section accurate to 0.001 inches, though the thickness between these points may vary by a few thousandths of an inch. This can be seen by comparing the disk shapes of probes E, F, and G, Figure 3. In reproducing these probes each half may be shaped completely before assembly, now that the appropriate shape is known.

The good disks were silver soldered to stainless steel tubing (Figure 1) of increasing outer diameter (for rigidity) to make an over-all stem length of approximately 22 inches (56 cm); the reason for this length is discussed in the next subsection. The internal diameter of this additional stem was 0.069 inches. The disk and stem together were the 'probe'.

Dynamic noise testing of the probes was done in a low speed, low turbulence wind tunnel with a 90 cm by 70 cm test section. The wind tunnel is in the Mechanical Engineering Department of U.B.C. It is a return type tunnel in which the air speed can be varied from 1 to 15 m sec^{-1}. The measured turbulence level is approximately 0.1%. Even in this low turbulence wind tunnel, other background noise necessitated working on quiet, windless nights. The probe to be calibrated was mounted near the middle of the test section; a special clamp was constructed to hold the probe at any preset angle relative to the air flow. The dynamic noise level was measured by comparing the pressure observed by the probe to the pressure at the static ring of the tunnel.

The dynamic pressure noise levels for the two probes used for most of

TABLE I

DATA FOR PLOTTING DISK CROSS-SECTIONS

PROBE E

side 1		side 2	
X	Z	X	Z
0.000	0.0000	0.000	0.0000
0.069	0.0285	0.106	0.0339
0.143	0.0379	0.184	0.0381
0.225	0.0421	0.263	0.0422
0.295	0.0435	0.360	0.0437
0.364	0.0436	0.432	0.0451
0.449	0.0429	0.507	0.0422
0.519	0.0410	0.589	0.0402
0.599	0.0413	0.669	0.0389
0.667	0.0403	0.719	0.0373
0.722	0.0394	0.784	0.0366
0.766	0.0387	0.790	0.0371
0.789	0.0388	0.857	0.0368
0.855	0.0387	0.913	0.0381
0.911	0.0397	0.978	0.0385
0.973	0.0402	1.038	0.0390
1.029	0.0408	1.124	0.0421
1.089	0.0418	1.190	0.0424
1.149	0.0432	1.235	0.0422
1.202	0.0435	1.307	0.0411
1.242	0.0422	1.364	0.0387
1.307	0.0424	1.415	0.0345
1.374	0.0399	1.482	0.0277
1.432	0.0345	1.578	0.0000
1.489	0.0285		
1.528	0.0235		
1.578	0.0000		

Diameter = 1.578 inches

Total Thickness = 0.087 inches

PROBE F

side 1		side 2	
X	Z	X	Z
0.000	0.0000	0.000	0.0000
0.086	0.0349	0.073	0.0336
0.132	0.0404	0.134	0.0414
0.179	0.0446	0.189	0.0453
0.240	0.0458	0.237	0.0458
0.292	0.0446	0.284	0.0458
0.341	0.0416	0.331	0.0458
0.388	0.0404	0.389	0.0436
0.435	0.0395	0.459	0.0413
0.479	0.0385	0.504	0.0408
0.533	0.0373	0.566	0.0392
0.578	0.0370	0.610	0.0382
0.624	0.0365	0.657	0.0371
0.686	0.0359	0.705	0.0361
0.731	0.0358	0.755	0.0362
0.772	0.0359	0.790	0.0362
0.789	0.0358	0.856	0.0362
0.827	0.0359	0.900	0.0373
0.879	0.0359	0.951	0.0380
0.930	0.0364	0.989	0.0381
0.989	0.0372	1.050	0.0398
1.063	0.0375	1.086	0.0408
1.108	0.0389	1.147	0.0421
1.151	0.0397	1.196	0.0433
1.193	0.0405	1.242	0.0455
1.240	0.0417	1.285	0.0450
1.277	0.0435	1.334	0.0450
1.347	0.0448	1.390	0.0445
1.383	0.0439	1.445	0.0404
1.422	0.0407	1.484	0.0358
1.468	0.0361	1.535	0.0247
1.580	0.0000	1.580	0.0000

Diameter = 1.580 inches

Total Thickness = 0.091 inches

TABLE I (continued)

PROBE G

side 1		side 2	
X	Z	X	Z
0.000	0.0000	0.000	0.0000
0.115	0.0339	0.110	0.0307
0.225	0.0426	0.200	0.0394
0.335	0.0442	0.325	0.0430
0.415	0.0459	0.435	0.0435
0.515	0.0436	0.525	0.0415
0.625	0.0411	0.615	0.0399
0.715	0.0394	0.705	0.0387
0.790	0.0379	0.790	0.0367
0.900	0.0383	0.900	0.0383
1.015	0.0399	0.995	0.0393
1.100	0.0426	1.095	0.0421
1.195	0.0434	1.185	0.0434
1.295	0.0425	1.290	0.0427
1.390	0.0374	1.375	0.0391
1.485	0.0338	1.470	0.0300
1.581	0.0000	1.581	0.0000

Diameter = 1.581 inches

Total Thickness = 0.088 inches

the experimental work can be seen in Figures 4 and 5. Each figure is four graphs. Three of the graphs, labelled as different constant wind speed, have axes of pitch and yaw which represent the alignment of the probe with respect to the mean wind. Pitch is rotation about a horizontal axis perpendicular to the mean flow; this simulated 'w'. Yaw is rotation about a vertical axis; this simulated 'v'. Zero angles represent the ideal alignment of the probe with respect to the mean wind: the stem parallel to the mean wind and the plane of the disk horizontal. The fourth graph shows the effect of a change in mean wind speed when the probe had the ideal alignment; this simulates 'u'. The values plotted are the ratios R_D of the measured dynamic pressure to the calculated stagnation pressure multiplied by - 1000. For example, in Figure 4 the value plotted at 0° pitch and 0° yaw when U = 6.1 m sec^{-1} is 10. Thus the measured dynamic pressure for this alignment and wind speed was $10\ P_s / -1000 = -0.01\ P_s$ where P_s is the stagnation pressure. An * plotted on the graphs means that the probe stalled. It had been decided above that an acceptable change in this ratio between the measured dynamic pressure and the calculated stagnation pressure for typical velocity fluctuations to be expected in an atmospheric boundary layer is about 0.001. This is a change of 1 between the values plotted on the first three graphs or a change of 1 along the vertical axis of the fourth graph. Superimposed on the dynamic noise plots, by means of dashed curves, are the statistical limits for the velocity fluctuations expected to occur over a smooth terrain with small roughness elements, such as over water. The outer curves contain 95% of the expected fluctuations in the wind, the inner curves 68%. For these calculations, the velocity fluctuations were assumed to have a Gaussian distribution. From the graphs it can be seen that for 95% of the expected angular or downstream wind variations the dynamic pressure noise of a probe operating in

a wind between 3.5 and 9 m sec^{-1} is about 0.001 to 0.002 of the stagnation pressure (a change of 1 to 2 on the graphs). Misalignment of the probe, mean wind shifts and non-Gaussian, low frequency velocity changes could cause the limit curves shown to shift to an area on the graphs where the dynamic pressure variation is larger than that shown. Thus a more realistic noise figure would be about 0.002 of the stagnation pressure giving a minimum signal to noise ratio of 5:1.

These probes were considered suitable for initial studies in a turbulent atmospheric boundary layer.

Transducer *et al*

The transducer and pneumatic filtering apparatus, which are connected to the end of the probe stem, are enclosed in a streamlined container (Figure 1). Once the size of this container was known, the stem length of the probe was chosen (by calculation and experimentation) to keep the sampling ports beyond any dynamic pressure noise due to blockage. The electrical output from the probe-transducer assembly (see Figure 1) was transmitted by cable to conditioning and recording equipment often up to 100 meters away.

The transducer system used to convert the pressure fluctuations into electrical signals was the 'Barocel Modular Pressure Transducing System' (Datametrics Inc., Watertown, Mass., U.S.A.). It consists of three units: a pressure sensor (Type 511), a signal conditioner (Type 1015), and a power supply (Type 700) (see Figure 6). The pressure sensor was a 0 to 10 mm Hg (0 to 1.3×10^4 dynes cm^{-2}) low internal volume model (0.1 cubic inch) with quick disconnect fittings. A diaphragm in the pressure sensor is deflected by any pressure difference between two inputs. One input is connected to the

probe, the other to a reference volume which acts as a reference pressure. Since the diaphragm is the common plate for two capacitors which are both excited at 10 kHz, it takes on a voltage proportional to the pressure difference. This electrical signal is fed to the signal conditioner by cable. Long cables, up to 150 meters, permitted remote operation. The signal conditioner accepts the amplitude modulated 10 kHz signal and converts it into a 0 to ±5 volt DC signal. Different full scale sensitivities are obtained by means of a resistance voltage divider. A null adjust, full scale adjust, quadrature adjust, and sensitivity adjust allow the system to be corrected for offsets, loading, ground loops, and calibration respectively while connected in the recording mode. In order to make these adjustments easily, a valve between the two inputs of the pressure sensor can be opened. This valve was closed while taking measurements. The quoted accuracy for the 'Barocel' system is about 0.5% of the reading; noise level is approximately 5 mv; and the transient response is less than 2 milliseconds. These specifications are more than adequate for the present requirements.

Before the pressure signal is converted into an electrical signal, it is subjected to pneumatic filtering. This filtering gives a band-pass characteristic to the electrical output. In order that most of the Reynolds stress range could be observed, the frequency range chosen for this study is about 0.003 to 10 Hz. The high frequencies are damped by viscosity in the small passages of the disk and probe stem. Through experimentation on the internal diameter and the lengths of the connections to the disk, it was possible to keep the frequency response flat to approximately 20 Hz. The low frequencies are eliminated by allowing the reference volume to follow the low frequency pressure fluctuations. This floating is accomplished by a small slow leak between the signal side and the reference side of the transducer.

A 27 gauge, 1/2 inch hypodermic needle was found to be a suitable leak. The positions of the high and low pass cutoffs are by design, not default, and are used to obtain optimum signal levels for the frequency range of interest. The frequency calibration is described in the next subsection.

Since temperature or volume changes within the probe and transducing system can also cause a pressure change (PV/T = constant), care is necessary, especially on the reference side, to keep these noise sources below the desired noise level. The limitations are a net temperature fluctuation of less than 10^{-4} C° and volume fluctuations of less than 3×10^{-5}%. To meet these restrictions, the entire transducing system and probe package has to be rigid and adequately insulated. A half litre vacuum flask (Figure 7) provides a pressure reference with volume and thermal stability. This is connected to one side of the transducer by 6 mm diameter, insulated, copper tubing. All other interconnecting passages are formed by drilling a solid block of acrylic plastic. The container for the Barocel sensor and reference volume is a cylindrical aluminum pipe with a streamlined cone on the upwind, probe side, and a flat plate on the downwind side (Figure 1). Inside this pipe, and attached to the front cone is a rack on which the transducer and reference volume are solidly mounted. When assembled, the back plate bolts into position forming a rigid, watertight container. The electrical connections are through the back of the case and watertight plugs are used so that the case can be disconnected from the long instrument cable. To make the attachment of the probe simple, a 'quick disconnect' fitting is provided on the front cone. To help maintain thermal stability, the outer surfaces of the case and probe are kept highly reflective. These precautions are sufficient to reduce temperature and mechanical noise sources to the level required.

Once the size of the transducer case was known, the length of the stem

of the probe had to chosen just sufficiently long enough to keep the disk away from the dynamic pressure field produced by either the case or the brackets used for holding the system. Potential flow theory was used to calculate the upwind pressure perturbation for a sphere and for an infinite cylinder. It was assumed that most of the objects producing blockage could be approximated by one of these. For a position x, upwind of a sphere, the pressure, p, is given by

$$p = \rho \left[-\frac{1}{2} U^2 \left(1 - \frac{a^3}{x^3}\right)^2 + \frac{1}{2} U^2 \right] ,$$

where a is the radius of the sphere, U is the mean air velocity, and ρ is the density of air. For the noise level required, the measurements would need to be about 8a away. Thus, assuming the case looked like a sphere to the airflow, the length of the stem needed to be about 50 cm. The size of the dynamic pressure perturbation for a model of the actual container was checked in a wind tunnel. The results are illustrated in Figure 8 and show that the stem length of about 8a was adequate. A similar calculation for an infinite cylinder, of radius a, perpendicular to the mean flow gives

$$p = \rho \left[-\frac{1}{2} U^2 \left(1 - \frac{a^2}{x^2}\right)^2 + \frac{1}{2} U^2 \right] .$$

For the same noise level, the probe disk must be 20a to 25a ahead of a cylinder. These two values were used as criteria in evaluating blockage by the case and cylindrical supports during measurements.

Amplitude and Phase Response

The pressure instrument (probe and transducer) was calibrated for amplitude and phase response. If the response is linear, as was assumed, then data can be corrected using the calibrations on the basis of the convolution theorem (e.g., Lee, 1960, p.28).

The arrangement used for calibrating the instrument is shown in Figure 9. A sinusoidally varying pressure was produced in a closed 5 gallon drum by oscillating a latex rubber diaphragm stetched over one end. The drum is shown in more detail in Figure 10. The diaphragm was oscillated by contact with a circular acrylic plastic plate that was attached to a Pye-Ling V45 vibration generator which was in turn driven by an amplified voltage from a signal generator. Figure 11 is the circuit diagram for the power amplifier. A Barocel transducer (see Figure 9) referenced to the atmosphere was used to directly measure the magnitude and phase of the pressure in the drum. Using a strip-chart recorder and an oscilloscope, this measured drum-pressure was compared with the pressure recorded by the pressure instrument when the probe was sealed inside the drum.

A sample calibration is shown in Figure 12; the measured dropoff is about 6 db/octave at the high frequency end and 3 db/octave at the low frequency end. It is representative of all calibrations done for that probe and transducer and is typical of those obtained for the different probes. The accuracy of the calibrations is approximately ±2% in amplitude and ±3° in phase.

To ensure that these calibrations were maintained, the instruments were calibrated before and after each group of field observations.

IN SITU CALIBRATIONS OF THE PRESSURE INSTRUMENT

Even though the probes had been tested in a wind tunnel and found to meet the initial requirements, much more confidence would be obtained if they were calibrated in typical atmospheric turbulence. This was done by measuring the turbulent pressure fluctuations in the air, with the developed probe, and comparing the results with simultaneous measurements of the pressure fluctuations at a surface port directly below. A surface pressure measurement does not have the problem of dynamic pressure contaminations provided the Reynolds Number of the port is sufficiently small (Shaw, 1960); a 0.025 inch diameter port was used to meet this requirement. If the same static pressure signals are measured by both the surface and air systems then suitable comparisons will show any dynamic pressure noise associated with the probe. The usual distance between air and surface measurements was 30 to 40 cm. This height was necessary to ensure that a typical mean wind and turbulence level were encountered. It was also sufficiently high to include any important vertical velocity effects in the frequency range to be analysed. Thus those pressure fluctuations with a vertical scale much greater than 30 to 40 cm could be reliably compared.

Surface Pressure Measurement

To obtain a surface pressure measurement which does not include any unwanted dynamic pressure fluctuations, the area surrounding the port should be smooth and level. There should be no small scale blockage in the vicinity of the port and any long, surface undulations should have scales large compared to the separation of the air and surface instruments. The transducer and

reference volume used for the surface measurement were identical with that used with the probe and were enclosed in a wooden box that could be positioned below ground level, Figure 13. Part of the top of this box was a 20 cm by 15 cm flat aluminum plate. By carefully positioning this plate and the rest of the box flush with the local terrain, all dynamic effects were eliminated over a surface port in the aluminum plate.

Since it was necessary to calibrate the surface system, the 0.025 inch port was not drilled directly into the aluminum, but instead into a 1 inch (2.5 cm) diameter brass plug. This plug could be removed from its tightly fitting position in the aluminum plate so that the port and the 4 inch (10 cm) long steel tubing which led from port to transducer could be calibrated without modification. The method of calibrating for amplitude and phase response was identical to the one used for the air system. A typical calibrations is shown in Figure 14. The connections between surface port, transducer and reference volume were similar to those used for the air pressure measurement. On some occasions the transducing system normally used for the air measurement was used for the surface measurement and vice versa.

The *in situ* field calibrations were done at two sites: Ladner and Boundary Bay (see Appendix A). At the Ladner site winds blew from the west perpendicular to a 40 meter wide asphalt runway. Upwind the terrain was mainly thick grass 5 to 10 cm high. The surface measurement was made 34 meters from the leading (windward) edge of the runway. Fine sand made a smooth transition between the box and the surrounding surface. At the Boundary Bay site, the terrain was more inhomogeneous. At this site the box containing the transducer for the surface pressure measurement was conveniently placed flush with the sand surface. However only an area within 2 to 3 meters of the box could be considered flat and smooth. Patches of grass, water-filled potholes,

and the occasional log were sometimes on the upwind side. Some effort was made to ensure that any turbulence generated by this inhomogeneous terrain was of a scale large compared to the separation of the sensors.

Comparison of Measurements: Surface and Air

The power spectra, coherence, and phase are used to compare the pressure signals measured by the probe in the air and surface port. If the two signals are the same, which is expected for large scales, they have the same power spectrum and phases and have unity coherence.

A comparison of power spectra, $\Pi(n)$, for five of the ten Runs taken at the Ladner site is shown in Figures 15 and 16. Included in these comparisons are three different probes and two different transducing systems. All the data were corrected for amplitude and phase response. The vertical bars on the lower curves denote typical 95% confidence limits (c.l.) for each estimate plotted. The vertical extent of the dashed line on the low frequency side of each curve indicates the amount by which each spectral pair in a given comparison were shifted vertically relative to the actual measured values. This shifting was done to accommodate more than one pair of spectra on the same vertical scale without hindering comparison of pairs of curves. Thus to return a pair of spectra to their true position with respect to the vertical axis, the entire curve must be shifted vertically until the dashed line becomes parallel with the abscissa or frequency axis. The two curves in Figure 15 are from measurements with a vertical separation of 40 cm. The same probe was used but the transducing systems were interchanged. For the three in Figure 16, the vertical separation was 32 cm. The only part changed in these three runs was the probe (probes E, F, and G were used). Each pair

of spectral estimates agree to ±20% (±10% in amplitude) for frequencies from 0.010 to 1 Hz. Differences in this frequency range appeared to be random from Run to Run. The values at the lowest frequency plotted in the spectra often differed by more than 20%. This was considered to be an effect of the analysis. The consistently lower surface pressure in the 1 to 10 Hz range was thought to be due to the internal boundary layer over the runway that resulted from the large surface roughness (z_o) transition (grass, $z_o \simeq 2$ cm; asphalt, $z_o \simeq 0.1$ cm). Using Panofsky and Townsend (1964), the predicted thickness of the internal boundary layer at the point of measurement is only 7 meters. When measurements were made with the pressure probe moved successively downwind from the surface port, the difference at high frequency became less definite, as would be expected. For the frequency range analysed, this set of observations showed that the amplitude of the pressure fluctuations within the flow could be measured to approximately ±10%.

The other requirement for the two signals to be the same is that the phase difference be zero for frequencies at which the coherence is high; that is, for vertical scale lengths large with respect to the vertical separation of the probes. The phase and coherence for the same 5 Ladner Runs are plotted in Figure 17. The coherence is approximately 0.95 for large scale fluctuations, falling off at the higher frequencies. This falloff is expected due to the vertical separation. The coherence less than 1 is an indication of the non-coherent noise between the two systems, including dynamic, thermal, volume fluctuation, and electrical noise. The phase difference for the scales with high coherence is within ±5°, which is as close as can be expected.

A similar comparison was made for some of the Boundary Bay observations. In most cases the pressure measurements in the air were 30 cm above the surface port; a few were 1 m. Four spectra from this site are shown in

Figure 18; the vertical separation is given in brackets after the Run number. The curves were shifted vertically with respect to the vertical axis in the same manner as done in Figure 15 (described above). Again each pair of spectral estimates are the same to ±20% in power, including the 1 to 10 Hz range. No specific internal boundary layers were expected at this site, however, from some wind directions a high frequency difference similar to that at Ladner was observed. The phase and coherence shown in Figure 19 are also similar to the Ladner results; coherences are 0.8 to 0.9 and phases are the same to ±10°.

It is felt that the instrument has been thoroughly tested in a turbulent air flow typical of atmospheric boundary layers with neutral stability and has proven to be suitable for making static pressure measurements in the air.

MICROSCALE PRESSURE FLUCTUATIONS OVER A FLAT BOUNDARY

Some aspects of the kinetics and kinematics of pressure fluctuations in a turbulent boundary layer were measured using the developed pressure sensing probe.

The observations were made at two sites: Spanish Banks and Ladner. The sites are described in Appendix A. The Spanish Banks' sites is located on a tidal flat with a tidal range of about 4 meters. However most of the observations used in this section were taken when the water was either absent or very shallow, leaving a surface of sand or water with small waves of wavelength less than half a meter. Four data Runs (Appendix C) taken when the water was deeper and larger waves were present are also used in this section. These four Runs were taken at a height sufficiently above the waves that the spectra did not show any influence from the waves similar to that found in observations taken closer to the waves. The wave influence on spectra is described in the next section. All observations were taken below a height of 6 meters. For both sites winds at the 5 meter level during observations were about 3 to 10 m sec^{-1}. The wind stress was assumed to be constant with height and for the surface roughnesses encountered was generally between 0.1 and 1 dynes cm^{-2}. The method used to evaluate the stress is given in Appendix B. The local stability at the Spanish Banks site was usually near neutral to slightly unstable during observations (see Appendix C), with a Gradient Richardson Number of 0 to -0.1. For this range velocity spectra show little dependence on stability (McBean, 1970). The stability was not measured at the Ladner site, however the observations were taken on cloudy (but dry) days when local buoyancy effects would be at a minimum. Thus stability was probably not important for most of these pressure observations, except for those spectral estimates

dependent on any stability at a higher elevation which, through the 'integral effect', could influence low frequency values. These sites were considered suitable for making pressure measurements typical of a turbulent atmospheric boundary layer.

Results obtained from observations at these sites are given in the following subsections.

Nondimensionalization of Pressure Spectra

Since the pressure is closely tied to the velocity, as shown by equation 2, the same nondimensionalization parameters should be valid. The importance of each of the possible parameters is considered in terms of the pressure spectra obtained in this study.

The parameters used to nondimensionalize velocity spectra are usually a time scale of z/U and an intensity of u_*^2. One other parameter that might be used is the stability, which would be more important for the pressure due to the 'integral effect' (equation 3). As has been previously mentioned all data were collected under conditions estimated to be of nearly neutral stability. Recent work (McBean, 1970) shows that the nondimensionalizing of velocity is relatively insensitive to stability under these conditions. Since the stability was nearly neutral during all Runs, it is assumed to be of secondary importance.

The influence of the 'integral effect' on pressure spectra is seen in observations taken simultaneously at two levels. Figure 20 shows spectra, Π, for 0, 1.8, 3.75, and 5.5 meter vertical separations. As in Figures 15 and 18 the dashed line indicates the vertical shift of each curve (as discussed on page 26). Figure 20 shows that there is no large systematic difference in spectral levels due to the vertical separation of the measurements. In contrast, spectra of the velocity components show a direct dependence on z

(see McBean, 1970) and can be nondimensionalized using the nondimensional frequency $f = \frac{n\ z}{U}$. The 'integral effect' appears to have removed any strong z dependence from the pressure spectra at these lower levels. Other observations with vertical separations give similar results.

It is difficult to define a U_p, or propagation velocity, for use in the nondimensionalizing. For example, an observation made at the bottom of the boundary layer, where the mean velocity is zero, has a pressure power spectrum similar to, if not identical with, that at, say, 1 meter, where the mean velocity is non-zero.

Since the pressure spectra will have some direct dependence on the mean wind but have been shown above to have little on z, frequency is not nondimensionalized in the analysis but is changed into a wave number defined by $k_p = \omega / U|_5$, where $U|_5$ is the mean wind at 5 meters.

The intensity of the pressure fluctuations was nondimensionalized by $\rho^2 u_*^4$. Since the same kinds of data were not available for each Run, three different methods of evaluating u_*^2 were used: direct measurement using a sonic anemometer (the most reliable method); calculation using the Φ_{11} method; and use of a drag coefficient of $C_D = 1.2 \times 10^{-3}$. Further discussion on the methods is contained in Appendix B.

Examples of pressure spectra which are nondimensionalized in this way are shown in Figures 21 and 22. For values of wave number k_p greater than 3×10^{-3} cm^{-1}, the spectra have approximately the same slope, -0.7. At lower wave numbers the slope is less steep and there is more scatter, similar to that which occurs in low frequency velocity spectra. The range of u_*^4 involved is 1×10^4 to 50×10^4. After nondimensionalizing, extreme values of $k\Pi(k)$, at a given k_p, now differ by a factor of 2 whereas the dimensional spectra differed by a factor of about 50. The variance between spectra could not be improved

with the present data since that of u_*^2 is about ±20% and of $\rho^2 u_*^4$ about ±40%. The levels of the nondimensionalized pressure spectra scatter within this value; therefore the scatter might be due entirely to the error in u_*^2 rather than to dependence on some other variable.

All spectra which were nondimensionalized in this manner are summarized in Figure 23. The value of $\frac{k\Pi(k)}{\rho^2 u_*^4}$ at $k_p = 10^{-2}$ cm^{-1} is plotted as a function of z. The mean is 3.5 ± 1. As noted earlier there is no noticable dependence on z.

The data given by Gorshkov (1967) do not seem to agree with these present results; they do not exhibit the U^4 dependence shown here. As the wind speed increased the intensity of his pressure spectra did not necessarily increase. It is not known however whether all of his measurements were taken with a nearly constant surface roughness.

From the present study, it appears that the pressure spectra below 5 meters in an atmospheric boundary layer of nearly neutral stability are adequately nondimensionalized in terms of the stress, ρu_*^2, and a wave number $k_p = \omega / U|_5$.

Shape and Intensity of the Spectrum

As with any turbulent variable, the shape and intensity of the power spectrum for pressure fluctuations gives some clue of the role of pressure at different frequencies.

Normalized pressure spectra, $\Pi(n)/\sigma_p^2$ (Hz^{-1}), are plotted in Figure 24. They are normalized by their integrals, which equal their variances σ_p^2, between 2.7×10^{-2} and 7.4×10^{0} Hz, the frequency range plotted. These

spectra, previously shown in nondimensional form in Figure 21, were chosen because associated velocity spectra are available. They are considered to be representative of all those obtained over a flat boundary. The observations were taken at heights of 3 to 5 meters; surface wind stress was approximately 0.8 dynes cm^{-2}. The spectra show a regular power law behaviour above 0.3 Hz, most of the variations between different spectra occuring at the low frequency end. Vertical lines indicate the 95% confidence limits (c.l.) of individual estimates.

The velocity spectra associated with the pressure spectra in Figure 24 are shown in Figures 25 and 26. $\Phi_{ii}(n)$ is the frequency spectral density for the i^{th} velocity component. These velocity spectra conform with the 'universal curves' obtained by McBean (1970).

The slopes of the velocity and pressure spectra in isotropic turbulence have been predicted from dimensional arguments (see Background p.9) to be -5/3 and -7/3 respectively. The -5/3 for the velocity spectra is a reasonable fit to the data for frequencies above the peak of the w spectrum, Figures 25 and 26; the straight line has this predicted slope. For the same frequency range, the pressure spectra, Figure 24, has a mean slope of about -1.7, significantly different from the -2.3 predicted. The approximate position of the peak of the w spectrum is indicated by the arrow. Despite the -5/3 slope of the velocity spectra in this frequency range, the turbulence may not be completely isotropic (Stewart, 1969). The suggestion is that the pressure is more sensitive than the velocity to any such anisotropy.

Three other indications that complete isotropy is not present in this frequency range are also found. Figure 27 is a plot of the u and w cospectrum, Φ_{13}. This has significant values near f = 0.6; that is, at the lower

frequencies of the -5/3 slope region of the velocity spectra. Thus this part of the flow cannot be described as isotropic. Also (to be shown later in this section, see Figure 46) significant energy flux out of the u velocity component by the pressure forces occurs through most of the frequency range 1 to 10 Hz. It is also shown later that throughout the higher frequencies, the turbulence cannot be described as completely isotropic since the pressure-velocity coherences do not become insignificant until near the highest frequencies plotted. Thus for these nondimensional frequencies studied (less than 10) the data seem to indicate a lack of complete isotropy. Because of the lack of isotropy these data are not a critical test of the -7/3 behaviour for pressure spectra in isotropic turbulence.

Even though the wave number range $\omega/U|_5 > 10^{-3}$ has been used to obtain the Kolmogoroff constant for velocity, it is questionable whether a rough estimate of the universal constant, K_p, in Obukhov's formulation (p.9) can be made since the pressure spectra do not have a -7/3 slope. A further difficulty in trying to evaluate K_p with the present data is the lack of any z dependence in the pressure spectra, $k\Pi(k)$ (see Figure 21). If the rate of dissipation, ε, is given by $u_*^3/\kappa z$ (the rate of energy production),

$$K_p = \frac{k\,\Pi(k)}{\rho^2\, u_*^4}\,(\kappa k z)^{4/3}.$$

Thus for the data obtained K_p would vary as $z^{4/3}$ and not be a constant.

A different theoretical argument predicting the slope of the pressure spectrum has been given by H. Charnock (personal communication to R.W. Stewart). Based on similarity asssumptions, he predicted a -1 slope. This is also not

present in the data for any significant range of frequencies.

The mean shape of the pressure spectra in Figure 24 is used for comparison with previously published pressure spectra, Figure 28. The latter were shifted vertically to lie near the mean curve from Figure 24. All of these spectra were obtained in the atmospheric boundary layer at comparable wind speeds. The observations by the two Russian authors, Golitsyn (1964) and Gorshkov (1967), are of surface pressure measurements; those by Gossard (1960) were taken in the air. The intensity of the Russian observations is of the same order of magnitude as that obtained using the developed probe, while Gossard's results are an order of magnitude larger. Nevertheless the mean slopes of these curves are similar to that obtained in the present study. At low frequencies some of the differences may have been due to sources other than the boundary layer turbulence; such as, internal gravity waves at higher elevations (Herron et al, 1969).

Variations from the well defined slope shown in Figure 24 were occasionally observed in this study; they were similar to those found by Gorshkov (1967). They could be attributed to a lack of stationarity and non-uniformity of the terrain.

A more detailed comparison between the pressure and the velocity is shown in Figure 29. Plotted against frequency are two curves representing the variance within narrow frequency bands of the nondimensional pressure and of the nondimensional sum of the three velocity components from Run 120/1. The values plotted are $\sqrt{\Pi(n)\ \Delta n}\ /(\ \rho u_*^2)$ and $(\ \Phi_{11} + \Phi_{22} + \Phi_{33}\ )\ \Delta n\ /\ u_*^2$ where Δn is the bandwidth. The velocity components and the stress were measured with a sonic anemometer at the same level as the pressure probe. The values have been plotted in this form to show how the relationship between the pressure variance and velocity variance changes for different scale ranges.

As can be seen both curves exhibit a similar shape. At high frequencies the pressure curves is roughly twice the velocity curve; at low frequencies, $f < 1$, the pressure curve is more than twice the velocity curve. Since the velocity curve is a function of z and the pressure curve is not (p.30) this relationship has some z dependence which would be most noticeable at the high frequencies, near and above the peak of the w spectrum. At lower frequencies the maxima and minima would not have a z dependence since they arise from u and v fluctuations of scales much larger than the observation height. The other Runs in this group (p.33) were at similar heights and have the same general properties. Batchelor evaluated, from the velocity correlation, a value for the rms amplitude of the pressure fluctuations in isotropic turbulence. His result was $\sqrt{\overline{p^2}} = 0.58\ \rho u^2$ (p.10). It is questionable whether this result can be compared with the present measurements since, as shown above, in the range analysed the turbulence was not completely isotropic. At the higher nondimensional frequencies, $f > 1$, Figure 29, where some semblance of isotropy may have existed, the root-mean-square pressure is about ten times that expected from Batchelor's relationship. This higher pressure might be due to interaction between the turbulence and the mean shear as suggested by Kraichnan (1956). He predicted that the major term would be of the form $\rho(\partial U/\partial z)(\partial w/\partial x)$. The scales of the turbulence at frequencies near $f = 1$ are of the order of 50 cm, sufficiently large that an interaction with the mean shear would be expected.

The spectra plotted in Figure 21 show that, at least for this group of data, there is no strong influence from the low frequency mesoscale phenomena which were found in pressure spectra by Gossard (1960). These spectra appear to drop off at these lower frequencies in a manner similar to the velocity spectra. These data are used to evaluate the relationship between the pressure variance and the surface stress assuming that the pressure fluctuations

arise entirely from boundary layer turbulence.

A linear plot showing the average of the nondimensionalized pressure of Figure 21 as a function of wave number is given in Figure 30. The curve is considered to be representative of all the data collected. The nondimensionalized pressure, $k\Pi(k)/(\rho^2 u_*^4)$, in Figure 30 was integrated with respect to ln k from a wave number, $k_p = \omega/U|_5$, of 10^{-5} to 2×10^{-2} cm^{-1}. The dashed lines indicate the curve used near the limits of the integration. This integration gives the root-mean-square pressure in terms of the surface stress, ρu_*^2:

$$\sqrt{\overline{p^2}} \simeq 2.6\ \rho\ u_*^2 \qquad (12).$$

This relationship is almost identical to that obtained from surface measurements in wind tunnels (Willmarth and Wooldridge, 1962). Since, as will be shown later, the nondimensionalized curve integrated to get the root-mean-square pressure is not a function of height, the relationship would be expected to hold at the surface. The magnitude given by equation (12) is in the range predicted theoretically by Kraichnan (1956).

In summary, the pressure spectrum is similar in shape to the velocity spectrum and has a variance of about $6.5\ \rho^2 u_*^4$.

Some Kinematics of the Pressure Fluctuations

From the simultaneous measurement of static pressure fluctuations at two points it is possible to deduce some properties of the structure of these fluctuations. Observations were spaced in each of the three principal directions. Phase and coherence are used to evaluate the orientation, scale size and propagation velocity of the fluctuations.

Coherence and phase between different pairs of points with purely

vertical (Δz) and purely transverse (Δy) separations are shown in Figures 31 and 32. The phases plotted are for frequencies at which the coherence was greater than 0.2. The separations used are suitable to observe any phase shifts that may be present in the pressure fluctuations in the frequency range of interest. For vertical separations of up to 5 meters, the average phase difference is near zero. Thus there is no preferred vertical orientation for a pressure fluctuation in this range. As expected, the average relative phase for transverse separations is not significantly non-zero.

From a comparison of the coherence and phase for two sensors with a downstream separation it is possible to estimate the 'decay rate' of the pressure fluctuations. Ideally, to conform with the 'frozen field hypothesis', the coherence should be 1 at all frequencies and at all downstream separations and a phase difference should result, the size of which depends on the downstream separation of the pressure sensors. A comparison of phase and coherence, Figure 33, shows that the signals become essentially incoherent for phase shifts of about 360° or approximately after one wavelength. Willmarth and Wooldridge (1962) found from wind tunnel studies using time lag covariances that significant energy had been lost by a pressure pattern that had travelled a distance of about two to three wavelengths (see their Figure 10). Time lag covariances would be expected to yield a larger and correct estimate of 'decay rate'.

From the coherence between two pressure signals at a given separation, a scale for the pressure fluctuations can be determined. When measuring the pressure with two pressure sensors at a fixed separation perpendicular to the mean flow, pressure fluctuations with a 'scale' size large compared to the separation of the sensors will often occur simultaneously in the two signals producing a high coherence, while fluctuations with a 'scale' size small compared to the separation cannot occur simultaneously. Those fluctuations with a 'scale' comparable to the probe separation can occasionally produce

some coherent signal at the two probes. Thus the pressure scale length at frequency n, $L_p(n)$, is defined as that separation at which the coherence falls through some low but measurable value. The frequency chosen is that at which

$$\Pi_{12} = \frac{1}{e^2}\,\Pi_1 \simeq \frac{1}{e^2}\,\Pi_2$$

where Π_{12} represents the coherent energy between two signals of energy Π_1 and Π_2, and e = 2.72. In other words, where the

$$\text{coherence} = \sqrt{\frac{\Pi_{12}^{\,2}}{\Pi_1\,\Pi_2}} = \frac{1}{e^2} = 0.14\ .$$

(For separations perpendicular to the mean flow, a scale based on the coherence is equivalent to a scale based on the correlation coefficient). The coherence of 0.14 represents a definite but low common energy between two pressure signals.

Representative coherences for the three different separation directions are given in Figures 31, 32, and 33. Since the frequency n_L at which the coherence falls to 0.14 depends on the propagation velocity, it is converted into a wavelength, λ_p, which is independent of the mean wind using

$$\lambda_p = \frac{U|_5}{n_L} \qquad (13).$$

It will be shown later that $U|_5$ is a close approximation to the actual propagation velocity of the pressure fluctuations for data analysed in this manner. λ_p is to be compared to L_p. If coherent noise[1] is present before

---

1 This can arise from wow and flutter in the analog tape recorder.

the coherence falls to 0.14 the curve is extrapolated by a straight line. Probe separations (equivalent to L_p for $n = n_L$) are plotted as points against λ_p for coherences of 0.14 on the log-log plot in Figure 34. The solid line drawn among the points has a slope of 1; that is, L_p varies directly as λ_p. All directions yielded similar L_p for a given λ_p (including downstream separation, since the decay time is about one cycle). Wind tunnel observations (Willmarth and Wooldridge, 1962) also found the two horizontal scales to be comparable in size. Thus, as a first approximation, the mean shape of a pressure fluctuation is spherical. An L_p of 100 cm corresponds to a λ_p of 210 cm. Therefore the actual size of the pressure fluctuations (L_p) is approximately 1/2 of a wavelength, λ_p. The choice of different coherences to determine the scale size changes only the proportionality constant between L_p and λ_p. The value of 0.14 is close to the practical limit.

Figure 34 also shows a family of curves of constant coherence plotted from the same Runs used in evaluating L_p. These are used to evaluate the influence of probe separation on data. As can be seen in Figures 31, 32, and 33, at a given separation, coherence falls off roughly linearly when plotted against ln n. This falloff is approximately the same in all cases and can be represented by coherence $\propto (\ln n)^{-0.7}$. This slope was used to plot lines of constant coherence in Figure 34. The coherence at a given separation, Figures 31 and 32, also has a plateau which decreases as the separation increases, as indicated on Figure 34. This plateau is not well defined and the corresponding probe separation values shown, for which a given plateau occurs, vary by about ±100%. The drop in coherence at the lower frequencies is thought to be due to noise.

These results of scale size and decay rate can be used to estimate the expected magnitude of the pressure fluctuations. Assuming that the pressure

fluctuations result from the complete acceleration or deceleration of a velocity fluctuation, the order of magnitude of $\frac{1}{\rho}\frac{\Delta p}{\Delta z}$ will be of the order of $\Delta u_i/\Delta t$, where Δ indicates the rms fluctuations from the mean. For Run 120/1 (Figures 24 and 25) at 0.7 Hz (bandwidth = 0.21 Hz), $w \simeq u \simeq v \simeq$ 10 cm sec^{-1}; $\Delta p \simeq 1$ dyne cm^{-2}. The gradient of p will act over a distance of about $L_p/2$. Thus for the example,

$$\Delta z = \frac{L_p}{2} = \frac{U|_5}{4\, n_L} \simeq 250 \text{ cm.}$$

These values give $\Delta t = \rho\, \Delta u_i\, \Delta z/\Delta p \simeq 3$ sec. This is comparable to the calculated 'decay time' of about 4 seconds assuming the distance required for appreciable decay of a pressure fluctuation is about 3 wavelengths (see p.38).

The propagation velocity is evaluated from the phase difference between two simultaneous pressure measurements with a downwind separation. Figure 33(b) shows the phase difference, Θ, for downwind separation (D) of about 0, 1, 2, and 4 meters. The measurement upwind was of surface pressure and that downwind was in the air (at 32 cm). The propagation velocity is calculated from

$$U_p = \frac{360°}{\Theta}\, D\, n_\Theta \qquad (14),$$

where n_Θ is the frequency at which the phase difference is Θ. The velocity, U_p, is then compared with the mean wind, $U|_{L_p}$, at the level L_p appropriate to the frequency n_Θ, since this height is more representative of the mean wind at which the pressure fluctuations of frequency n_Θ originated. The mean wind at level L_p is interpolated from observed cup profiles. The height L_p is calculated by taking $U|_5/n_\Theta = L_p'$ as a first approximation and then letting

$L_p = U|_{L_p}/n_\theta$. The second step adds less than a 10% correction. Table II gives the results of the velocity comparison. Four different phase differences were used: 90°, 180°, 270° and 360°. Since the scale size L_p is different for each phase difference, the $U|_{L_p}$ used for comparison with U_p is evaluated for each phase shift. The Ladner observations, considered to be the most accurate because of low instrument noise and steady state mean flow, give values of

TABLE II

Pressure Propagation Velocity, U_p, as a Fraction of $U|_{L_p}$

Site	L	L	L	L	B.B.	B.B.	S.B.	S.B.	S.B.
Run	320/2	425/1	425/2	426/1	137/2	142/1	196/1	196/2	196/3
$U\|_5$ m/sec	7.7	6.1	5.2	6.1	4.1	4.3	3.7	3.4	3.7
D (m)	0.96	2.0	3.1	4.1	0.56	0.56	4.3	2.7	1.5
$\frac{U_p}{U\|_{L_p}}$	0.90	0.97	1.49	1.08	0.96	0.95	1.20	1.15	1.10
	0.91	0.93	1.17	1.04	0.99	0.99	1.30	1.15	1.00
	0.96	0.91	1.04	0.99	1.10	1.05	1.10	1.14	1.05
	1.00	0.86	0.98	0.93	1.30	1.20	1.05	1.10	
Av.	0.94	0.92	1.17	1.01	1.07	1.05	1.16	1.14	1.05

1.0 ± 0.1 (from 4 Runs) for $U_p / U|_{L_p}$. Similar observations at Spanish Banks give 1.1 ± 0.15 (from 3 Runs) and at Boundary Bay, 1.05 ± 0.1 (from 2 Runs). Thus the pressure field travels at about the local mean wind speed, the higher frequencies or smaller scales travelling slower than the lower frequencies or larger scales. Calculations by other investigators working in wind tunnels (see Willmarth and Wooldridge, 1962) give an asymptotic value of about $0.8\ U|_\infty$ for the propagation velocity. This difference is considered to be due to the choice of the mean wind used for the comparison. The value of $U|_\infty$ for the atmospheric boundary layer could easily be 15 to 20% higher than the wind at height L_p, which would account for the difference. The difference in

propagation velocities as a function of frequency has also been observed in wind tunnels.

To compare the pressure fluctuations with the velocity fluctuations, similar analysis was done on some velocity data. The data comes partly from observations taken by others at the institute, using sonic and hot-wire anemometers, and partly from the hot-wire anemometer observations at Ladner. Figure 35 shows examples of coherences for two velocity sensors, and Figure 36 a composite of all such graphs. Though the data are more scattered it is assumed that the velocity and pressure behave similarly and the best fit line is drawn for separations proportional to λ_v. The scale L_v corresponding to $\lambda_v = U/n_L = 100$ cm is about 30 cm, where L_v is defined as before from the frequencies at which the coherence is 0.14. Therefore the size of the velocity fluctuations is approximately 1/3 of that given by λ_v. The coherences fall off approximately as $(\ln n)^{-0.8}$, about the same as for the pressure field. Velocities are also in phase at points separated vertically and across the stream, and the propagation velocity is about U, as expected. These results indicate that the pressure and velocity fluctuations are similar in geometry and are advected at the same rate.

Pressure-Velocity Relationships

In this subsection a number of pressure measurements taken in conjunction with velocity measurements are used to establish some of the relationships between the two. The results apply to the pressure-velocity relationship for most of the scale range for which there is an active Reynolds stress. *A priori*, there is no specific relationship expected. If the pressure were passive, the phase might be Bernoulli type (p varying as $-u^2/2$). If active, and responsible for

the transfer of energy between components, such as is required for a tendency to isotropy, a quadrature component in the $\overline{pu}$ product would be required in turbulent shear flow (see equations 4). If pressure is doing work across a plane, then the velocity component normal to the plane and in the direction towards the fluid receiving energy would on the average be in phase with the pressure. If the energy were being extracted from a velocity component, the velocity would on the average be directed up the fluctuating pressure gradient, or decelerating; the sign would be reversed for a gain of energy.

Typical measured coherence and phase relationships between p and the velocities u and w are plotted in Figures 37, 38, 39 and 40. Positive phases labelled p-u, p-w, etc., means that p leads u, w, etc., respectively. Figures 37 and 38 use data from the sonic, with the pressure probe placed about 25 cm upwind of the center of the sonic paths; this positioning of the probe was checked in a wind tunnel to ensure that no significant dynamic pressure noise would be present. The pressure signal was corrected for its resulting phase lead using Taylor's hypothesis. For comparison, a plot of u-w phase and coherence is shown in Figure 41. Data obtained from the pressure probe and a hot-wire, 4 cm to the side and 5 cm behind the probe, are plotted in Figures 39 and 40. In all the figures the approximate peak of the w spectrum is marked by an arrow for ease of comparison with standard velocity spectra. These plots show that the pressure is 'in phase' with u at low frequencies (the opposite of Bernoulli type) with coherences up to 0.8, while at high frequencies the phase difference becomes about 135° (indicating that some energy transfer was taking place) with coherences of about 0.1 to 0.2. The phase transition is associated with a loss of coherence in $\overline{pu}$. The division between the 'in phase' and 'large phase difference' is at a frequency somewhat higher than at the peak of the w spectrum. The coherence in the $\overline{pw}$

relationship shows a gradual decrease from about 0.5 at low frequencies to near zero at high frequencies; the corresponding phase change is gradual from about 180° to near 0°. Some of this loss of coherence in the $\overline{pw}$ relationship at the highest frequencies may be due to probe separation. As would be expected the measured $\overline{pv}$ coherence is near zero for the same frequency range.

The reason for the well defined change in the p-u phase can be seen from a plot, Figure 42, of wavelength, λ_p, at this transition, as a function of z (height of observations above the surface). The wavelength is calculated using the first data point after the phase transition to near 135°. Also shown is a dashed line indicating the scale size, L_p, of the pressure fluctuations for the transition frequency ($L_p \simeq \frac{1}{2} \lambda_p$ as evaluated in a previous subsection, p.37). All points fall near or below the line $L_p = z$. That is, all pressure fluctuations with a scale size larger than z have a different phase relationship from those with scale size less than z. This is attributed to the larger scale fluctuations 'feeling' the bottom. A positive pressure at large scales is associated with a negative (downward) w (see Figure 38). Since $\overline{uw}$ on the average is negative (Figure 41), the positive pressure is here associated with a positive u. Thus there is a zero phase relationship at large scales between p and u. For turbulence scales smaller than the measurement height, a different relationship results from their independence from the bottom.

Even though the major source of the low frequency pressure fluctuations is attributed to air motions interacting with the surface, not all w fluctuations produce corresponding pressure fluctuations. The coherence between the pressure and w is lower than between pressure and u at these scales (see Figures 37 and 38). Since it is felt that this is real and not due to the instrumentation, the flow must contain significant w fluctuations which do not

produce corresponding u or p fluctuations. As can be seen by comparing Figures 41 and 38, the u-w and p-w coherences are both about 0.5 at these scales.

Further evidence that most of the pressure at low frequencies is associated with deceleration of vertical velocities near the surface can be seen from the coherence between velocity and two pressure measurements near the surface, Figure 43. One pressure sensor was at the surface and a hot-wire anemometer and a pressure probe were together at 30 cm. The surface pressure signal has a higher coherence with downstream velocity fluctuations than does the pressure signal from the pressure measurement in the air. The mean difference in coherence is about 0.1 with the 30 cm separation. The two pressures are in phase for frequencies less than 5 Hz, Figure 33(b). Since the two pressure signals have the same spectral level and 0° phase with respect to the velocity, the difference in coherence is the result of the in-phase pressure at the surface being on the average larger than the in-phase pressure at the level of the velocity sensor. This means that the pressure gradient is on the average directed upward. A calculation, Table III, page 47, shows this for Run 319/1. Thus at large scales the majority of the pressure fluctuations were associated with the turbulence interacting with the surface.

The coherences between u and p, at this low level, Figure 43, are significantly smaller than those typically measured at higher levels as shown in Figures 37, 39, and 40. This is thought to be an example of the 'integral effect' (p.6) where the air motions contributing to $\overline{uw}$ may be decelerated by the boundary without the associated velocities arriving simultaneously at the boundary.

Data collected, using a hot-wire for measuring u and the surface pressure measuring technique to obtain p, were compared to the results of Gorshkov

TABLE III

Vertical Pressure Gradient at the Surface

Data from Run 319/1 (see Figure 43)

$U|_5 = 10$ m sec^{-1} $\quad u_*^2 \simeq 0.4$ m^{2}sec^{-2}

frequency Hz	B.W. Hz	$\overline{\Delta pu}$ (1)	$\sqrt{\Phi_u}$ cm sec^{-1}Hz$^{-1/2}$	Δp (2) dynes cm^{-2}	$\Delta p/\Delta z$ dynes cm^{-3}
0.026	3.1×10^{-2}	-6.3×10^{3}	4.6×10^{2}	2.4	-7.7×10^{-2}
0.059	3.1×10^{-2}	-4.2×10^{3}	3.6×10^{2}	2.1	-6.8×10^{-2}
0.090	3.1×10^{-2}	-2.2×10^{3}	3.0×10^{2}	1.3	-4.2×10^{-2}
0.12	3.1×10^{-2}	-1.2×10^{3}	2.4×10^{2}	0.87	-2.9×10^{-2}
0.17	6.1×10^{-2}	-6.0×10^{2}	1.8×10^{2}	0.81	-2.7×10^{-2}
0.23	6.1×10^{-2}	-5.8×10^{2}	1.7×10^{2}	0.83	-2.8×10^{-2}
0.41	1.2×10^{-1}	-2.5×10^{2}	1.1×10^{2}	0.79	-2.6×10^{-2}
0.54	1.5×10^{-1}	-2.0×10^{2}	1.1×10^{2}	0.73	-2.4×10^{-2}
0.72	2.1×10^{-1}	-1.5×10^{2}	9.5×10^{1}	0.73	-2.4×10^{-2}
0.97	2.7×10^{-1}	-9.5×10^{1}	7.2×10^{1}	0.62	-2.1×10^{-2}

(1) This value was obtained by vectorially subtracting the cross spectral values between the velocity and the two pressure signals. The units are (dynes cm^{-2}) (cm sec^{-1}) (Hz^{-1}).

(2) $\Delta p = (\overline{\Delta pu} \quad \Phi_u^{-1/2} \quad \text{B.W.}^{-1/2})$ is a magnitude for that part of the pressure difference ($p_{ground} - p_{air}$) which is coherent with u and lies within the appropriate bandwidth.

(1968). When similar spacings are used, the correlation coefficient (defined as the cospectrum divided by the square root of the product of the two spectral densities) is similar in magnitude to the values he obtained, but of the opposite sign. The only suggestion that can be put forward for the difference in the results is the different method used to obtain a surface pressure free of dynamic noise. Because the general features of his results can not be reproduced, they are not compared further with the present data.

Energy Transfer by Pressure Forces

Two aspects of energy transfer by pressure forces are evaluated. The first is the $\partial\overline{pw}/\partial z$ term, representing the net effect of pressure forces in the total turbulence energy budget of the boundary layer. The second is the $\overline{u\partial p/\partial x}$ term by which pressure forces transfer energy to or from the u velocity component.

For the evaluation of the relative size of the $\partial\overline{pw}/\partial z$ term , the equation for the boundary layer energy budget was integrated (see Background, p.8), the term $-\overline{uw}\ \partial U/\partial z$ becoming $-\overline{uw}\ U\big|_z$ and $-\frac{1}{\rho}\frac{\partial}{\partial z}\overline{pw}$ becoming $-\frac{1}{\rho}\overline{pw}\big|_z$. These two terms represent the rate of working by Reynolds stress (the energy feeding term) and the pressure forces on a column of height z and unit area. These terms are compared for five Runs, each of approximately 1/2 hour duration. The spectra of p, u, w, v, $\overline{uw}$, and $\overline{pw}$ are plotted in Figures 28, 22, 22, 23, 24, and 44 respectively. The integral of $\overline{pw}$ is negative; that is, the transfer of energy is downwards. The calculated terms are summarized in Table IV, page 49. The ratio

$$R = \frac{-\frac{1}{\rho}\overline{pw}}{-\overline{uw}\,U},$$

is plotted in Figure 45 as a function of z. As can be seen, the ratio R is approximately equal to 0.1 for z between 2 and 6 meters. The Run at 1.5 meters has some wave generation present, therefore the assumption of no energy flux through the bottom boundary is not completely valid.

TABLE IV

The $\overline{pw}$ Term in the Boundary Layer Energy Budget

Run	$U\|_5$ $m\ sec^{-1}$	z m	$-\overline{uw}$ $cm^2 sec^{-2}$	σ_w/u_*	$-\overline{pw}/\rho$ $cm^3 sec^{-3}$	$-\frac{1}{2}\overline{q^2 w}$ $cm^3 sec^{-3}$	$-\overline{uw}\,U$ $cm^3 sec^{-3}$	$R = \frac{\overline{pw}}{\rho \overline{uw} U}$
110/1	7.1	5.5	698	1.32	6.3×10^4	-6.5×10^4	50.5×10^4	0.125
110/2	7.4	4.0	729	1.25	5.5×10^4	-5.5×10^4	52.5×10^4	0.105
120/1	6.5	3.4	580	1.40	3.7×10^4	-2.4×10^4	39.5×10^4	0.095
120/2	6.2	4.8	443	1.47	2.7×10^4	-3.9×10^4	29.0×10^4	0.094
121/1	6.4	1.5	463	1.40	2.3×10^4	-6.5×10^4	27.0×10^4	0.084

Another term in the boundary layer turbulent energy budget is $-\frac{1}{2}\frac{\partial \overline{q^2 w}}{\partial z}$, where $q^2 = u^2 + v^2 + w^2$. When integrated between the surface and height z this is approximated by $-\frac{1}{2}\overline{q^2 w}\big|_z$, which (when positive) represents vertical energy flux into the unit column by the turbulence. The ratio of this flux to $-\overline{uw}U$ is about -0.1 (roughly balancing the $-\overline{pw}$ term).

The energy transferred by the $-\overline{u\partial p/\partial x}$ term in the energy budget of the

u velocity component was calculated from the simultaneous measurements of u and p. A hot-wire positioned about 7 cm to the side and 4 cm to the back of the pressure probe was used to measure u. Necessary phase corrections were applied using Taylor's hypothesis. The energy flux was calculated using the quadrature spectrum between u and p. This technique was checked by differentiating the pressure term to obtain $\frac{\partial p}{\partial x} = -\frac{1}{U}\frac{\partial p}{\partial t}$ and calculating its cospectrum with u. The two caluclation agree within ±10%. Figures 46 and 47 show the results in nondimensional form. As can be seen when integrated between values of kz from 0.05 to 20, the rate of energy loss (per unit volume) from the u fluctuations is about 0.3 to 0.7 $\rho u_*^3/(\kappa z)$, where κ is von Karman's constant.

As shown in the Background section, it would be expected that if data were available for the entire range of turbulent scales, the integral would have a maximum value of about 0.67, provided that the turbulence eventually becomes isotropic. Both w and v fluctuations are possible sinks for this energy, however for the scale range observed the w fluctuations are expected to be the major sink, since the w gains energy in this scale range, and v has already acquired significant energy at scales larger than those observed. Since the turbulence has not become fully isotropic within the scale range observed, further energy flux is expected at kz larger than that observed. For these reasons the integral (the energy loss from the u component) should at a maximum be less than 0.67. The relatively large variation in the measured integral including two larger than 0.67 could have resulted from the lack of complete stationarity and the length of the runs being too short for statistical reliability. The observed energy loss from the u velocity component has a mean value of about 0.45 $\rho u_*^3/\kappa z$; this is sufficient to account for that acquired by w fluctuations in this same frequency range.

The energy transfer by $-\overline{u\partial p/\partial x}$ can be discussed in terms of two scale

ranges. The first in which energy is lost is at low values of kz where the w spectra first have appreciable energy. The ratio Φ_w/Φ_u is shown in Figures 46 and 47 for comparison. The second range which contains most of the energy loss measured occurs just after the peak of the w spectrum; that is, where the turbulence becomes free of the surface (p.45). The energy transfer in most cases drops off toward zero at the high frequencies (that is, high kz). This is considered to be real rather than due to probe separation although values were not plotted beyond those shown since probe separation may be becoming important in the calculations by this point. This can be seen by evaluating the appropriate scale size for the fluctuations (see Figure 34).

From these energy flux measurements it appears that, in the total energy budget below 5 meters, under neutral conditions, the assumption of small contribution by the pressure term is reasonable. Not only is the term small but it is also partially bablanced by the turbulent flux term. However for the energy budget of the individual velocity components near the frequency range where the turbulence is carrying the stress, the pressure terms are very important as expected and as has been shown for the u component.

MICROSCALE PRESSURE FLUCTUATIONS OVER WIND GENERATED WATER WAVES

When a wind blows over water, waves can be generated through the action of the surface pressure fluctuations. Measurements were taken to evaluate some properties of the static pressure in this role. The region of interest is the air layer close to the water surface where the turbulent velocity correlation $\overline{uw}$, which normally carries the boundary layer stress, transfers energy to a pressure field which is generating the waves. The exact mechanism of this transfer, the study of wave generation is an area of active research (Dobson, 1969; Manton, 1970). Recent measurements (Dobson, 1969) indicated that a large fraction of the momentum transferred to the water was via the waves. Dobson measured the transfer directly from pressure measurements on the water surface. In contrast, the present measurements were Eulerian, taken a short distance above the crest of the waves and are concerned with the nature of the air flow over the waves.

The data were collected at the Spanish Banks site (see Appendix A). Most of the observations were taken when the wind blew from an easterly direction. The statistics of the wave field at this site for winds from this direction have been thoroughly studied by Garrett (1970). His measurements indicated that the non-uniform fetch which produced an asymmetry to the directional spectra did not prevent the wave frequency spectrum from attaining the 'equilibrium form' (see Phillips, 1966, p.109ff.). In this study the waves from both east and west were checked for the existence of an equilibrium range; that is, where the high frequency spectrum is of the form n^{-5}. The conditions at this site are considered suitable for obtaining measurements typical of the wave generation mechanism.

During most of the observations the water depth was 3 to 3.5 meters and

the tidal current small. The influence of water depth and tidal current on wave frequency and amplitude was considered; the correction was usually less than 10%. For example, waves of 3 second period were typical for the peak of the wave spectrum at this site. These waves have a wave number $k = 2\pi/\lambda$, of about 4.9×10^{-3} cm^{-1} in 3 meters of water as compared to 4.5×10^{-3} cm^{-1} assuming infinite depth.

A wave probe, pressure probe and velocity sensor were mounted on one of the instrument masts near the platform (see Appendix A for detail). The velocity measurements referred to in this section were made with a single 'u-wire' probe which measured the downstream fluctuations. These three sensors were placed as nearly as practical in a line perpendicular to the mean wind direction; that is, along wave crests. Phase differences due to non-alignment were corrected using the 'frozen field' hypothesis. The spacing crosswind between sensors was of the order of 5 to 10 cm with the wave probe normally operating at the mid-point. A minimum height of the air sensors was typically 30 to 50 cm above mean water level. The 'visual' wave amplitude during active generation by east winds (in which the waves are fetch limited) was about 15 to 20 cm. On one occasion the sensors were within 10 to 15 cm from the tops of the higher waves. In this position the case for the pressure transducer was occasionally hit by the waves.

More than twenty Runs were made under a variety of wind conditions (see Data Summary, Appendix C). Most of the useful information comes from four groups of Runs; the Runs within each group were taken sequentially. These four groups labelled A, B, C and D are used as representative of the results. Since all the data have some common properties, a single Run is used as an example for detailed description. The spectra, coherences and phase relationships for the four groups of data are then described, followed by a discussion

which summarizes the information and presents conclusions.

Example Spectra

A plot illustrating the typical characteristics of spectra over waves, Figure 48, is for data obtained from two pressure sensors, a hot-wire measuring u and a wave probe. The two pressure probes were separated vertically. The lower pressure sensor and the hot-wire anemometer were at a height of 90 cm above mean water level; the upper pressure sensor was 50 cm higher. The wind was from the west at 3.6 m/sec, slightly slower than the phase speed, C, of the waves at the peak of the wave spectrum.

The pressure spectra, Figure 48, always contain a 'hump' superimposed on a spectrum which is similar to that found over a flat boundary. The extent in bandwidth of the pressure hump is denoted by a double arrow labelled 'H'. This hump corresponds closely with the wave spectrum, though not exactly proportionally. For example, the slope on the high frequency side of the hump is not always -4.5 to -5 as it is for the waves. The humped portion of the spectrum for the higher level pressure sensor, p_u, is similar to that for the lower sensor, p_L, but is smaller in amplitude, particularly at high frequencies, as would be expected. At higher frequencies than at the 'humped' portion, the two pressure spectra do not align, as they do at the frequencies below the hump, the lower level having a higher intensity. Observations at similar levels over land and at higher elevations over water do not show this high frequency difference, as may be seen from Figures 18 and 20. The spectral slopes at higher frequencies than at the hump are the same as those observed at similar heights over a flat boundary.

To compare the wave induced pressure, p_w, observed in different Runs and

at different frequencies and heights, some measure of this pressure is required. The question arises as to what fraction of the pressure amplitude in the hump is associated directly with waves, and what is associated with random turbulence. Since, as will be shown later, the coherence between the pressure and the waves at higher frequencies than at the hump is essentially zero, this region of the spectrum can be said to result from random turbulence. It is assumed that the spectral slope associated with the random turbulence in the frequency range of the hump will be similar to that observed outside of it. Thus as a first approximation the pressure amplitude, p_w, in the hump, associated directly with the waves may be taken to be the difference between the intensity measured and the straight line projections from the high frequency tail (see dashed lines in Figure 48).

The spectrum for the u-velocity measured near the waves, Figure 48, does not have as dominant a hump as that observed in the pressure spectra. At frequencies on either side of the range marked by 'H', the velocity spectrum is similar to that observed in the absence of waves; for example, the -5/3 region exists at the higher frequencies.

The wave spectra from observations at the site did not always have the equilibrium form at all frequencies. Generally, the high frequencies exhibited the -4.5 to -5 slope, however this slope often did not continue to very near to the peak of the spectrum. The lowest frequency to which the equilibrium wave spectrum was considered to exist is marked by an arrow labelled 'eq. peak', see Figure 48.

All data associated with wave generation have been treated in the same way. As a check on the analysis methods, the data were occasionally reanalysed to include hanning. Hanning does not alter the results significantly.

Data

A. Runs 60/4, 119/1, 119/2, 119/3

This group of data consists of four sequential Runs recorded during an east wind. The instruments used were the wave probe, two pressure sensors spaced vertically 50 cm apart, and a hot-wire measuring downstream fluctuations. The lower pressure sensor and the velocity sensor were about 30 cm above mean water level. Figure 49 shows the wave spectra recorded during each of the Runs. The time of the Run is given in brackets after the Run number. Visually the highest wave was about 10 cm in amplitude; the root-mean-square amplitude is about 3 cm. The spectra have a secondary peak at a frequency near 0.25 Hz, thought to be due to waves generated elsewhere and propagating into the region (Garrett, 1970). The sequence 60/4 to 119/3 show that the wave field was growing in time under almost steady but slowly increasing winds (see Table V, Appendix C). The mean wind, $U|_5$, was about 4.5 m sec^{-1}, giving a value for $(U|_5 - C)$, where C is the phase speed of the waves, of about 2 m sec^{-1} at the main peak ('eq. peak') of the wave spectrum. Figures 50 to 53 show spectra for the four Runs. All exhibited properties similar to those described for the example shown in Figure 48. The phase and coherence between the lower pressure (p_L) and the wave amplitude (η_a), and between the two pressures (p_L and p_u) are plotted in Figures 54 and 55 respectively. A phase shift in the p-η relationship occurred at the wave peak and continued out over the equilibrium wave spectrum. As will be shown later, this shift of about 30 to 50° from 180° is associated with the wave generation. The corresponding coherences are about 0.3 to 0.4. At lower frequencies than at the 'eq. peak' coherences are higher and phase differences are near 180°. This is associated with the residual longer waves. The phase

information indicates that these low frequency waves were not being actively generated. Figure 55, a plot of the coherence and phase of the two pressure signals shows that they are in phase to ±5° throughout the extent of the hump. Data not associated with waves at $n < 0.1$ are not plotted. Thus most of the phase shift between p and η occurs below the lower pressure sensor, with almost no shifting occuring in the next 50 cm vertically. Figure 56 shows the observed u-η coherence and phase. Coherences are low at all frequencies. The non-zero coherence at frequencies outside the range marked 'H' would be expected simply from random coherence because of the finite length of sample. The highest coherence, about 0.3, occurs for waves of frequencies lower than the frequency at the equilibrium peak. Within the frequency range where active generation is occuring, coherences are small, less than 0.1. The cross correlation between u^2 and η gives results similar to that shown for u and η. The phase shows no definite pattern, with grouping near both 140° and 40°. This group of Runs (A) represents the most detailed observations taken.

B. Runs 167/1/1, 167/1/2, 167/2, 167/3

This group of four data Runs was also recorded during east winds. The wave spectra for all four are shown in Figure 57. As can be seen, the wave spectra are almost identical, implying steady state, fetch-limited conditions. The root-mean-square wave amplitude for these Runs is about 6 cm. The 5 meter mean wind was 7 to 8 m sec^{-1} giving a value of $(U|_5 - C)$ at the peak of the wave spectrum of about 4.5 m sec^{-1}. The only instrument used besides the wave probe was a single pressure probe, positioned about 40 cm above mean water level. Figures 58 to 61 show the spectra for these Runs. They are similar to the previous group of Runs (A), except that the peak of the pressure hump is at a lower frequency than the peak of the wave spectrum.

This is thought to be due to waves travelling against the mean wind, which had been refracted to the site from the other side of Point Grey, see Figure 85. Such waves, travelling from the west during a SE wind have been measured (Garrett, 1970) by means of a directional wave array. In order to substantiate the above reason for this abnormal p-η relationship, the amplitude of the Fourier coefficients for the pressure and wave signals of Run 167/3 was plotted, Figure 62. This shows that the energy in the pressure signal at frequencies lower than the peak of the wave spectrum is directly associated with wave energy. This is true for all the other Runs in this sequence. To show that these pressure magnitudes are in accord with this hypothesis the pressure amplitude was calculated assuming that the air responds in a potential flow manner to the measured wave amplitude. For example, for Run 167/1/2, at 0.27 Hz, bandwidth Δn = 0.077 Hz, $\sqrt{2\Pi(n)\Delta n}$ = 5.3 dynes cm^{-2} and $\sqrt{2\Phi_\eta(n)\Delta n}$ = 1.3 cm. From a potential flow calculation using the mean wind at the pressure observation level

$$\sqrt{2\Pi(n)\Delta n} = \rho\,(U + |C|)\,k\,\sqrt{2\Phi_\eta(n)\Delta n}\;e^{-kz}$$
$$= 4.9 \text{ dynes } cm^{-2}$$

with the usual definitions (Lamb, 1932, section 231). The calculated and measured values agree to within the accuracy of the assumptions. Thus in this group of data the pressure signal at frequencies lower than the frequency at peak of the wave spectrum is not that normally encountered in wave generation. The phase and coherence between pressure and waves for these Runs are shown in Figure 63. As before, the phase shift at the wave generation frequencies is about 30 to 50°, with coherences of 0.5 to 0.6. For the frequency range where the waves were propagating against the wind, the coherence is higher and phase differences are about 180°, as would be expected for a potential type of flow.

This group of Runs have the highest values of $(U|_5 - C)$ for the data obtained.

C. Runs 164/1, 164/2

This group consists of two examples in light WNW or NNW winds of 2.5 and 4 m sec^{-1}. The waves at the peak of the wave spectrum were travelling about 2 m sec^{-1} faster than the wind. They had been generated by strong winds in Howe Sound and had then fanned out from the mouth, part travelling into the English Bay region. The root-mean-square wave amplitude is about 9 cm. The waves travelled at a small angle to the wind, arriving from a direction of about NW. The instruments used were the wave probe, a single pressure sensor and a 'u-wire'. The latter two were located about 50 cm above the mean water level. The spectra for these Runs are shown in Figures 64 and 65. The p-η phase and coherence are given in Figure 66; coherences are high; phase differences are near 180°. Figure 67 shows phase and coherence for u-η. At this low wind speed, the coherence is higher than for all other Runs and the phase differences are about 180°.

D. Runs 80/3, 60/1, 60/2

This group of three Runs is typical of the data obtained when the value of $(U|_5 - C)$ at the peak of the wave spectrum is near zero. In the examples used here, the wind was from the west. The wave, pressure and u-velocity spectra are shown in Figure 68. The high frequency end of the wave spectrum, partially cut off in the graph, follows the -5 slope, and therefore can be considered as part of the equilibrium spectrum. The root-mean-square wave amplitude for these Runs is about 6 cm. The mean wind was 4 to 4.5 m sec^{-1}. Observations were taken at about 50 cm above mean water level. The phase and coherence for p-η and u-η, Figures 69 and 70 are similar to previous examples.

p-η phase shifts are near 180° when $(U|_5 - C)$ is small and negative, increasing as $(U|_5 - C)$ increases. For waves near the peak of the wave spectrum, where $U|_5/C \lesssim 1$, the u-η phase difference is near 180°. This final group are representative of the eight Runs for which $(U|_5 - C)$ is near zero at the peak of the wave spectrum.

Discussion

Compared to the pressure spectrum over a flat boundary, that measured close to a wavy water surface is greatly modified. The most prominent change is the 'hump' in the pressure spectrum that is associated with the wave spectrum. The intensity in this hump is up to 10 times larger than the spectral intensity expected for a flat boundary under similar wind conditions. Remnants of the hump are observed during normal wave conditions up to heights z between $\lambda_w/2$ and λ_w where λ_w is the wavelength of the waves. This can be estimated from the plots of the pressure spectra by using the highest frequency at which the hump is definable. For Run 173/3 in Figure 48, this occurs for p_u at a frequency $n \simeq 0.9$ Hz. Waves of this frequency have a wavelength $\lambda_w \simeq 200$ cm; the measurement height was 140 cm. For Run 167/1/1, Figure 60, corresponding figures are $n = 1.5$ Hz, $\lambda_w \simeq 70$ cm and $z = 30$ cm.

A hump, similar to that observed, would be expected even if no mean wind or turbulence was present, and the wave field was simply propagating past the pressure sensor. This could be described by a potential flow solution (Lamb, 1932, section 231). The pressure (phase and magnitude (p_p)) predicted by the potential flow solution were checked in the field. Figure 71 shows the results obtained on still, windless days when a swell was propagating past the instrument mast. The pressure and wave height were

recorded on a strip-chart recorder instead of the usual method on magnetic tape. The values plotted each came from the average of about 100 estimates of individual amplitudes. The measured and predicted values agree within about 10%. Phase differences for p-η were 180°, within the accuracy of the method. Thus potential flow theory adequately predicts the pressure field (and hence supposedly the velocity field) for propagating waves in the absence of wind.

When there was a wind, it might have been expected that the pressure could have been approximated by using a velocity of $(U|_5 - C)$ in the potential flow solution; that is,

$$p_w \simeq - \rho \eta_a k (U|_5 - C)^2 e^{-kz} ,$$

where η_a is wave amplitude. This behaviour was not found for the present data. For example, for the $(U|_5 - C) = 0$ between 0.3 and 0.4 Hz in Run 164/2, Figure 65, and near the peak of the wave spectrum in Runs 80/3 and 60/2, Figure 68, there is no indication of a drop in the measured p_w.

Two cases have already shown that the measured pressure was closely approximated by potential flow calculations; one for $U|_5/C = 0$ and the other for $U|_5/C$ negative. However when $U|_5/C > 0$ the data does not have such a simple interpretation.

The non-dimensional variables which might cause variations in the pressure (p_w) associated with the waves are: kz, representative of the fractional height of the observations in terms of wavelength; $k\eta_a$ representative of the wave slope; and $U|_5/C$, the ratio of the mean wind at 5 meters to the phase speed of the waves. η_a can be approximated by $\sqrt{2\Phi_\eta(n)\Delta n}$ where $\Phi_\eta(n)$ is the wave spectral density and Δn is the $\frac{1}{2}$octave bandwidth for a narrow band of

frequencies. When the wave spectrum has the equilibrium form, the product $k\eta_a \simeq k\sqrt{(\Phi_\eta(n)\Delta n)}$ can be taken as a constant. For simplicity, pressure data from one 'fixed height' above mean water level and only for the frequency range where the waves have the equilibrium form are initially considered. In practice this 'fixed height' ranged from 30 to 50 cm. Thus, for this data, kz and $k\eta_a$ are constant at any fixed frequency. In Figure 72, $p_w(n) = (\sqrt{2\Pi(n)\Delta n} - \sqrt{2\Pi_o(n)\Delta n})$ is plotted against $U|_5/C$ with frequency as a parameter. $\Pi_o(n)$ is the background pressure spectrum illustrated by the dashed lines in Figure 48. The points on the ordinate in Figure 72 are derived from the limiting cases of $U|_5/C = 0$ which are assumed to be given at each frequency by the potential flow solution

$$p_w(n) = \rho \sqrt{2\Phi_\eta(n)\Delta n}\; k\, C^2\, e^{-kz} \qquad (15)$$

These calculations use the mean values from the measured wave spectra and the 'fixed height' z of 40 cm. The values of k and C at a given frequency were obtained from the solution for small amplitude gravitational waves: $C^2 = \frac{g}{k}\tanh kh$ and $n = \frac{kC}{2\pi}$. As can be seen, Figure 72, the data tends to group along lines which could be approximately extrapolated to the potential flow calculations. As $U|_5/C$ increases, the pressure intensity at all frequencies also increases. There is no indication of a distinctly different behaviour near $U|_5 = C$.

With this plot (Figure 72) as background, data from all heights were considered in terms of the nondimensional variables kz, $U|_5/C$, $k\sqrt{2\Phi_\eta(n)\Delta n}$, and p_w/p_o where $p_o = \rho k\sqrt{2\Phi_\eta(n)\Delta n}\, C^2$. The product $k\sqrt{2\Phi_\eta(n)\Delta n}$ was chosen to be constant although it is not exactly so for this data, varying by about 20%. This is not important provided the role of $k\eta_a$ in p_w is the same as in

p_o. Two plots are used, Figures 73 and 74, in which p_w/p_o is shown as a function of $U|_5/C$ at constant kz and vice versa. The results in Figure 73 are similar to those already shown in Figure 72, with little change resulting from the additional data available for heights other than 40 cm. Figure 74 shows a less definite dependence of nondimensional pressure on kz than on $U|_5/C$ as shown in Figure 73. Straight lines representing constant values of kz have been drawn by hand among the data plotted in Figure 73. It is felt that there is insufficient data to warrant a closer fitting of 'curves' and there are no theoretical predictions to act as guidelines. Acting as a first approximation, the data in Figure 73, as represented by the lines shown are summarized by the formula

$$p_w(n) = \rho k \sqrt{2\Phi_\eta(n)\Delta n}\, C^2 \exp(0.27\, U|_5/C - kz(1 - 0.08\, U|_5/C)) \tag{16}$$

The lines shown in Figure 74 representing constant values of $U|_5/C$ are calculated from this formula, and agree very closely with those drawn independently on the basis of the data alone. The limiting case of $U|_5/C = 0$ is the potential flow solution as given by equation 15. There is sufficient accuracy to show that as $(U|_5 / C)$ increases, the slope of the lines decreases. Thus as the wind increases, the pressure decay vertically at a given wave number is increasingly less than the exponential decay in potential flow. Equation 16, used to relate the observations to an empirical formulation, becomes physically unrealistic if extended to large values of $U|_5/C$, beyond the data plotted. If $U|_5/C = 12.5$ is substituted into equation 16 all z dependence disappears and at $U|_5/C > 12.5$ equation 16 has the pressure increasing vertically; the opposite of that which would be expected to occur. This 12.5 value for $U|_5/C$ could represent a wavelength of 10 cm and a $U|_5$ of

5 m sec^{-1}. Therefore the formula given should not be extrapolated to regions outside that covered by the data, approximately $0 < U|_5/C < 7$ and $0.5 < kz < 3$, without caution, particularly at larger values of $U|_5/C$.

It is noticed that calculated pressures at frequencies where the equilibrium wave spectrum did not exist have magnitudes similar to those predicted by equation 16.

It is possible to check the vertical dependence shown in equation 16 using the simultaneous measurements at two levels described in Data Group A (p.56). By taking the ratio of the pressure, $p_w(n)$, at the two levels, a Δz dependence would be left. In terms of equation 16

$$\frac{p_w(n)|_{z_1}}{p_w(n)|_{z_2}} = \exp\left(- k\Delta z + 0.08 \frac{U|_5}{C} k\Delta z \right) \qquad (17)$$

for $z_1 > z_2$. Measured values of this ratio and those calculated from equation 17 are plotted in Figure 75 against $k\Delta z$. The fit is reasonable.

In summary, the pressure hump has a magnitude which is similar to the potential flow solution in very low winds; it increases monotonically as U increases and decays vertically at a rate less than exponential, the higher the mean wind, the slower the decay.

The surface pressure spectra obtained by Dobson (1969) have a similar type of pressure hump, but in general it is not as well defined as those obtained in the present study (his low frequency intensities were in general an order of magnitude larger). There was some question as to how to compare Dobson's data with the present results since his instrument followed the water surface, and hence his measurements were not Eulerian. Nevertheless it seems reasonable to compare Dobson's spectra with values predicted by

equation 16, setting z = 0. Thus

$$\Pi(n) = \rho^2 k^2 C^4 \Phi_\eta(n) \exp(0.54 U|_5/C)$$

A comparison for three cases is shown in Figure 76 for which the values of $\Phi_\eta(n)$ were taken from data in Dobson's thesis. One of high wind speed runs (4b) and two low wind speed runs (2a and 2 b) were chosen. Since no extrapolation of the pressure spectra, similar to that represented by the dashed lines in Figure 48 was obvious, no attempt was made to remove the energy associated with random turbulence. At frequencies near the peak of the wave spectrum, see Figure 76, this should not give any large error since the hump pressure is expected to be about an order of magnitude larger than the pressure associated with random turbulence. For each run three curves of pressure intensity are compared: Dobson's total spectral estimate, Dobson's spectral estimate with $\rho g \eta_a$ removed, and the spectral estimate predicted by equation 16. As can be seen the data collected by Dobson appear to agree reasonably well (within a factor of about 2) with the values predicted by the formula. Therefore equation 16 may predict the hump pressure, $p_w(n)$, down to the wave surface.

The pressure which generates the waves is the component of the pressure, $p_w(n)$, which is in quadrature with the wave. Even though the pressure fluctuations associated with the waves are up to one order larger than that expected from the random turbulence, the coherence with the waves is only about 0.4 to 0.6. This suggests that the process of wave generation is intermittent and hence that the phase difference between pressure and waves fluctuates significantly.

It was shown in earlier diagrams that the average phase difference observed at about 50 cm above the waves during active wave generation is such

that pressure lags the waves about 140 to 120°. In the absence of active generation the phase is near 180°. Figure 77 is a composite of average p-η phase differences plotted against $U|_5/C$. This plot includes all of the data from Data Groups A to D (page 56 to 60) for frequencies within the extent of the equilibrium wave spectrum ($\Phi_\eta(n) \propto n^{-5}$). The data are labelled with a different symbol to indicate the data group. Most of the large angles associated with wave generation occur for $U|_5/C > 2$ and do not show any further shift from 180° for increasing $U|_5/C$; in fact, if anything, the opposite appears to be true. For all other data either those outside the range of the equilibrium wave spectrum for which $0 < U|_5/C < 2$ or those travelling against the wind for which $U|_5/C < 0$ the phases were 180° ± 10° with no definite trend.

The fact that the large p-η phase difference occurs at values of $U|_5/C$ greater than about 2 is thought to be due to the relative height of the critical level and wave amplitude η_a for these particular groups of data. The 'critical height', z_c, is the height at which U = C (Phillips, 1966, p.91). For the data plotted in Figure 77 the critical height is well above the waves for $U|_5/C$ near 1. Values of $U|_5/C \simeq 2$ are necessary before the critical height approaches a value equal to the wave amplitude. This can be seen from the use of Figure 78. In deriving the curves in this figure a logarithmic wind profile and a roughness length of 0.01 cm[1] are assumed. The plot is to show which wave frequency has an amplitude equal to the critical height, given a fixed mean wind at 5 meters. Plotted are a family of curves representing the critical height for different 5 meter winds at various wave frequencies. The curve of $\eta_a = \sqrt{2\Phi_\eta(n)\Delta n}$ against frequency is for the measured equilibrium

---

1 This value of roughness length is approximately equivalent to a drag coefficient $C_D = 1.2 \times 10^{-3}$.

wave spectrum described above in Data Groups A, B, C and D. Once a value of $U|_5$ is known, there will be a different z_c for every wave frequency, but only one which has a $z_c = \eta_a$. For example, in Data Group A, page 56, $U|_5$ is about 5 m sec^{-1}. In Figure 78, $Z_c = \eta_a$ at 0.62 Hz when $U|_5 = 5$ m sec^{-1}. This frequency of 0.62 Hz is near the frequency at which the large p_L-η phase shifts occur as shown in Figure 54. For waves of this frequency $U|_5/C \simeq 2$. Therefore when replotting the entire set of phase differences from Figure 54 into Figure 77, the large phase shift from 180° occurs at about $U|_5/C = 2$. This can also be shown for all the other data groups. Thus the large p-η phase shift from 180° occurs only for those waves which have a $z_c \lesssim \eta_a$.

Dobson's (1969) results, before $\rho g \eta_a$ was removed, gave a comparable phase distribution when plotted against $U|_5/C$ (M.J. Manton, personal communication), although the scatter is larger than for the present data and the shift from 180° appeared to increase continuously with increasing $U|_5/C$. When $\rho g \eta_a$ was removed from his signal, the phases between surface pressure and waves were larger by 20 to 50°.

The energy flux to the waves by the action of surface pressure, noting that $w|_\eta = \frac{\partial \eta}{\partial t}$, can be represented by

$$\begin{aligned} En &= \overline{pw(n)}\,\big|_{z=\eta} \\ &= \sum_i (\omega_i \; Quad(p\eta)\big|_{n_i}) \Delta n_i \big|_{z=\eta} \end{aligned} \tag{18}$$

Values of En were approximated using the pressure measured above the waves. Since active wave generation was present for group A and group B (page 56) one example was taken from each. The results are shown in Figure 79. Using the pressure measurement above the waves shows maximum energy flux at the peak of the wave spectrum labelled 'peak' in the figure. The integrals shown on the graphs are approximately one fifth of the values obtained

by Dobson (1969) at a comparable wind speed. Cases in which the waves were moving faster than the wind, or the waves were in the opposite direction to the wind; that is, there was no z_c; did not have the phase shifts necessary for such energy transfer, see Figures 54, 63, 66 and 69.

It is surprising that there is not an obvious 'hump' of energy in the velocity spectra through the frequencies near the peak of the wave spectra in view of the large increase in energy observed in the pressure spectra. It is difficult to make an estimation of the expected amplitude of the velocity fluctuations associated with the waves or with the observed pressure since the relationships between them are not known. A rough estimation of the amplitude of the expected velocity fluctuations can be made using data from group A, page 56. The two vertically spaced pressure measurements can be used to evaluate a vertical pressure gradient. Assuming that this gradient is accelerating or decelerating the air vertically, an approximate velocity may be inferred from $\frac{1}{\rho}\frac{\Delta p}{\Delta z} \simeq \frac{\Delta w}{\Delta t}$. For example, in Run 119/2, Figure 52, at n = 0.55 Hz (bandwidth = 0.15 Hz) the Δp vertically is approximately 2.5 dynes cm^{-2} over a distance of Δz = 50 cm; this can be easily obtained from Figure 52 since at this frequency the coherence between the two pressure signals is 1 and the phase difference is 0° (see Figure 55). Since a typical Δw must be accelerated (or decelerated) during one quarter of a cycle, $\Delta t \simeq 0.45$ sec. This gives $\Delta w \simeq 18$ cm sec^{-1}, assuming $\rho \simeq 1.2 \times 10^{-3}$ gm cm^{-3}. The corresponding observed value of $\sqrt{2\Phi_u(n)\Delta n}$ in this frequency band is 17 cm sec^{-1} ($\Phi_u(0.55\ \text{Hz}) = 10^3$ $cm^2 sec^{-2} Hz^{-1}$) which is comparable with that calculated for Δw. However this is only a rough agreement, since the relationship between u and w is not known near waves, and the u was measured next to the lower pressure sensor rather than at a position midway between the pressure sensors where the prediction would be most valid. Nevertheless the velocities observed may be sufficiently high to account for the observed

vertical pressure gradients which are required to produce them. It is also possible that some of the observed pressure in the frequency range referred to as the 'hump' may result from the 'integral effect' (p.6) with motions near and below the wave crests requiring the pressure observed at the higher level above the wave crests.

The potential flow solution (p.62) predicts a phase difference between u and η of 180° for either no wind, or a mean wind constant with height and slower than the phase speed of the waves. This u-η phase difference of 180° and the restriction on the wind speed are approximately those shown for the coherent part of the observed u-η signals. The phases between velocity u and wave height η plotted in Figures 56, 67 and 70 for the Data Groups A, C and D respectively are generally near 180°. The few points near 40° in Figure 56 are for waves travelling from an unknown direction. When the wind speed is faster than the phase speed of the waves, the coherence is low, <0.1, and phases are random. The 180° phase difference occurs only for those frequencies when most or all of the air below 5 meters has a speed less than the wave speed, as required by the potential flow calculations. A comparison of Figures 55 and 56, 66 and 67, and 69 and 70 shows that the u-η 180° phase difference occurs only when the p-η phase differences are also near 180°. It is shown above (p.66) that this range of p-η phases near 180° corresponds to a critical height z_c well above the wave amplitude (η_a); that is, when the wind at the observation levels is less than the phase speed of the waves ($z_c >> \eta$).

An example of the strong influence the wave field has on the turbulence in the air above is seen in the p-u cross correlation. Over a flat boundary it was found that the p and u were in phase for those scales (L_p) larger than the local height of the observations, shifting to the neighbourhood of 135° at smaller scales. The coherence and phase of p and u over waves are shown in

Figures 80 and 81. The broad features appear to be the same as those obtained from observations over a flat boundary, Figures 39 and 40, except for the lower coherence through the region of the 'hump'. However the frequency of the phase 'transition' is entirely different, being much lower than over land. Figure 82 shows the wavelength λ_p of the pressure at the phase transition compared to those obtained over a flat boundary. The scales, $L_p \simeq \lambda_p/2$, at the transition are several times larger than those expected over a flat boundary at a similar height. In every case it was found that this phase transition over waves occurred at the frequency of the peak of the pressure hump when the pressure spectra were plotted as $n\Pi(n)$. In most cases this also corresponded to the peak of the $n\Phi_\eta(n)$ wave spectrum. The behaviour of the p-u coherence and phase at frequencies above the phase transition is similar to that found over a flat boundary, except the transition occurred at a lower frequency. The wavelength of the waves appears to introduce through the pressure field a new length scale with which the turbulence interacts.

In parallel with the observations over a flat boundary there was a large energy loss from the u-velocity component at frequencies above the phase transition. Using the same method as was used earlied, the nondimensional energy flux from the u-component,

$$-\overline{u\frac{\partial p}{\partial x}} \Big/ \rho\frac{u_*^3}{\kappa z} ,$$

was calculated for the observations over waves. The results are plotted against kz in Figures 83 and 84. The distribution of energy flux is similar to that found over a flat boundary. Most of the flux occurred at scales immediately above the transition. For those values of kz associated with the peak of the wave spectrum, the sign of the flux is often positive and the

magnitude is highly variable. The integrals under the curves are similar to those found for the data collected over a flat boundary being typically between 0.3 and 0.4. Thus the energy loss from the u-component to the other velocity components is similar in magnitude to that found over the flat boundary layer but occurs at a nondimensional height kz which is lower by an order of magnitude than over land.

SUMMARY OF RESULTS

An instrument was developed to measure the static pressure fluctuations within the turbulent flow of the atmospheric boundary. From an *in situ* calibration, which compared the pressure measured by the developed instrument with that measured by a reliable surface measuring technique, the accuracy of the new instrument was found to be about ±10% in amplitude and ±5° in phase. This instrument was used to measure some of the properties of the static pressure fluctuations found over a flat boundary and over water waves. The data included the mean square pressure, spectral intensity and shape, coherence and phase between two pressure measurements separated in each of the three coordinate directions, pressure-velocity relationship for all three velocity components, horizontal pressure gradient-velocity relationships, and pressure, wave, downstream-velocity relationships.

For all observations over a flat boundary the root-mean-square pressure resulting from the boundary layer turbulence is about 2.6 times the mean stress; thus the pressure can be nondimensionalized by the stress. The spectral distribution was found to be only weakly dependent on height, in contrast to the velocity which is directly dependent. At frequencies above the peak in the vertical velocity spectrum, the pressure spectra have a mean slope of about -1.7; the slope is less steep at lower frequencies. A scale was defined for the pressure fluctuations based on the coherence between two simultaneous pressure measurements. This scale was found to be the same in all three coordinate directions; thus, to a first approximation, the individual pressure fluctuations are spherical. The phase measurements agree with this interpretation. From near-surface, simultaneous measurements with a downstream separation, the propagation velocity of a pressure fluctuation was

estimated. When this rate was compared to the mean wind at a level corresponding to the size of the pressure fluctuations they were found to be about equal. In this same measurement, consistent phase differences in the cross-spectrum could not be traced further than about 360° before the signals became incoherent.

The simultaneous measurement of pressure and velocity showed that the downstream velocity fluctuations are approximately in phase with pressure at low frequencies, while at higher frequencies there is large phase difference of about 135°. This phase difference is a function of the height of observations, the in-phase portion occuring for pressure scales larger than the measurement height. At these larger scales the pressure appears to be interacting directly with the surface; smaller scales are effectively free of the surface. Measurements at the surface support this interpretation.

Pressure measurements were used to calculate the energy flux by pressure forces in two cases. In the first, the energy flux out of the downstream velocity fluctuations was found to be about 0.35 of the net energy source to the downstream component. A possible sink for this energy is into the vertical and crossstream velocity fluctuations; the vertical velocity fluctuations are developing in this same frequency range. In the second case, the pressure divergence term was found to be a small fraction, about 1/10, of the energy feeding term in the net energy budget of a boundary layer. The terms were compared in integrated form.

Pressure measurements near wind generated water waves showed a large hump in the spectrum at the wave frequencies. The amplitude of this hump increased, and the rate of its decay vertically decreased, as the mean wind speed increased. The phase difference between pressure and waves during active wave generation is about 135°, pressure lagging waves, and does not

change vertically for measurements at heights greater than the wave crests. In non-generating conditions the phase difference is near 180°. The active generation occurs only when the critical height is low enough to be near crest heights or lower. Wave generation, inferred from these observations above the surface, occurs most actively at the peak of the wave spectrum.

The pressure-downstream velocity relationship over waves is different from that found for similar observations over a flat boundary. Instead of the phase transition occuring at a frequency dependent on the size of the pressure producing scales which are directly proportional to the height, it occurs at the frequency of the peak of the wave spectrum. Energy transfer out of the downstream velocity component measured near the waves is similar to that found for observations over a flat boundary, only it is shifted to larger scales at a given height. The measurements suggest some strong interaction between the normal boundary layer turbulence and the more organized flow over the waves.

These measurements made with the developed instrument have provided the first reliable pressure data within a turbulent boundary layer.

BIBLIOGRAPHY

Ampex Co. (1966) Instruction Manual, FR-1300 Recorder/Reproducer. Calif., U.S.A.

Batchelor, G.K. (1960) The Theory of Homogeneous Turbulence. Cambridge University Press, 197pp.

Blackman, R.B. and J.W. Tukey (1959) The Measurement of Power Spectra. Dover Publications, Inc., New York, 190pp.

C.F. Casella and Co. Ltd., Instruction Leaflet - #3034/RA, Sensitive Anemometer. London, England.

Deardorff, J.W. (1970) A three-dimensional numerical investigation of the idealized planetary boundary layer. J. Fluid Mech. 41 pt.2: 453-480.

DISA Elecktronik A/S (1967) Instruction and Service Manual, Type 55D05 Battery Operated C.T.A. Herlev, Denmark.

Dobson, F.W. (1969) Observations of normal pressure on wind-generated sea waves. Ph.D. dissertation, University of B.C., 240pp.

Garrett, J.F. (1970) Field observations of frequency domain statistics and nonlinear effects in wind-generated ocean waves. Ph.D. dissertation, University of B.C., 176pp.

Golitsyn, G.S. (1964) On the time spectrum of micropulsations in atmospheric pressure. Izvestiya, Geophysical Series, No.8:1253-1258. (Am. Geophys. Union translation:761-763)

Gorshkov, N.F. (1967) Measurements of the spectrum of pressure micropulsations in the near-earth layer of the atmosphere. Izvestiya, Atmospheric and Oceanic Physics, 3 (4):447-451. (Am. Geophys. Union translation:255-257)

Gorshkov, N.F. (1968) On micropressure-fluctuations in the near-earth layer. Izvestiya, Atmospheric and Oceanic Physics, 4 (4):460-462. (Am. Geophys. Union translation:259-261)

Gossard, E.E. (1960) Spectra of atmospheric scalars. J. of Geophys. Res., 65(10):3339-3351.

Herron, T.J., I. Tolstoy and D.W. Kraft (1969) Atmospheric pressure background fluctuations in the microscale range. J. of Geophys. Res., 74(6):1321-1329.

Hinze, J.O. (1959) Turbulence, An Introduction to Its Mechanism and Theory. McGraw-Hill Book Co., Inc. Toronto. 586pp.

Hume, D. (1967) Instruction Manual, Wind Profile System. Institute of Oceanography, University of B.C., Vancouver.

Hume, D. (1969) Instruction Manual, Capacitive Wave Probe. Institute of Oceanography, University of B.C., Vancouver.

I.E.E.E. Transactions on Audio and Electroacoustics. Special Issue on Fast Fourier Transform and its Application to Digital Filtering and Spectral Analysis. June 1967, AU15(2).

Kaijo Denki Co. Ltd. (1967) Instruction Manual, Model PAT-311 Ultrasonic Anemometer thermometer. Tokyo, Japan.

Kraichnan, R.H. (1956) Pressure fluctuations in turbulent flow over a flat plate. J. of the Acoustical Soc. of America, 28(3):378-390.

Lamb, Sir H. (1932) Hydrodynamics (6th ed.). Cambridge University Press (reprinted by Dover Publications, Inc., New York, 1945), 738pp.

Lee, Y.W. (1967) Statistical Theory of Communication. John Wiley and Sons, Inc., New York, 509pp.

Lumley, J.L. and H.A. Panofsky (1964) The Structure of Atmospheric Turbulence. Interscience Publishers, New York, 239pp.

Makino Co., Ltd., Instruction Manual, Makino's Photoelectric Anemometers. Tokyo, Japan.

Manton, M.J. (1970) Theoretical studies of the generation of surface waves and the propagation of internal waves in the sea. Ph. D. dissertation, University of B.C., 175pp.

McBean, G.A. (1970) Similarity of turbulent transfers near the surface. Ph.D. dissertation, University of B.C., 150pp.

Panofsky, H.A. and A.A. Townsend (1964) Change of terrain roughness and the wind profile. Quart. J. Roy. Meteorol. Soc. 90:147-155.

Phillips, O.M. (1966) The Dynamics of the Upper Ocean. Cambridge University Press, London, 261pp.

Shaw, R. (1960) Influence of hole dimensions on static pressure measurements. J. Fluid Mech., 7:550-564.

Stewart, R.W. (1969) Turbulence and waves in a stratified atmosphere. Radio Science, 4(12):1269-1278.

Townsend, A.A. (1955) The Structure of Turbulent Shear Flow. Cambridge University Press, London.

Weiler, H.S. and R.W. Burling (1967) Direct measurements of stress and spectra of turbulence in the boundary layer over the sea. J. Atmos. Sci., 24(6):653-664.

Willmarth, W.W. and C.E. Wooldridge (1962) Measurements of the fluctuating pressure at the wall beneath a thick turbulent boundary layer. J. Fluid Mech., 14:187-210.

APPENDIX A

EXPERIMENTAL SITES, INSTRUMENTS, AND TECHNIQUES

The primary objective when collecting data in the field was to obtain recorded data in raw form for later analysis. Data were collected at one of three different sites; over water or sand at the SPANISH BANKS SITE, over asphalt and cut grass at the LADNER SITE, or over sand at the BOUNDARY BAY SITE. Even though a typical length of recorded data, or a 'Run', was about 30 minutes each expedition providing several Runs lasted from one day to a few weeks, chiefly dependent on the weather. Analog signals from instruments responding to static pressure, wind velocity and wave height were recorded on magnetic tape. Auxiliary data were logged manually; typically these included the mean wind profile and direction at both land and sea sites, with wet and dry bulb temperatures, water temperature, currents and mean water level added at the Spanish Banks site.

The method and instruments used to obtain these measurements, along with a description of the sites, is given in the following paragraphs.

Experimental Sites

(i) Spanish Banks Site

All over-water observations in this thesis are from the Spanish Banks site. It is located on a tidal flat on the south side of English Bay, Figure 85, 1/2 km from shore.

The site has two common wind directions, easterly or westerly, both suitable for recording data. Wind speeds up to 10 m/sec are not uncommon,

5 m/sec is more typical. An easterly wind has an asymmetric fetch of about 7 km; this asymmetry was considered when choosing recording conditions. Winds from the west usually occurred when the wind was from the north-west in the Strait of Georgia. Thus even though the fetch to the west is about 50 km, the wave and wind field would not necessarily be uniform over this distance.

A hut on pilings, called the platform, provided living and working space, Figure 86 (a) and (b). It was accessible by walking at mean low tides, by boat at higher tides. The maximum tidal range is approximately 4 m. Vertical aluminum masts located about 50 m to the seaward side of the platform were used as mounts for instrument sensors. These masts, about 7 m high and 15 cm in diameter, rested on the sand and were held rigid by a tripod bracing arrangement. A carriage on the masts could be raised or lowered hydraulically and turned electrically by controls at the platform to accommodate changes in tide and wind. Sensors mounted on brackets were placed such that there was negligible interference from the masts. Cables, weighted to the bottom, connected the sensors to the hut where signals were conditioned and then recorded. The AC electrical power for operating the equipment was supplied by a 3 kw ONAN generator, fed through a SORENSON AC power regulator. The voltage and cycles of the AC power were monitored to ensure that they remained within instrument requirements.

(ii) Ladner Site

The Ladner site is located on an asphalt runway at an abandoned airport, Figure 87, an area now part of the Canadian Forces Station, Ladner. Facilities at the site were arranged by a fellow graduate student, G.A. McBean.

Grass growing between the runways was normally cut, providing a reasonably

uniform terrain for about 1 km in all directions. Typical roughness elements were about 10 to 30 cm high in the grassed area and less than .5 cm on the runways. The station is surrounded by farmland and tidal flats; the nearest buildings or other large obstructions upwind (west) were always more than 2 km away.

The instrument sensors were mounted at fixed levels on a 5 m mast which was aligned with the wind by rotating it manually. Some surface pressure measurements were made at this site in winds up to 10 m/sec. A hole was dug in the asphalt runway to contain the box used for the surface measurements, Figure 88. Cables led downwind to the signal conditioners and tape recorder that were in the back of an I.O.U.B.C. truck, Figure 89. B.C. Hydro electrical power, 115 VAC, was available from a nearby outlet.

(iii) Boundary Bay Site

The Boundary Bay site is located approximately 75 m from the high tide line on the mud flats of Boundary Bay, Figure 90. The flats to the south of the site were free of obstruction except for the occassional log or patches of grass. Changes in surface elevation were about 10 cm; the potholes which occurred were filled with water. The area to the north is farmland. Along the high tide line is a 2 m high dike. Since this site was used for instrument calibration only, uniform terrain was not critical.

The instrument box used for surface pressure measurements was placed flush with the surrounding surface in an area which was uniform and flat for a few meters. Mean wind profile measurements were made on a 4 m aluminum mast. Other instruments were attached to a 2 m aluminum stand. As at the Ladner site, the electronics were kept in an I.O.U.B.C. truck and electrical power was obtained from a nearby outlet.

Instruments and Observational Techniques

(i) Analog Data Recording

The analog data were recorded on 14-track 1" magnetic tapes using an AMPEX Model FR-1300 Recorder/Reproducer (Ampex Co., 1966) portable tape recorder. Signals were recorded FM using the IRIG scheme. An input level of ± 1 volt rms produces ± 40% deviation from the center frequency. Most data were recorded at $7\frac{1}{2}$ ips. At this speed, the frequency response was flat (within 1.0 db) from 0 to 2.5 kHz, and the rms signal to noise ratio was 44 db; adequate for the purpose. One feature of this tape recorder which is very useful is the two sets of tape heads; one set for recording and the other for simultaneous monitoring. A separate switching box permitted any two of the signals being recorded to be viewed on the dual beam oscilloscope.

(ii) Sonic and U-Wire

The turbulent velocity components were measured with a KAIJO-DENKI three dimensional ultrasonic anemometer-thermometer (Kaijo-Denki Co. Ltd., 1967) referred to as the 'sonic' and the downstream component using a DISA Type 55D05 battery operated constant temperature hot-wire anemometer (Disa Elecktronik A/S, 1967) referred to as a 'u-wire' or 'hot wire'. The sonic used has a probe with a path length of 20 cm. Thus for typical mean wind speeds, less than 10 m/sec, velocity fluctuations from DC to greater than 10 Hz could be measured before the effect of averaging over the 20 cm path became important. The junction box and probe were mounted at a well exposed position on the mast, usually more than 1 m from the main mast . A 100 m cable connected the junction box to the remaining electronics, in the hut or

truck. The analog output of the sonic is ± 1 v peak to peak with offsets to adjust for the mean wind. Accuracies are about ± 3% of the full scale ranges of 1 m/sec, 3 m/sec and 10 m/sec.

The u-wires were mounted either separately from, or attached to, the pressure measuring instrument. Coaxial signal cable and compensating cable led to the Disa u-wire electronics which give an analog signal output. The signal had the DC level and gain adjusted before recording; this additional equipment was built by E. Jerome, a fellow graduate student. The accuracy of the instrument is limited by the calibration of the probes. Most probes used were calibrated in a wind tunnel initially, then checked against cup anemometers or the sonic in the field. The calibration was probably known to ± 15%.

(iii) Cup Anemometers

The mean wind speed profile was measured with cup anemometers, normally positioned with a logarithmic spacing at levels between .5 and 5 m. The cups were mounted on arms up to 50 cm from the main mast. For most Runs more than one cup was in working order. A different set was used at each of the sites: I.O.U.B.C. Wind Profile System at the Spanish Banks site (Hume, 1967), MAKINO system at the Ladner site (Makino Co. Ltd.), and CASELLA system at the Boundary Bay site (C.F. Casella and Co. Ltd.). All these systems are of the counter type, where either a photocell or a reed switch is pulsed by the turning cups; the pulses are then modified to drive a counter which counted the total number of pulses. The I.O.U.B.C. and Makino systems include an rms meter for instantaneous visual monitoring. The total counts from each cup were obtained at timed intervals, usually spanning the period of analog data recording; the mean wind at fixed levels was read from the

calibration curves. The calibration of the cups was checked in a wind tunnel. The mean wind for any other level was obtained graphically using a best line fit to the cup readings plotted on a log-linear plot. For observations over water, the winds have been referenced to a coordinate system moving with the mean current. Results are accurate to .1 m/sec. Observations were analysed only when the mean wind speed and direction were later found to be reasonably steady; if a 5 minute average wind speed changed by more than 20 to 30% from the previous 5 minute average, conditions were considered to be non-stationary and the Run was not used.

(iv) Wave Probe

Two different systems were used for wave height measurements, both employed a capacitive type of wave probe. The probe consisted of a brass rod 150 cm long and .635 cm (1/4 inch) in diameter covered with a sleeve of teflon .0254 cm (1/100 inch) thick which was sealed at one end and attached by a water tight connection to a coaxial cable at the other. The brass rod formed one plate of a capacitor, the teflon the dielectric and sea water the other plate; as the water height changed so did the capacitance. This rod was held in a bracket arranged so that it could be mounted vertically on the masts. The two systems used different methods of measuring the capacitance. One system is the equipment as modified by a fellow graduate student (Dobson, 1969) in which the wave probe capacity is part of the frequency controlling network of a blocking oscillator; the FM signal was returned to the platform, demodulated with a VETTER Model 3 FM Recording Adaptor and then recorded on magnetic tape. The other system (Hume, 1969) used a constant current source to charge the capacity of the probe and measured the time taken to charge to a given voltage level; the ratio of this time to the cycling time of 10^{-4} sec

was converted to an analog signal. The resolution is 1/1000 of the range; a sensitivity adjustment allowed use of different wave height ranges. The system has very little drift.

The probes were calibrated before and after each field trip by holding the probe at different depths in a tank of salty water. The probe was frequently wiped with an oily cloth to keep the wetting characteristics constant; this improved the reproducibility of the calibrations. Figure 91 shows typical calibrations for the two systems. Both systems should give wave height to ±10%.

(v) Water Height and Current

Mean water height was measured by reference to bands of reflecting (for working at night) tape on one of the masts. The tape interval was 1/2 meter; the mean could be estimated to ±10 cm.

The surface current was obtained by measuring with a stop watch the time taken for a piece of tissue paper to travel 7.5 m between two of the supporting members of the platform. Direction was by reference to topographic features. The tidal current normally flows in an east-west direction with speeds up to 30 cm/sec. The measuring technique gave results to ±1 cm/sec. Some current speeds at various depths were measured with a calibrated Savonius rotor current meter. The speed did not vary with depth within the top meter.

(vi) Air and Water Temperature

Wet and dry bulb temperatures were obtained to ±0.1 C° from mercury in glass thermometers. These thermometers were mounted in a sun screen that

could be moved to a well exposed location on the platform. Water temperature was obtained by immersing a similar thermometer in the upper few cm of water below the platform. All thermometers were calibrated against a laboratory standard.

APPENDIX B

ANALYSIS OF DATA

The data analysis can be considered in two parts; that concerned with the statistical description of variables such as turbulence or waves and that concerned with the general description of the flow by mean values such as stress or stability.

The statistical analysis was done digitally, using an IBM 7044 or 360 computor at the U.B.C. Computing Center.

Since the data was initially recorded analog, conversion to digital form was necessary. This was done using an analog to digital converter (10 binary bits) designed and built at I.O.U.B.C. Up to ten channels of information could be sampled sequentially in a cross-channel sweep, with a delay of approximately 45 micro-seconds between channels. The time between cross-channel sweeps could be varied from about 3×10^{-2} to 2×10^{-4} sec.

Provided that data is band limited to frequencies less than n_{max}, and the data is digitized at a minimum rate of $2n_{max}$, Blackman and Tukey (1959, p.117) show that all such data can be represented in frequency space with no aliasing. To reduce aliasing the signals were filtered with matched linear phase shift filters before digitizing. Since most of the data were recorded at tape speeds of $7\frac{1}{2}$ ips and reproduced for digitizing at 60 ips (which increased all frequencies by a factor of 8), the cutoffs of the filters were designed accordingly. In real time the filter cutoff (3 db down) was at about 20 Hz and the folding frequency, n_f, for most of the data was set at 31 Hz (i.e., data were digitized at 500 Hz).

The output of the analog to digital converter was written on an IBM compatible magnetic tape using a Control Data Corporation 8092 Teleprogrammer

at the U.B.C. Computing Center.

The method used to obtain statistical information from the data on the digital tape requires two steps. The first step uses a main program, 'FTOR', which takes the time series digital data and creates a second magnetic tape containing the corresponding complex Fourier coefficients of the data. This step makes use of the 'Fast Fourier Transform' algorithm, 'FFT' (I.E.E.E. Transactions, Special issue on Fast Fourier Transform, June 1967). The second step takes these Fourier coefficients and produces spectra, etc., from programs built around a main program called 'SCOR'. These basic programs were written by J.R. Wilson and J.F. Garrett of this institute (see J.F. Garrett, 1970).

In 'FTOR', the maximum number of data points per block that can be handled is 10,240. The actual number of points used in each block is the number of channels times the number, N, of data points from each channel, where the latter has to be a power of 2. The FFT technique then produces complex Fourier coefficients for each channel for harmonic frequencies from the fundamental frequency of 1 cycle per block to n_f, the folding frequency. This is done sequentially for all blocks in the entire Run. For a half hour Run, with 4 to 6 channels of data, the total number of data blocks, M, was typically 30 to 50.

When analysing a time series of length $N\Delta t$, where Δt is the number of seconds between data points, the Fourier coefficients are calculated for specific angular frequencies, $\omega_r = \frac{2\pi r}{N\Delta t}$, where r is an integer. If the time function to be analysed contains a frequency, ω_o, not equal to an ω_r, this produces a set of Fourier coefficients that peak near the frequency ω_o and fall off asymptotically as $1/(\omega - \omega_o)$ (Blackman and Tukey, 1959, p.33) or as $1/(\omega - \omega_o)^2$ for the spectral estimates. This is essentially the spectral

window for the initial part of the analysis. To improve the window, the Fourier coefficients could be 'hanned' using the formulation

$$\left.\begin{aligned} A_r &= -\tfrac{1}{4} A'_{r-1} + \tfrac{1}{2} A'_r - \tfrac{1}{4} A'_{r+1} \\ \text{and} \quad B_r &= -\tfrac{1}{4} B'_{r-1} + \tfrac{1}{2} B'_r - \tfrac{1}{4} B'_{r+1} \end{aligned}\right\} \qquad (19)$$

where A_r and B_r are the cosine and sine coefficients, respectively. The window for the hanned coefficients gives a spectral falloff rate of $1/(\omega - \omega_o)^6$. Hanning was used only in a few special cases.

The program 'SCOR' uses the coefficients from 'FTOR' to obtain the desired statistics (see J.F. Garrett, 1970). The complex Fourier coefficient, C_{rm}, for the r^{th} harmonic in the m^{th} block, can be written as

$$C_{rm} = A_{rm} + i\, B_{rm}\,, \qquad (20)$$

where $i = \sqrt{-1}$. The spectral energy density, S, is then obtained for the frequency, $n_r = r/N\Delta t$, by multiplying C_{rm} by its complex conjugate and dividing by 2. The values of S are then grouped into bands. For this work, half octave bands are used for the frequency range where there are more than 5 spectral estimates (5 harmonics) per half octave. However, since the individual spectral estimates at the lower frequencies are more than half an octave apart, the first 9 bands are preset to a larger bandwidth so that at least one coefficient is included in each band. When averaged over all blocks the spectral energy density for a band, S_b, can be written as

$$S_b(n_b) = \frac{N\,\Delta t}{1 + r_2 - r_1} \sum_{r=r_1}^{r_2} \frac{1}{M} \sum_{m=1}^{M} \frac{A_{rm}^2 + B_{rm}^2}{2} \qquad (21)$$

where $n_b = \frac{\sqrt{r_1 r_2}}{N\,\Delta t}$ is the geometric mean of the end frequencies and the bandwidth, B.W. $= \frac{1 + r_2 - r_1}{N\,\Delta t}$. Typically, the number of bands in each analysis is 23, with a minimum frequency of 2.7×10^{-2} Hz and a maximum of 3.0×10^{1} Hz.

The cospectrum between, say, data channels 1 and 2 was estimated from

$$Co_{12}(n_b) = \frac{N\,\Delta t}{1 + r_2 - r_1} \sum_{r=r_1}^{r_2} \frac{1}{M} \sum_{m=1}^{M} \frac{A_{1rm}A_{2rm} + B_{1rm}B_{2rm}}{2} \qquad (22);$$

the quadrature spectrum from

$$Qu_{12}(n_b) = \frac{N\,\Delta t}{1 + r_2 - r_1} \sum_{r=r_1}^{r_2} \frac{1}{M} \sum_{m=1}^{M} \frac{A_{2rm}B_{1rm} - A_{1rm}B_{2rm}}{2} \qquad (23);$$

the coherence from

$$Coh_{12}(n_b) = \frac{\sqrt{Co_{12}^2(n_b) + Qu_{12}^2(n_b)}}{\sqrt{S_{b1}(n_b)\,S_{b2}(n_b)}} \qquad (24);$$

and the phase from

$$\Theta_{12}(n_b) = \tan^{-1} \frac{Qu_{12}(n_b)}{Co_{12}(n_b)} \qquad (25).$$

Confidence limits were calculated directly by assuming each block to be an independent sample of the data. If the difference between the spectral estimate for each block and the mean over all blocks is assumed to have a Gaussian distribution, then these differences can be used to find the 95% confidence limits. The assumption is reasonable only if M, the number of data blocks, is quite large, which is true for most of the Runs.

Information on the spectral shape at lower frequencies was obtained from an additional program (G.A. McBean, 1970) which uses the same techniques as already discussed but with the block averages as data points or by digitizing data at a lower frequency.

The data had to be corrected for instrument and filter response. A program written by Dobson (1969) was used for phase correction; it also appropriately adjusted the Co- and Quad-spectra. Amplitude corrections were done by hand.

Since some wave data were collected when there was a significant mean water current, the frequency had to be corrected. In order to do this the influence of the water current on the wave frequency, ω_η (rad/sec), was removed by means of the equation

$$\omega_\eta = -\frac{g}{2U_w} \pm \frac{1}{2}\sqrt{\left(\frac{g}{U_w}\right)^2 + \frac{4g}{U_w}\omega_m} \qquad (26)$$

where U_w is the mean current and ω_m is the measured wave frequency.

In addition to the spectral description, the flow was described in terms of mean conditions including the surface stress and stability.

The surface stress was estimated by three different methods: direct measurement, the 'Φ_{11} method', or using a drag coefficient.

The direct measurement method involved estimating the stress from the variance of $\overline{uw}$ ($\tau = -\rho\overline{uw}$); the velocity components were measured with a sonic anemometer. Coordinate rotation was used to correct for non-alignment with the mean wind by appropriately adjusting the calibration coefficients to be used in the SCOR program. This method for finding the stress is considered the most accurate.

The 'Φ_{11} method' estimates the stress from a knowledge of the magnitude of downstream velocity fluctuations in the inertial subrange (Weiler and Burling, 1967). For this range, the spectral density of the downstream velocity fluctuations (Φ_{11}) at wave number k is approximately

$$\Phi_{11}(k) = K' \varepsilon^{2/3} k^{-5/3} \qquad (27)$$

where ε is the rate of energy dissipation and K' is the Kolmogoroff constant, taken to be 0.5. Assuming that the rate of production of turbulent energy is equal to the rate of dissipation and that the wind profile is logarithmic, and using equation (27), the stress ($\tau = \rho u_*^2$) can be written:

$$\rho u_*^2 = 3.86\, \rho \left(\frac{z}{U}\right)^{2/3} n^{5/3}\, \Phi_{11}(n) \qquad (28).$$

The value of $\Phi_{11}(n)$ at the frequency n was taken from a plot of log Φ_{11}

against log n for which a best fit -5/3 line was drawn.

For observations over water a drag coefficient, C_{D5}, was occasionally used to relate the 5 meter mean wind, in cm/sec, to the surface stress by the formula

$$\tau = \rho u_*^2 = C_{D5} \rho U|_5^2 \tag{29}$$

where $C_{D5} = 1.2 \times 10^{-3}$. A plot of the drag coefficient as a function of wind speed, Figure 92, uses values of stress estimated from direct measurement and the Φ_{11} method. As can be seen, all the methods are compatible and each suitable for estimating a value for the surface stress.

The stability of the air over water was estimated in terms of the gradient Richardson Number, Ri_G. It can be written as

$$Ri_G = \frac{g}{\theta} \frac{\partial\theta/\partial z}{(\frac{\partial U}{\partial z})^2} \tag{30}$$

for $\theta = T_A (1 - 0.61 h_{sp})$, where g is the gravitational acceleration, T_A is the air temperature, U is air velocity, z is height, and h_{sp} is specific humidity. θ is a virtual temperature, which includes the effect of both air temperature and humidity on the buoyancy. Ri_G was calculated in a difference form: the difference between the value at some height z and at z = .01 cm. It is assumed that at this lower height $U|_{.01} = 0$ and $T_{.01} = T_w$ (surface water temperature). Then

$$Ri_G = \frac{980}{\theta_{mean}} \frac{(\theta_z - \theta_{.01})}{(U|_z)^2} \sqrt{.01\, z}\ (\ln z + 4.61) \tag{31}$$

where the θ's were calculated from

$$\left.\begin{aligned} \theta_z &= T_A\,(1 + 5.0 \times 10^{-4}\, h_{re}\, e_{sa}|_z) \\ \text{and} \quad \theta_{.01} &= T_w\,(1 + 5.0 \times 10^{-2}\, e_{sa}|_{.01}) \end{aligned}\right\} \qquad (32)$$

The relative humidity, h_{re}, and the saturation vapour pressure, e_{sa}, were obtained from handbook tables using the mean wet and dry bulb and surface water temperatures observed during a Run. It is intended that this method of estimating the stability should give at least an order of magnitude value for comparison within this study and with other studies.

APPENDIX C

DATA SUMMARY

TABLE V (see below) lists the 'mean' conditions under which each of the Runs mentioned in this report were taken. Some data from unlisted Runs were used in the more general summary plots. They were taken under conditions similar to those shown. The table is presented in two sections: part A gives data for measurements associated with a flat boundary, and part B gives data for measurements associated with waves. The Runs are in numerical order within each section. The site abbreviations used were: 'S.B.' for Spanish Banks, 'L' for Ladner, and 'B.B.' for Boundary Bay. Measurements at the Spanish Banks site are used in both parts since observations were taken both when the water was shallow or absent and when the water was deeper and active wave generation was present. The 'duration' is the total time, in minutes, of digitized data. Most of the Runs were originally about half an hour in duration, however instrument saturation or drift often necessitated using shorter pieces of data for analysis. The value for the stress, $\tau = 1.25 \times 10^{-3} u_*^2$, is followed by a number, 1, 2, or 3, in brackets. This number indicates the method used to evaluate the stress: (1) for direct measurement, (2) for the Φ_{11} method, and (3) for the drag coefficient. If two instruments at different levels were used, the heights above the surface (or mean water level) are given in succeeding lines. The water current at the Spanish Banks site generally flowed in an east-west direction. Listed after the magnitude of the current is the directions given as E for a current flowing <u>from</u> the east, and W for flow <u>from</u> the west. As mentioned in Appendix A, for observations over water, the winds have been referenced to a coordinate system moving with the mean current. For Runs in section B of the table, the

difference between the 5 meter wind and phase speed of the waves at the peak of the wave spectrum, ($U|_5 - C$), is given; the frequency of the peak is given in brackets after this velocity difference.

TABLE V

MEAN DATA FOR RUNS

A. FLAT BOUNDARY

RUN	DATE	SITE	tt (1)	$U\|_5$ (2)	WIND DIR	Ri_G (3)	τ (4)	z (5)	U (6)	h (7)	U_w (8)
72/1	Mar 21/69	S.B.	18	6.8	270°	-0.01	0.650(2)	2.0	6.5	1.0	0
72/2	Mar 21/69	S.B.	19	6.2	270°	-0.02	0.511(2)	2.0	6.0	1.0	0
73/1	Apr 3/69	S.B.	16	8.2	100°	-	0.974(2)	2.0	7.8	1.0	0
73/2	Apr 6/69	S.B.	10	3.9	260°	-	0.287(2)	3.5	3.9	0	-
73/3	Apr 6/69	S.B.	11	5.5	260°	-	0.221(2)	1.00	4.5	0	-
110/1	Aug 8/68	S.B.	27	7.2	285°	-	0.870(1)	5.5	7.1	0	-
110/2	Aug 8/68	S.B.	26	7.2	285°	-	0.910(1)	4.0	7.4	0	-
120/1	Aug 8/68	S.B.	22	6.8	270°	-	0.724(1)	3.4	6.5	0.75	0.40W
120/2	Aug 8/68	S.B.	30	6.5	280°	-	0.553(1)	4.8	6.2	1.2	0.40W
121/1	Aug 8/68	S.B.	27	5.8	275°	-	0.479(1)	1.5	5.4	2.2	0.63W
132/2/1	Sept 4/68	B.B.	9	3.7	280°	-	-	0.30	3.4	-	-
133/3/1	Sept 17/68	B.B.	26	6.1	270°	-	-	1.00	5.1	-	-
133/3/2	Sept 17/68	B.B.	17	7.0	270°	-	-	1.00	5.9	-	-
137/1	Sept 17/68	B.B.	18	5.8	270°	-	-	0.30	5.0	-	-

TABLE V (continued)

A. (continued)

RUN	DATE	SITE	tt	$U\|_5$	WIND DIR	Ri_G	τ	z	U	h	U_w
137/2	Sept 27/68	B.B.	25	4.1	295°	-	-	0.30	3.4	-	-
141/2/1	Apr 3/69	S.B.	18	7.8	120°	-0.01	0.900(2)	2.0	7.5	1.0	0
141/2/2	Apr 3/69	S.B.	9	7.8	120°	-0.01	0.900(2)	2.0	7.5	1.0	0
141/3	Apr 3/69	S.B.	19	7.6	130°	-0.01	0.900(2)	2.2	7.3	1.0	0
142/1	Sept 27/68	B.B.	16	4.3	280°	-	-	0.30	3.5	-	-
165/2	Mar 12/69	S.B.	13	4.4	280°	-0.02	0.277(2)	2.5	4.3	2.0	0
172/1	Mar 20/69	S.B.	12	5.3	270°	-0.04	0.367(2)	1.5	5.0	1.5	0
172/2	Mar 20/69	S.B.	20	5.9	270°	-0.04	0.518(2)	3.0	5.7	1.0	0
173/1	Mar 20/69	S.B.	19	6.8	280°	-0.03	0.611(2)	2.5 4.6	6.5 6.8	0.7	0
173/2	Mar 20/69	S.B.	22	7.4	280°	-0.02	0.941(2)	2.0 2.5	7.0 7.1	1.0	0.25W
186/3	Apr 7/69	S.B.	15	3.6	280°	-0.02	0.156(2)	2.5	3.6	0.5	0
186/4	Apr 7/69	S.B.	9	3.7	270°	-	0.196(2)	3.0 5.1	3.6 3.7	0	-
186/5	Apr 7/69	S.B.	8	2.7	270°	-	0.136(2)	1.25 6.75	2.6 2.7	0	-

TABLE V (continued)

A. (continued)

RUN	DATE	SITE	tt	$U\|_5$	WIND DIR	Ri_G	τ	z	U	h	U_w
196/1	Jul 15/69	S.B.	13	3.7	270°	-0.12	0.189(3)	0.46 1.05	- -	0.20	0
196/2	Jul 15/69	S.B.	20	3.4	270°	-0.29	0.160(3)	0.46 1.05	- -	0.20	0
196/3	Jul 15/69	S.B.	8	3.7	270°	-0.13	0.189(3)	0.20 0.76	- -	0.30	0
200/2	Jul 17/69	S.B.	23	4.7	260°	-0.01	0.302(3)	4.0 4.5	4.6 4.6	2.0	0.64W
205/1	Jul 19/69	S.B.	30	3.8	260°	-0.04	0.197(3)	5.0	3.8	1.0	0.30W
205/2	Jul 19/69	S.B.	23	3.8	260°	-0.03	0.197(3)	5.0	3.8	1.0	0.46W
318/1	Aug 23/69	L	30	4.8	270°	-	1.23 (1)	0.40	3.5	-	-
318/2	Aug 23/69	L	31	4.8	270°	-	1.17 (1)	0.40	3.3	-	-
319/1	Jan 27/70	L	24	9.9	270°	-	3.84 (2)	0.32	6.7	-	-
319/2	Jan 27/70	L	22	9.8	270°	-	3.84 (2)	0.32	6.7	-	-
320/1	Jan 27/70	L	32	8.8	270°	-	1.84 (2)	0.32	6.0	-	-
320/2	Jan 27/70	L	29	7.7	270°	-	1.16 (2)	0.32	5.3	-	-
425/1	Jan 27/70	L	24	6.1	270°	-	0.862(2)	0.32	4.1	-	-

TABLE V (continued)

A. (continued)

RUN	DATE	SITE	tt	$U\|_5$	WIND DIR	Ri_G	τ	z	U	h	U_w
425/2	Jan 27/70	L	23	5.2	260°	-	0.756(2)	0.32	3.5	-	-
426/1	Jan 27/70	L	32	6.1	270°	-	0.862(2)	0.32	4.1	-	-

TABLE V (continued)

B. NEAR WAVES

RUN	DATE	SITE	tt	$U\|_5$	WIND DIR	Ri_G	τ	z	U	h	U_w	$U\|_5 - C$ (9)
60/1	Mar 27/69	S.B.	16	4.3	250°	-0.01	0.274(3)	0.40 0.90	3.5 3.8	2.5	0.22E	0.2(0.32)
60/2	Mar 27/69	S.B.	12	4.7	250°	0.001	0.331(3)	0.50 1.00	3.9 4.1	2.5	0.22E	0.6(0.32)
60/4	Apr 2/69	S.B.	22	4.1	130°	-0.05	0.252(3)	0.30 0.80	2.9 3.3	3.0	0	1.7(0.65)
80/3	Mar 27/69	S.B.	17	3.9	260°	-0.01	0.228(3)	0.30 0.80	3.3 3.5	2.5	0.22E	-0.2(0.32)
119/1	Apr 2/69	S.B.	15	4.1	90°	-0.05	0.252(3)	0.40 0.90	3.5 3.7	3.0	0	1.8(0.70)
119/2	Apr 2/69	S.B.	19	4.7	120°	-0.04	0.331(3)	0.30 0.80	4.1 4.3	3.0	0	2.3(0.65)
119/3	Apr 2/69	S.B.	17	4.8	120°	-0.04	0.344(3)	0.30 0.80	3.8 4.2	3.0	0	2.2(0.60)
164/1	Dec 18/68	S.B.	14	2.6	290°	-0.19	0.101(3)	0.50	2.2	3.5	0	-2.3(0.25)
164/2	Dec 18/68	S.B.	16	4.1	340°	-0.09	0.252(3)	0.60	3.5	3.5	0	-1.5(0.18)
167/1/1	Dec 14/68	S.B.	19	8.1	115°	0.02	0.985(3)	0.50	6.3	3.5	0.24E	5.0(0.50)
167/1/2	Dec 14/68	S.B.	18	7.2	120°	0.02	0.776(3)	0.50	5.7	3.5	0.24E	4.1(0.50)
167/2	Dec 14/68	S.B.	14	7.9	100°	0.03	0.935(3)	0.30	5.8	3.5	0.24E	4.8(0.50)

TABLE V (continued)

B. (continued)

RUN	DATE	SITE	tt	$U\|_5$	WIND DIR	Ri_G	τ	z	U	h	U_w	$U\|_5 - C$
167/3	Dec 14/68	S.B.	6	6.4	125°	0.05	0.615(3)	0.30	4.8	3.5	0.24E	3.3(0.50)
173/3	Mar 20/69	S.B.	14	3.6	240°	0.02	0.194(3)	0.90 1.40	3.1 3.2	2.5	0.30W	-0.5(0.30)

(1) Duration (minutes)

(2) Mean wind at 5 meters (m sec^{-1})

(3) Gradient Richardson Number

(4) Surface Stress (dynes cm^{-2})

(5) Instrument height (m)

(6) Mean wind at the instrument height (m sec^{-1})

(7) Water depth (m)

(8) Current (m sec^{-1})

(9) $U|_5 - C$ at the peak of the wave spectrum (m sec^{-1})

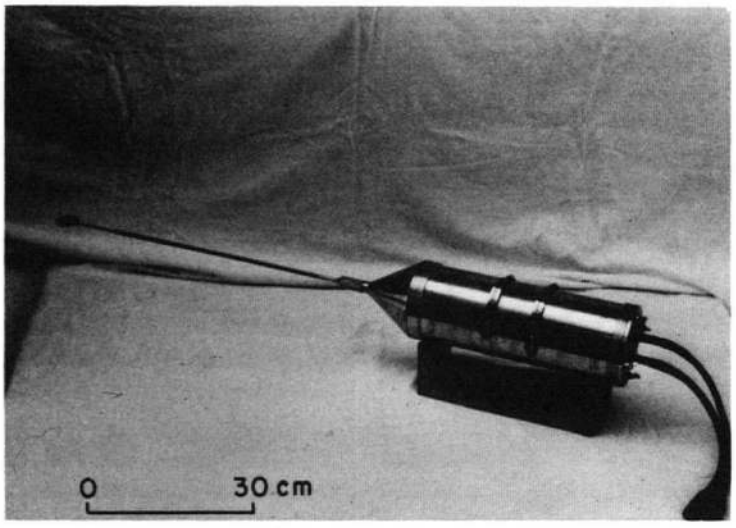

(a)

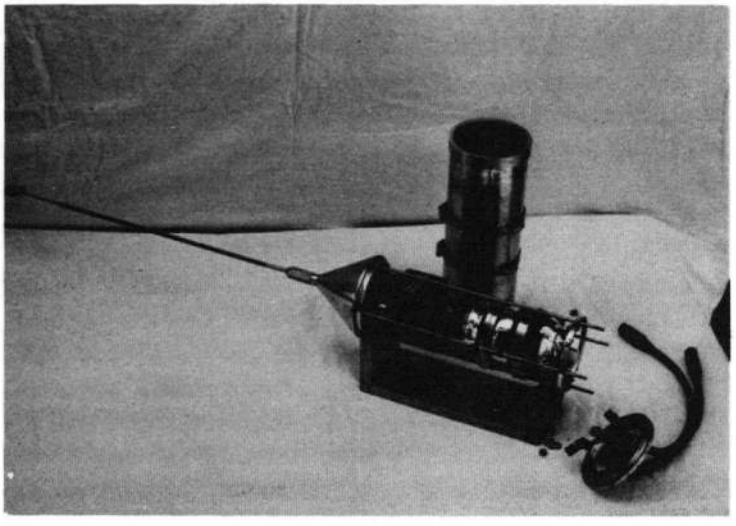

(b)

Figure 1. Pressure instrument used to measure the static pressure fluctuations within the turbulent flow
(a) assembled
(b) with cylinder removed

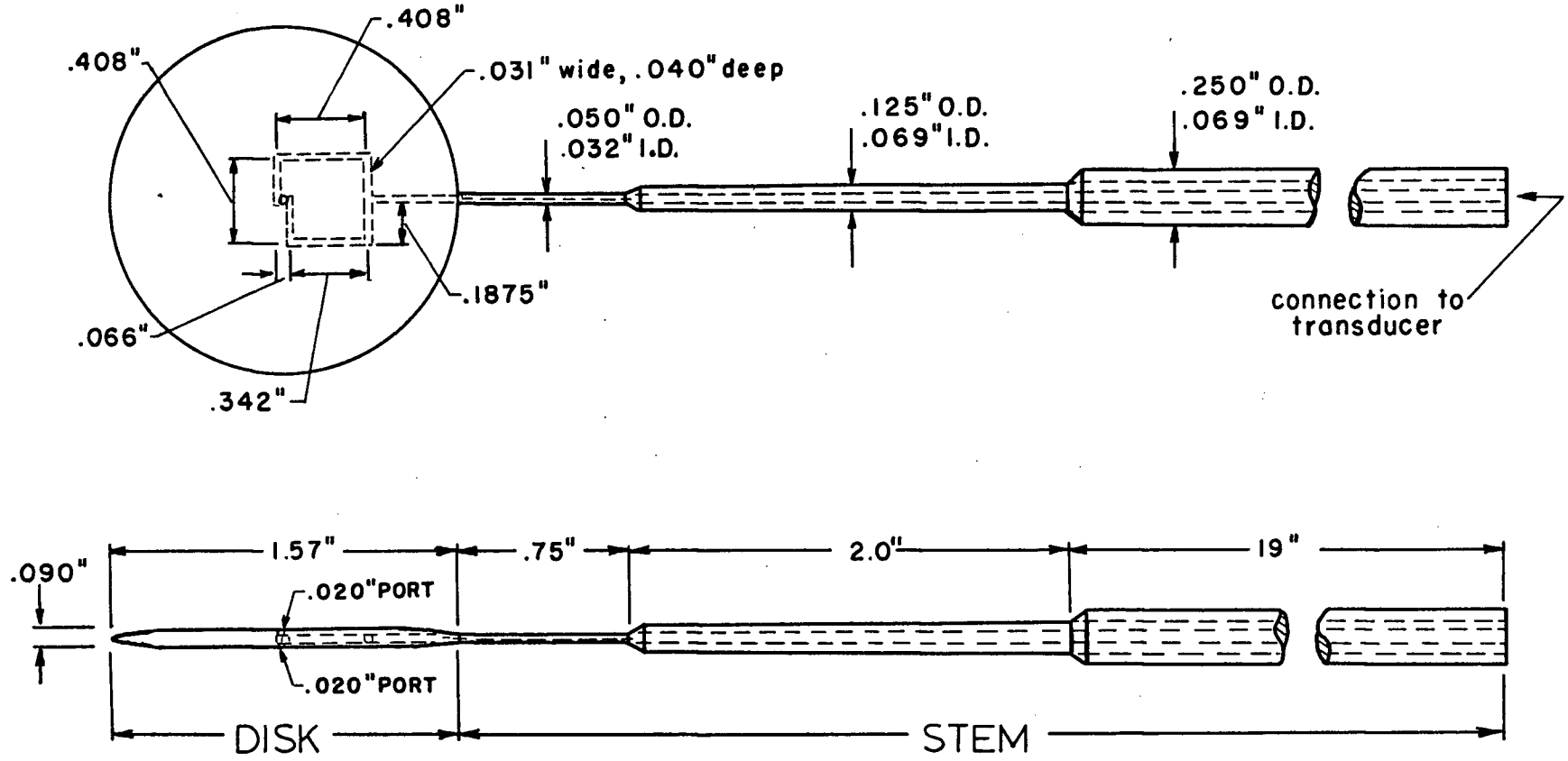

Figure 2. Probe developed for measuring static pressure fluctuations within the turbulent flow

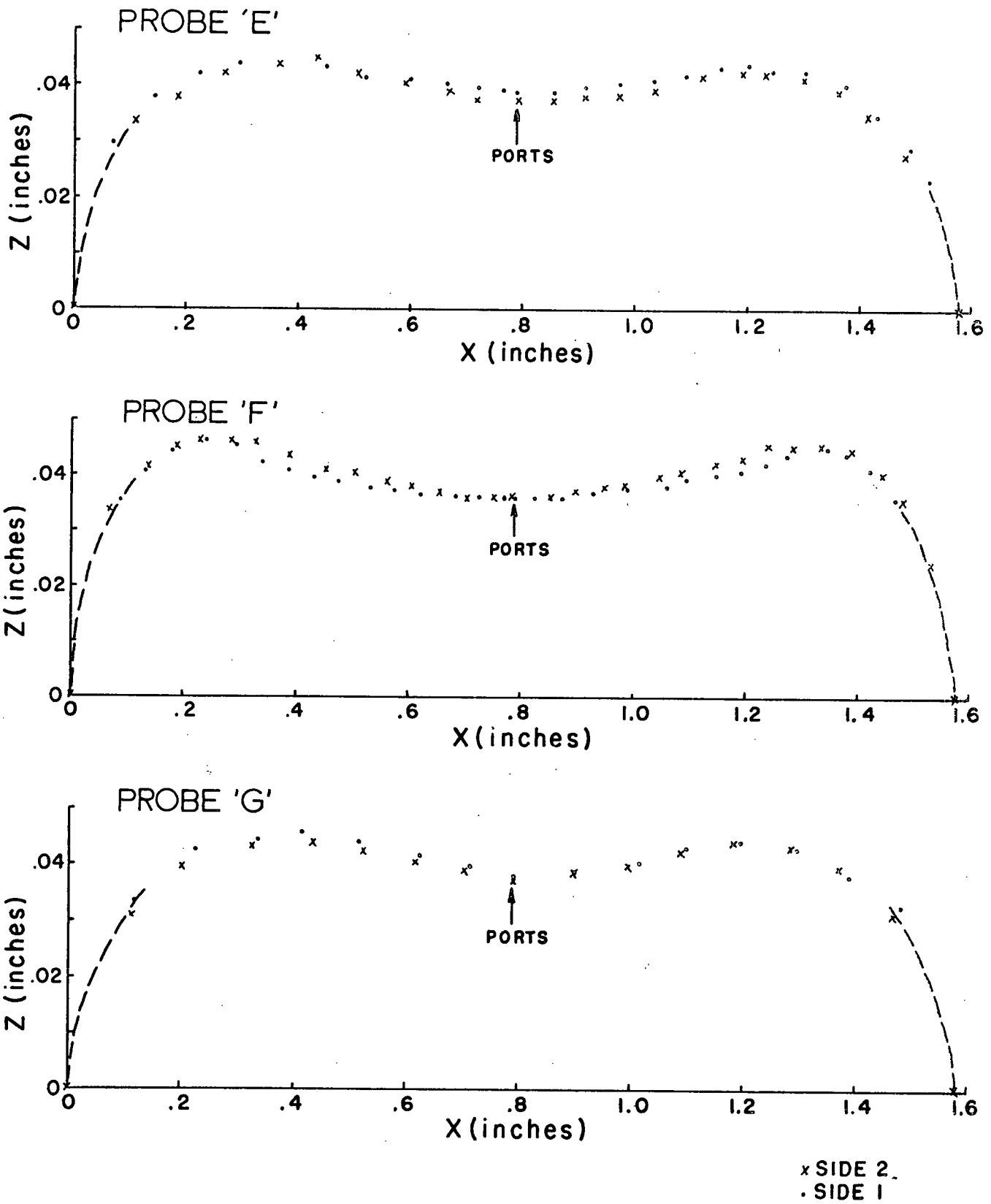

Figure 3. Cross-sections of the disks of probes E, F, G

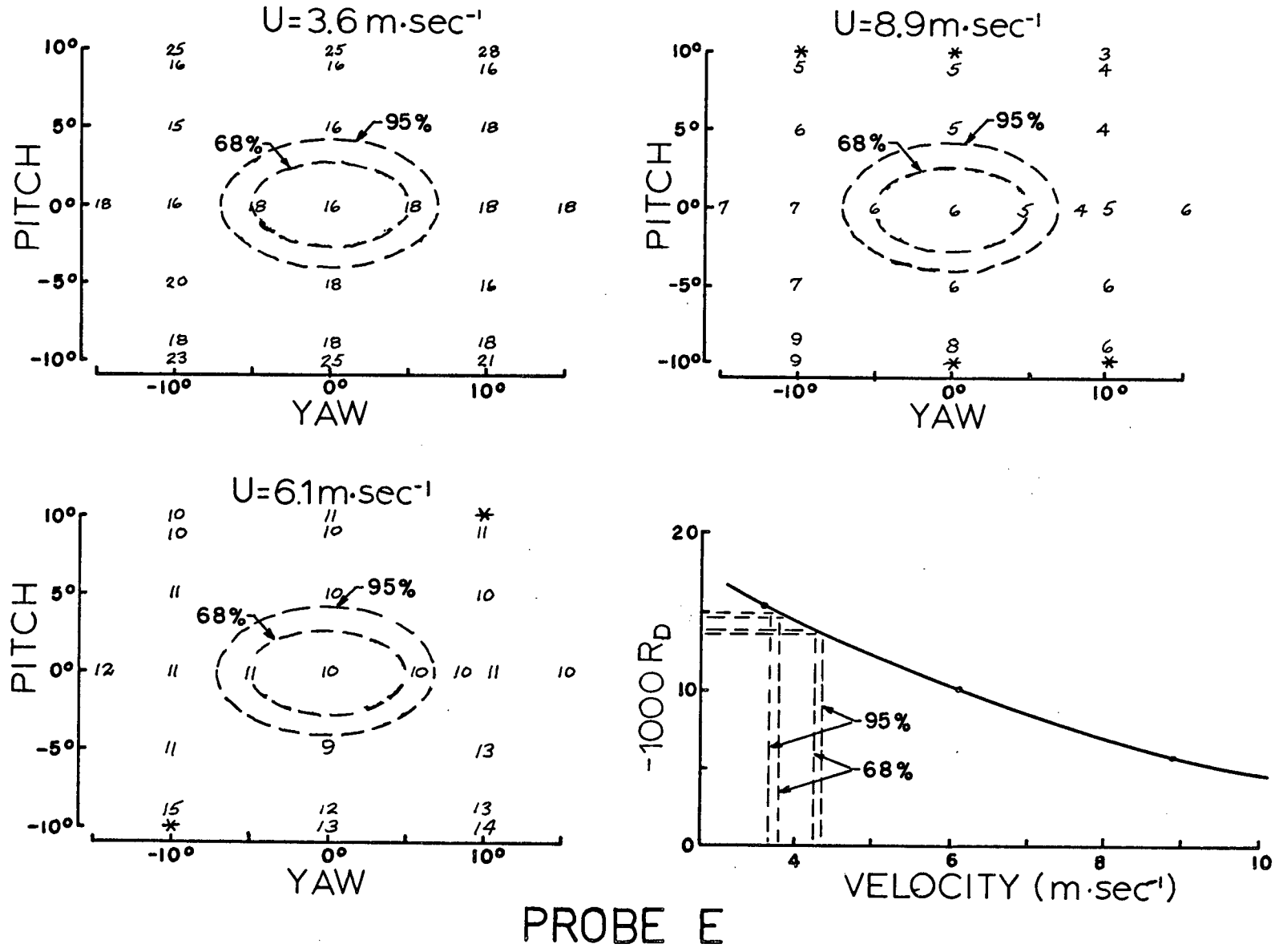

Figure 4. Dynamic pressure noise test for Probe E at different wind speeds

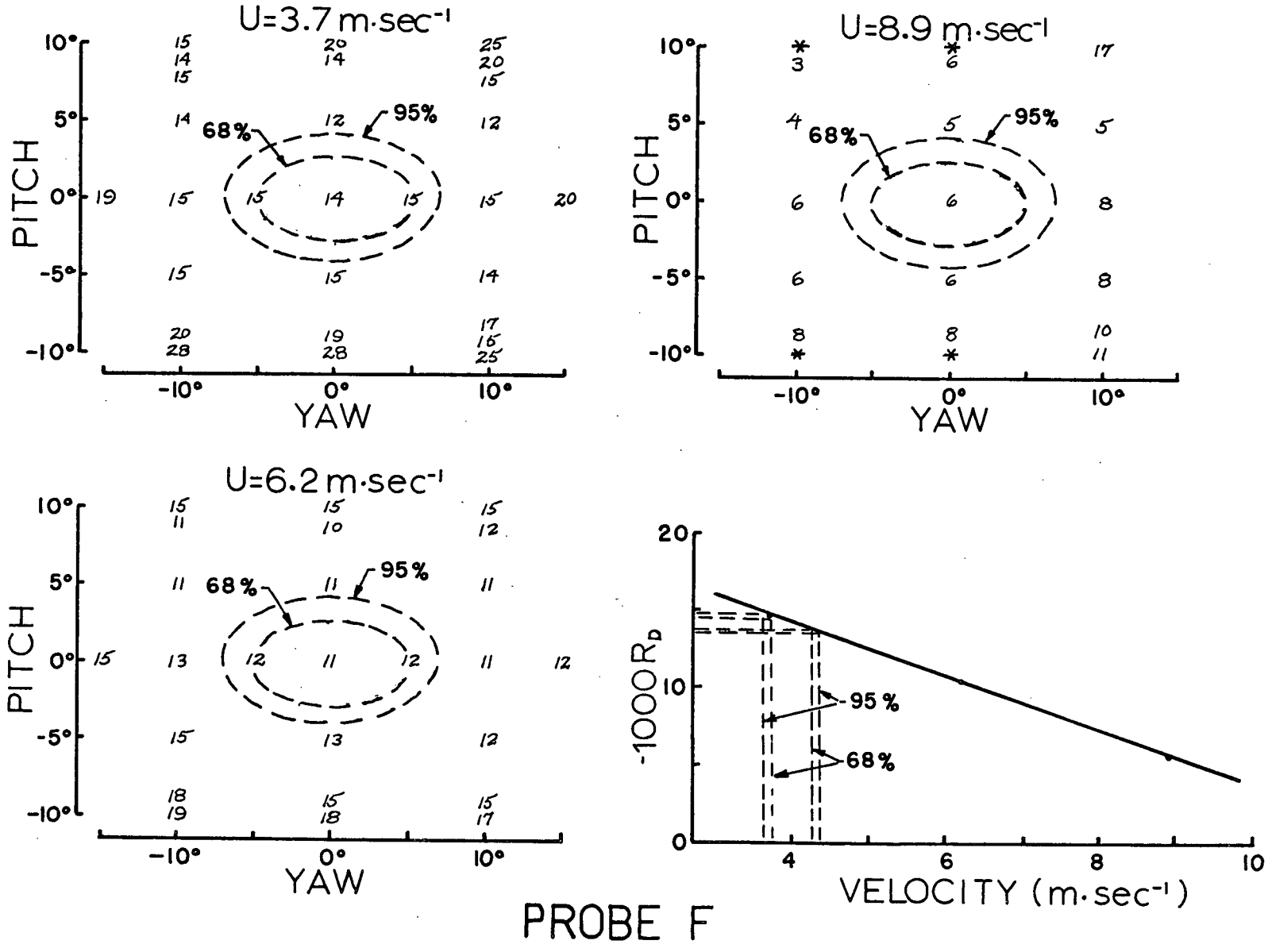

Figure 5. Dynamic pressure noise test for Probe F at different wind speeds

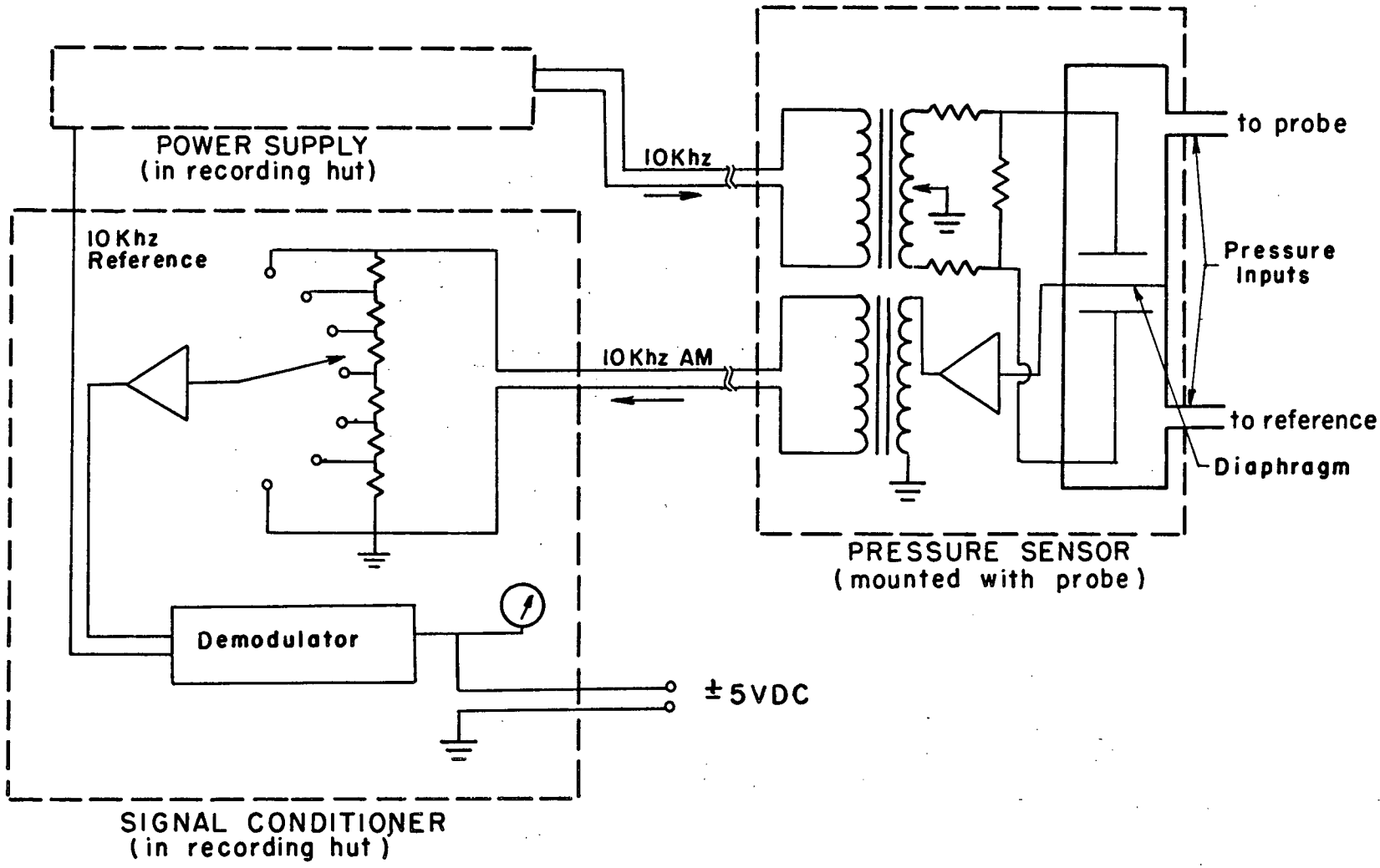

Figure 6. Schematic of the Barocel transducing system

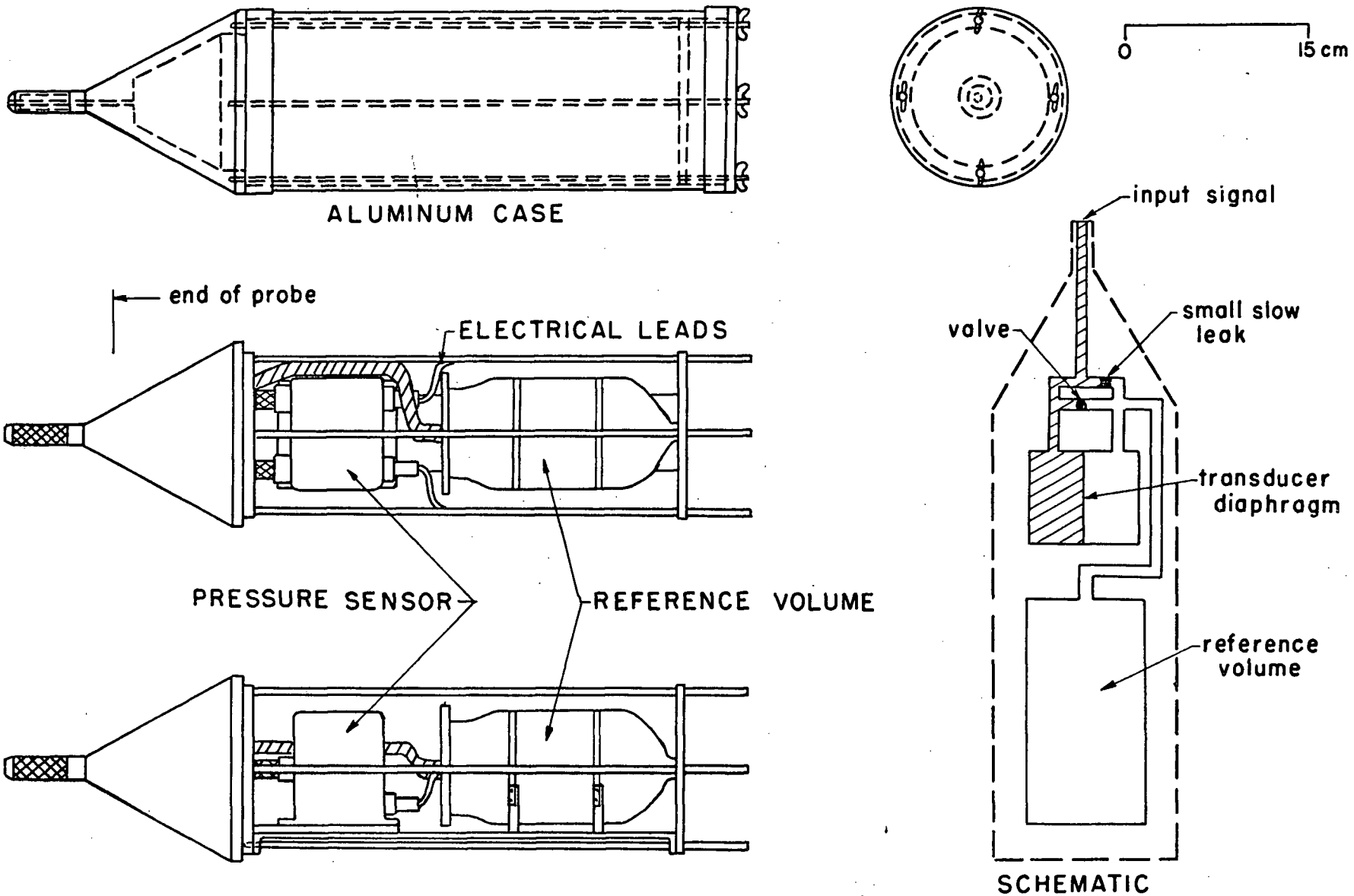

Figure 7. Barocel pressure transducer and reference volume in their container

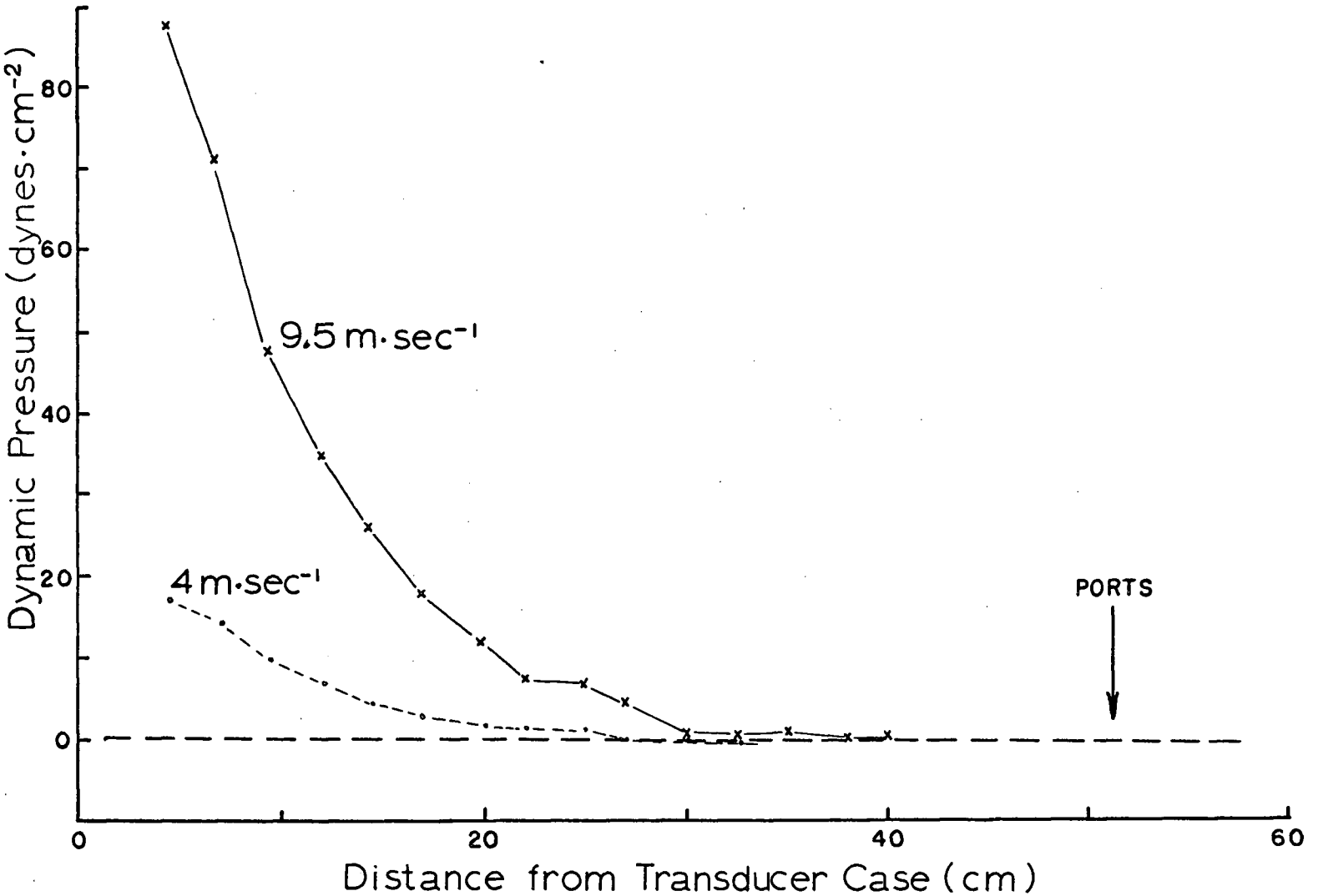

Figure 8. Results of wind tunnel test for the dynamic pressure distribution in front of the transducer case

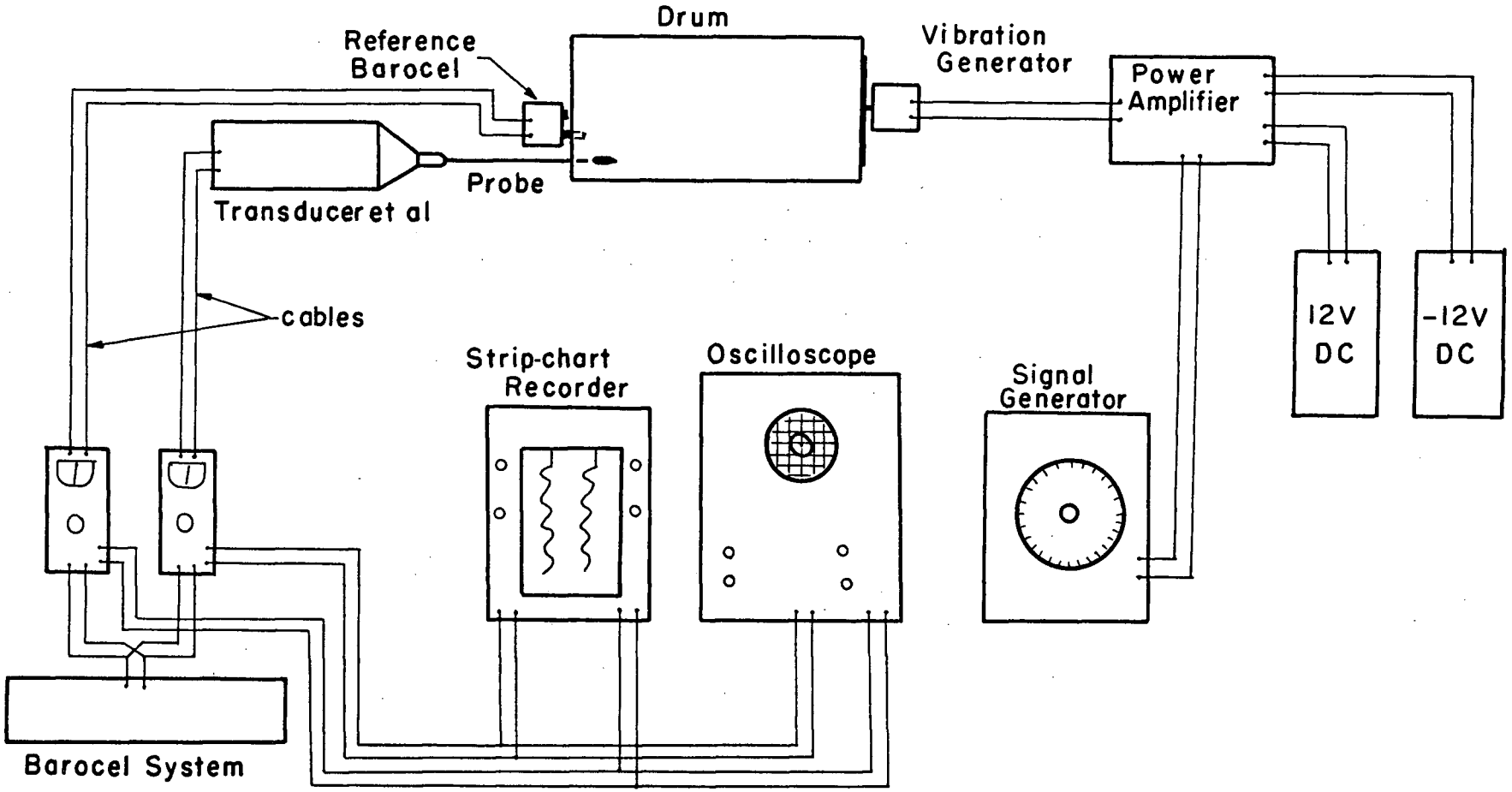

Figure 9. Arrangement used for calibrating the pressure instrument for amplitude and phase response

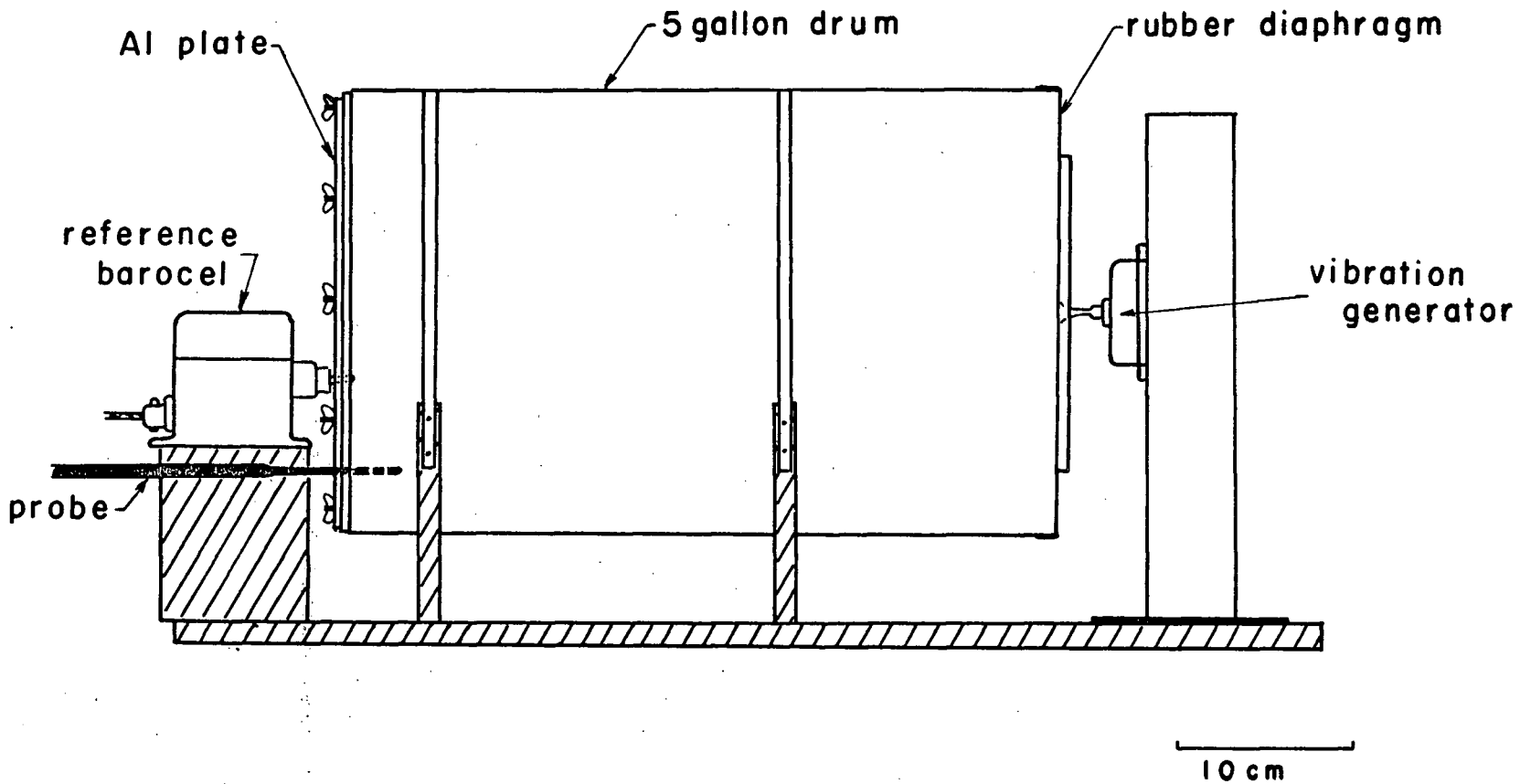

Figure 10. Detail of the drum used to create a sinusoidally varying pressure

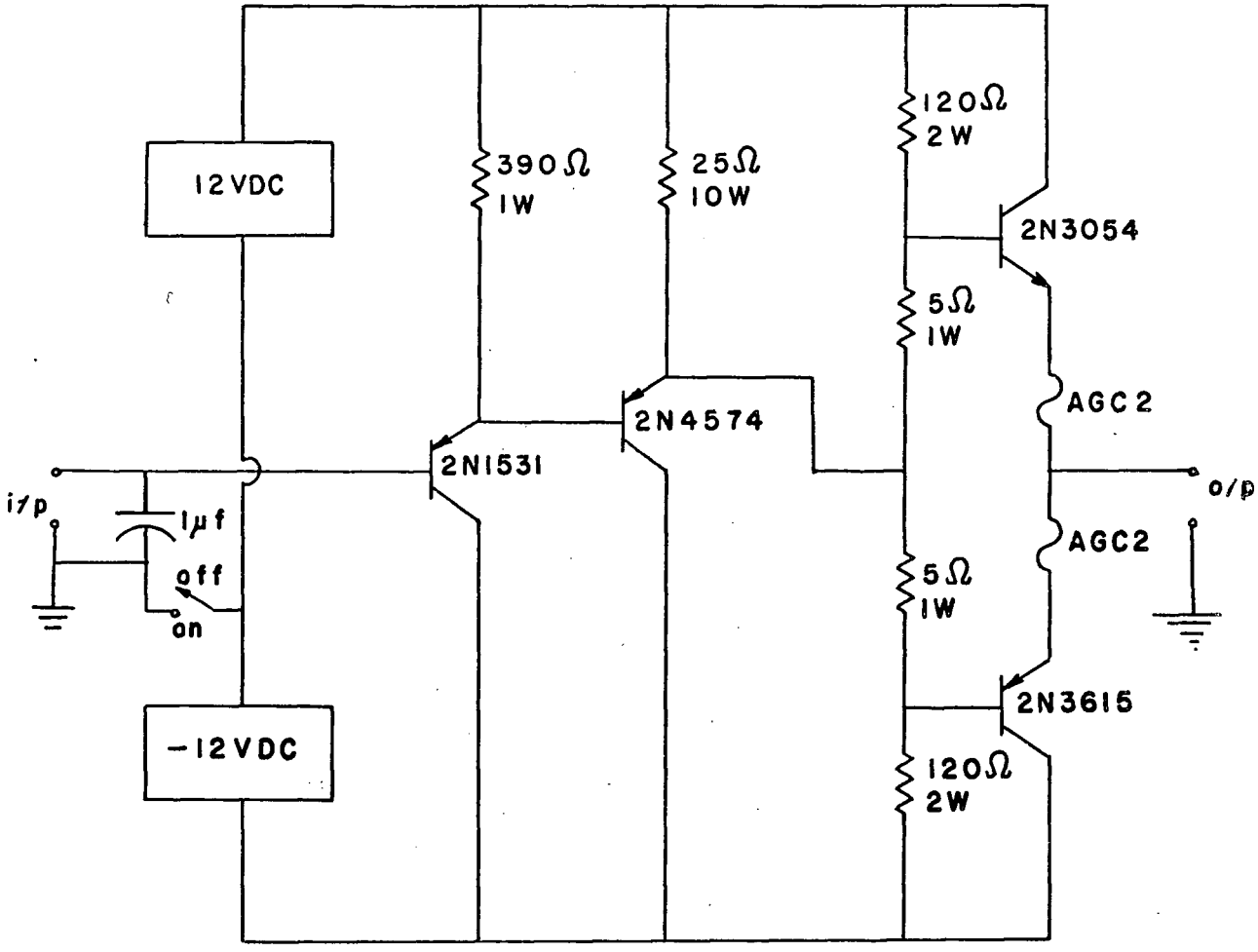

Figure 11. Circuit diagram for power amplifier used to drive the vibration generator

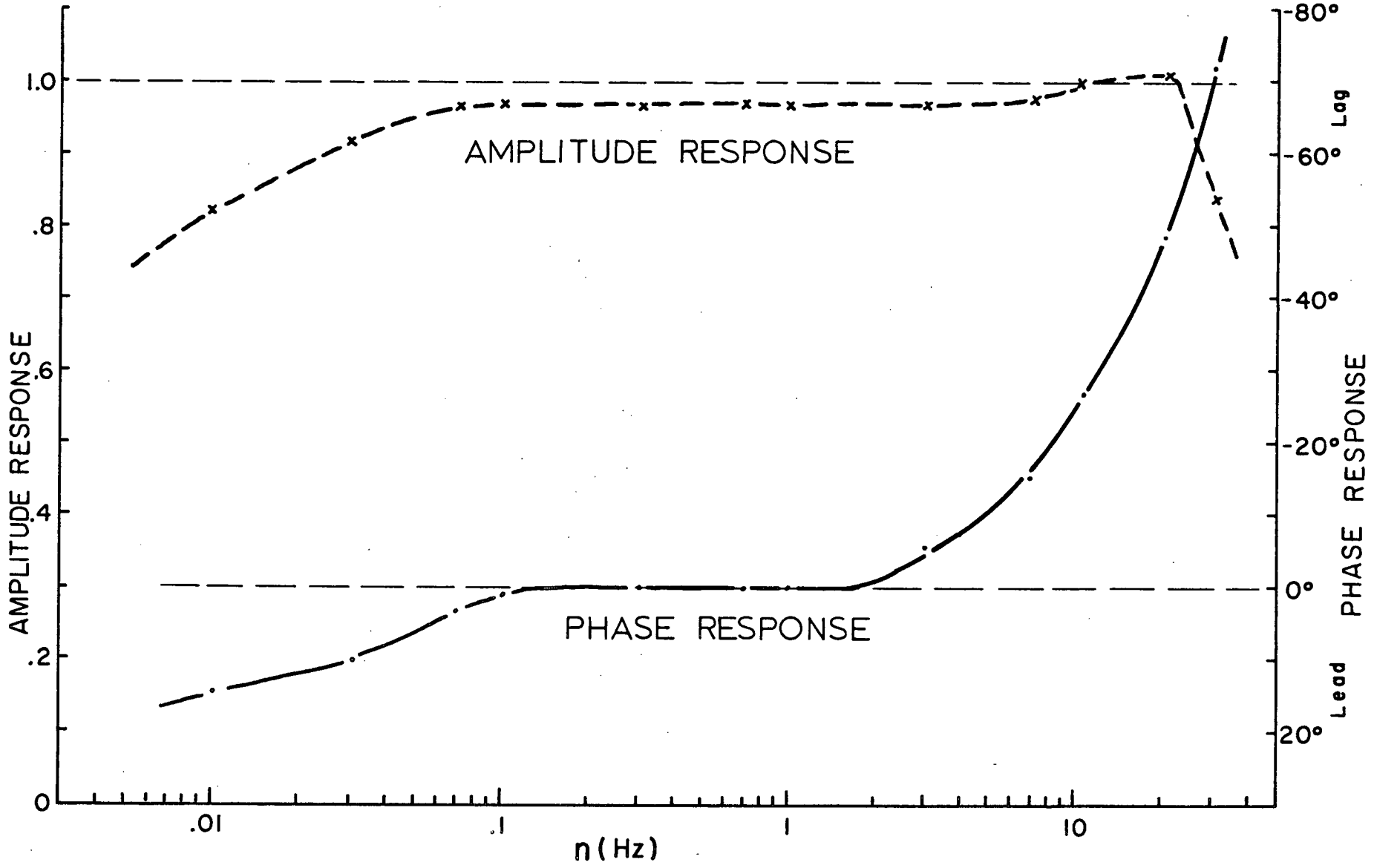

Figure 12. Sample frequency calibration of the pressure instrument (probe and transducer)

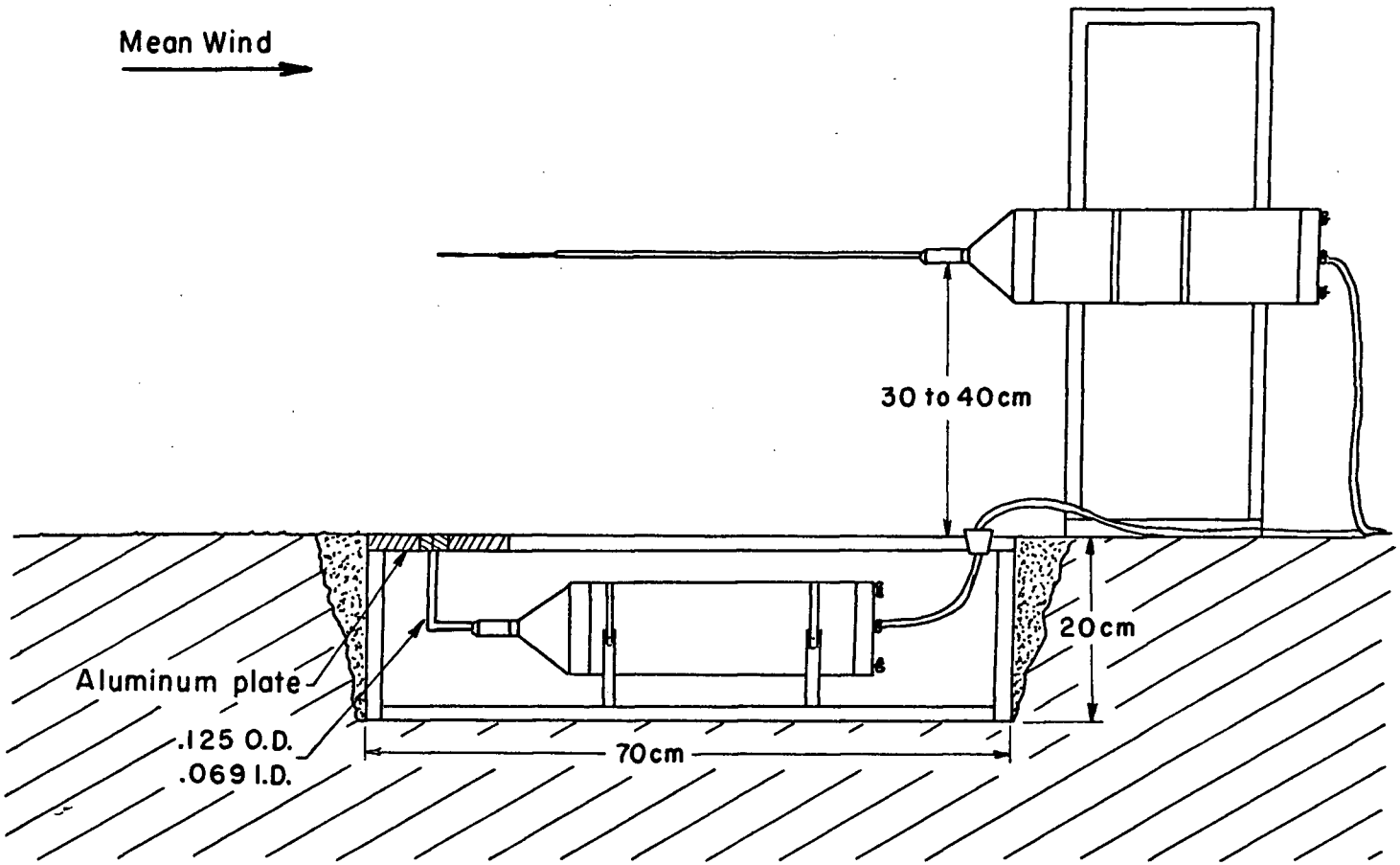

Figure 13. Arrangement used for calibrating the pressure instrument *in situ*

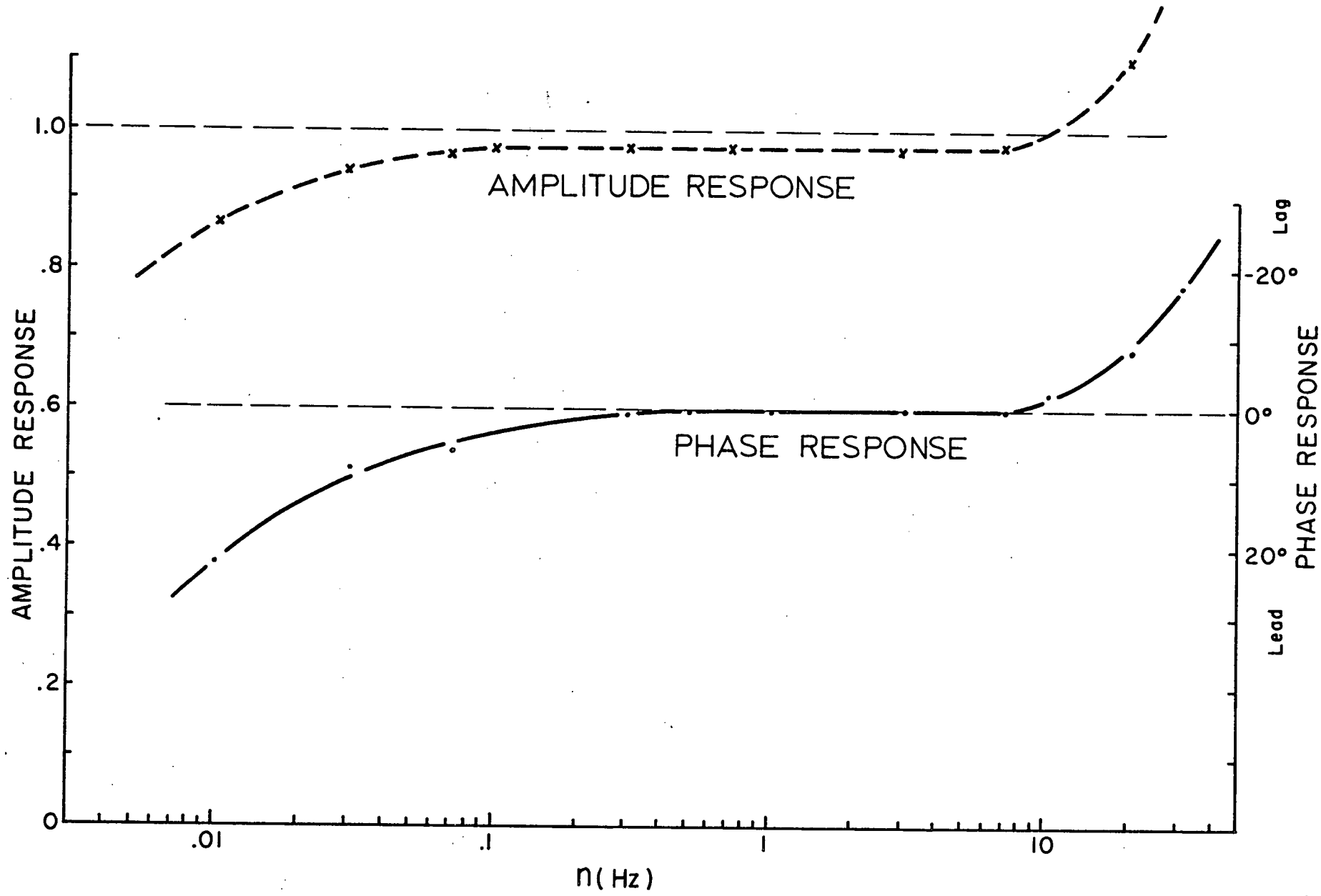

Figure 14. Sample frequency calibration of the system used for the surface pressure measurement

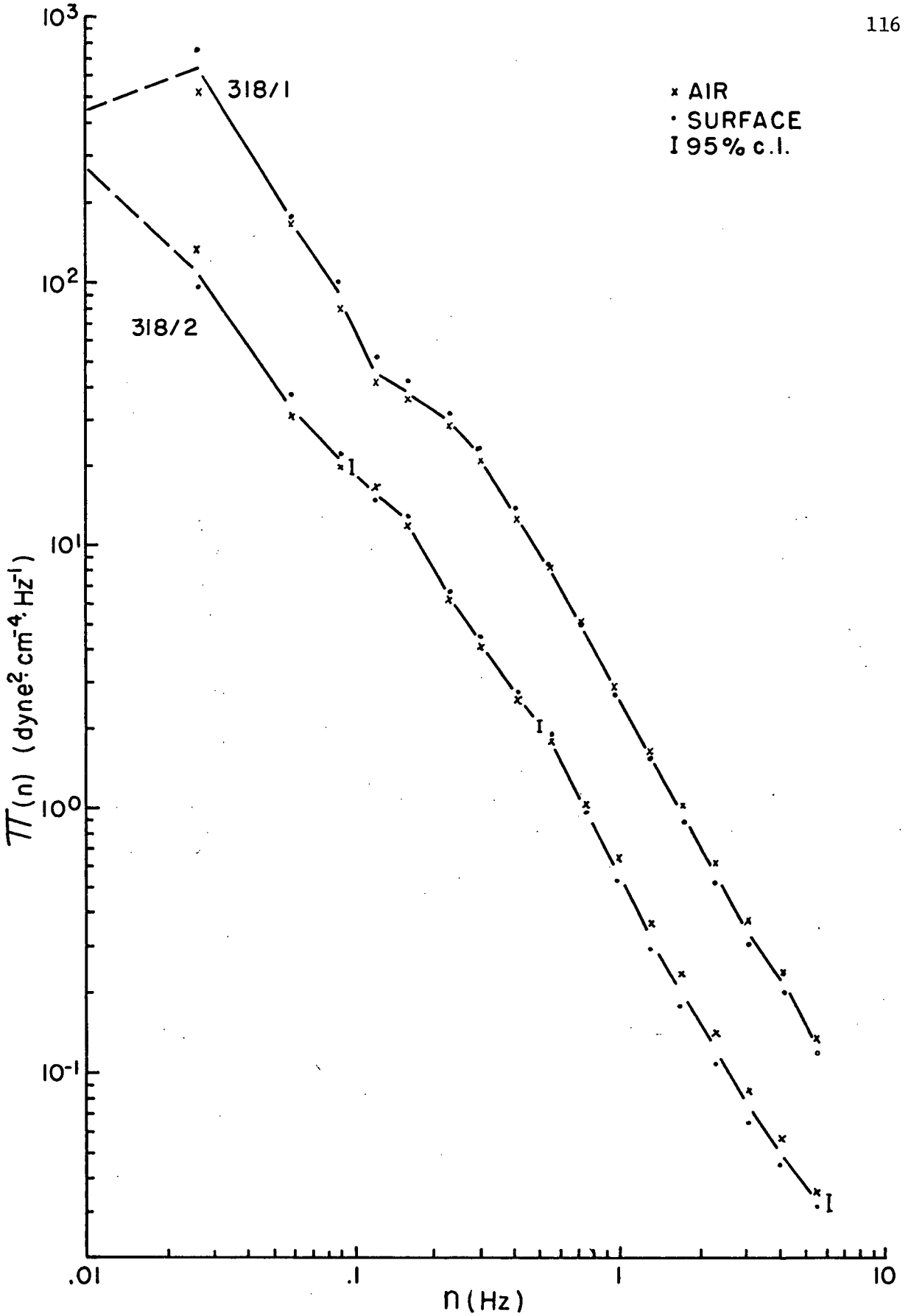

Figure 15. Spectral comparison of the static pressure measured in the air and at the surface; the separation was 40 cm vertically. These measurements were taken at the Ladner site.

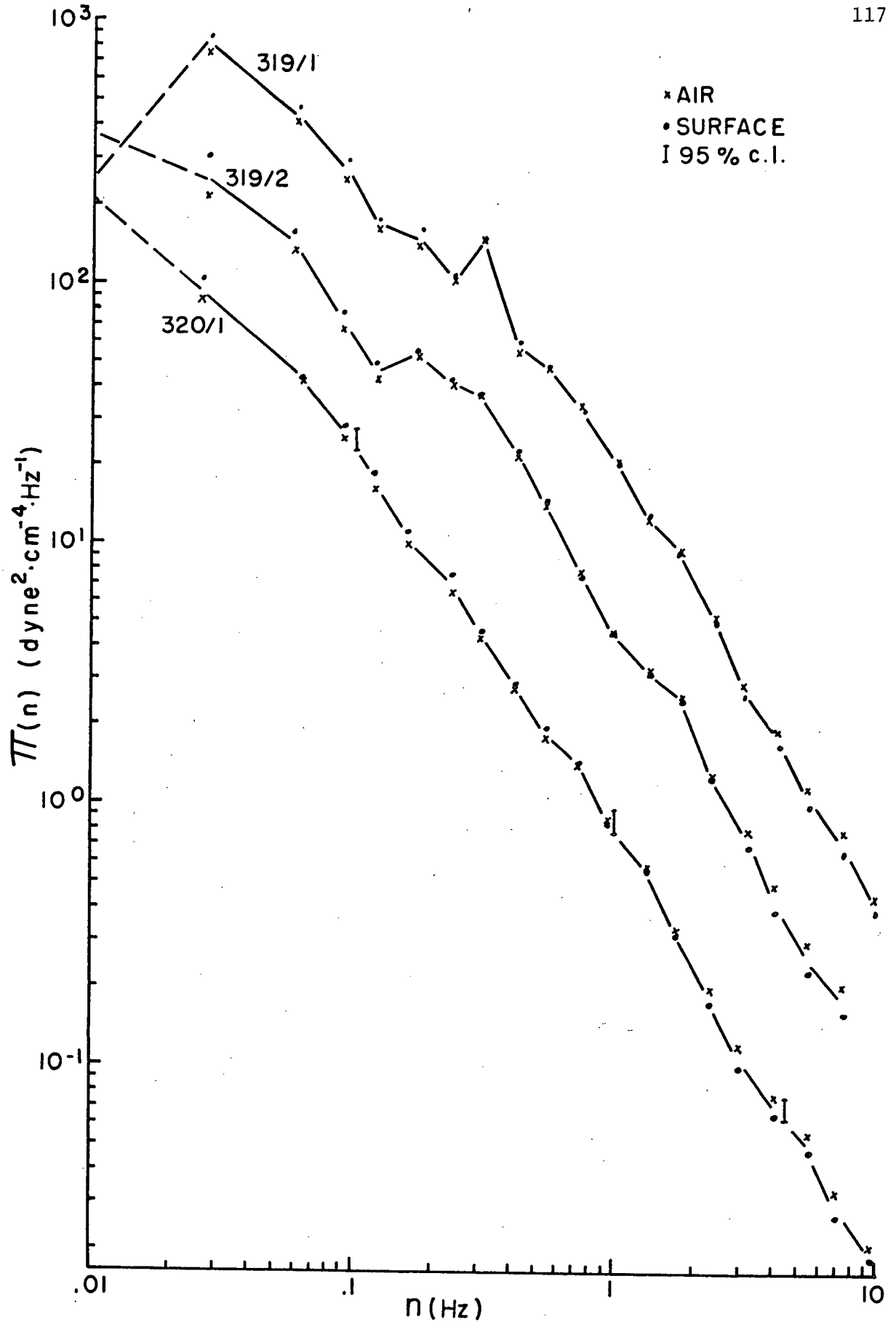

Figure 16. Spectral comparison of the static pressure measured in the air and at the surface; the separation was 32 cm vertically. These measurements were taken at the Ladner site.

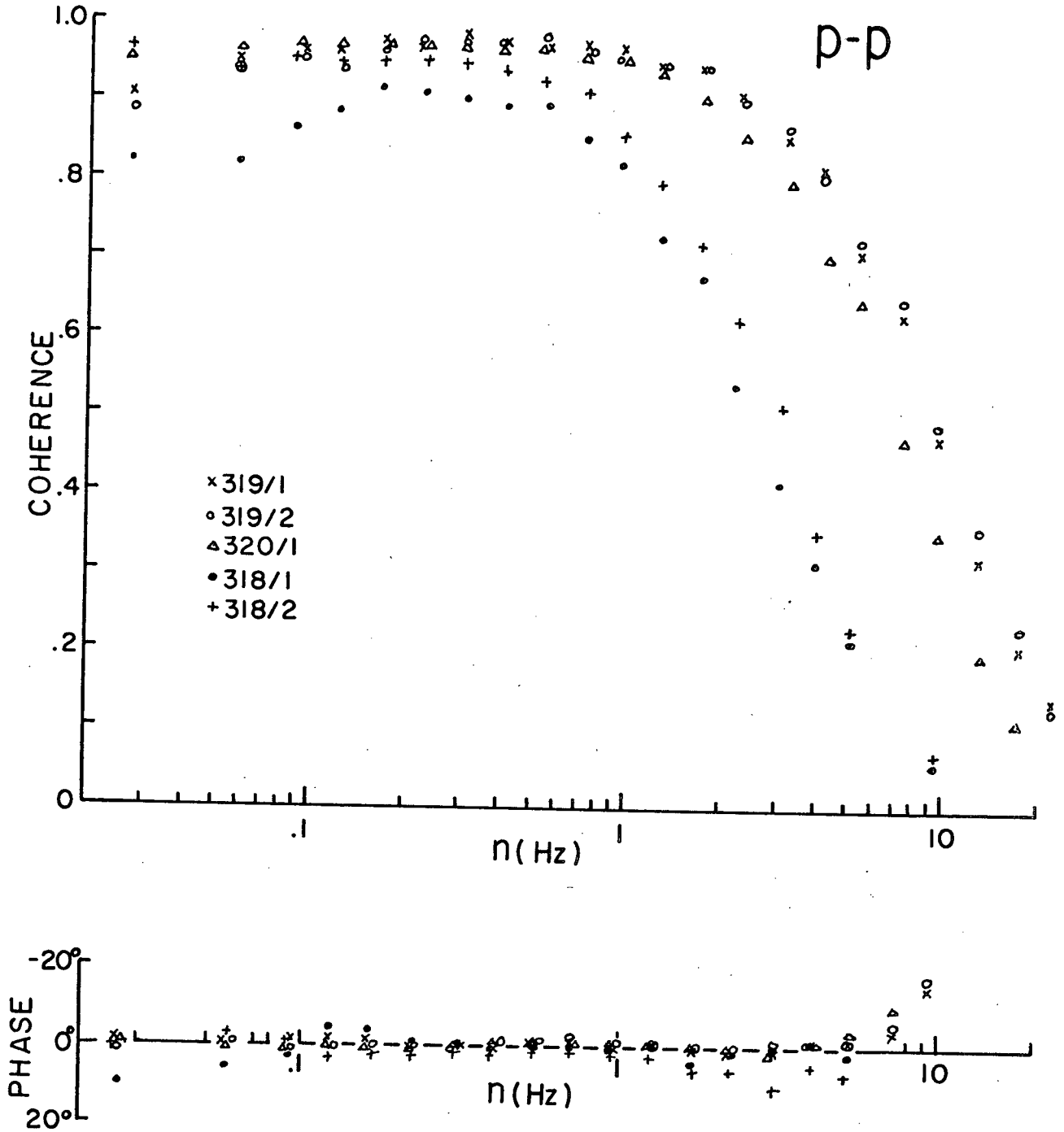

Figure 17. Coherence and phase between the static pressure measured in the air and at the surface. These are the Ladner Runs.

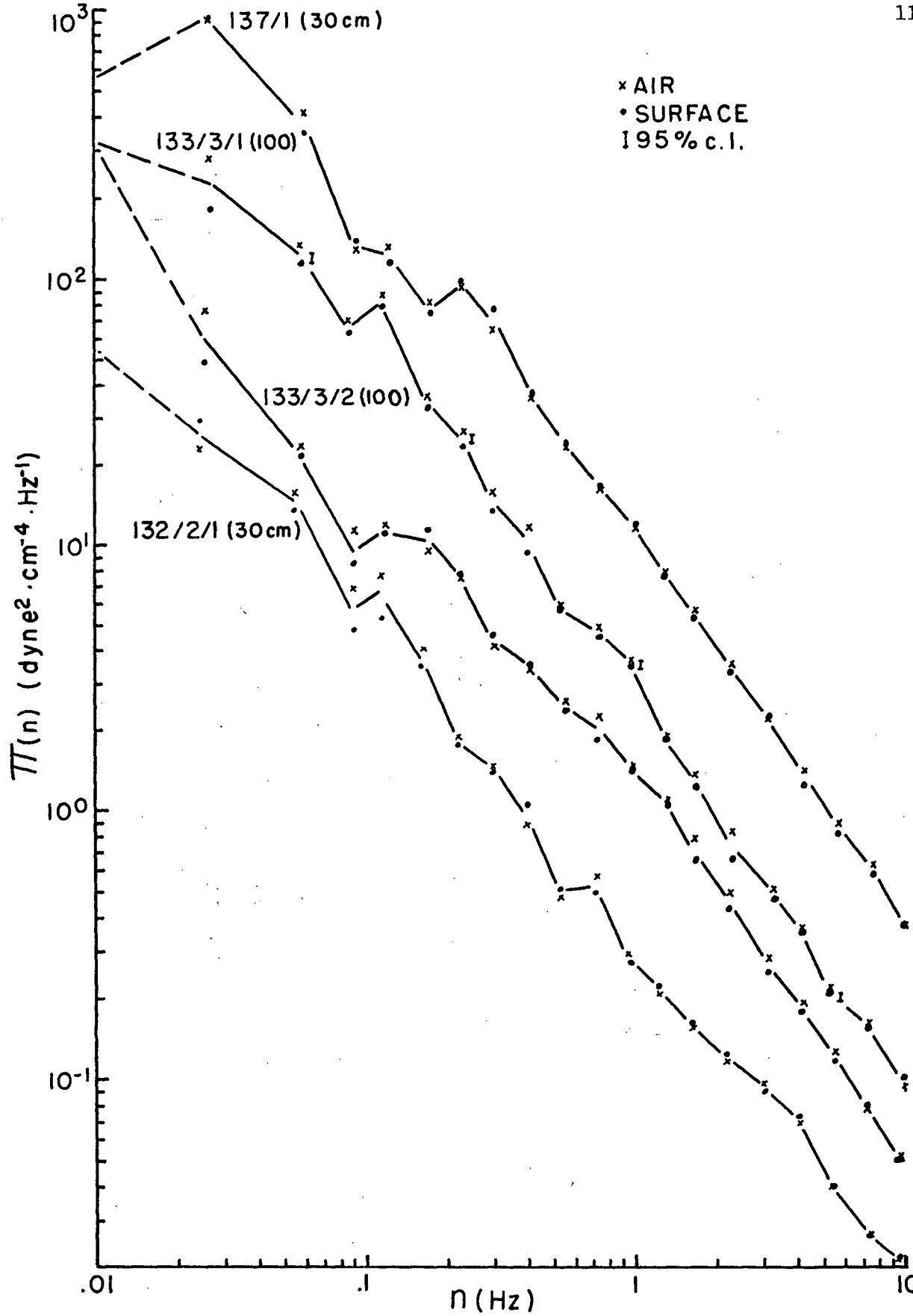

Figure 18. Spectral comparison of the static pressure measured in the air and at the surface; the separation vertically, in meters, is given in brackets after the Run number. These measurements were taken at the Boundary Bay site.

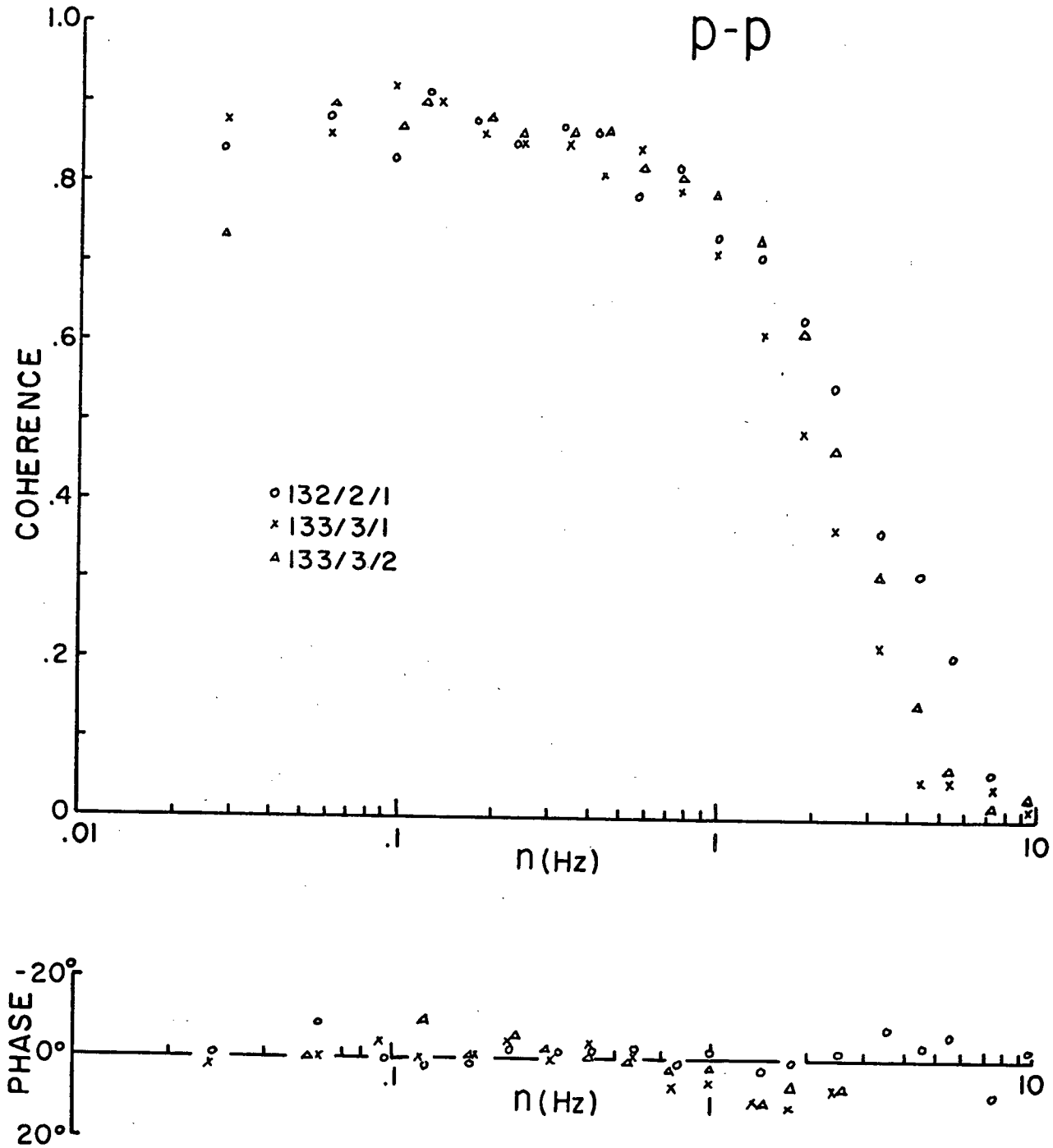

Figure 19. Coherence and phase between the static pressure measured in the air and at the surface. These are the Boundary Bay Runs.

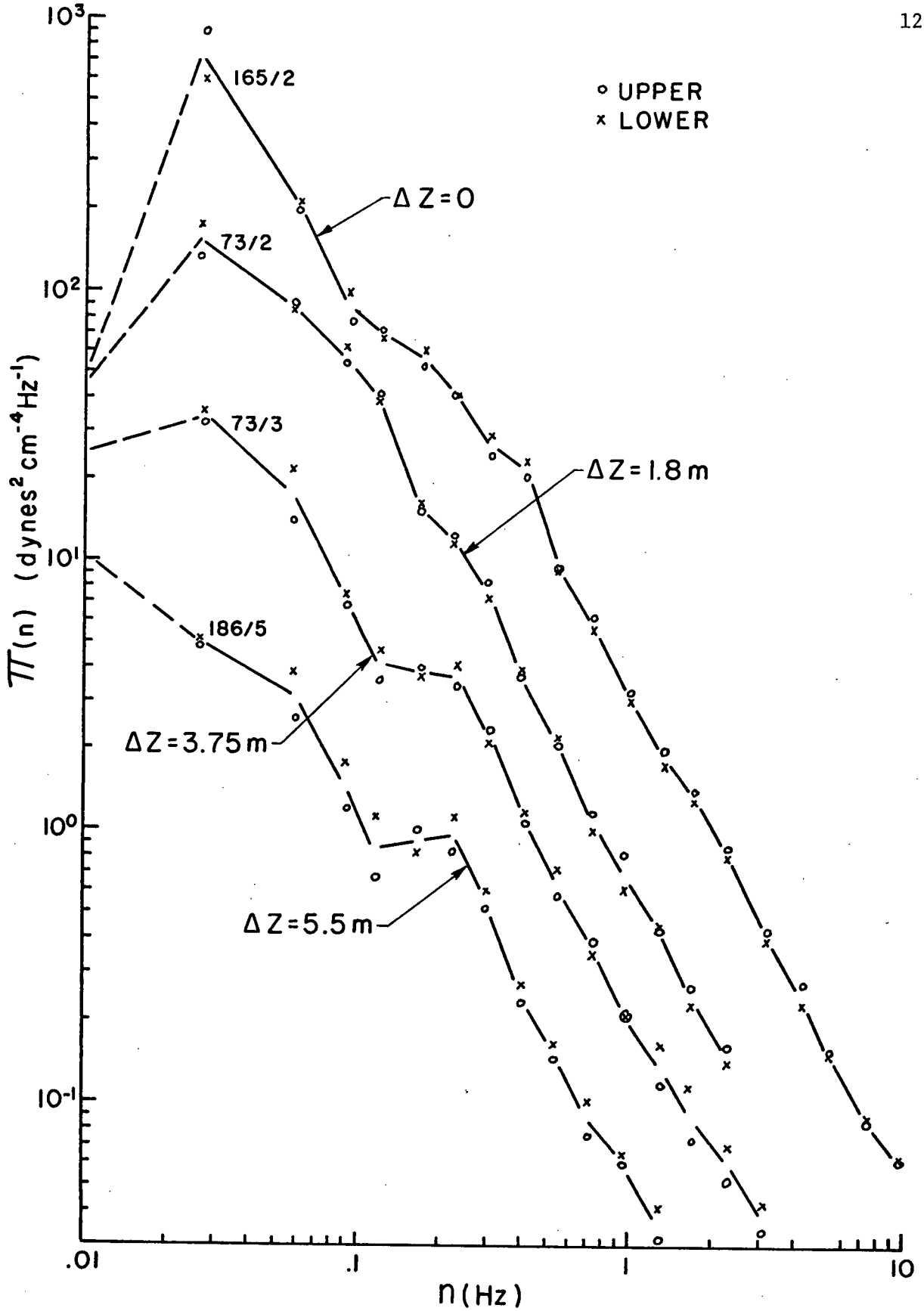

Figure 20. Comparison of pressure spectra measured simultaneously at two different heights. Δz is the difference in height, given in meters.

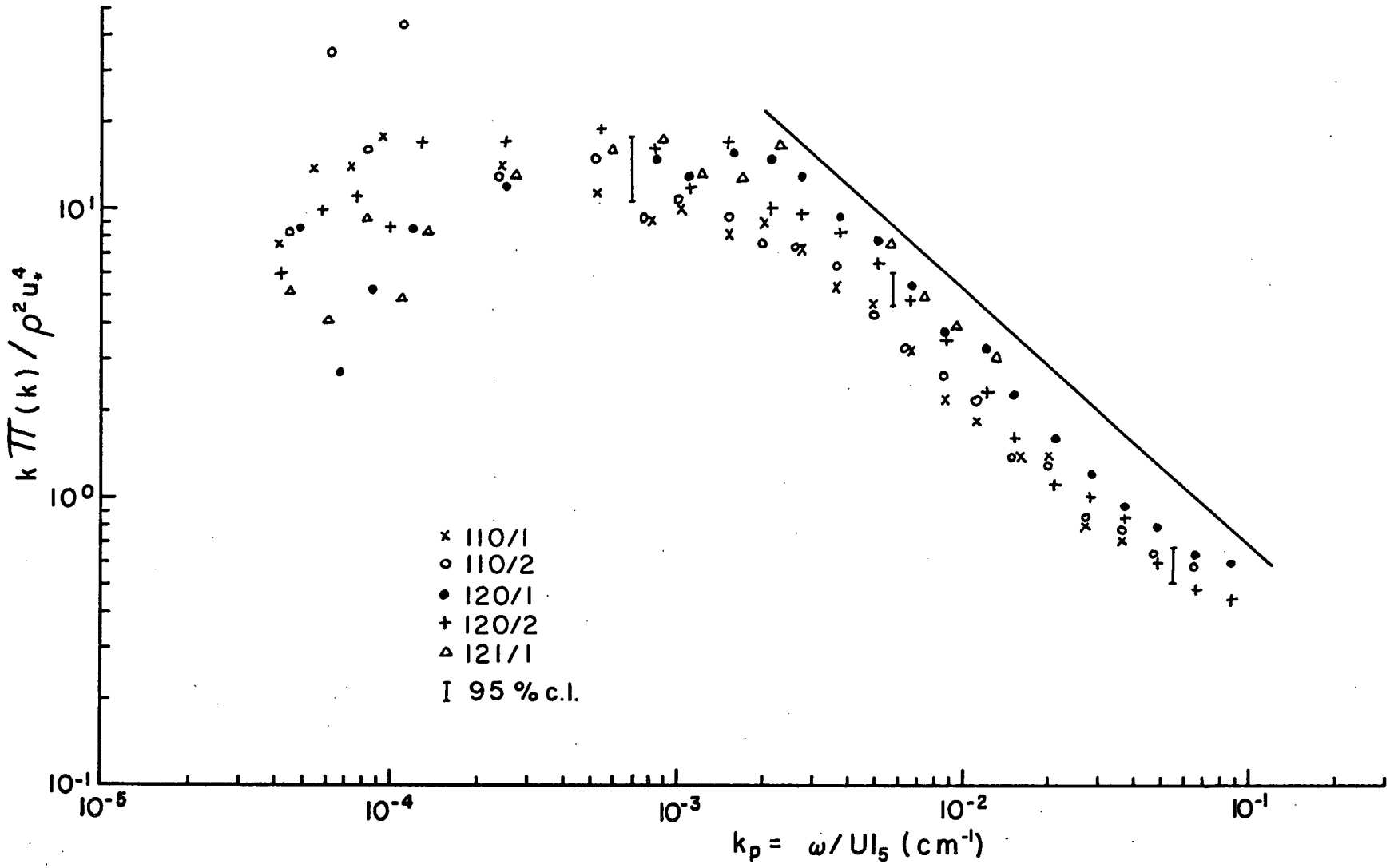

Figure 21. Nondimensional pressure spectra. Observations taken over water.

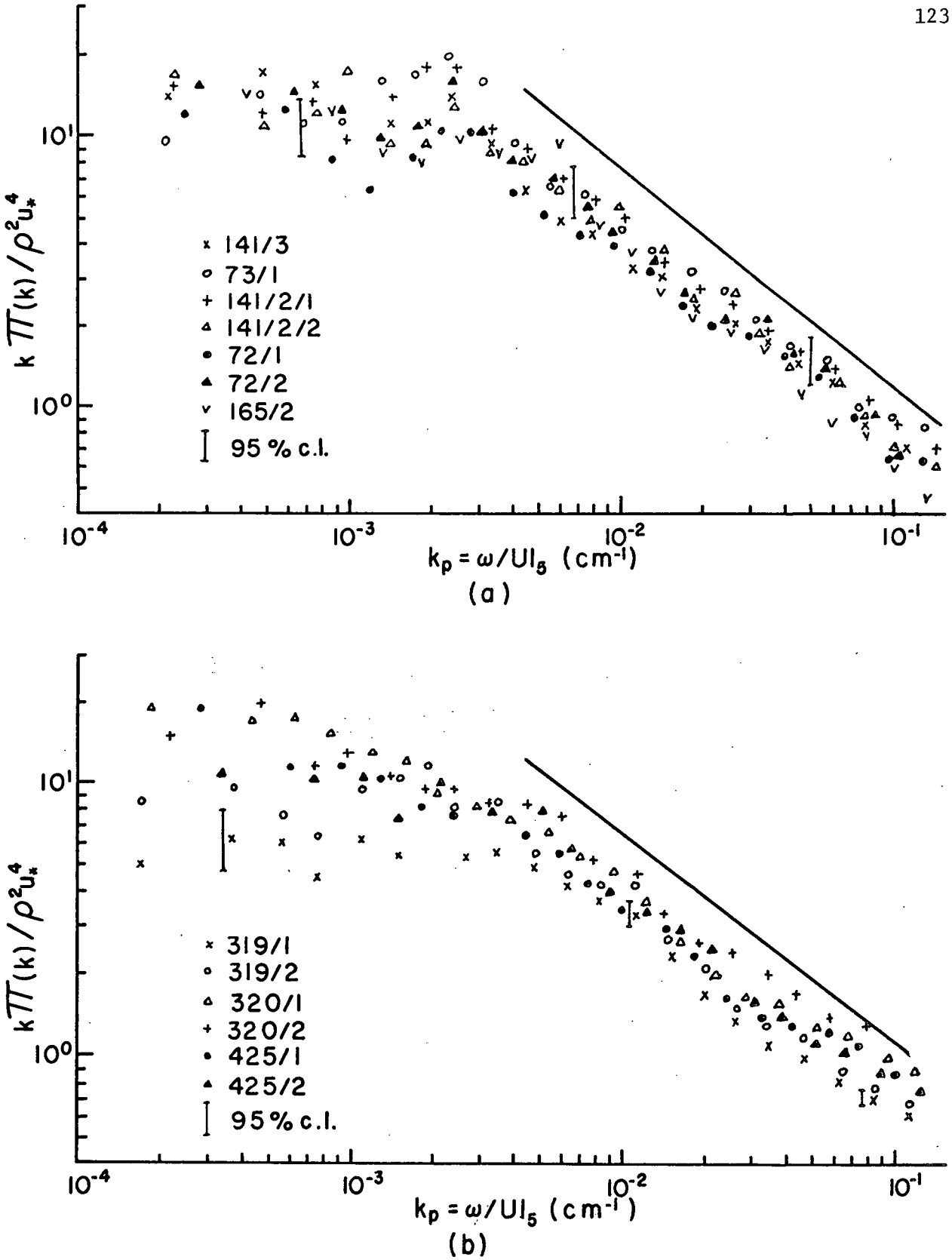

Figure 22. Nondimensionalized pressure spectra. Observations taken over

(a) water

(b) land

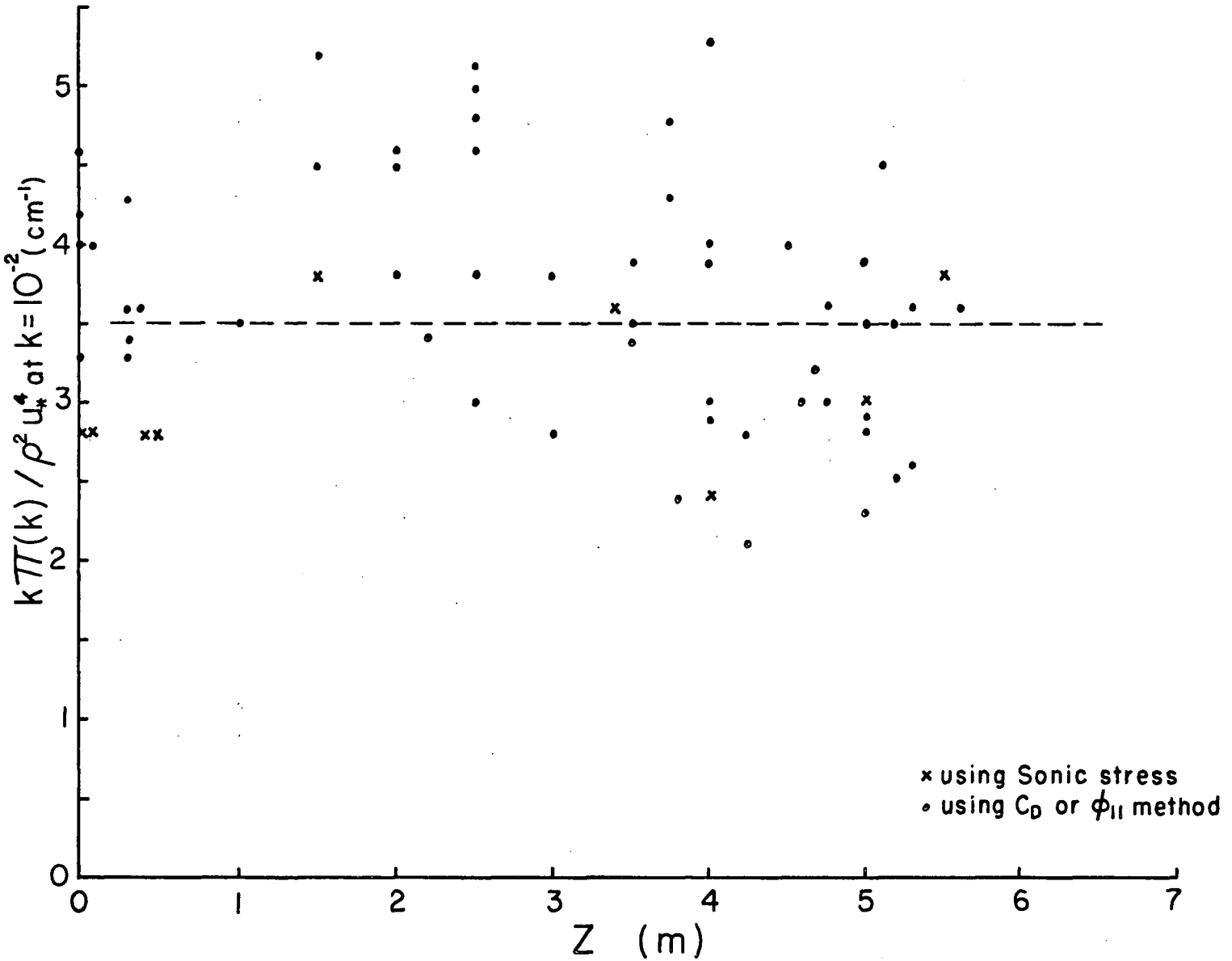

Figure 23. Summary of the nondimensionalized pressure spectra. Values plotted are $k\Pi(k)/(\rho^2 u_*^4)$ at a k of 10^{-2} cm^{-1}.

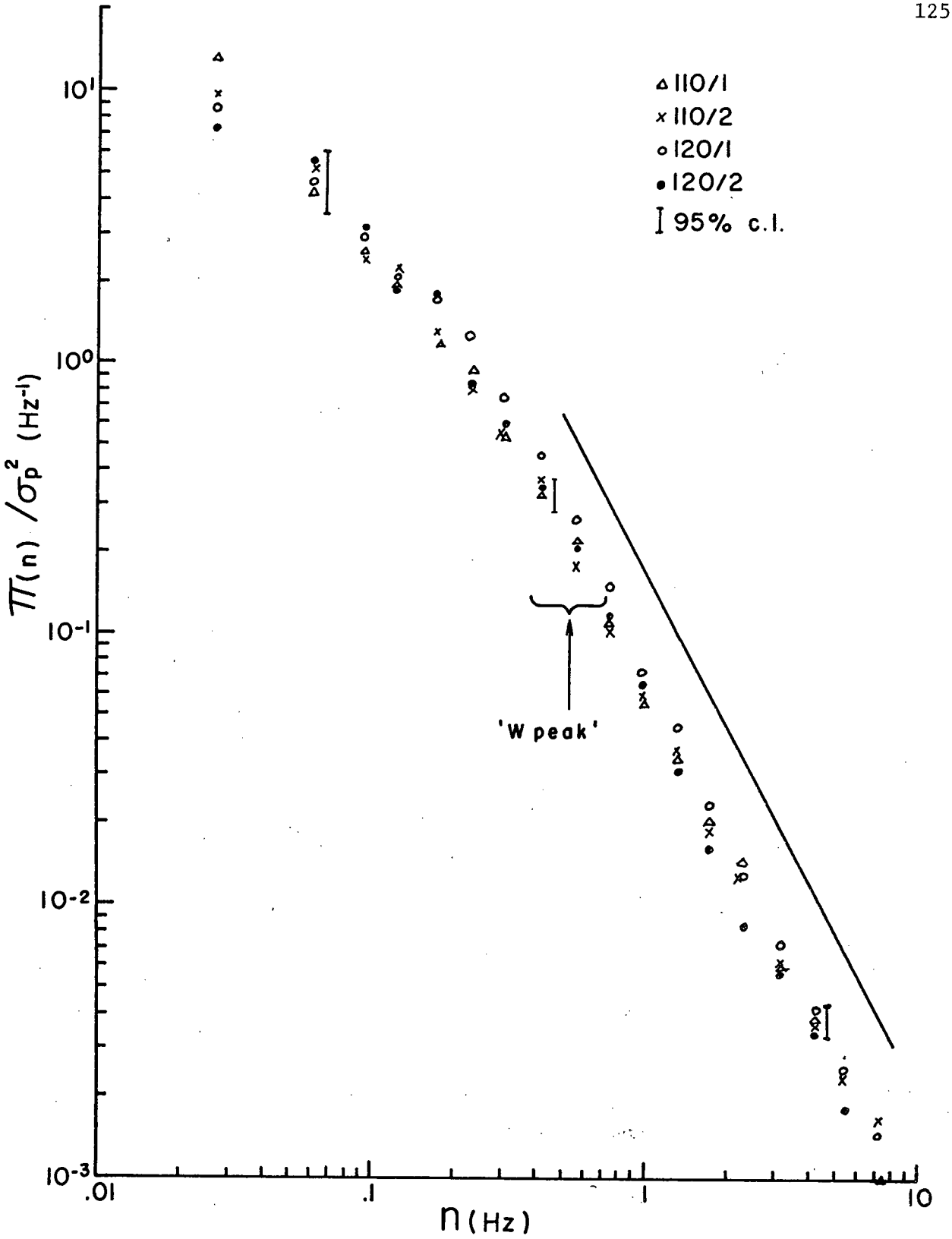

Figure 24. Normalized pressure spectra normalized by their variance.

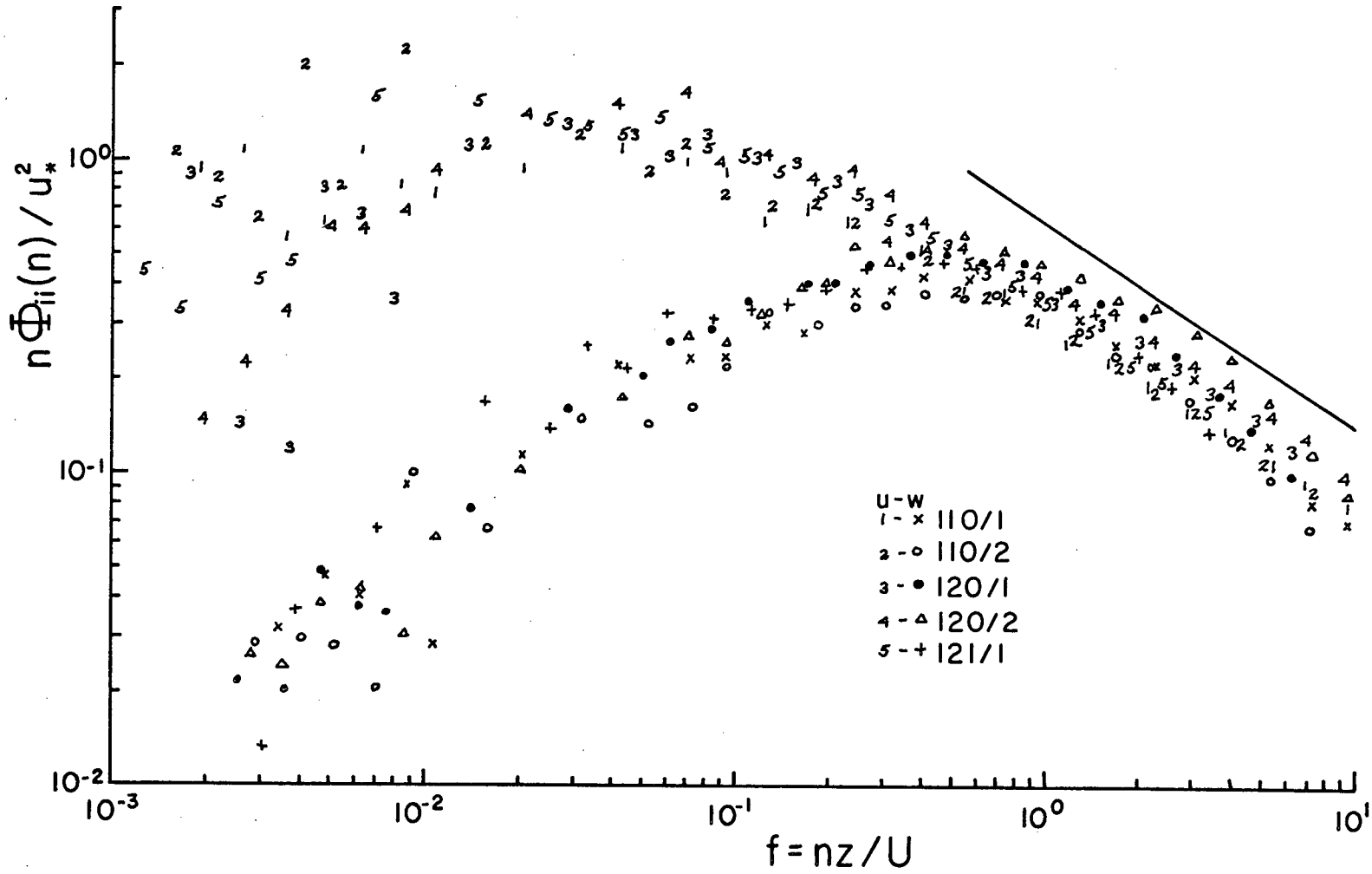

Figure 25. Nondimensionalized u and w spectra

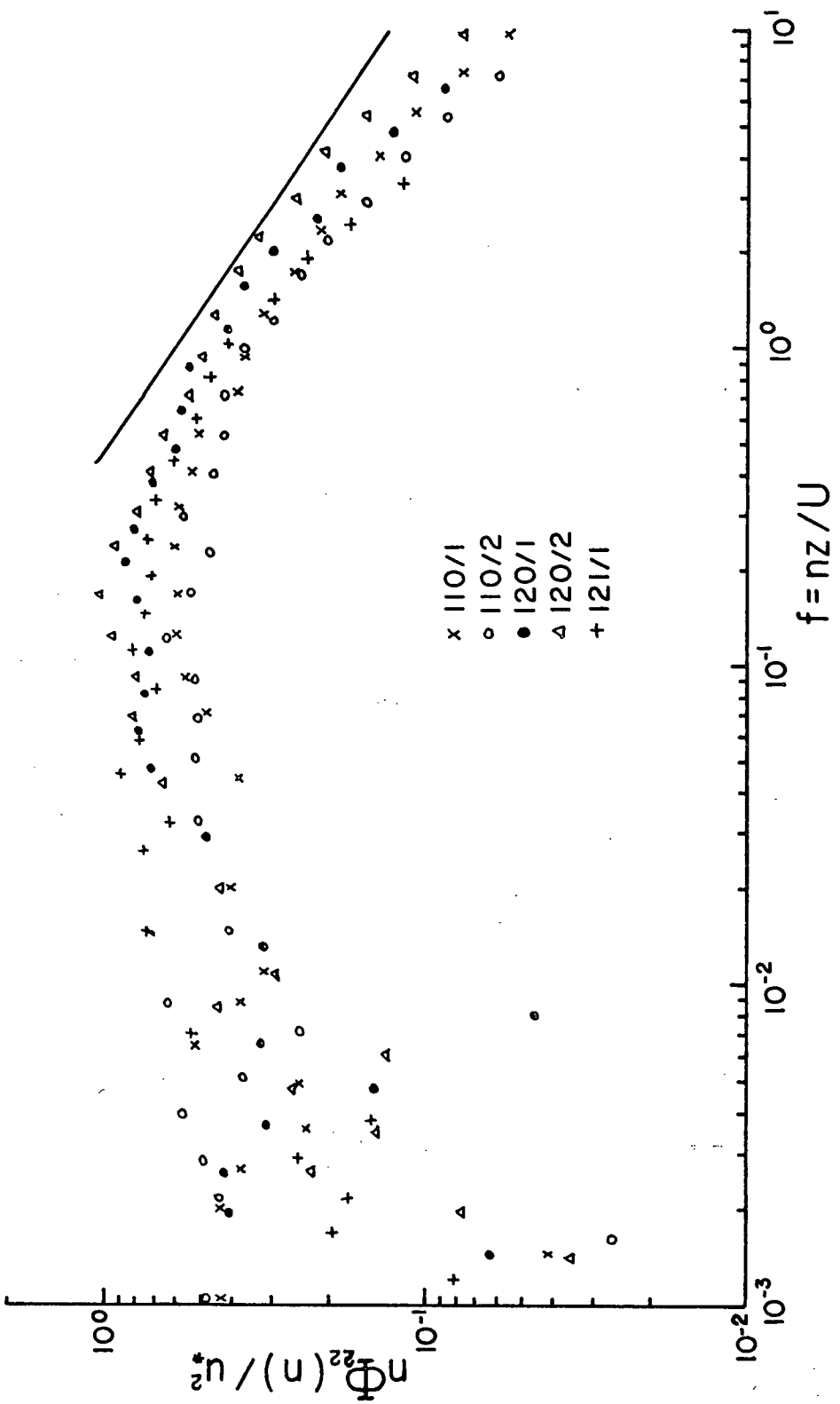

Figure 26. Nondimensionalized v spectra

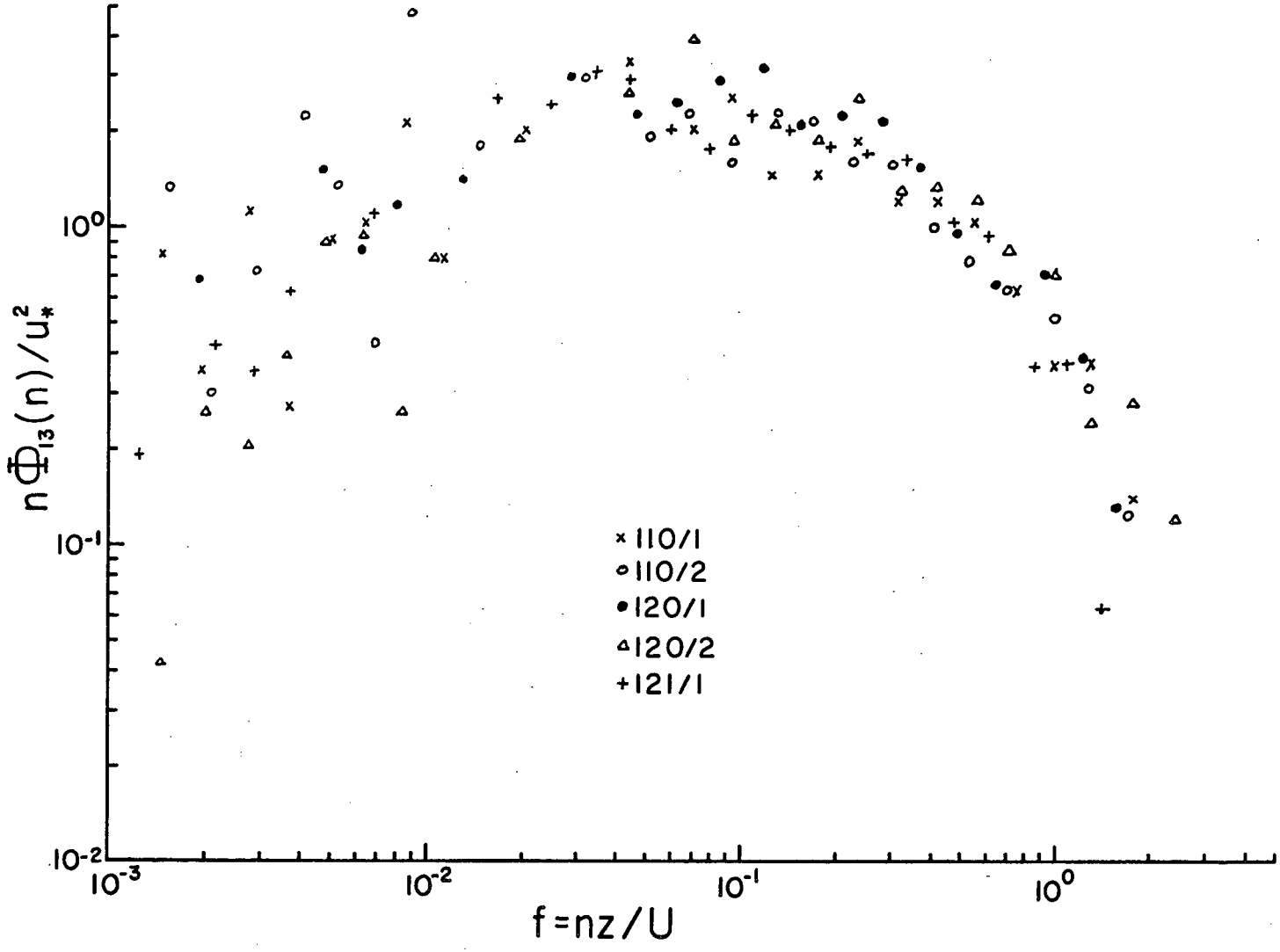

Figure 27. Nondimensionalized $\overline{uw}$ spectra

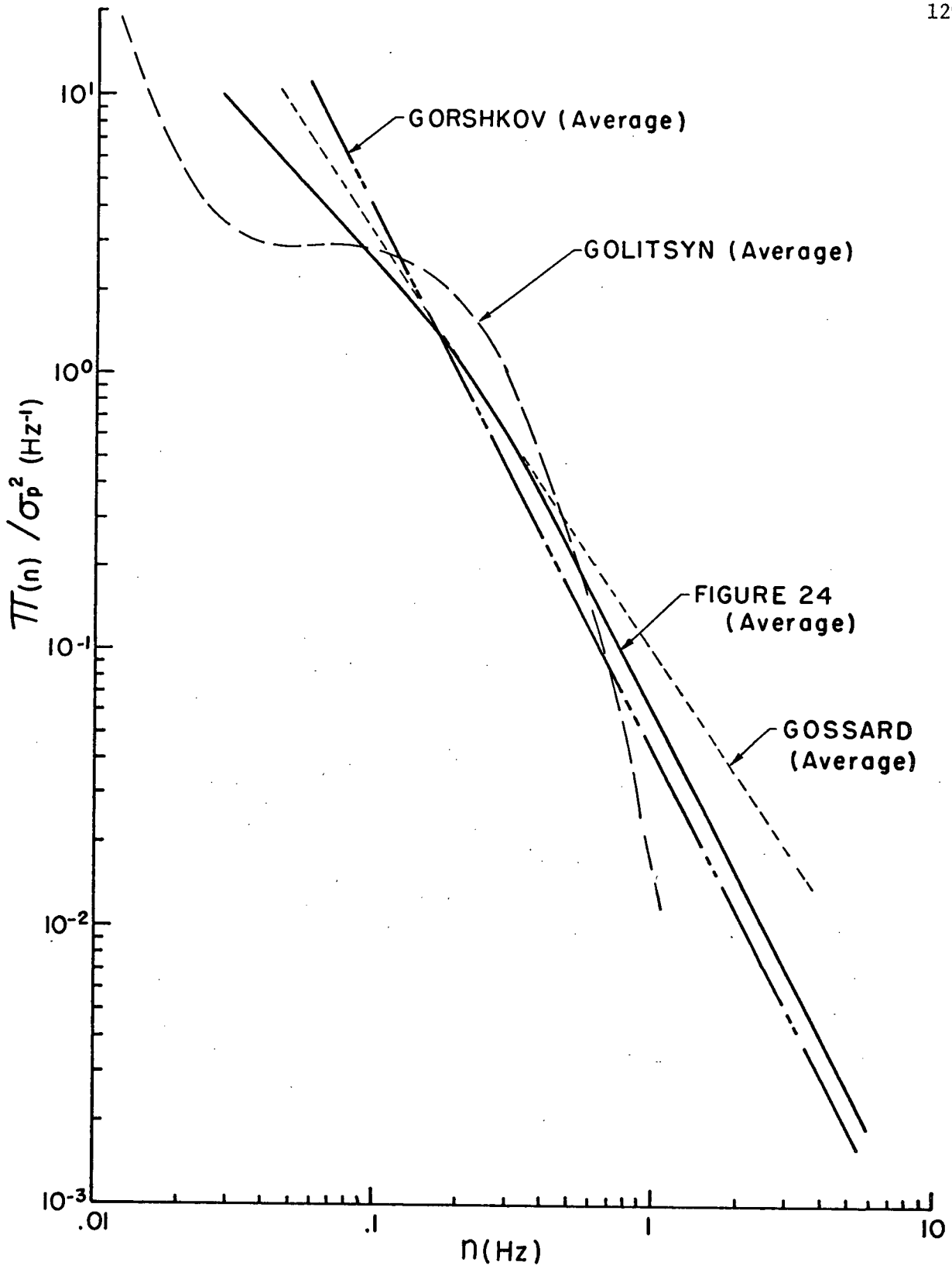

Figure 28. Comparison of the spectral slope of pressure spectra

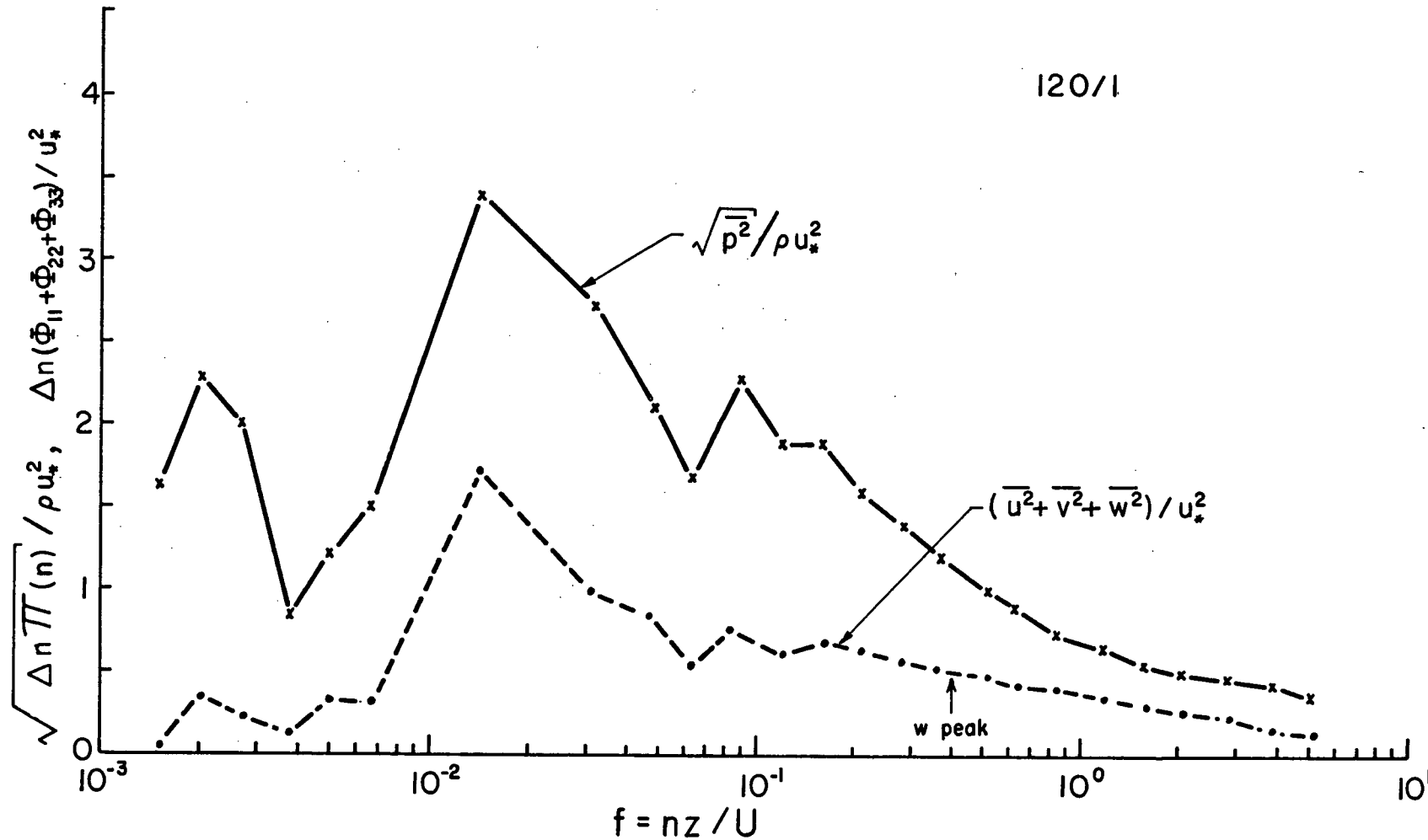

Figure 29. Comparison between the nondimensionalized variance of the pressure and of the velocity components for Run 120/1 for different frequency bands

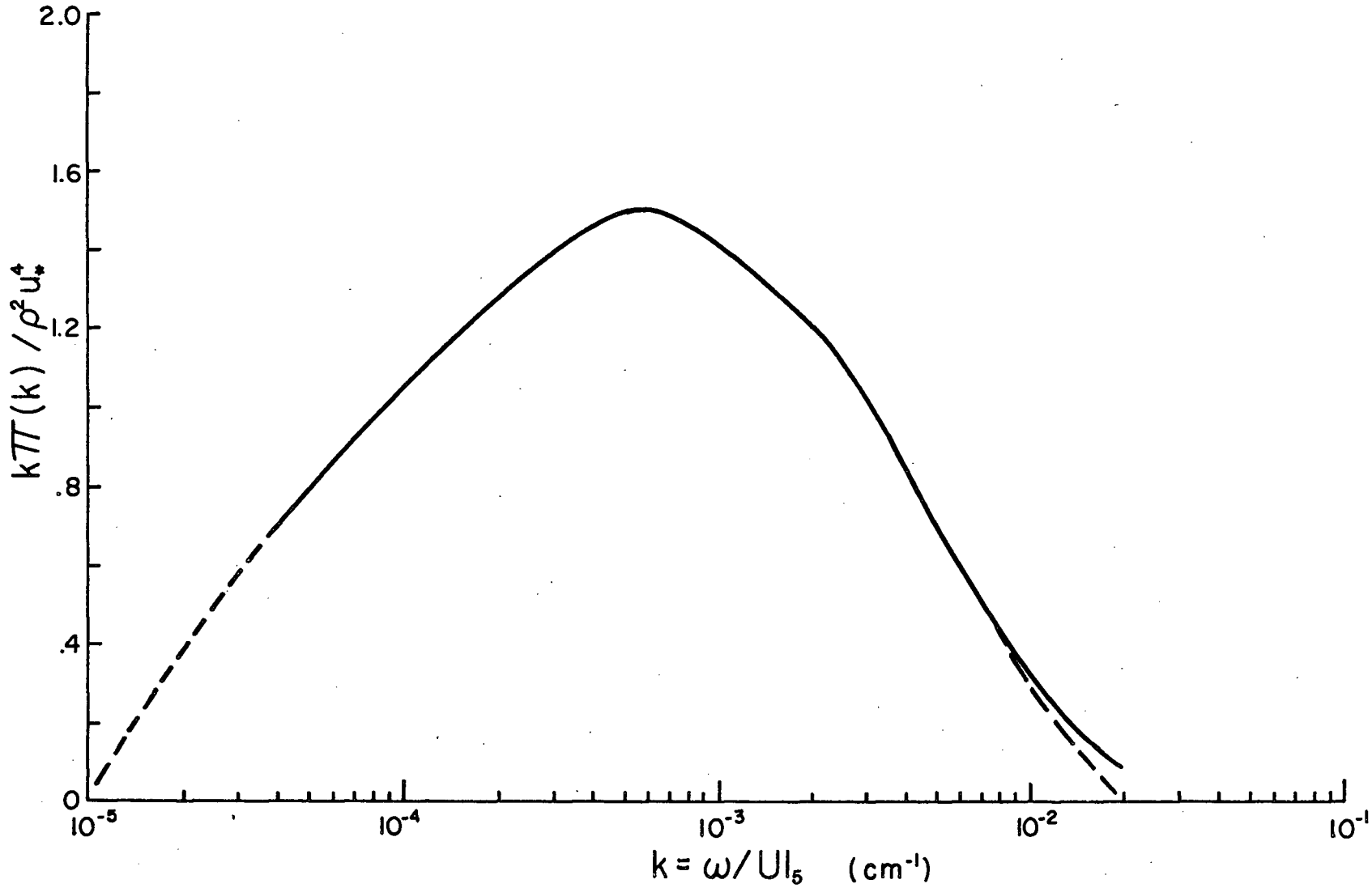

Figure 30. Nondimensionalized pressure spectra. The curve is the mean of data given in Figure 21; the dashed lines are extrapolated from the solid curve.

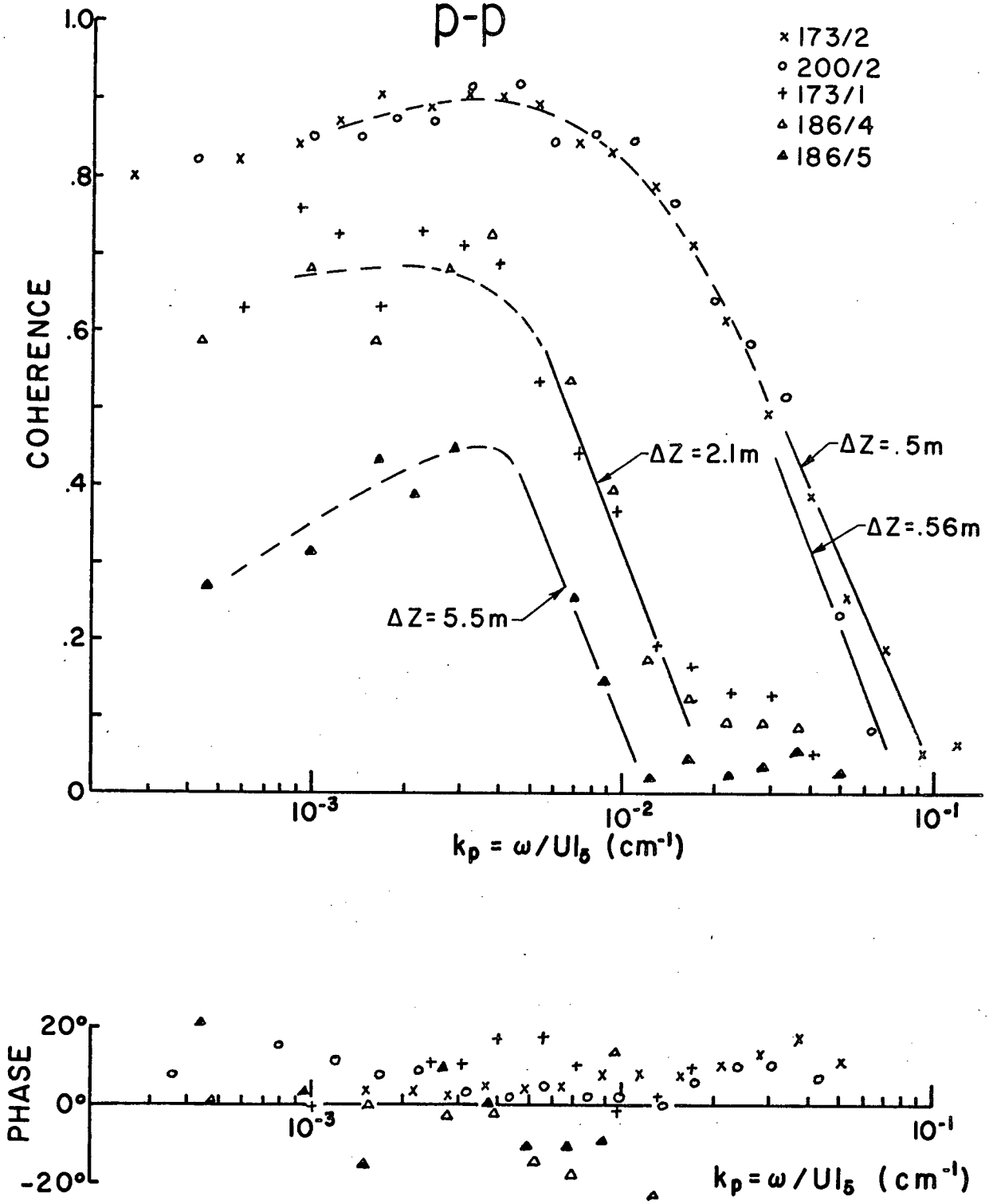

Figure 31. Coherence and phase between two pressure measurements with various vertical separations
Phase positive means p upper leads p lower.

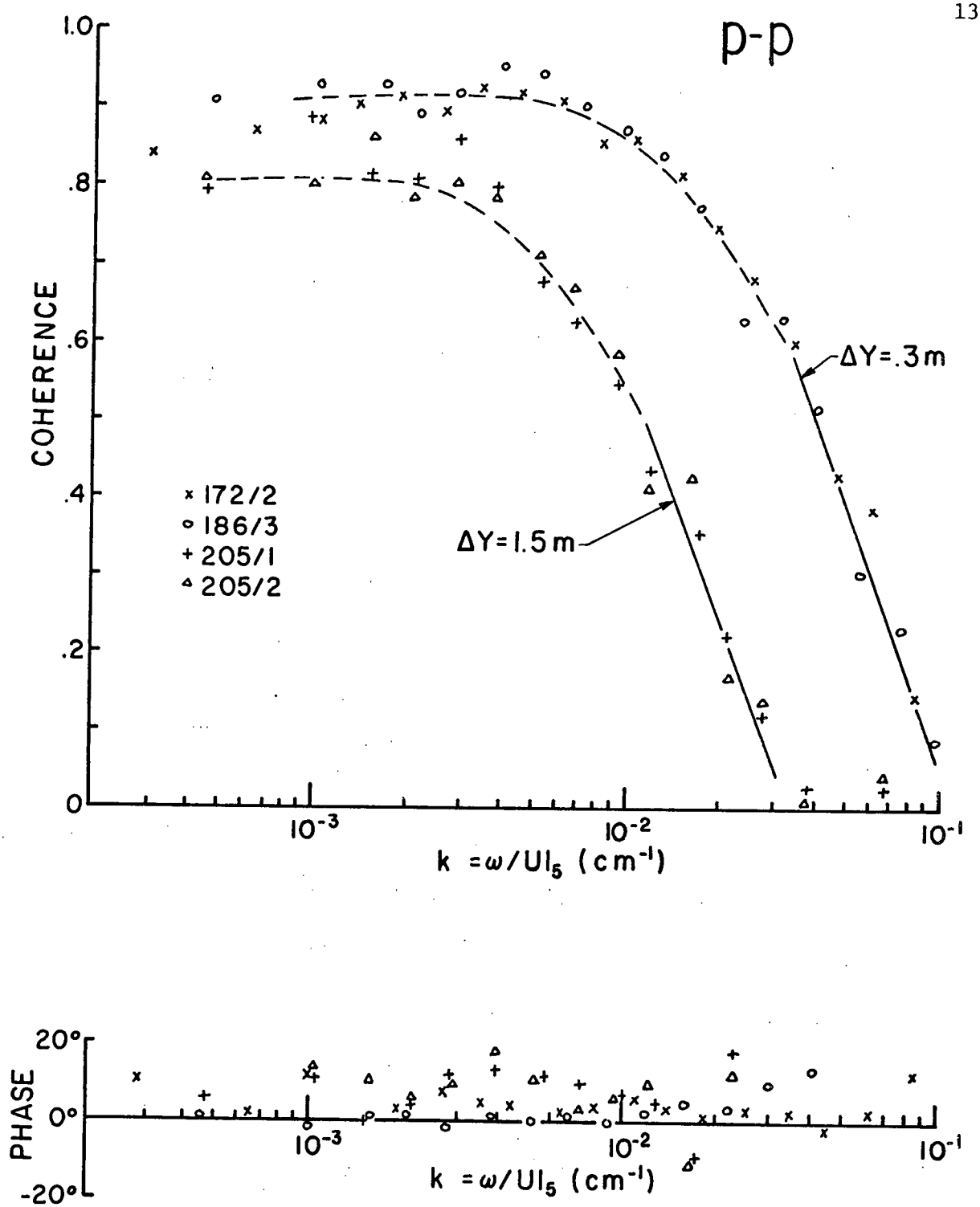

Figure 32. Coherence and phase between two pressure measurements with various crossstream separations

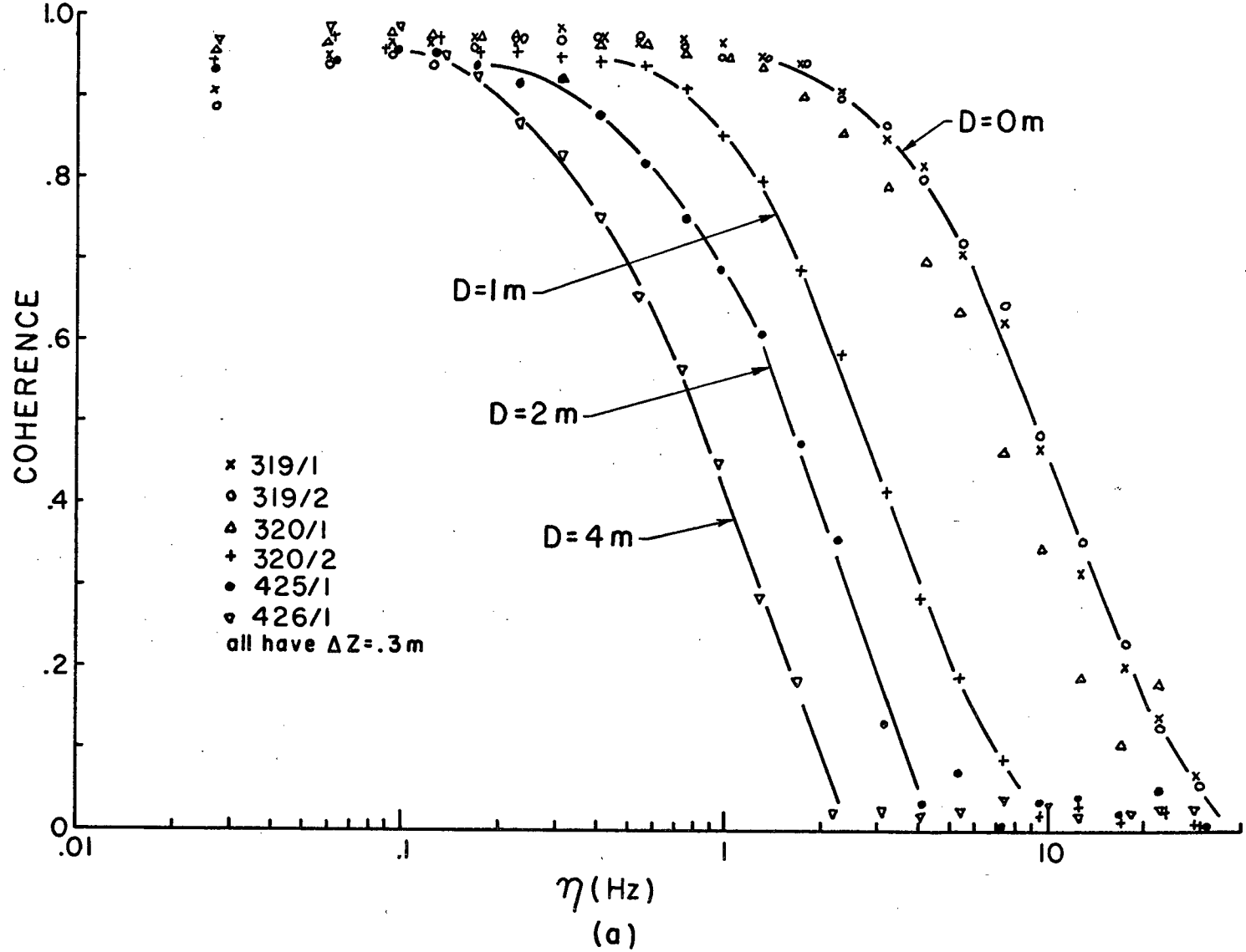

Figure 33(a). Coherence between two pressure measurements with a downwind separation

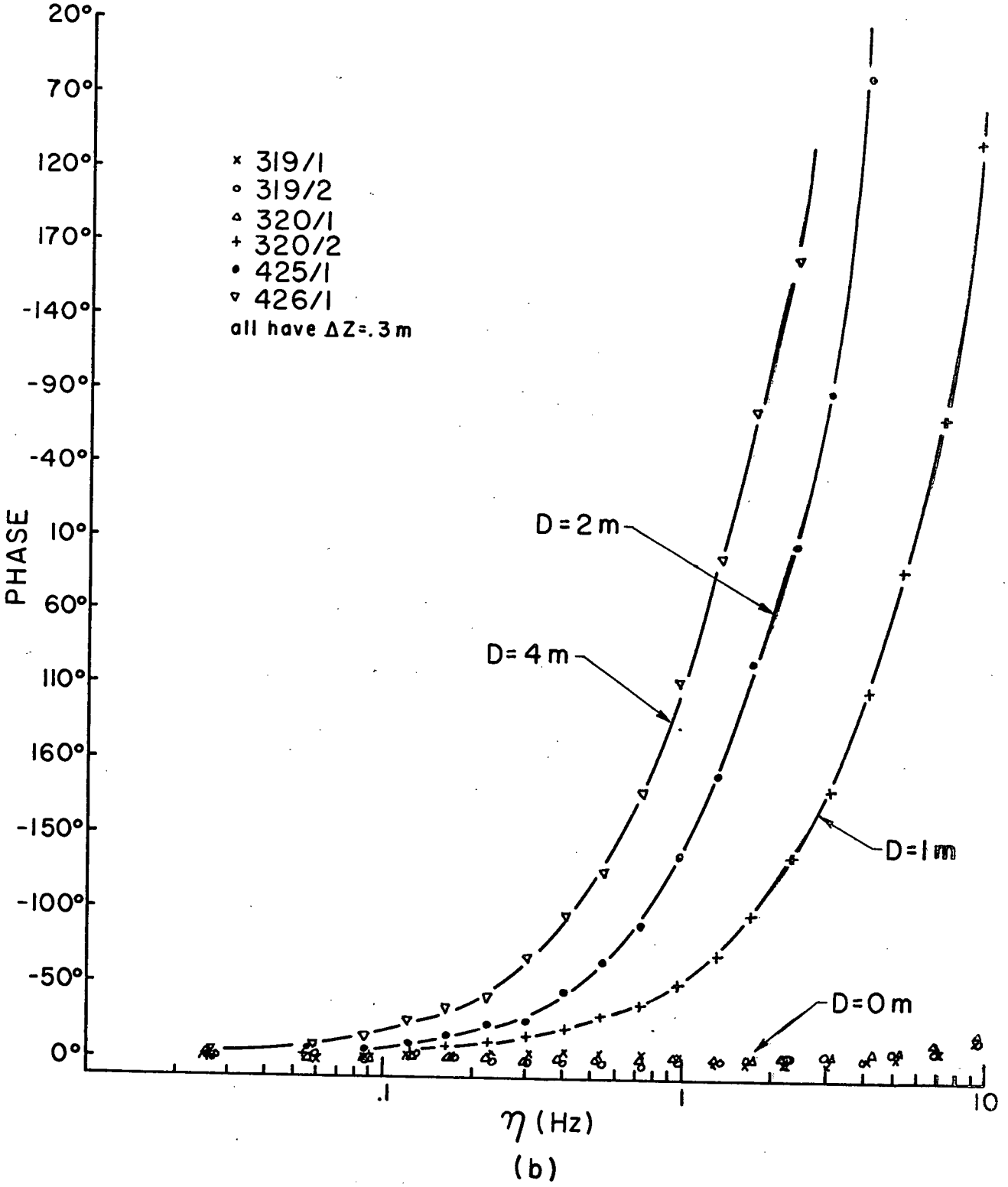

Figure 33(b). Phase between two pressure measurements with a downwind separation

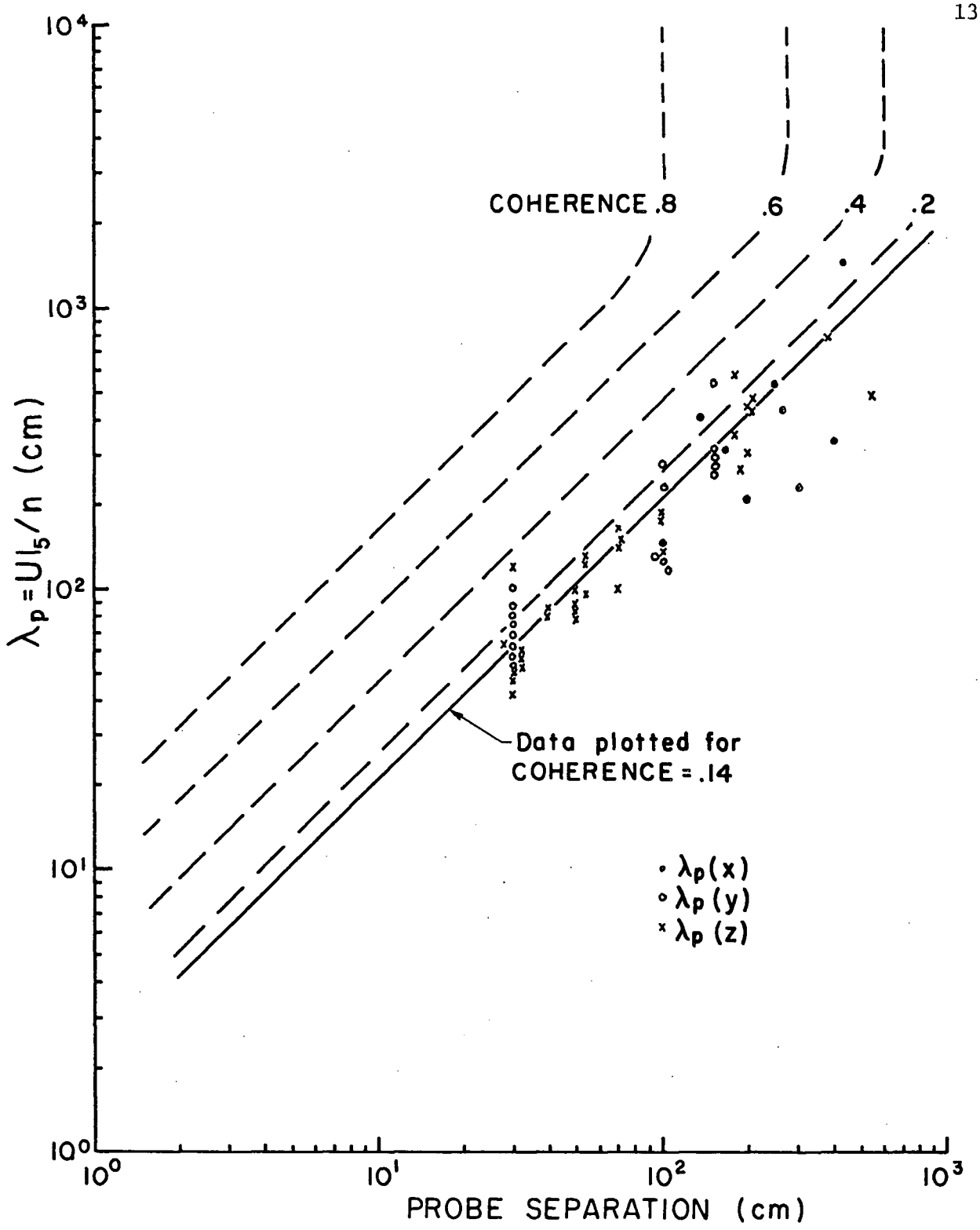

Figure 34. Fixed coherences between two pressure signals for various probe separations.
The values plotted are for a coherence of 0.14.

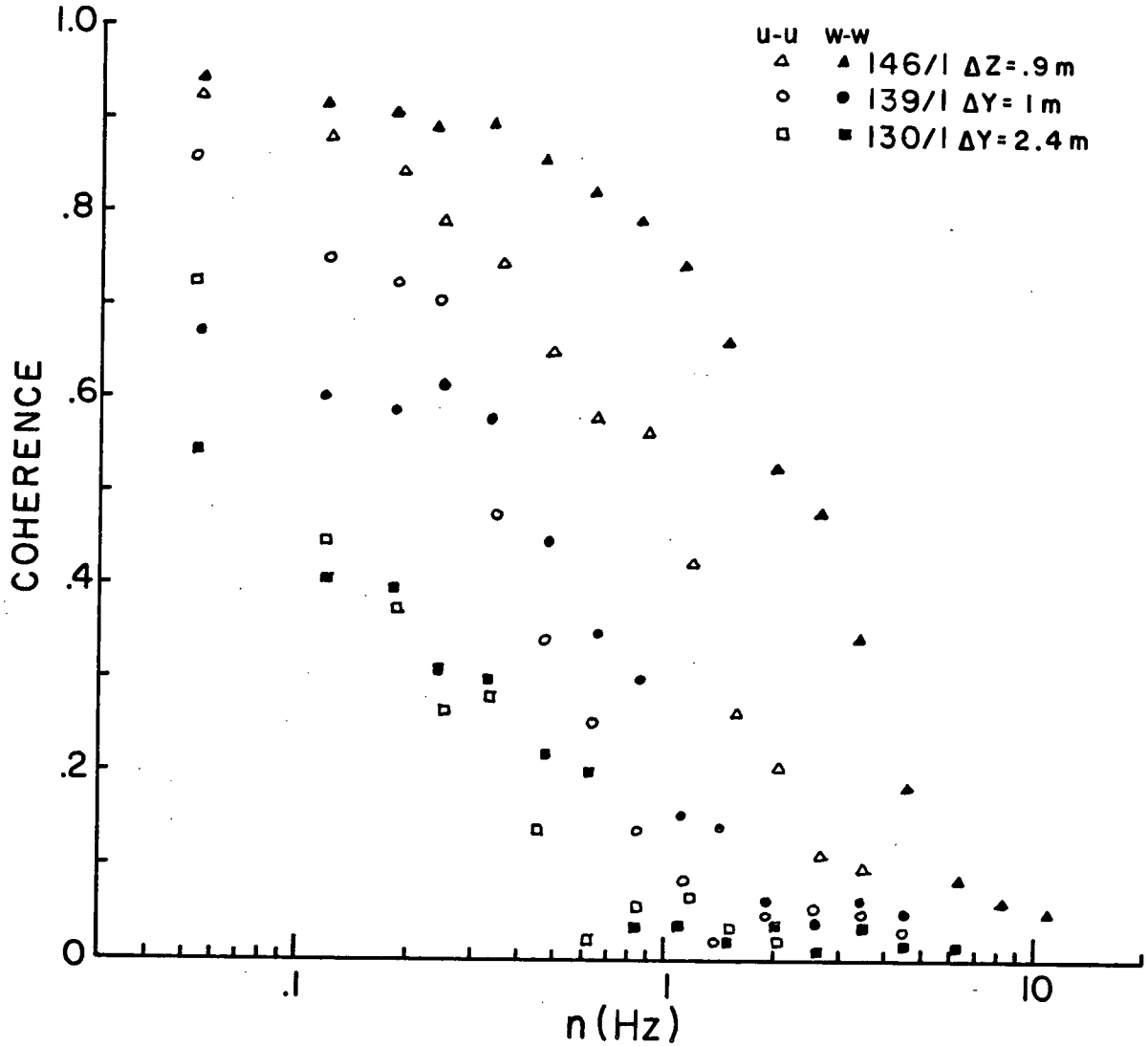

Figure 35. Coherence between two velocity measurements with different separations

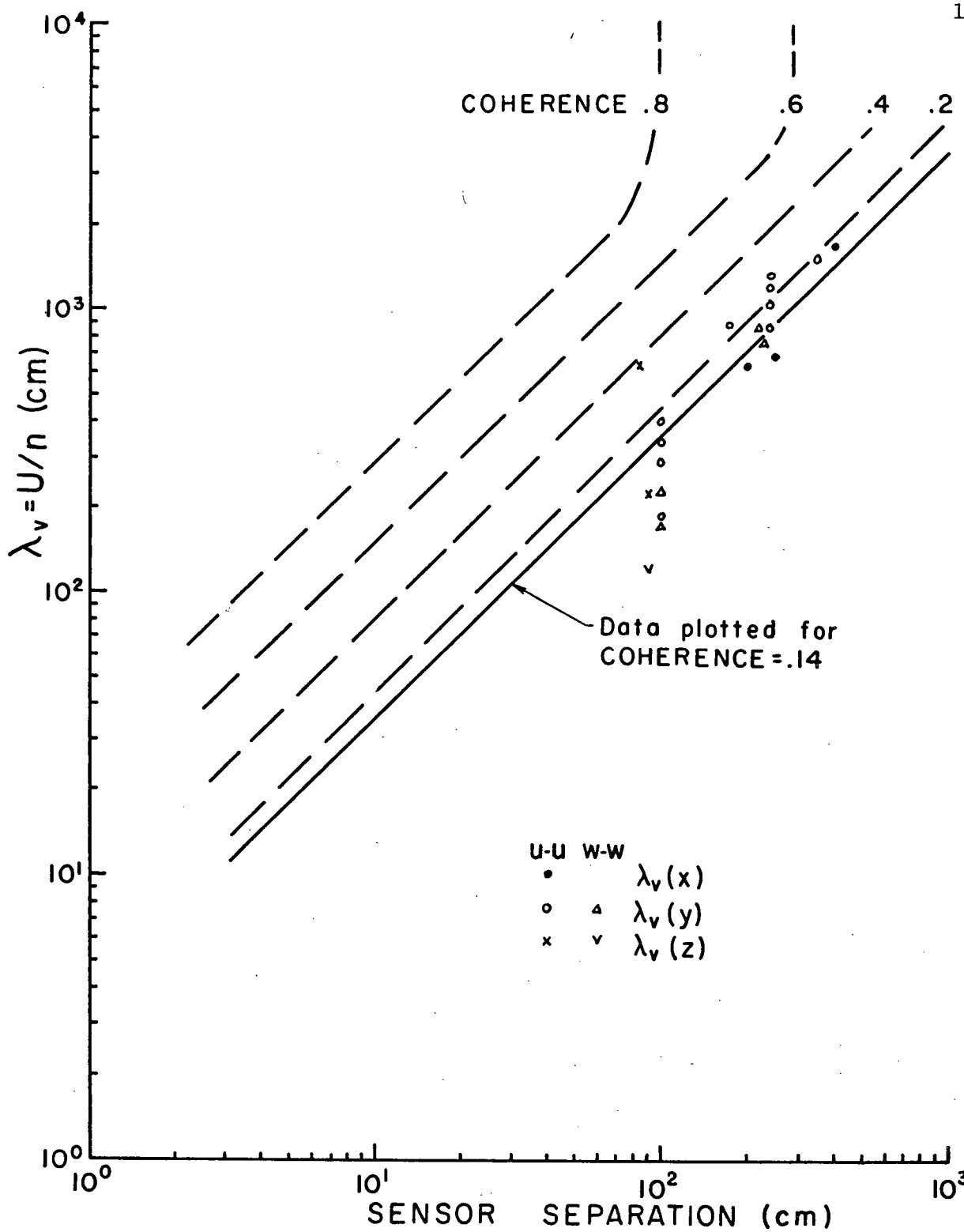

Figure 36. Fixed coherences between two velocity signals for various sensor separations. The values plotted are for a coherence of 0.14.

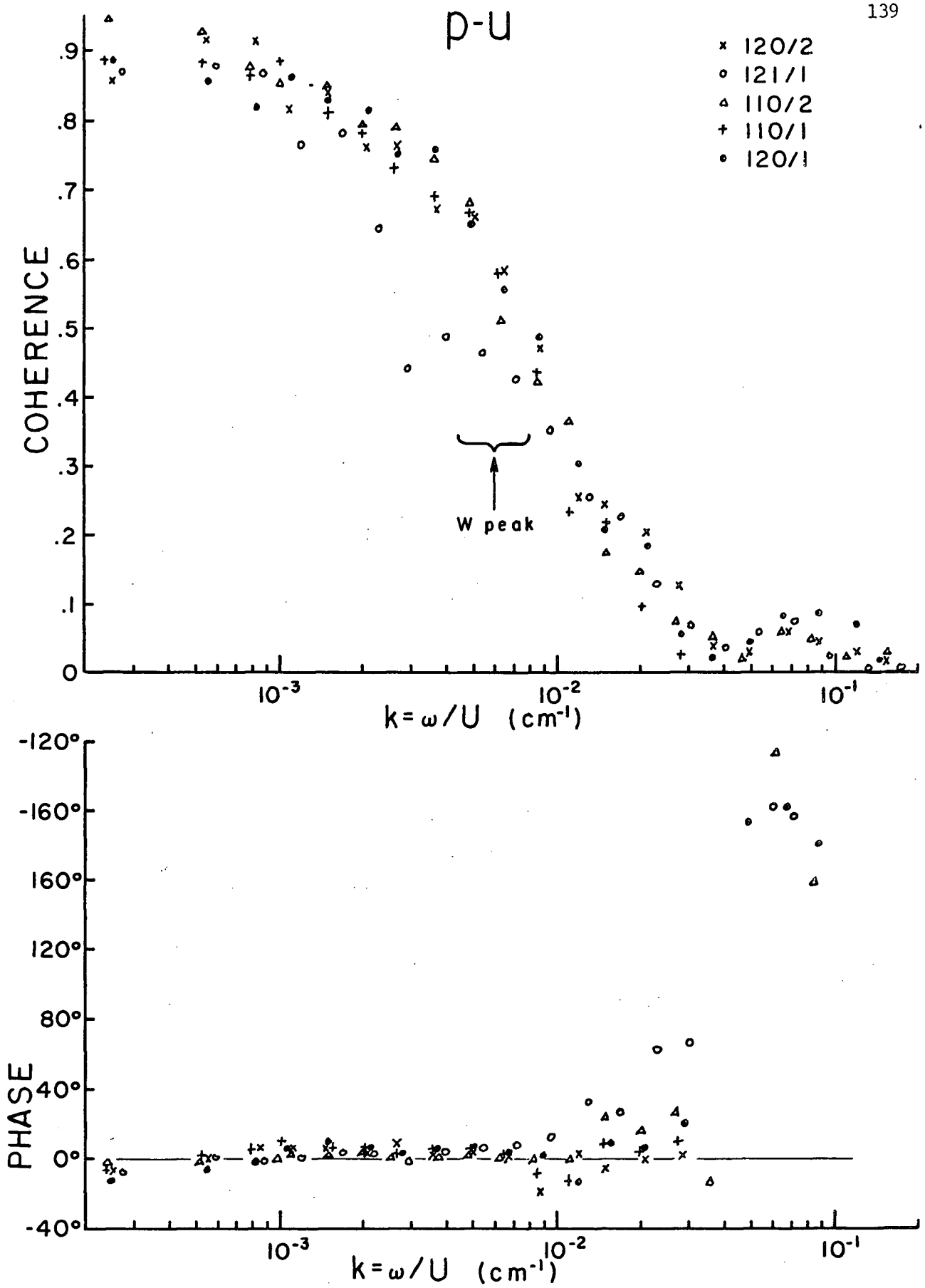

Figure 37. Coherence and phase between p and u, u measured with a sonic. Height of observations ranged from 1.5 to 5.5 meters. Phase positive means p leads u.

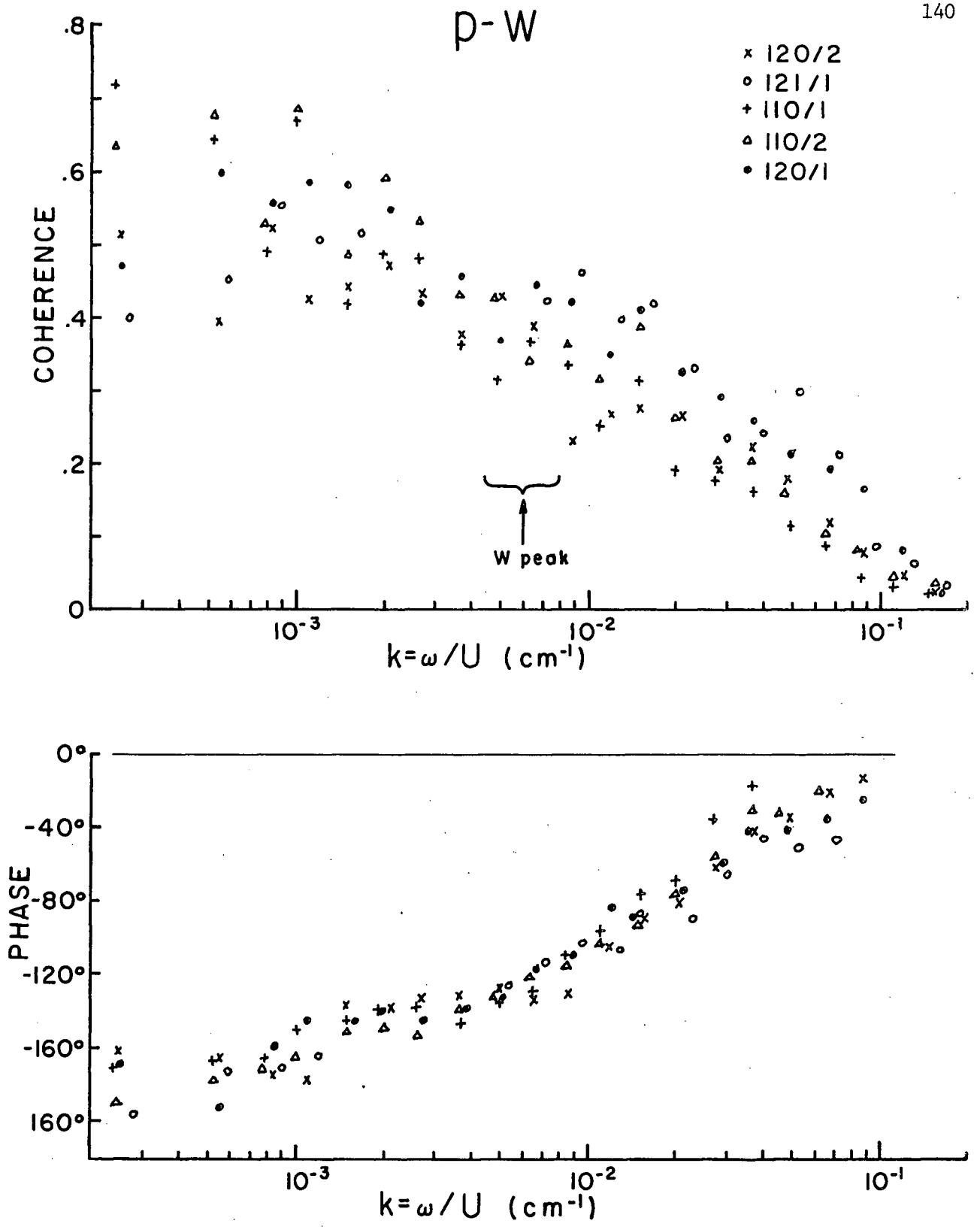

Figure 38. Coherence and phase between p and w, w measured with a sonic. Height of observations ranged from 1.5 to 5.5 meters. Phase positive means p leads w.

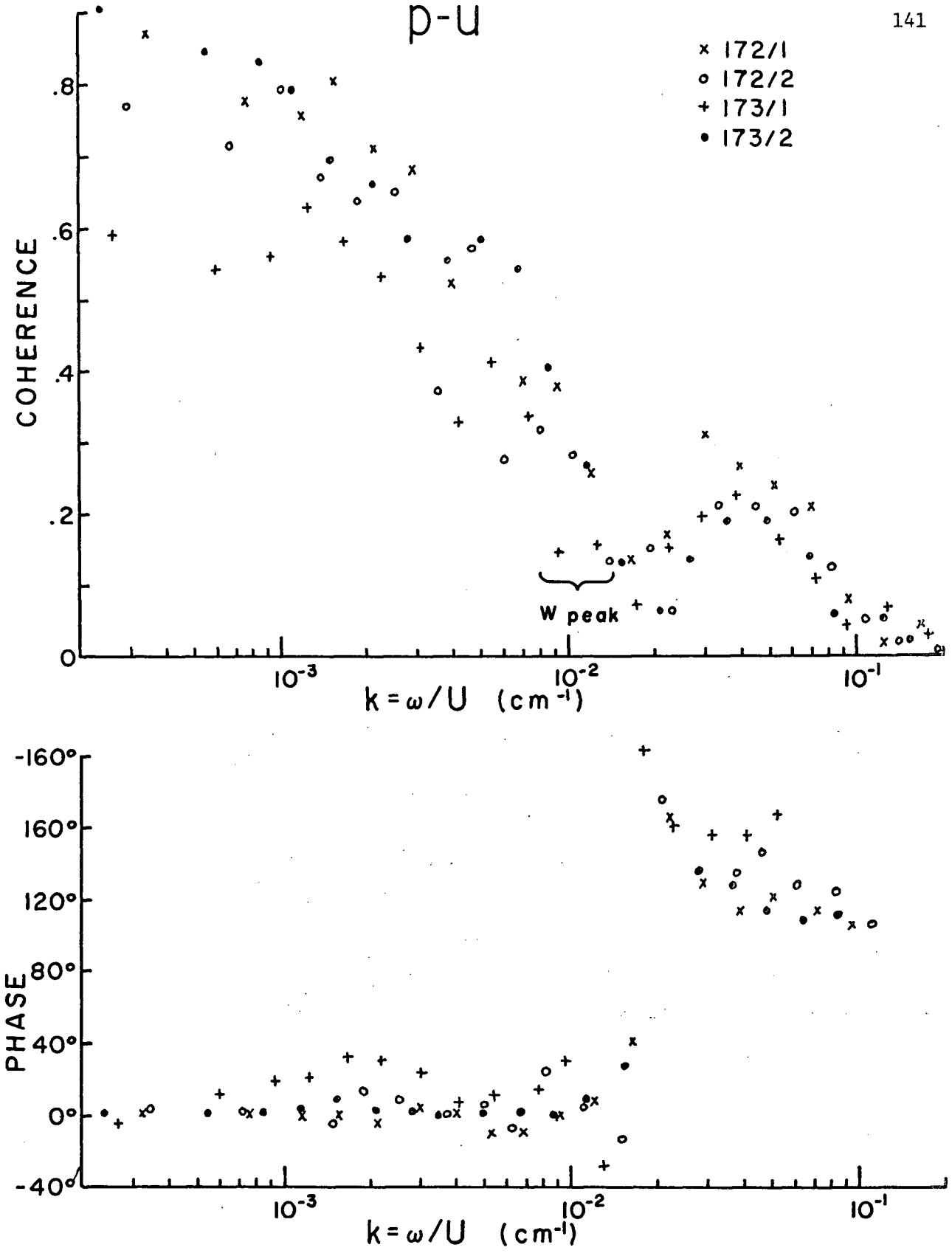

Figure 39. Coherence and phase between p and u, u measured with a hot-wire. Height of observations ranged from 1.5 to 3 meters. Phase positive means p leads u.

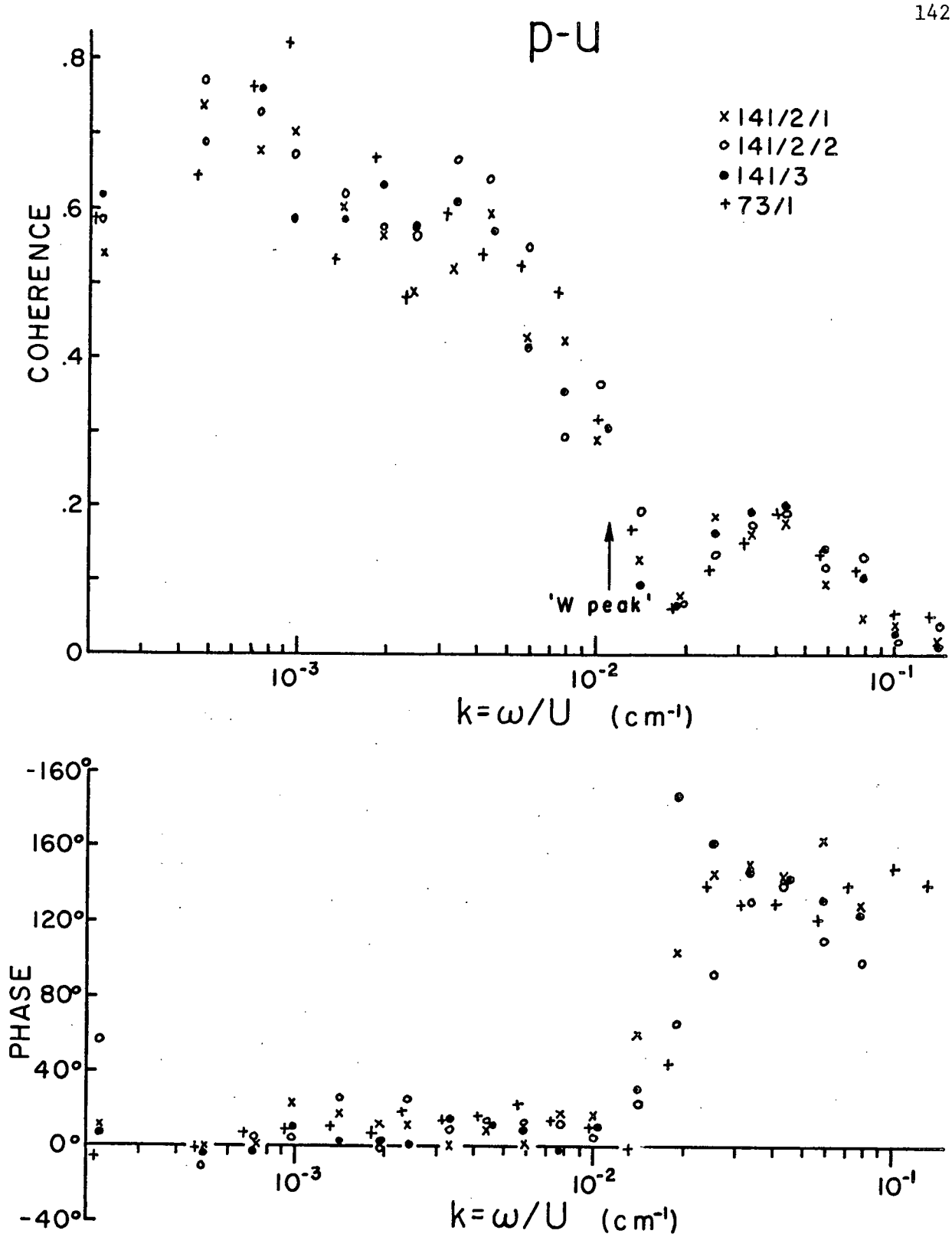

Figure 40. Coherence and phase between p and u, u measured with a hot-wire.
Height of observations was 2 meters.
Phase positive means p leads u.

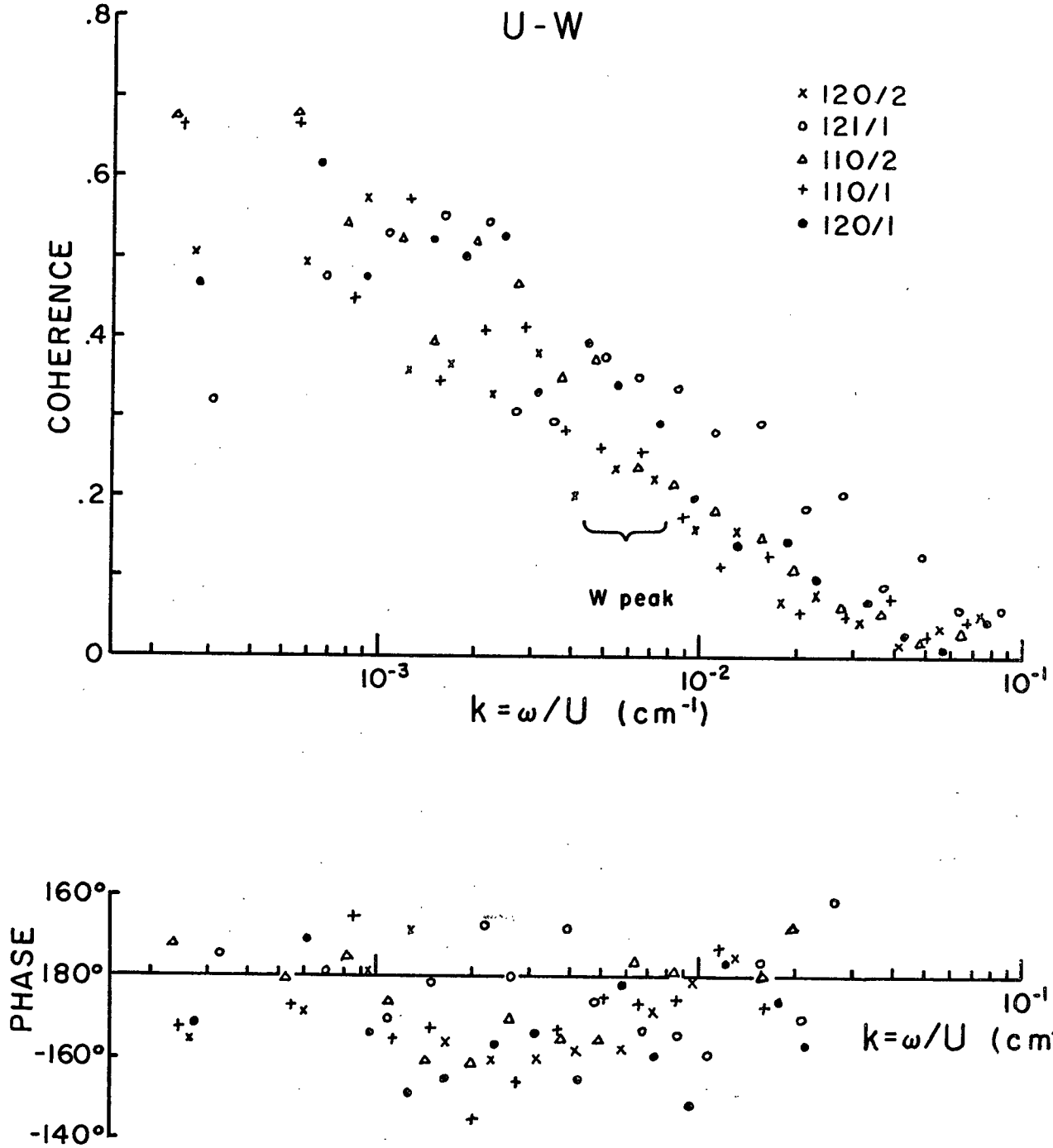

Figure 41. Coherence and phase between u and w, velocity components measured with a sonic.
Height of observations ranged from 1.5 to 5.5 meters.
Phase positive means u leads w.

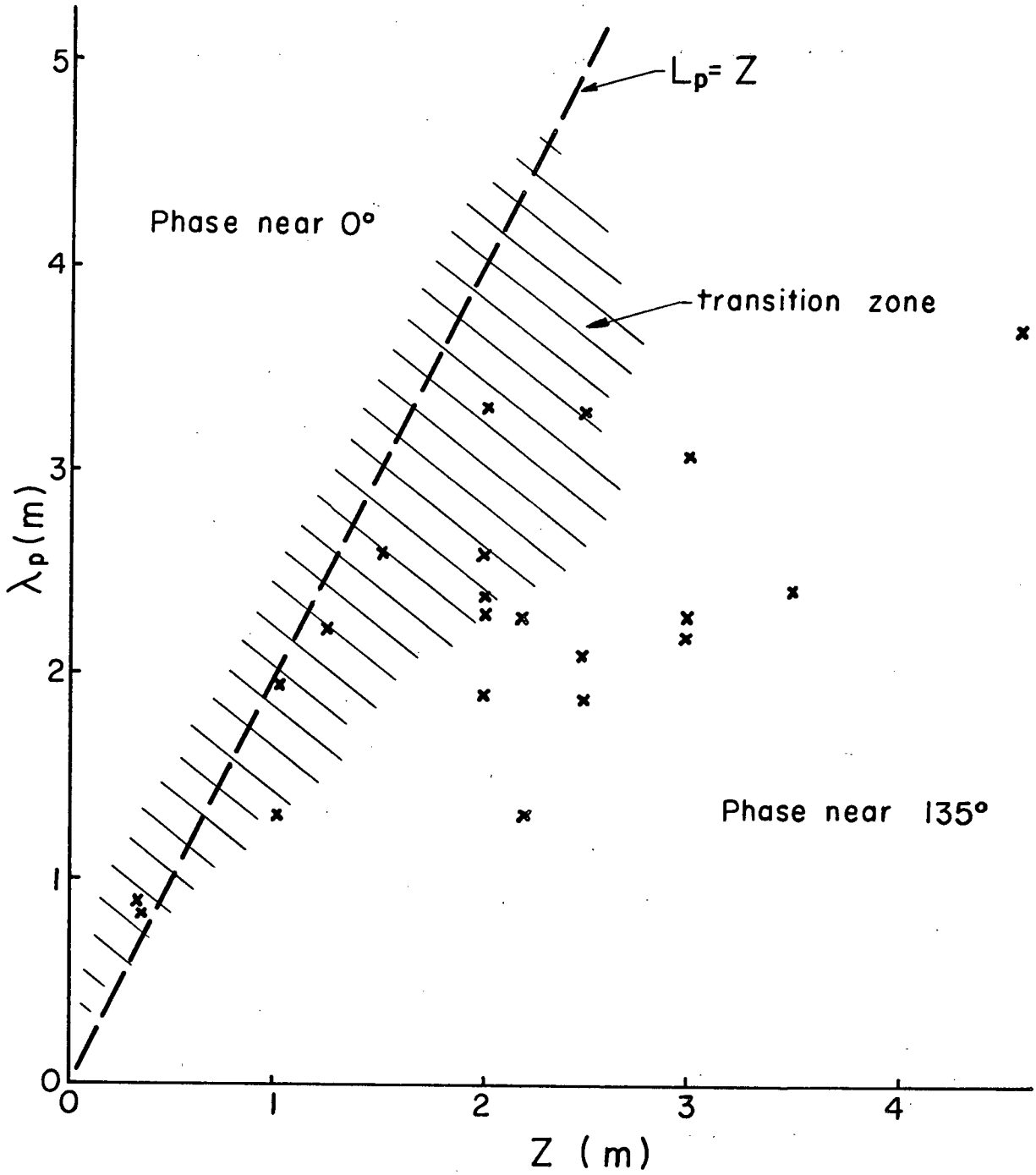

Figure 42. Wavelength of the pressure fluctuations associated with the p-u phase transition, as a function of observational height. The broken line is the measured scale size.

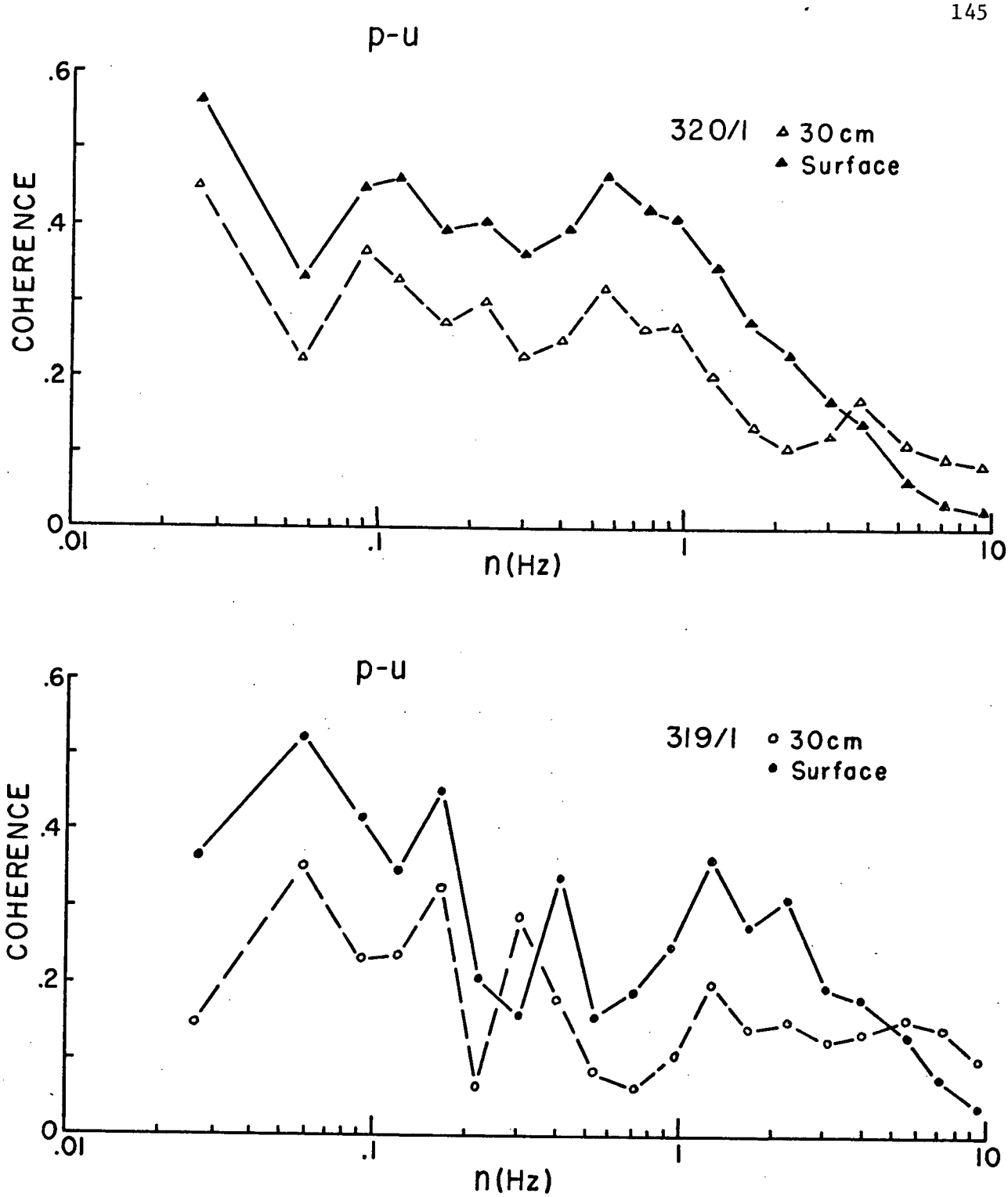

Figure 43. Coherence between downstream velocity, u, and two pressure measurements. One pressure sensor was beside the u sensor, one was at the surface, 30 cm below.

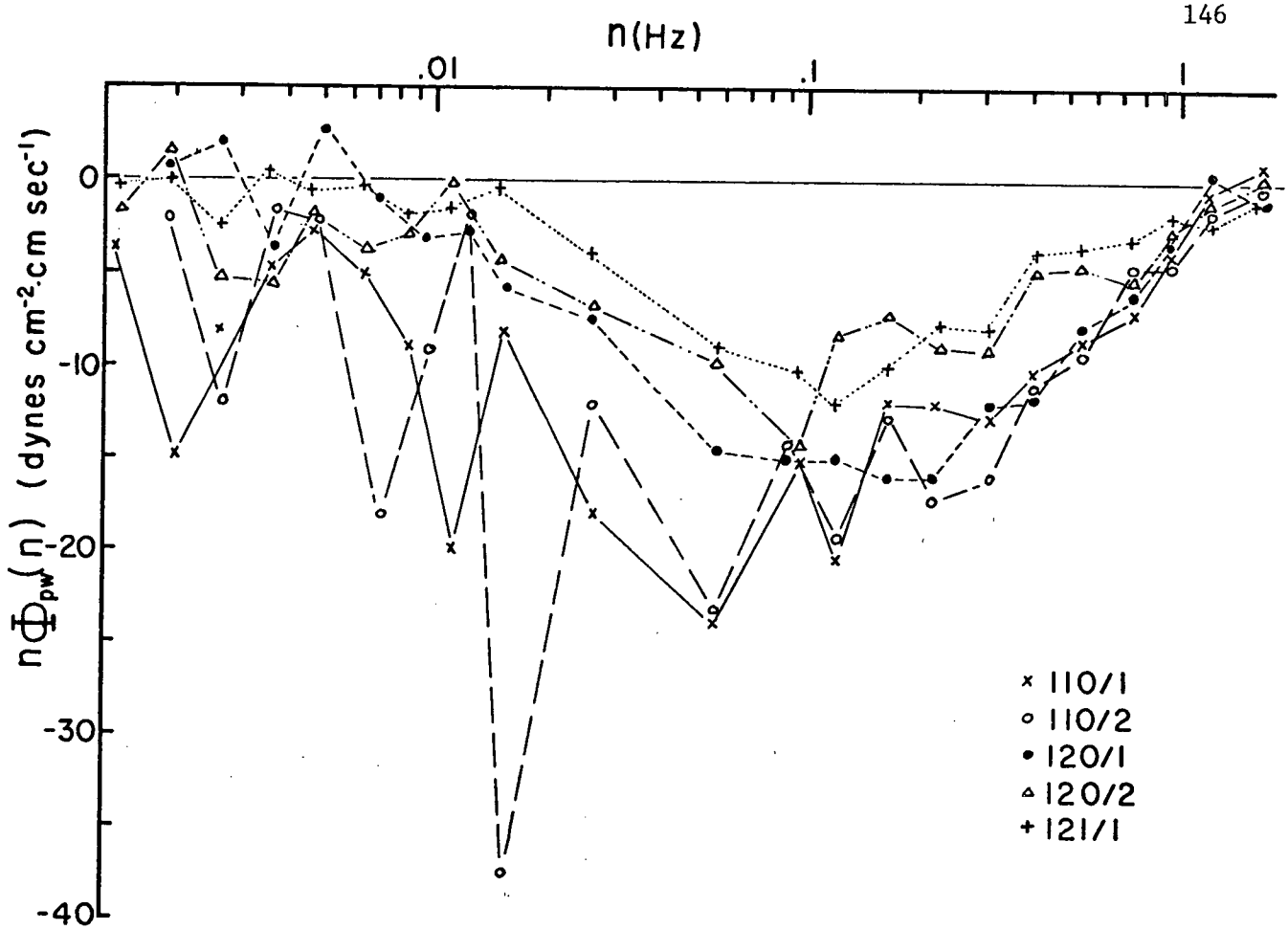

Figure 44. Spectra of $\overline{pw}$

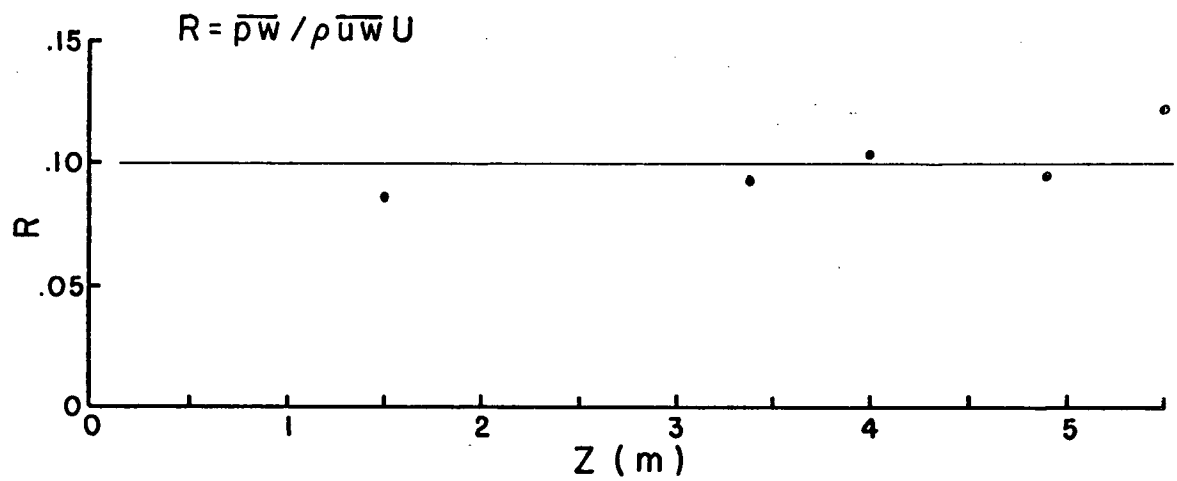

Figure 45. Ratio of the $\overline{pw}$ and $\overline{uwU}$ terms of the integrated net energy budget equation.

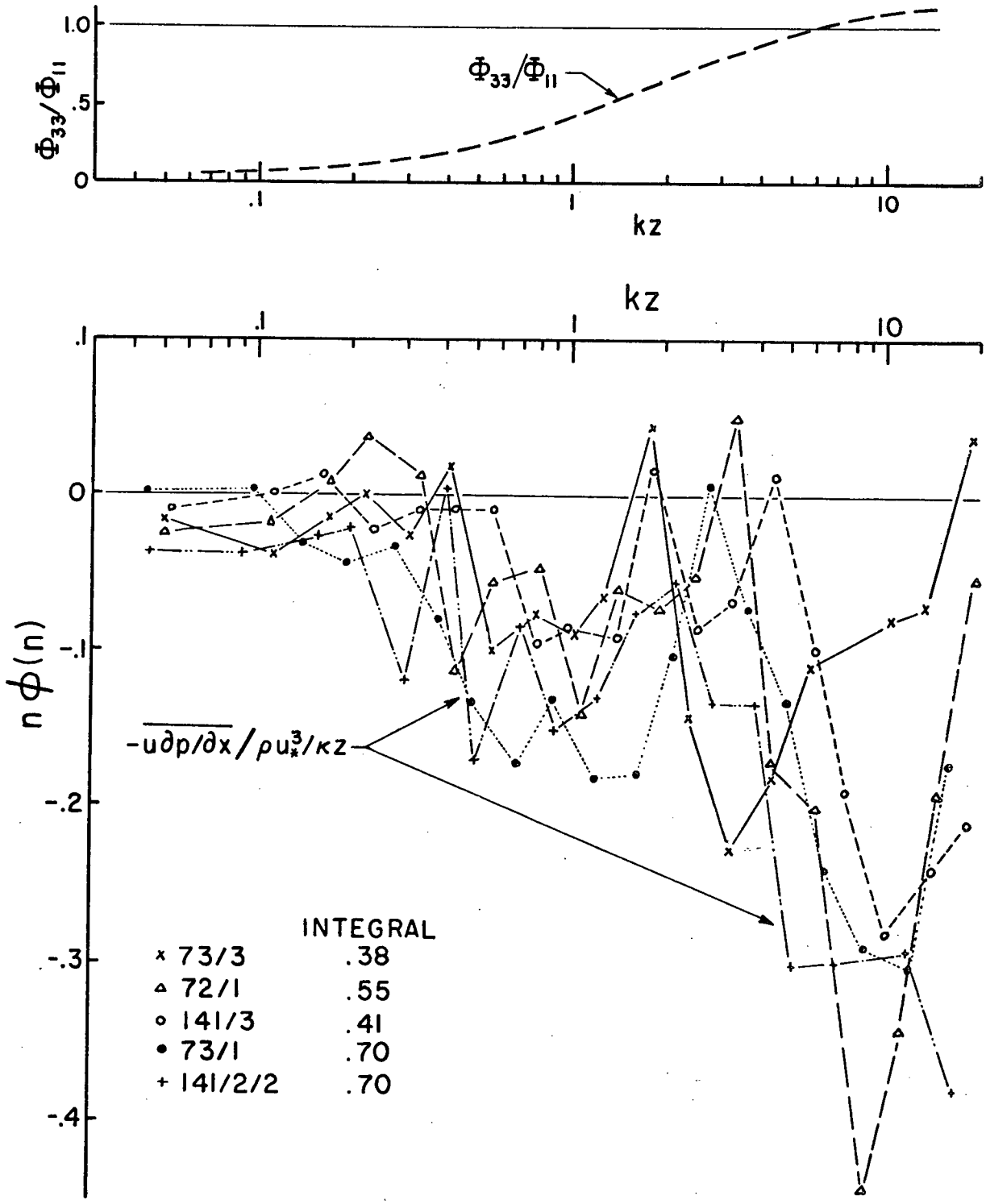

Figure 46. Spectral distribution of the energy flux, by pressure forces, from the u velocity component. The integral given is for kz from 0.05 to 20.

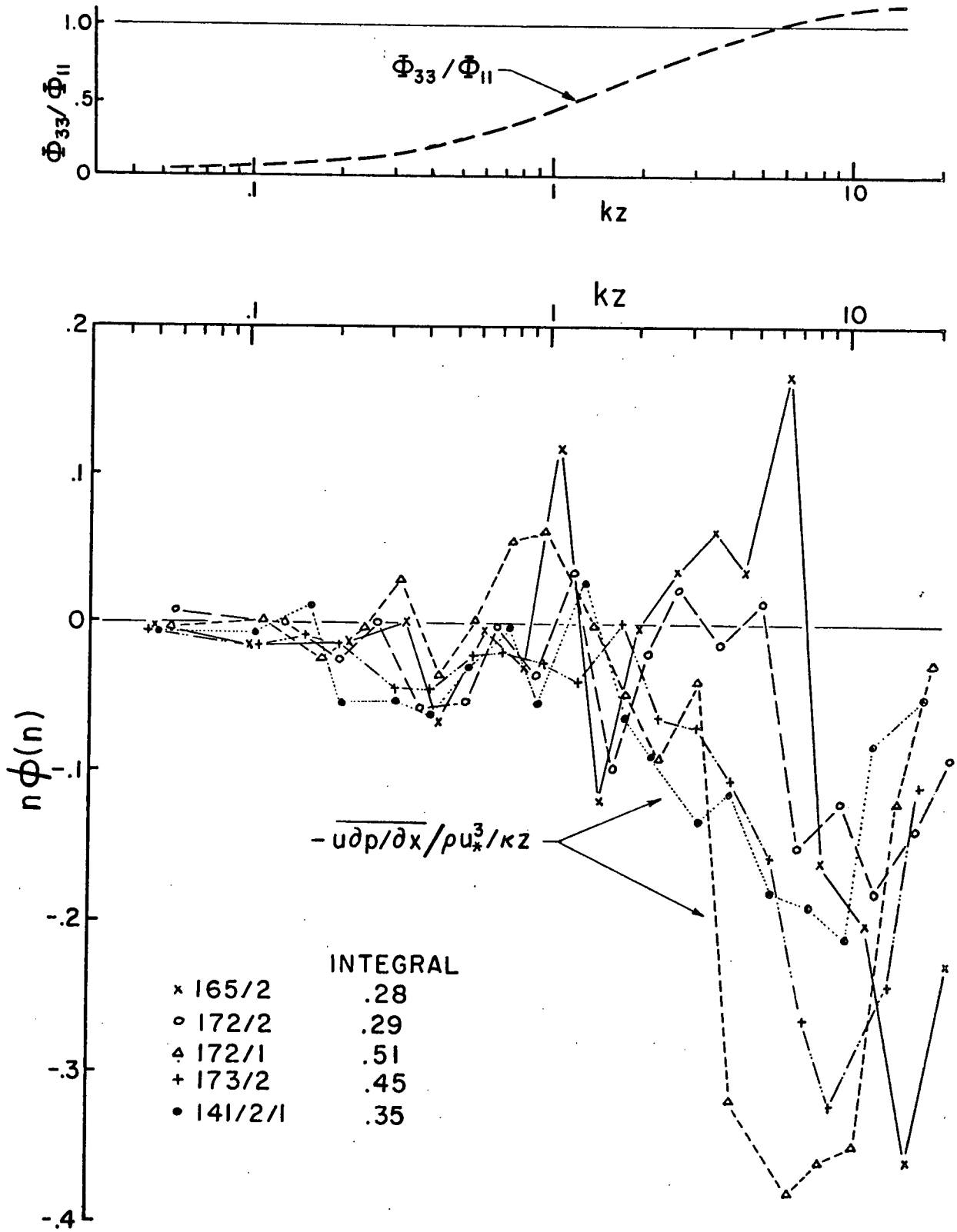

Figure 47. Spectral distribution of the energy flux, by pressure forces, from the u velocity component. The integral given is for kz from 0.05 to 20.

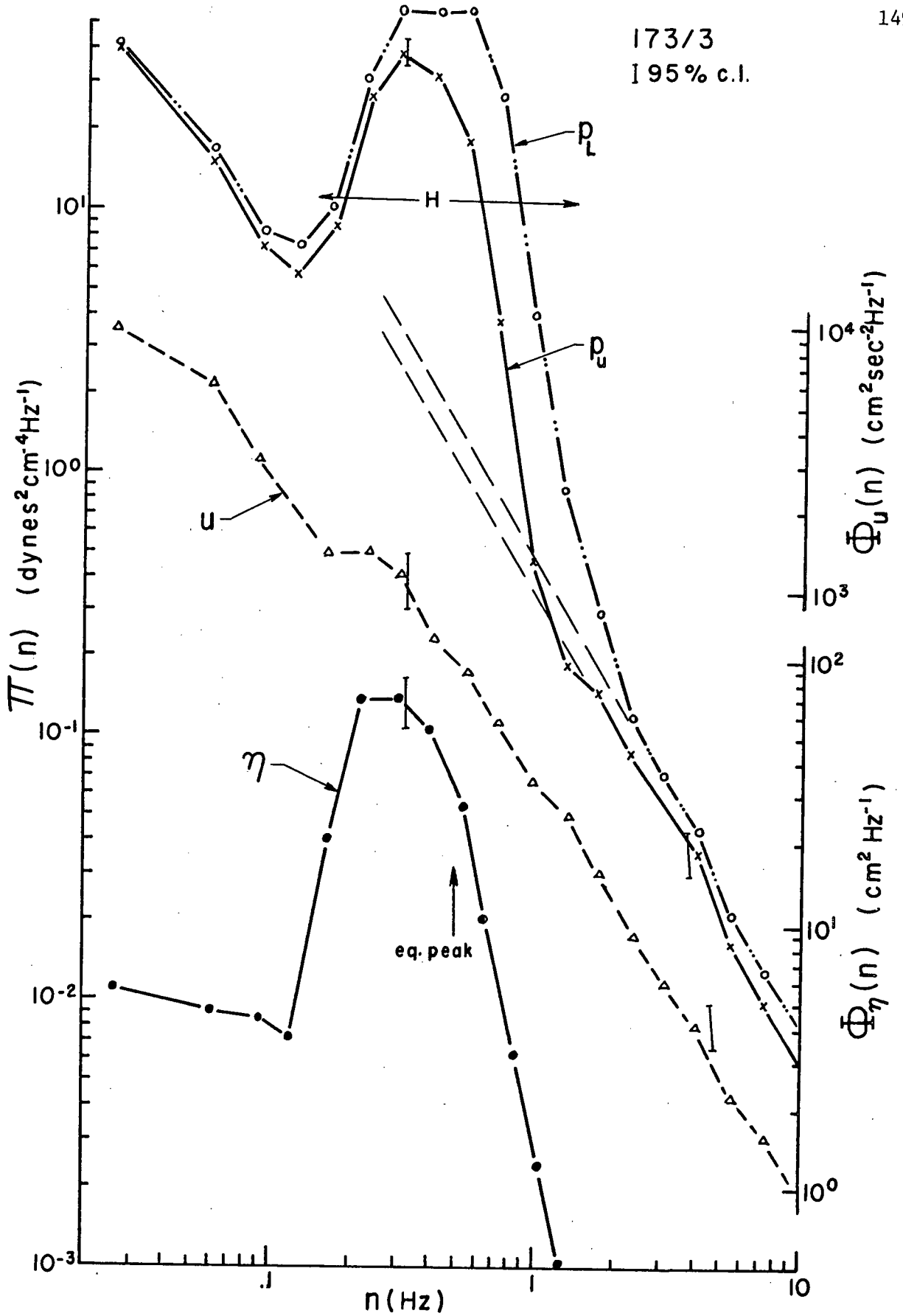

Figure 48. Pressure, velocity, and wave spectra for Run 173/3.

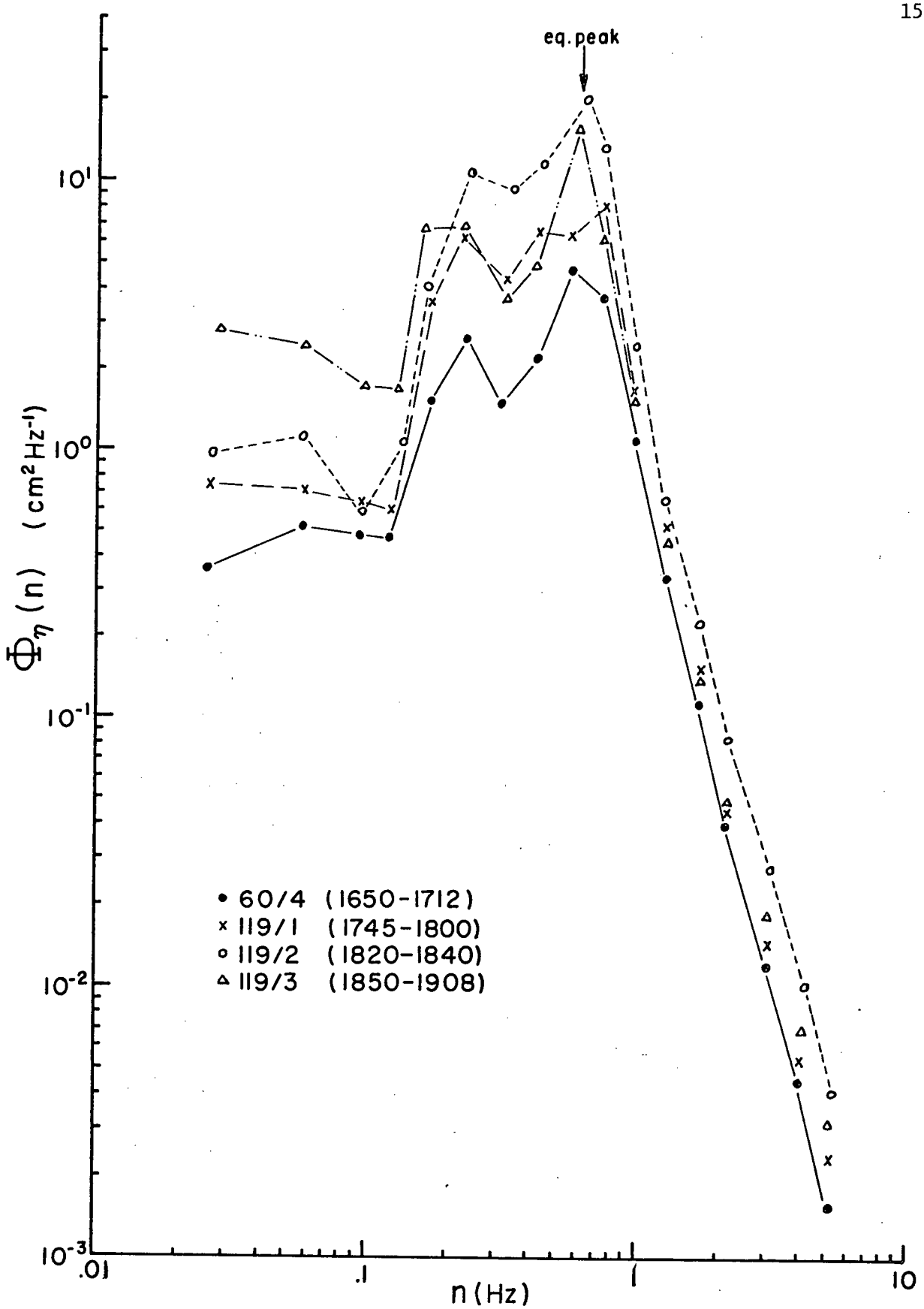

Figure 49. Wave spectra of Data Group A. The time of start and end of each Run is given in brackets.

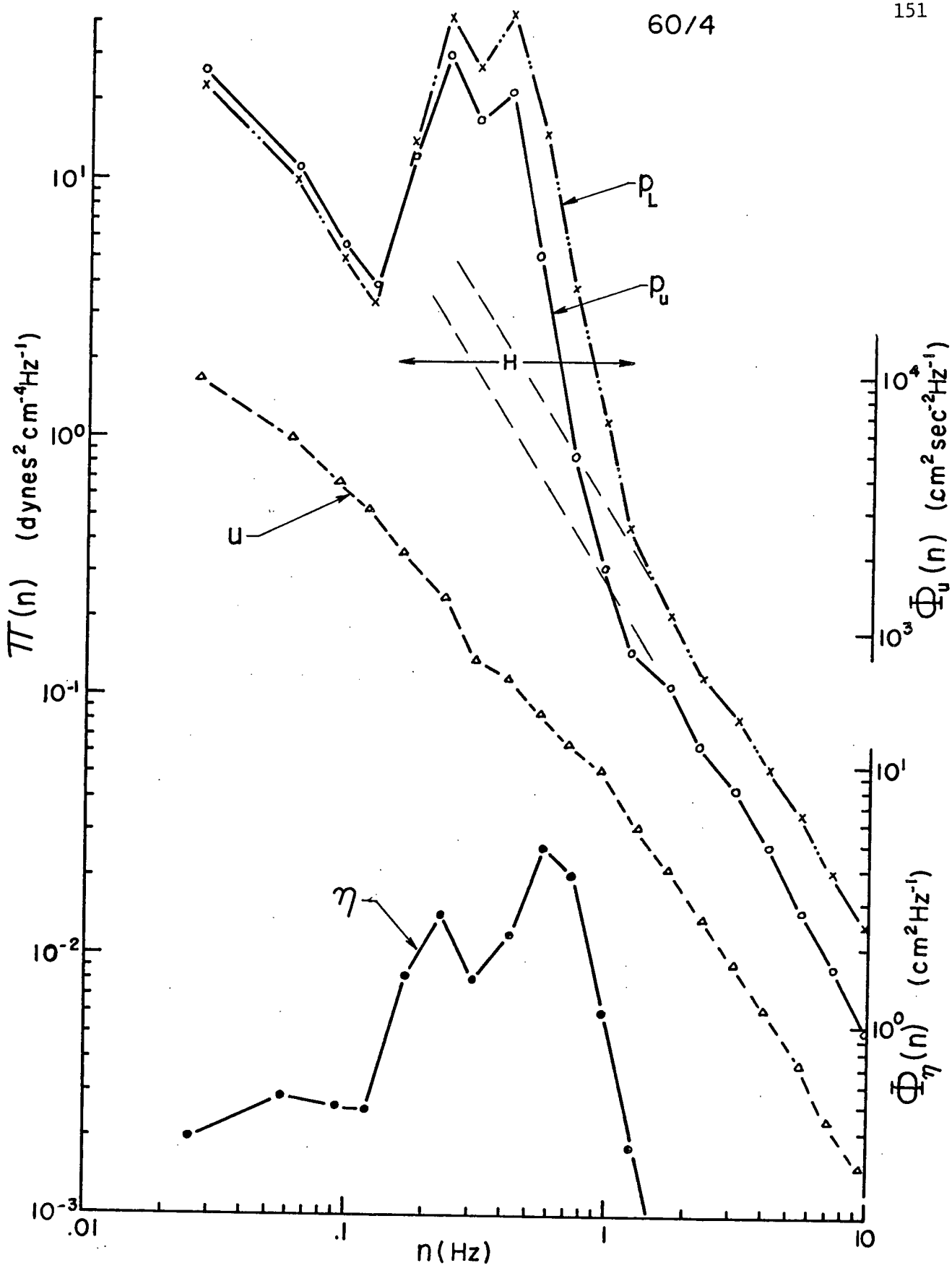

Figure 50. Pressure, u velocity and wave spectra for Run 60/4.

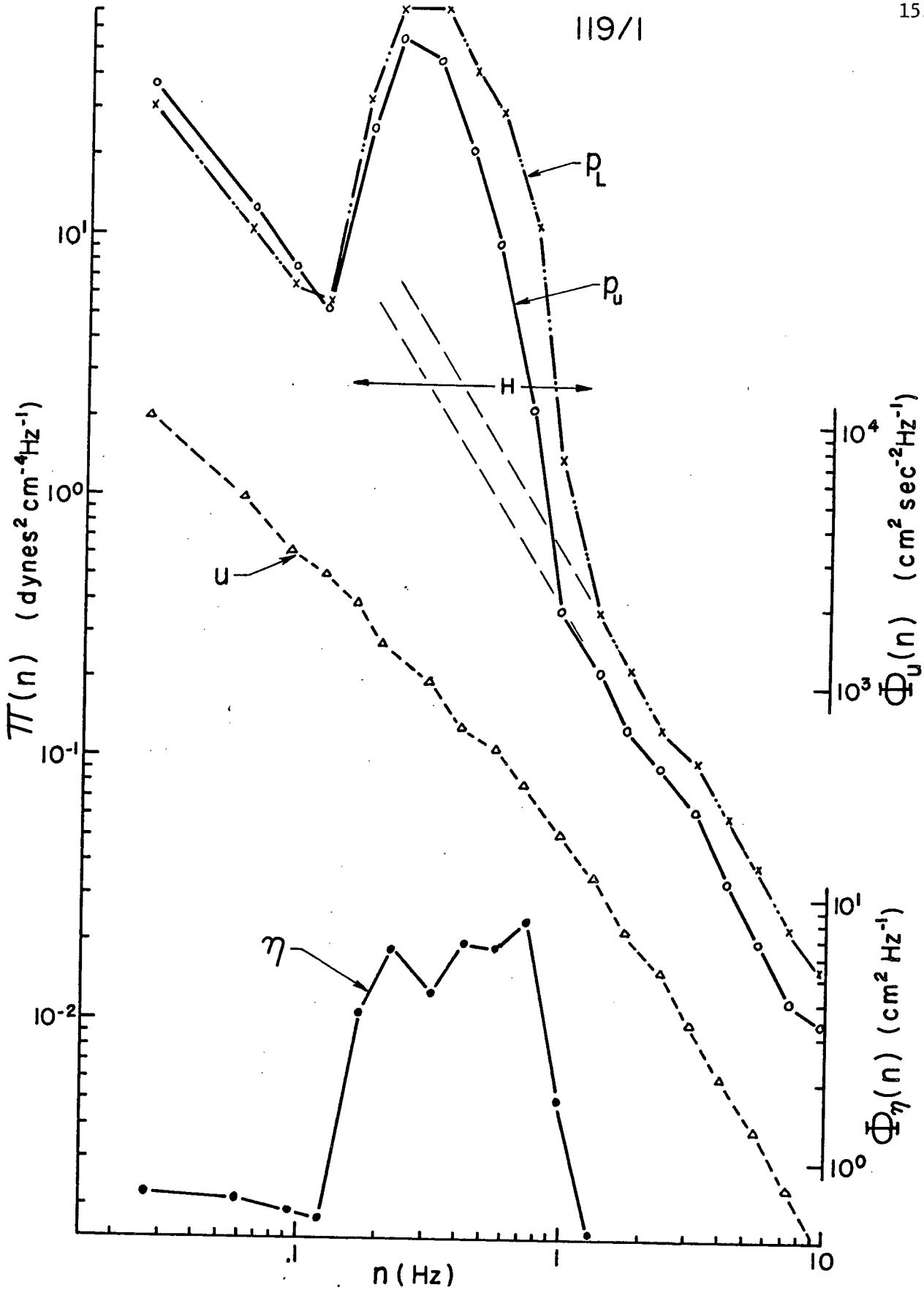

Figure 51. Pressure, u velocity and wave spectra for Run 119/1

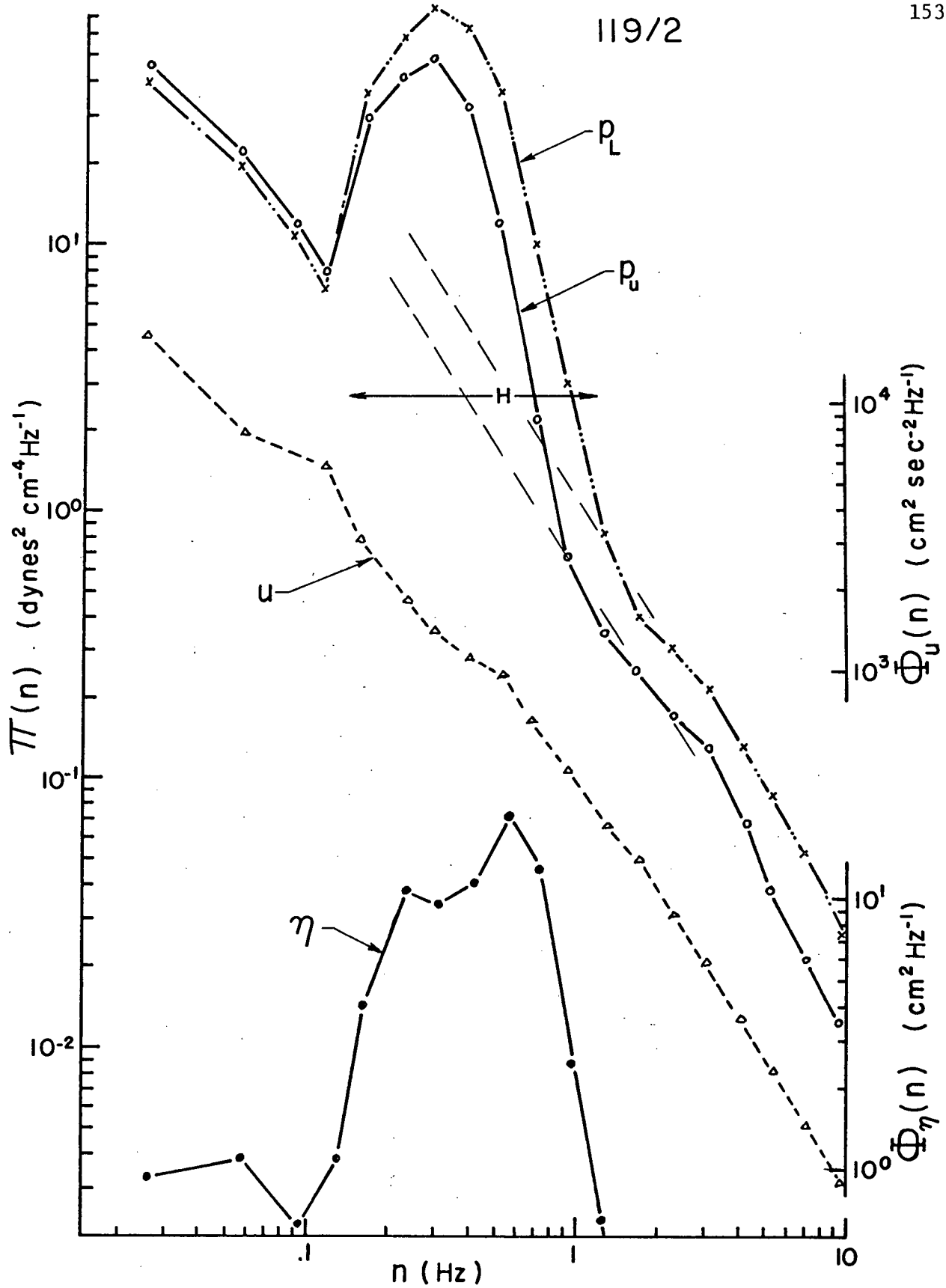

Figure 52. Pressure, u velocity and wave spectra for Run 119/2

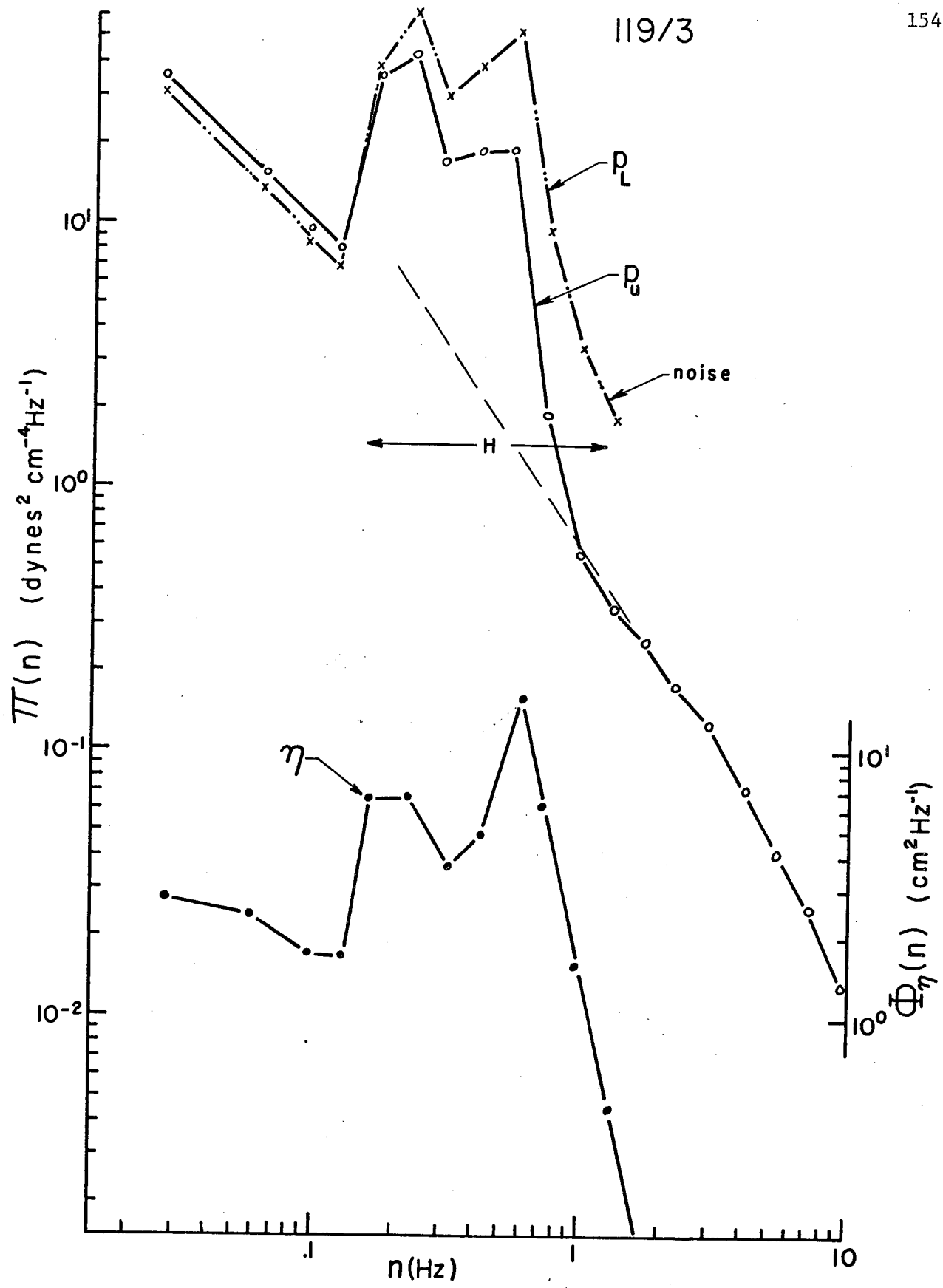

Figure 53. Pressure and wave spectra for Run 119/3

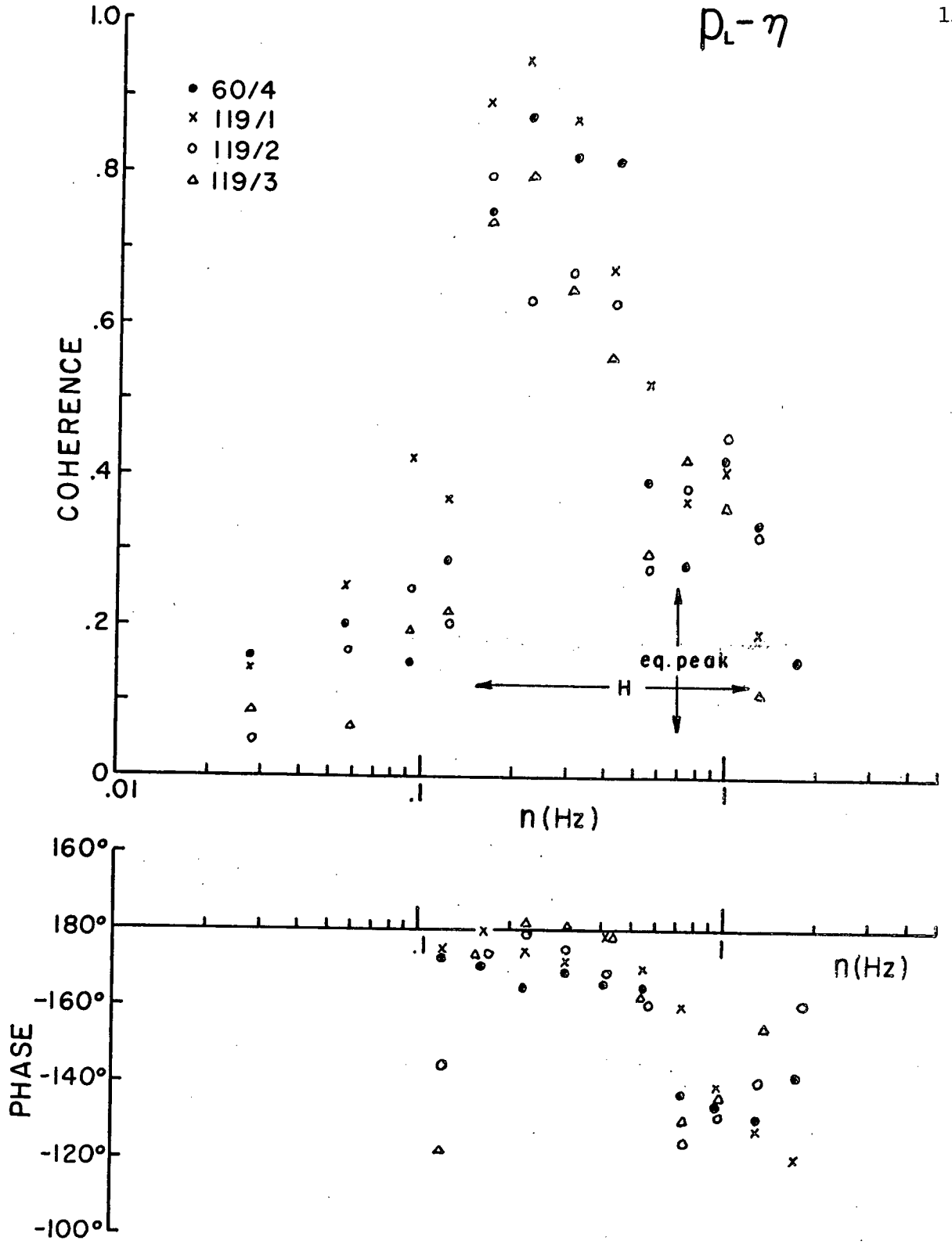

Figure 54. Coherence and phase between the lower pressure sensor and the waves: Data Group A. $p_L - \eta$ phase positive means p_L leads η.

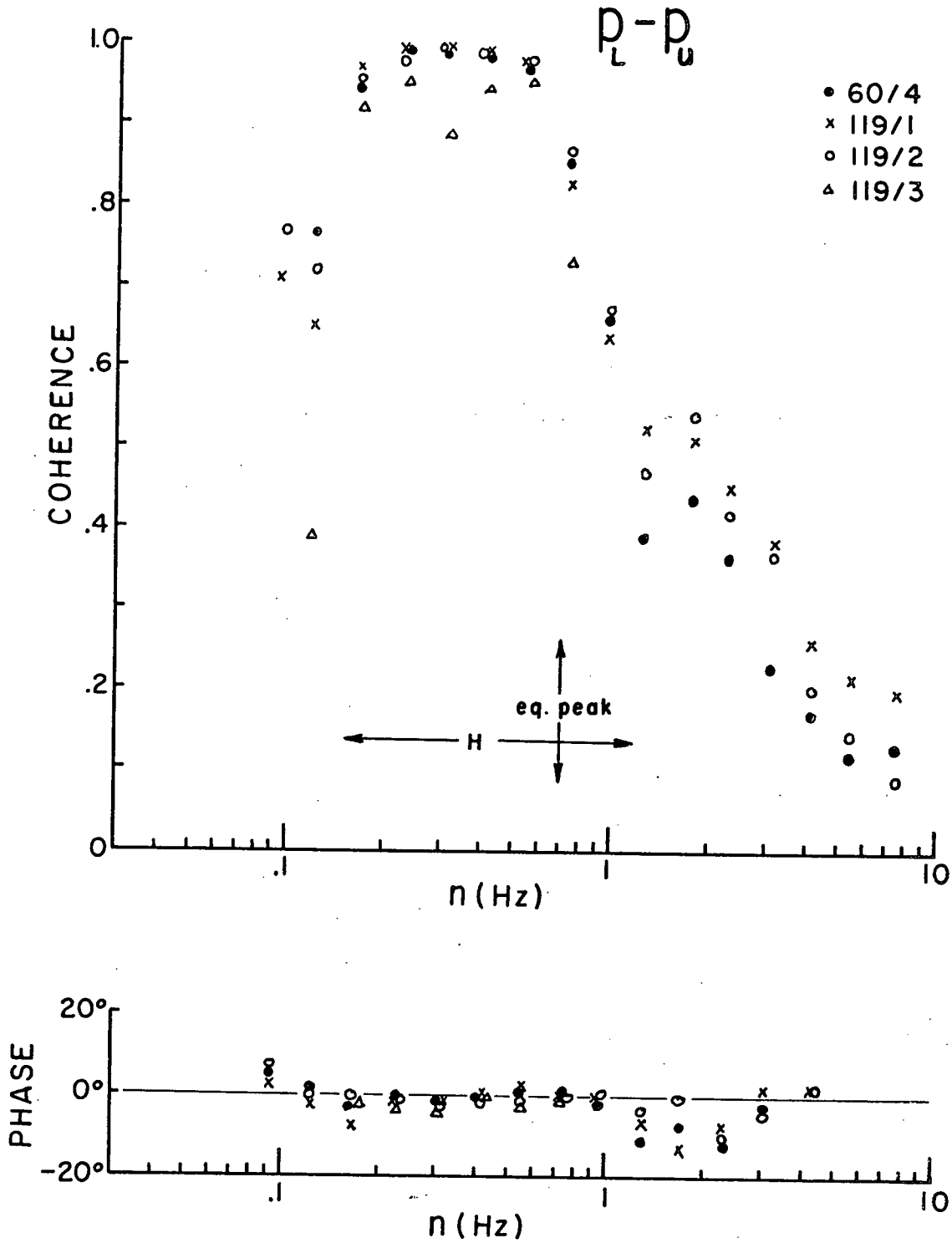

Figure 55. Coherence and phase between the two pressure sensors: Data Group A. $p_L - p_u$ phase positive means p_L leads p_u.

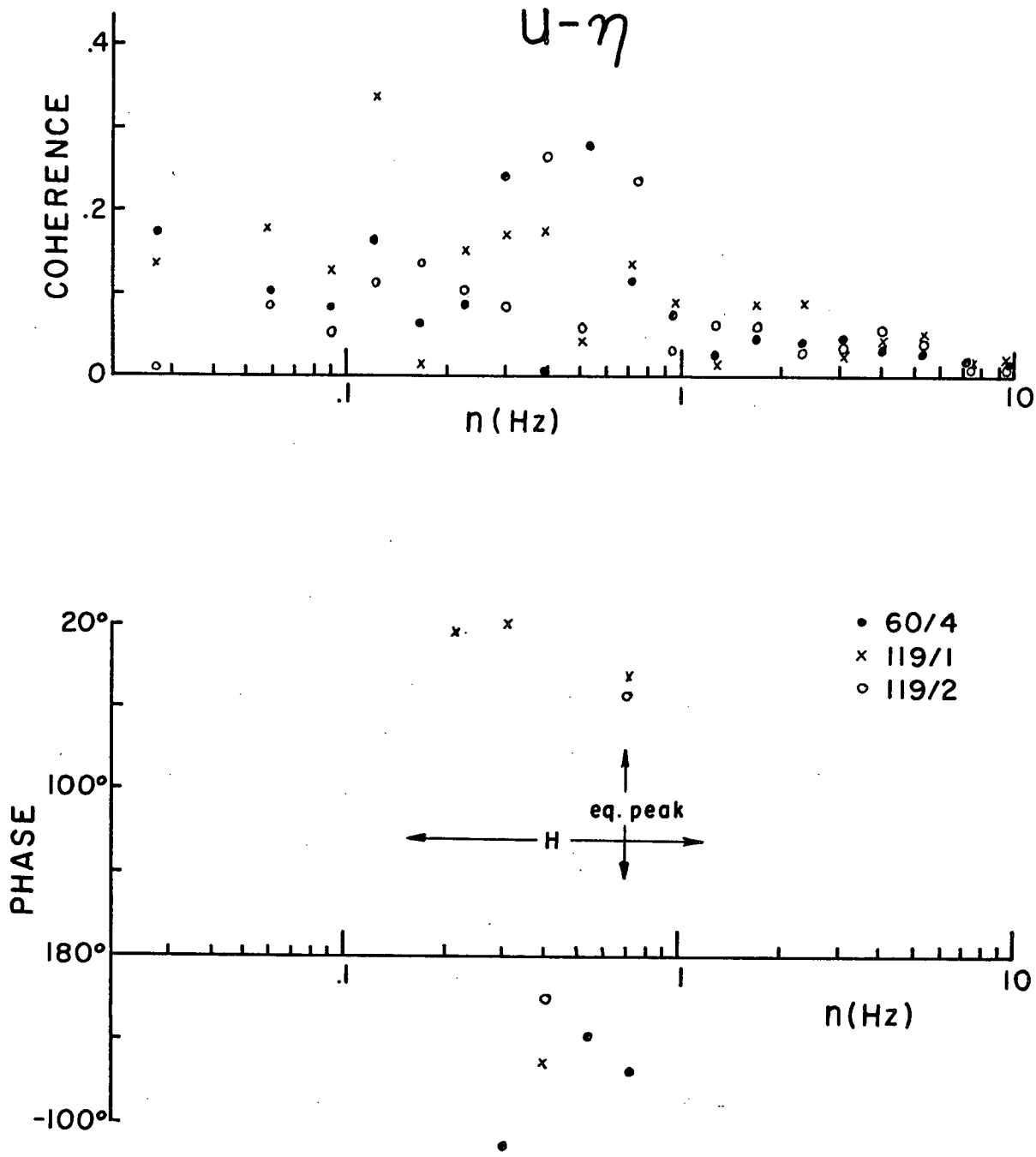

Figure 56. Coherence and phase between the u velocity and waves: Data Group A. u-η phase positive means u leads η.

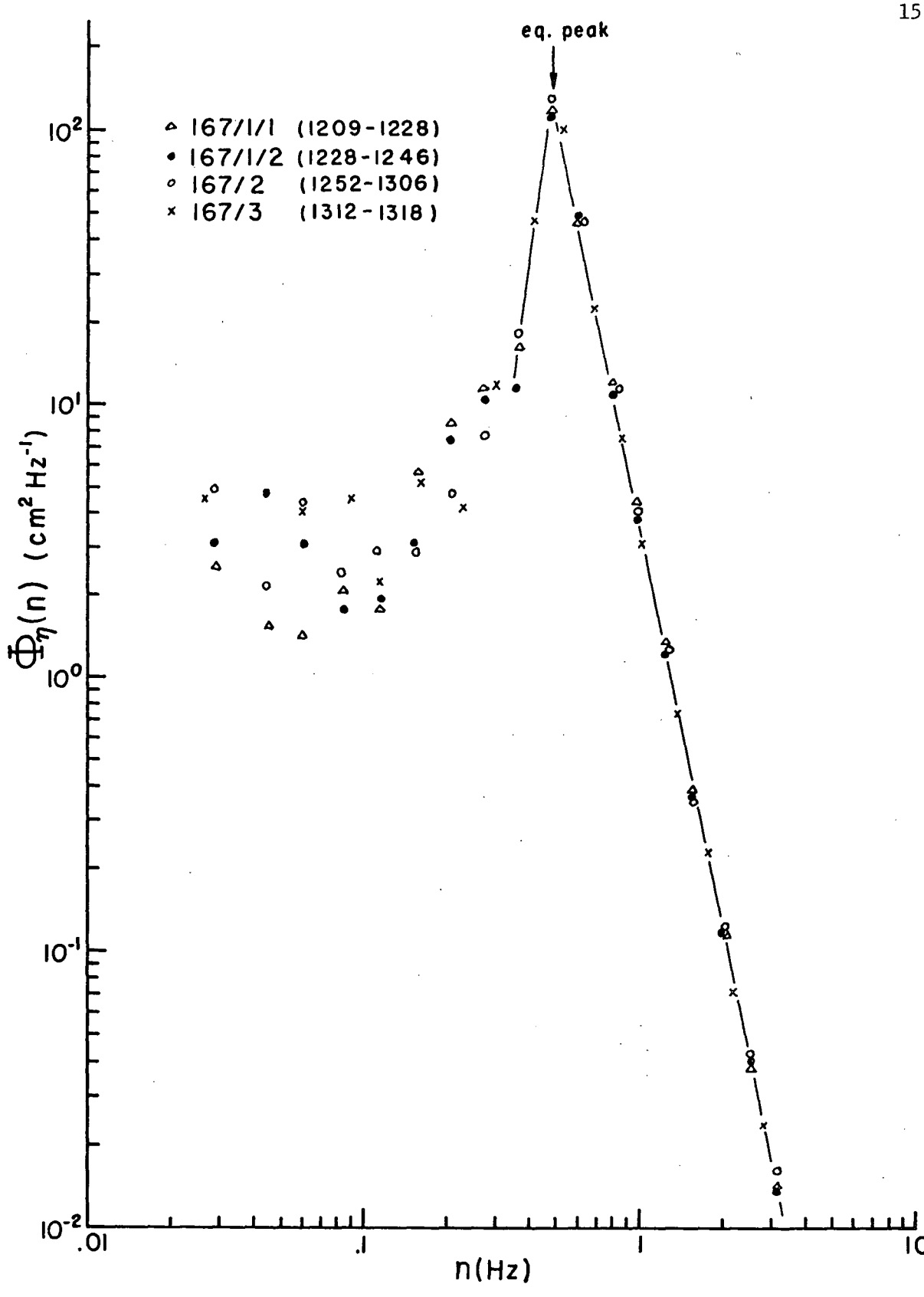

Figure 57. Wave spectra for Data Group B. The time of start and end of each Run is given in the brackets.

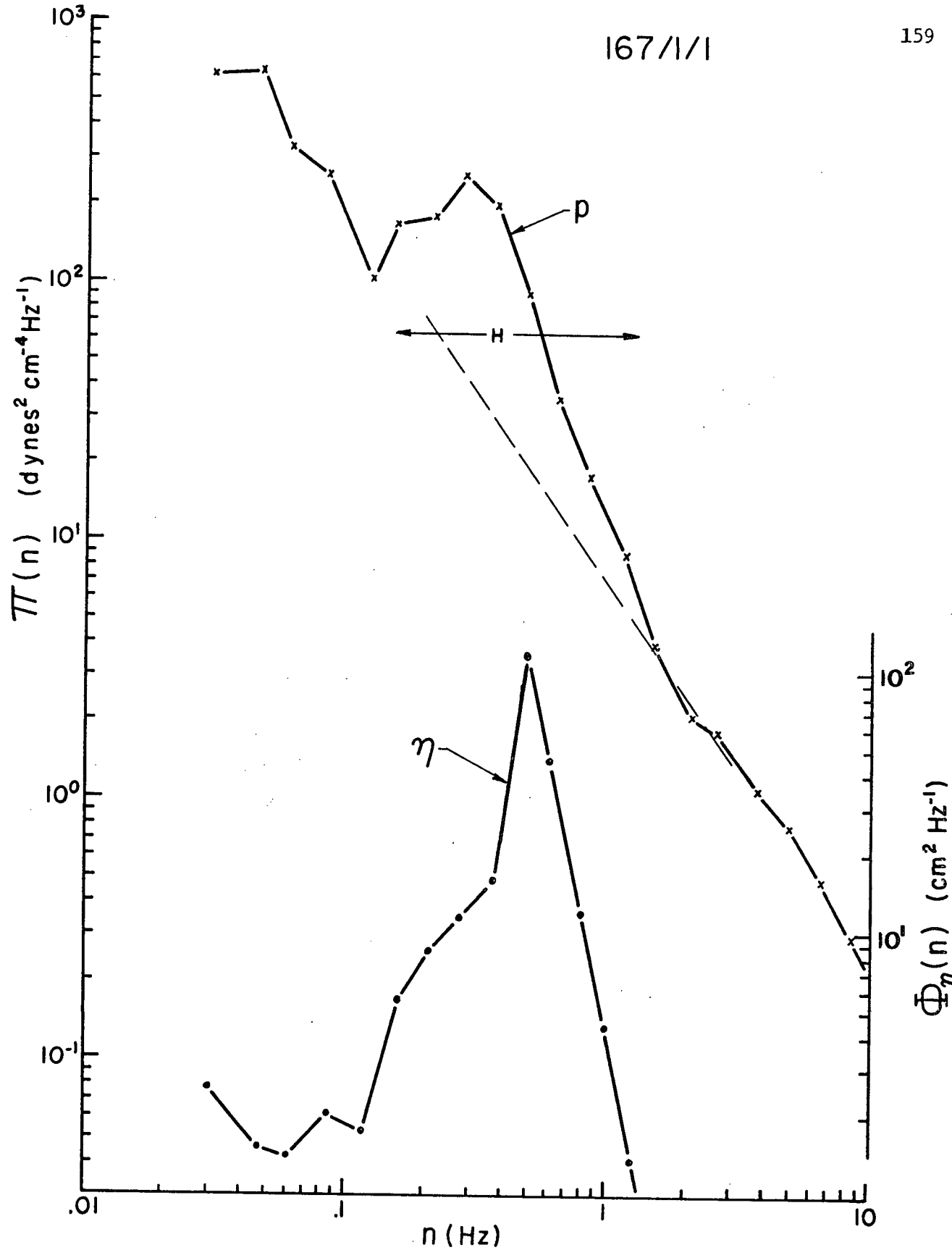

Figure 58. Pressure and wave spectra for Run 167/1/1

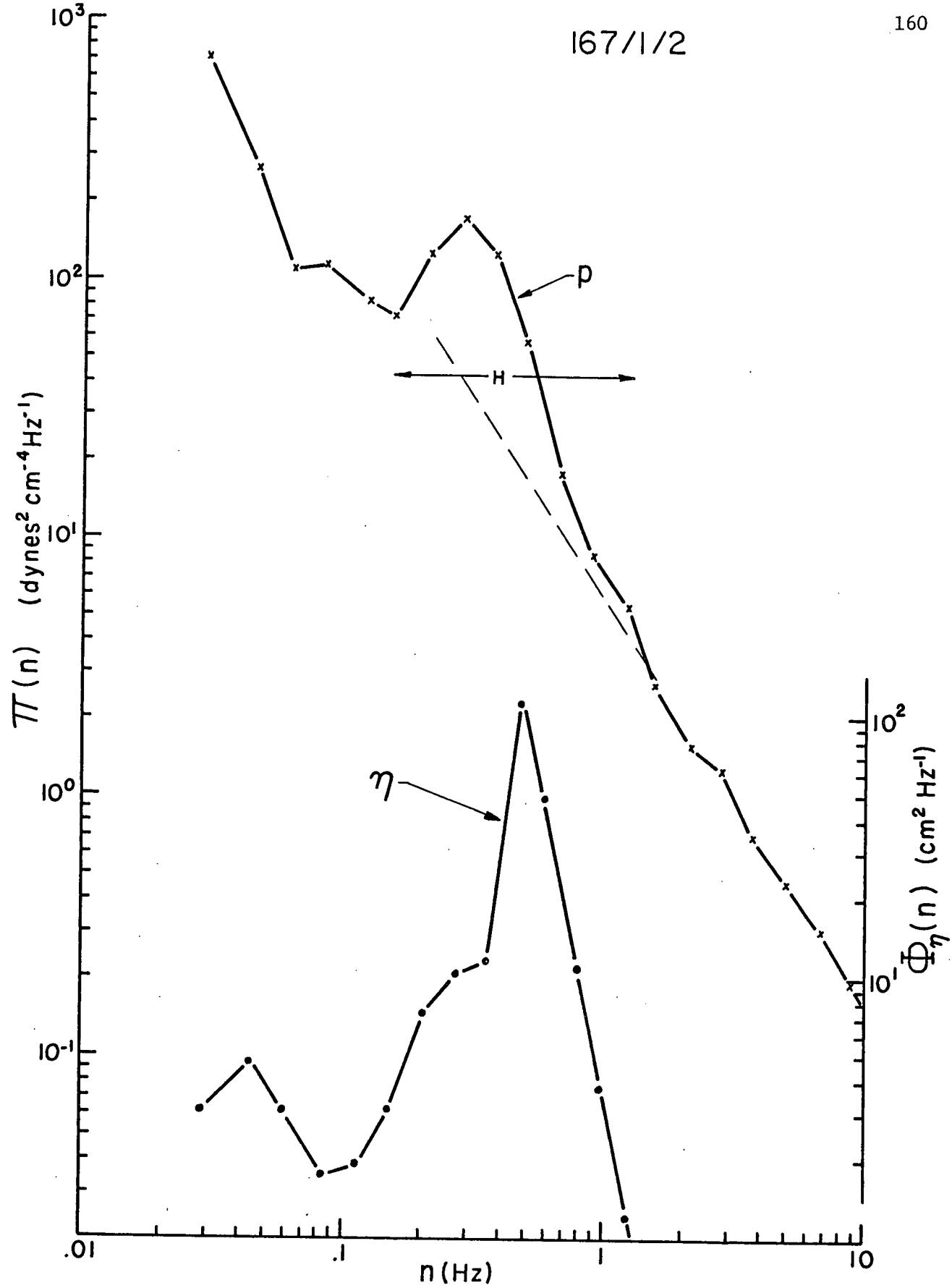

Figure 59. Pressure and wave spectra for Run 167/1/2

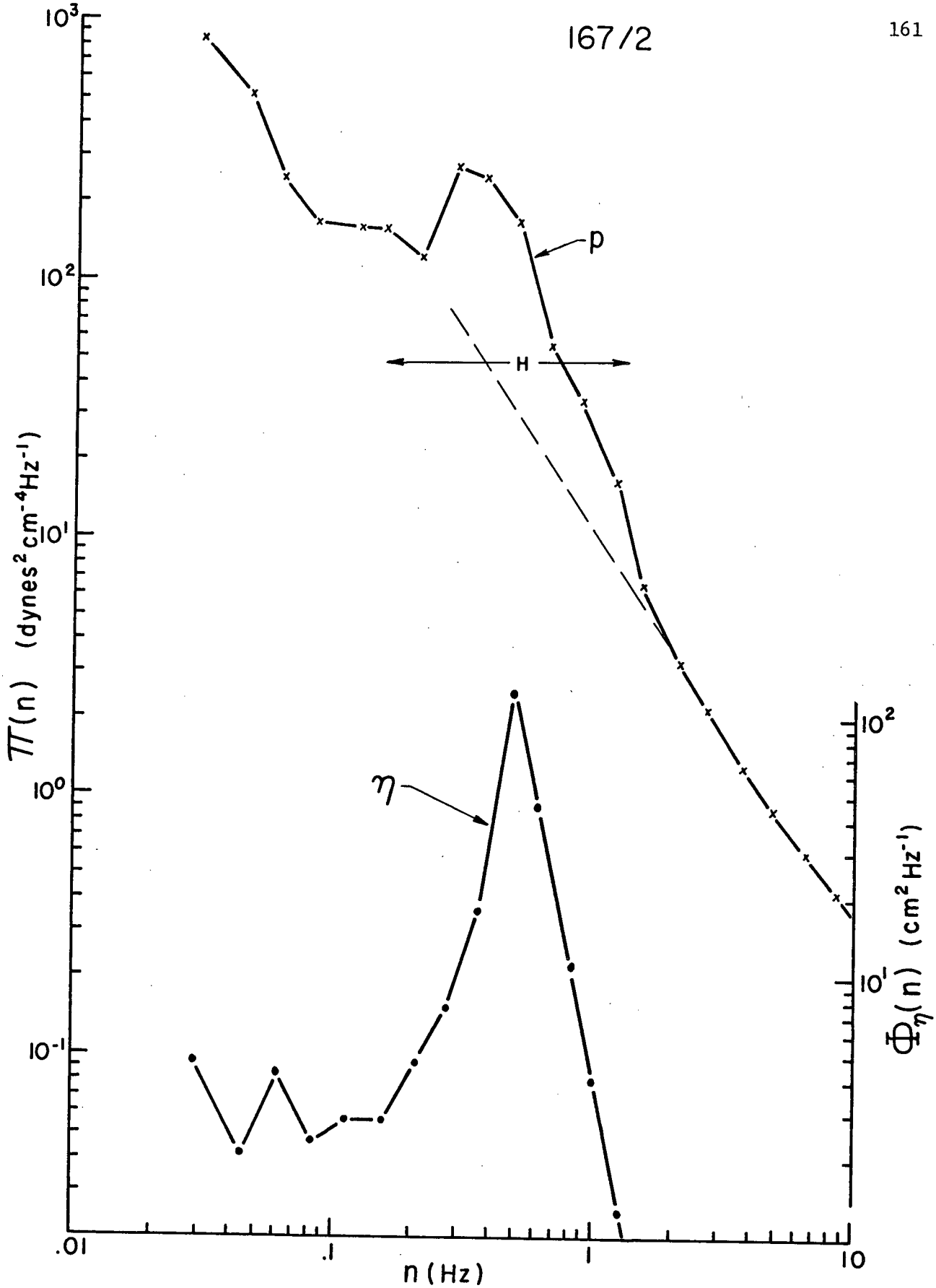

Figure 60. Pressure and wave spectra for Run 167/2

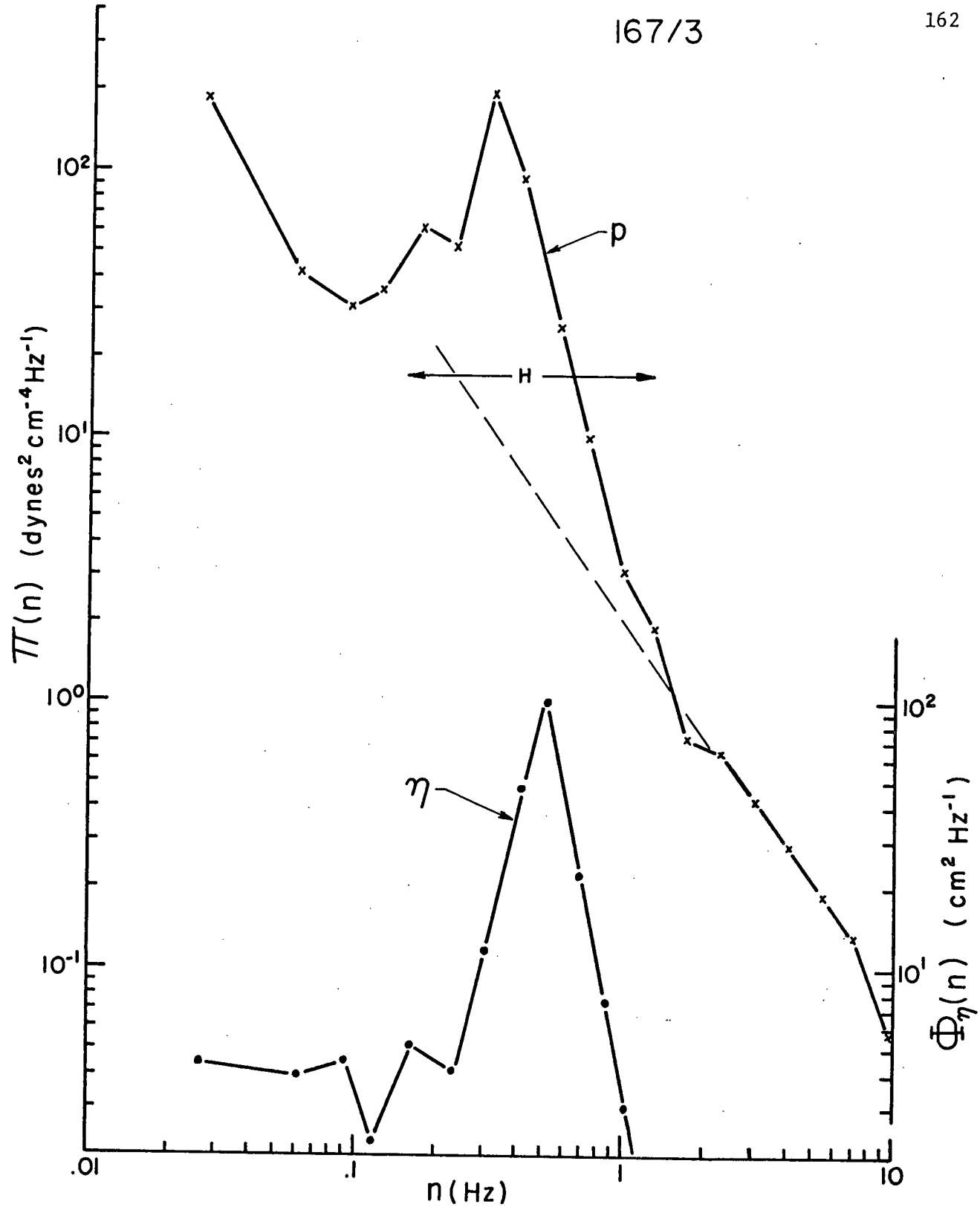

Figure 61. Pressure and wave spectra for Run 167/3

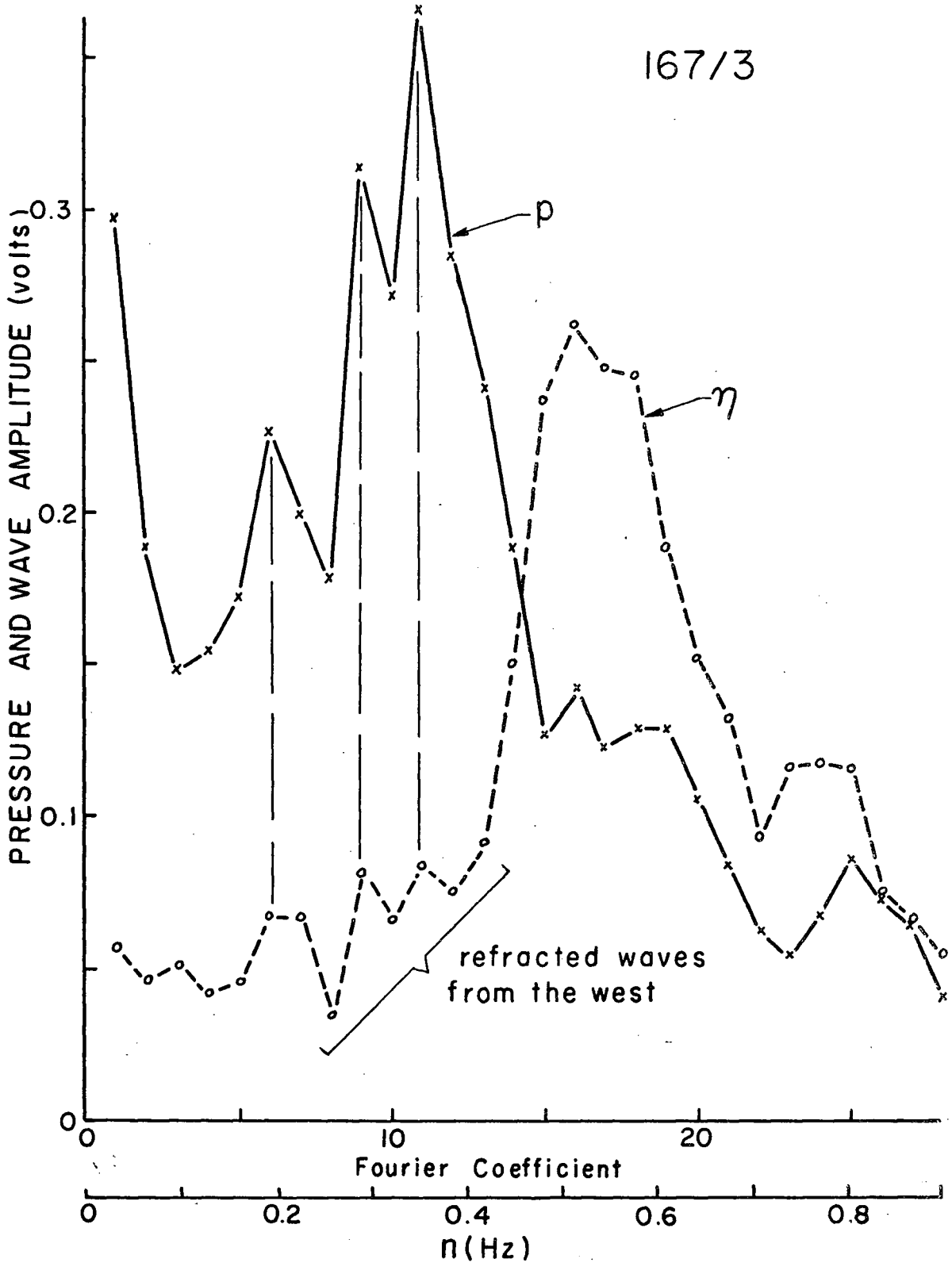

Figure 62. Amplitude of the Fourier coefficients for pressure and waves of Run 167/3

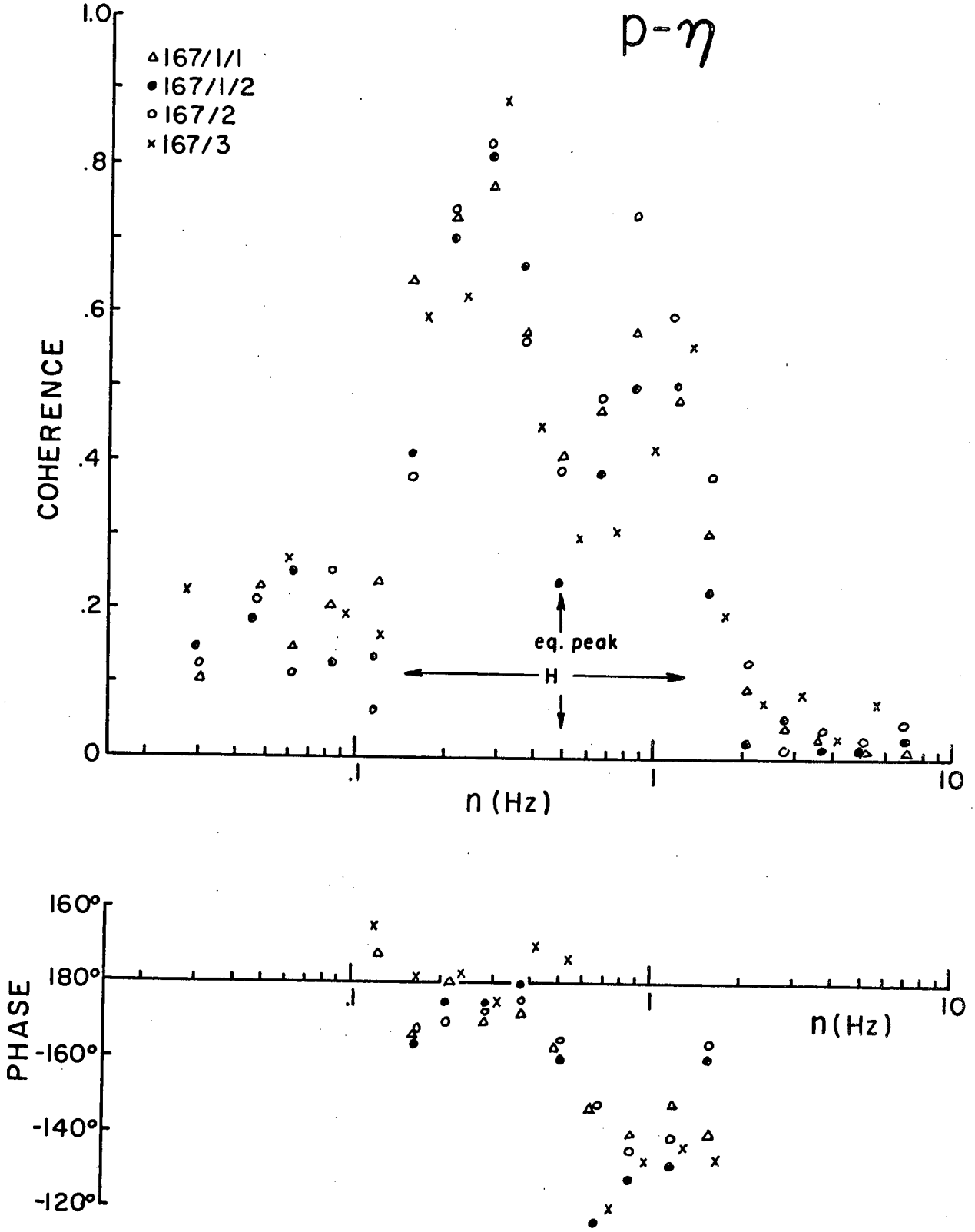

Figure 63. Coherence and phase between the pressure and waves: Data Group B. p-η phase positive means p leads η.

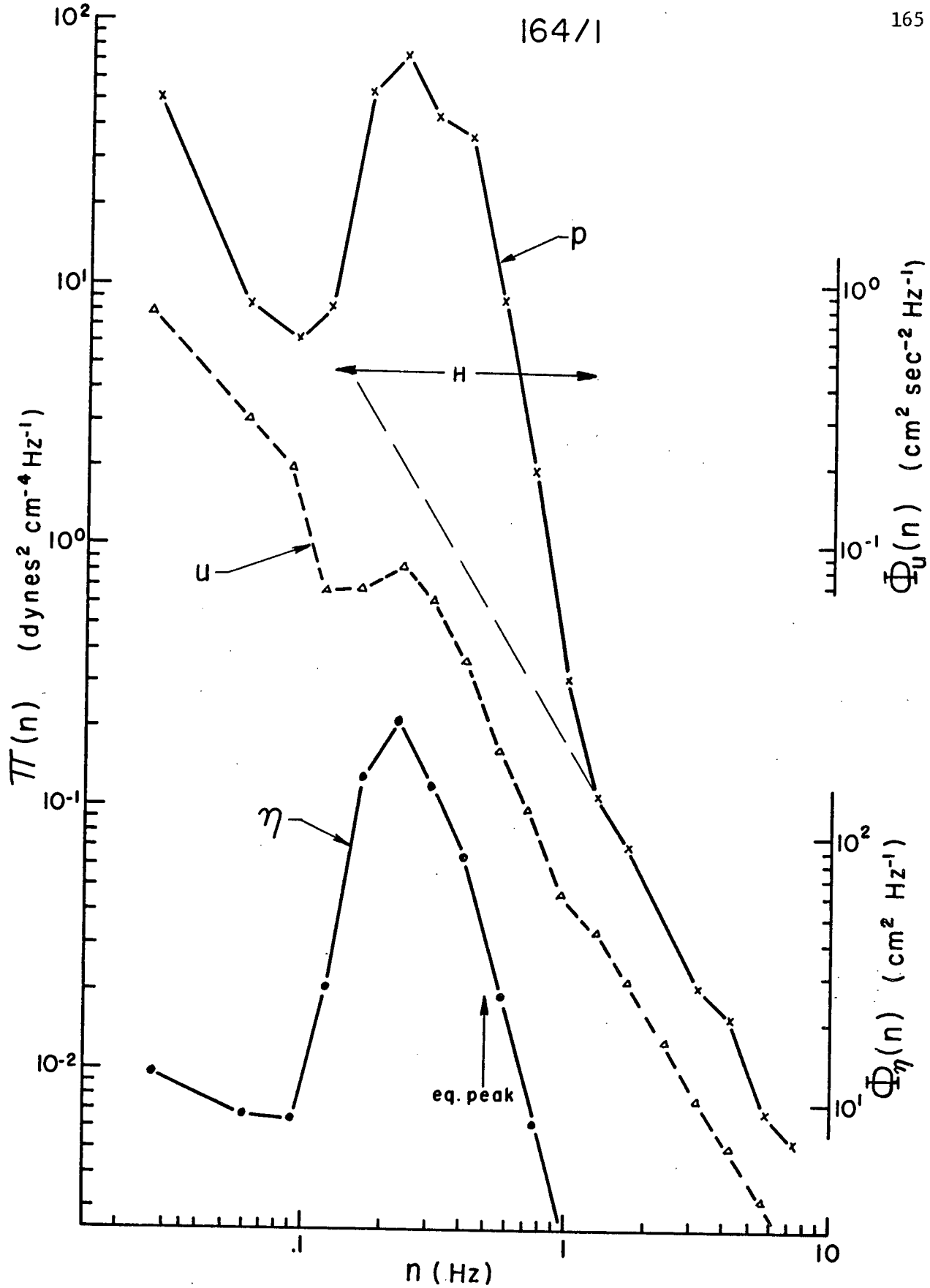

Figure 64. Pressure, u velocity and wave spectra for Run 164/1

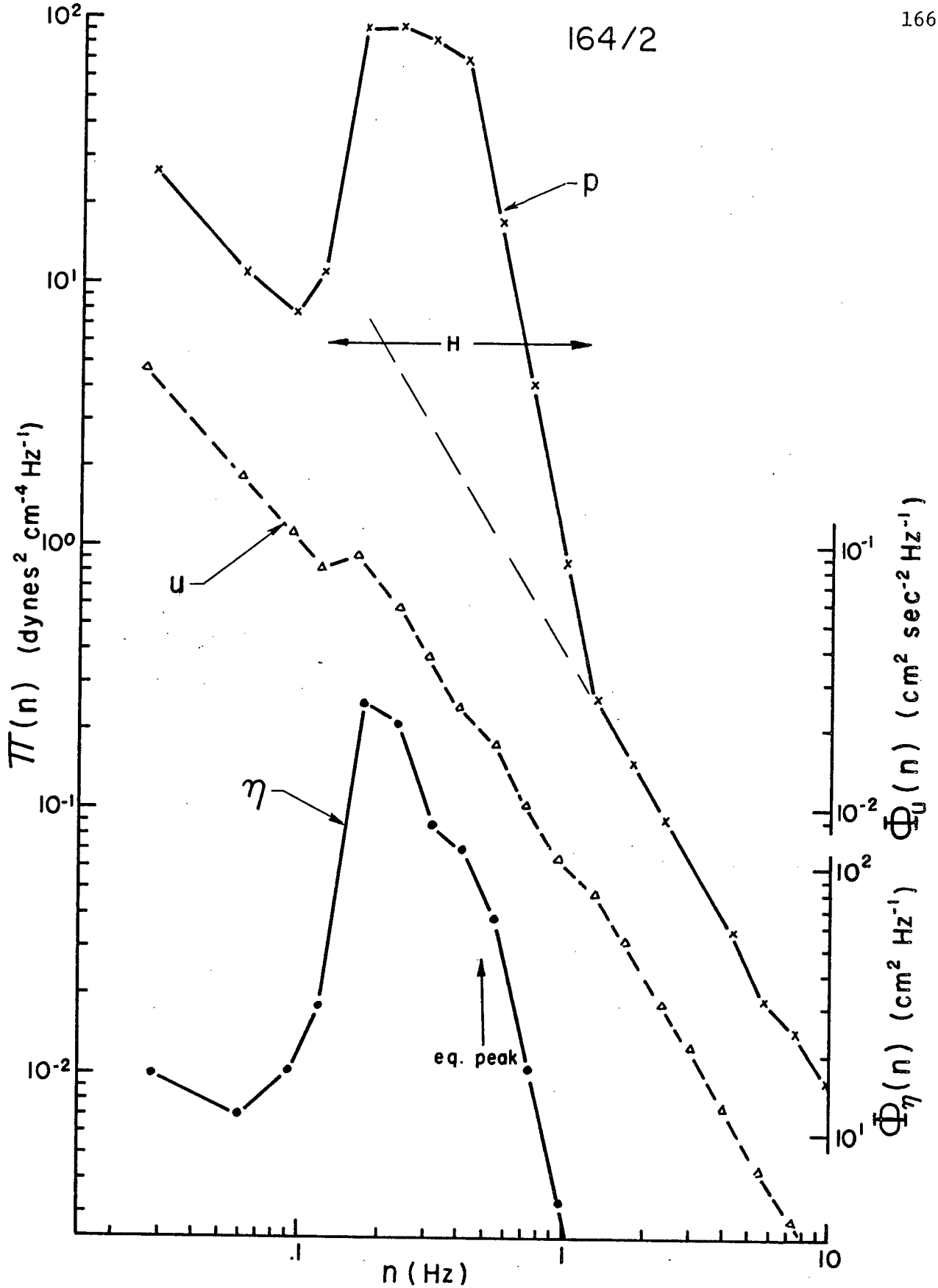

Figure 65. Pressure, u velocity and wave spectra for Run 164/2

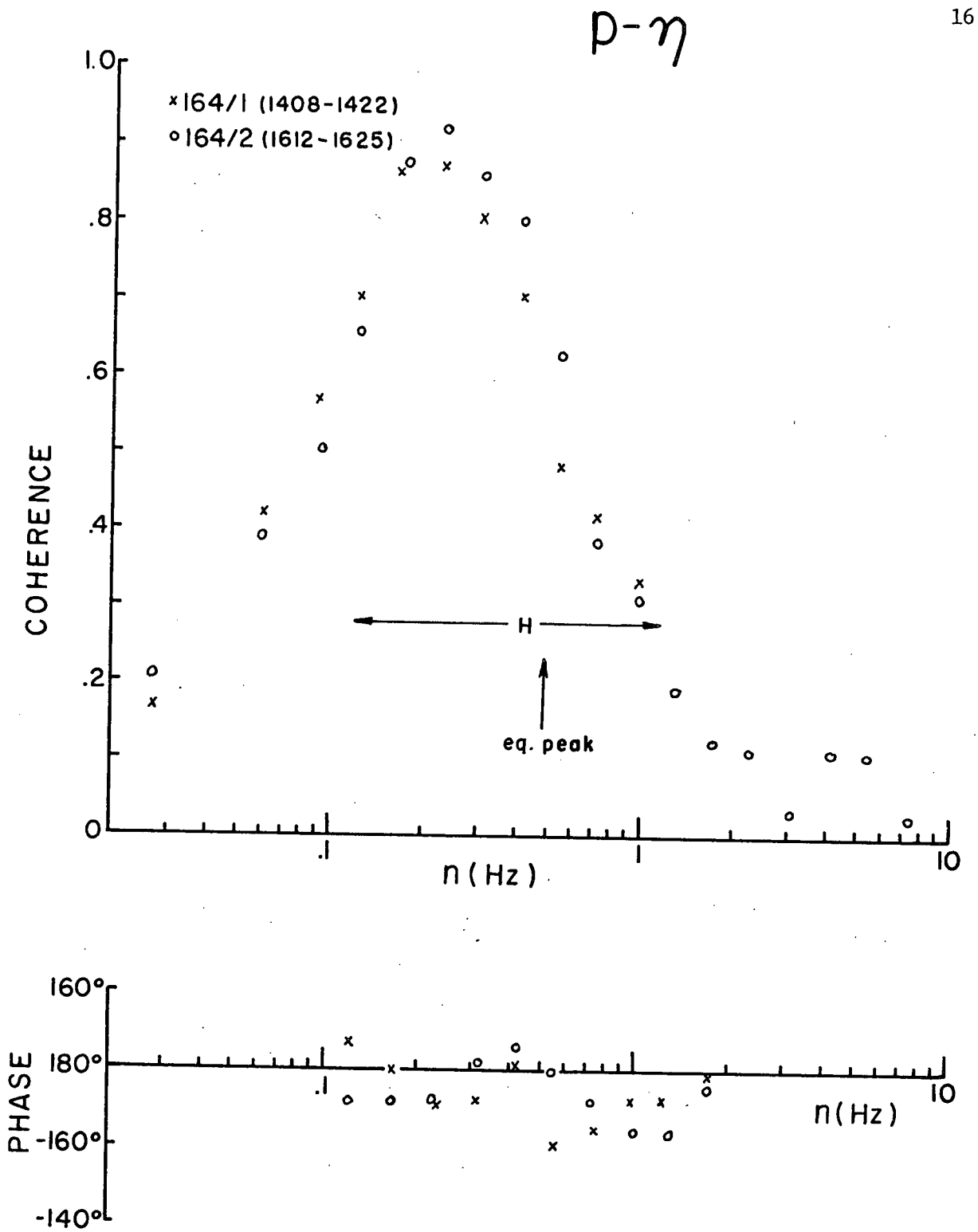

Figure 66. Coherence and phase between the pressure and the waves: Data Group C. p-η phase positive means p leads η

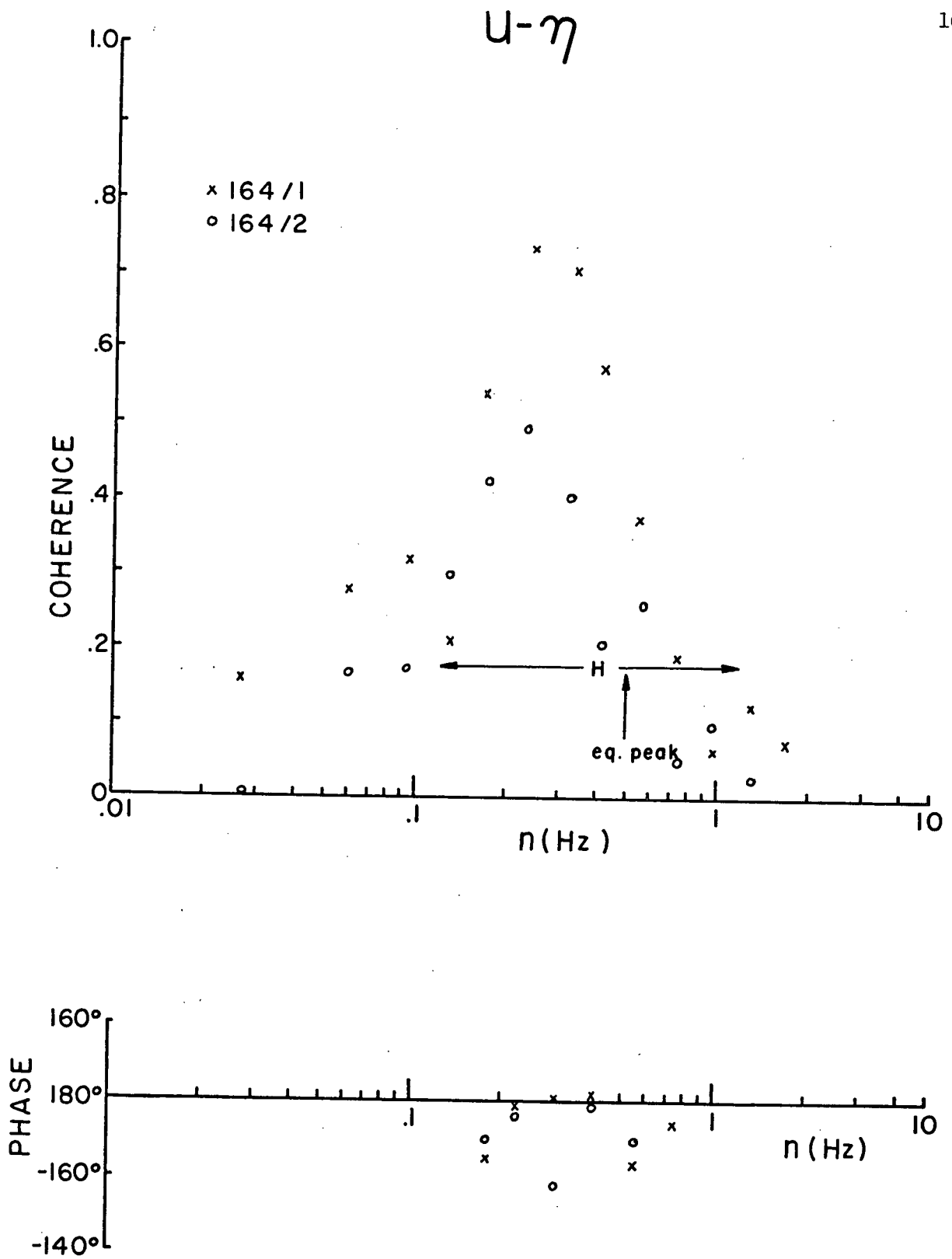

Figure 67. Coherence and phase between the u velocity and the waves: Data Group C. u-η phase positive means u leads η.

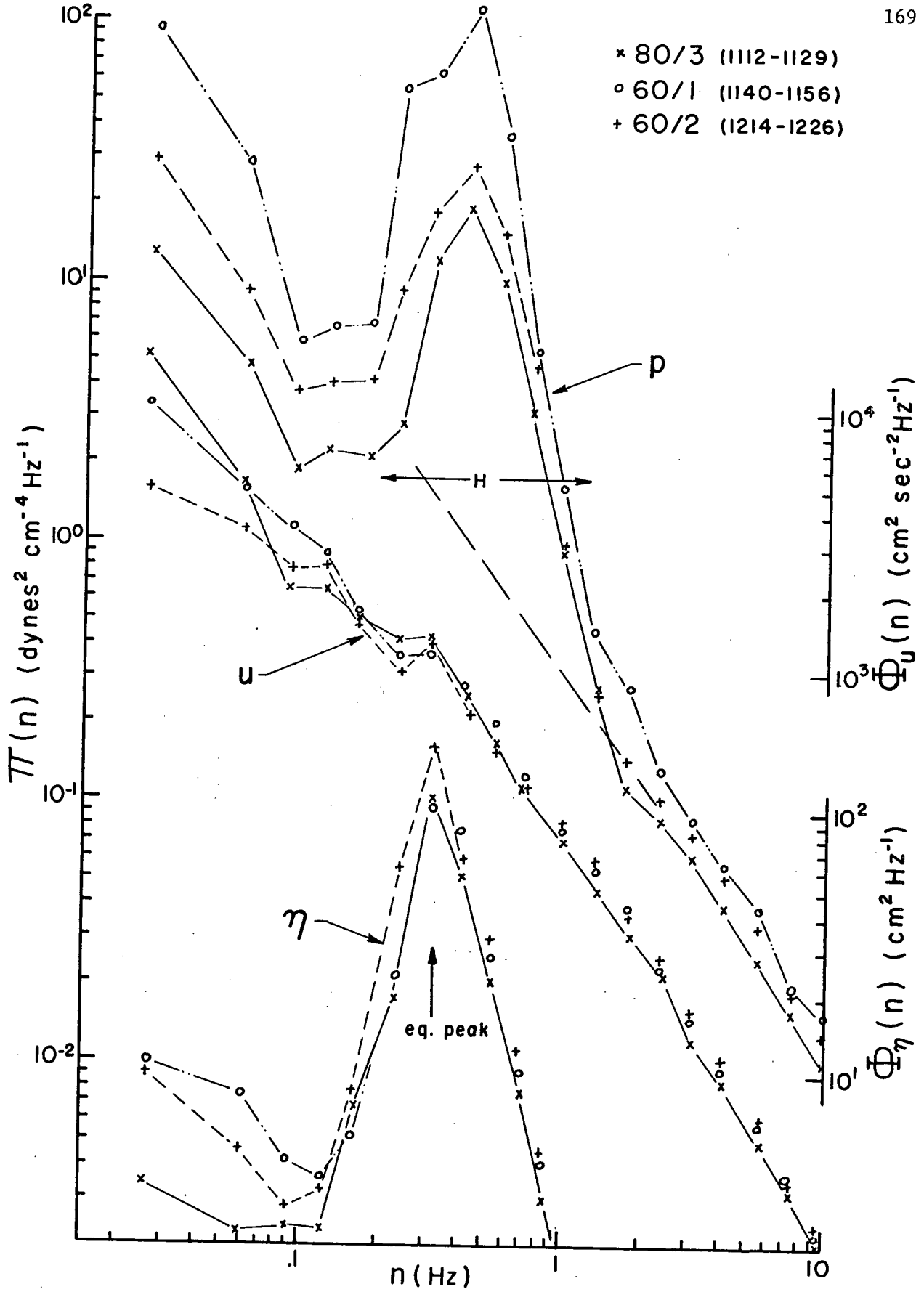

Figure 68. Pressure, u velocity and wave spectra for Data Group D

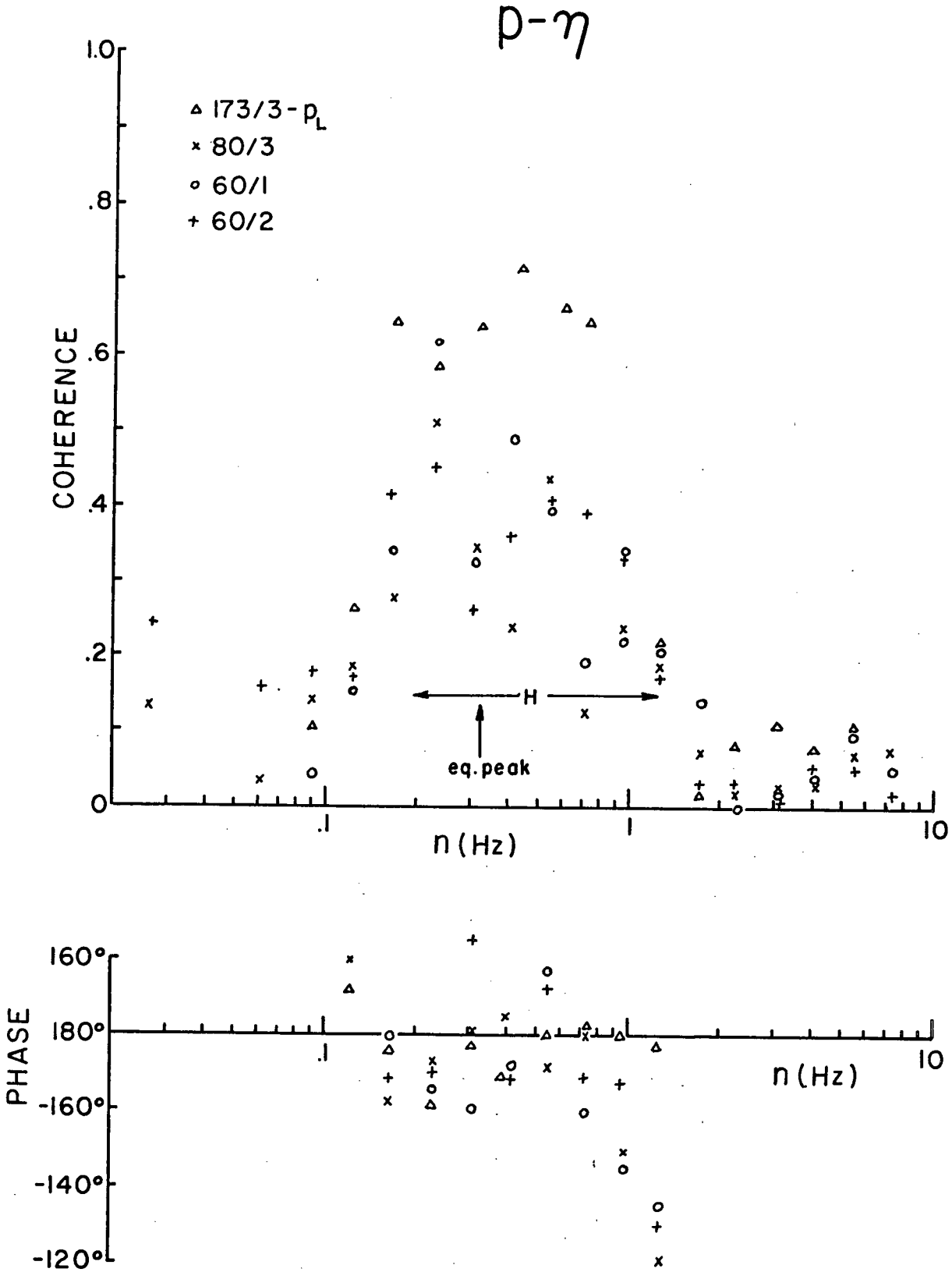

Figure 69. Coherence and phase between the pressure and the waves: Data Group D. p-η phase positive means p leads η

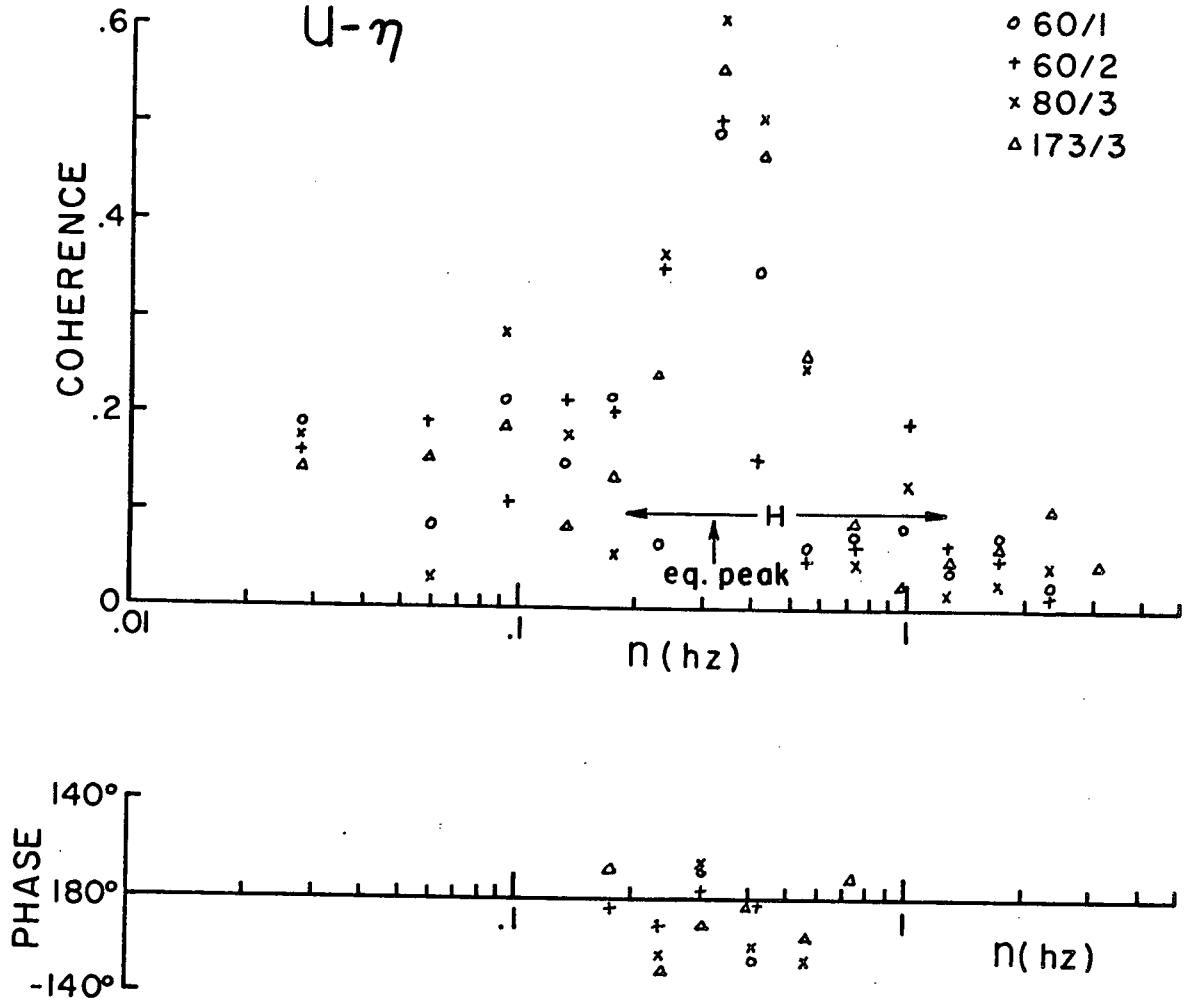

Figure 70. Coherence and phase between the u velocity and the waves: Data Group D. u-η phase positive means u leads η.

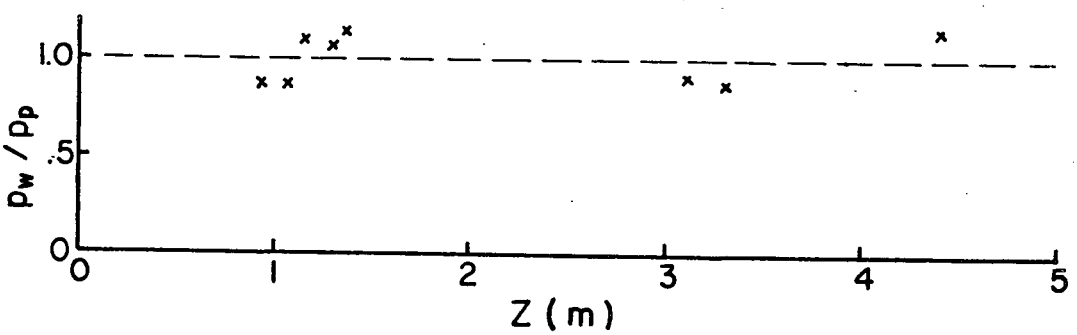

Figure 71. Ratio of measured to predicted pressure amplitude for propagating waves with no wind.

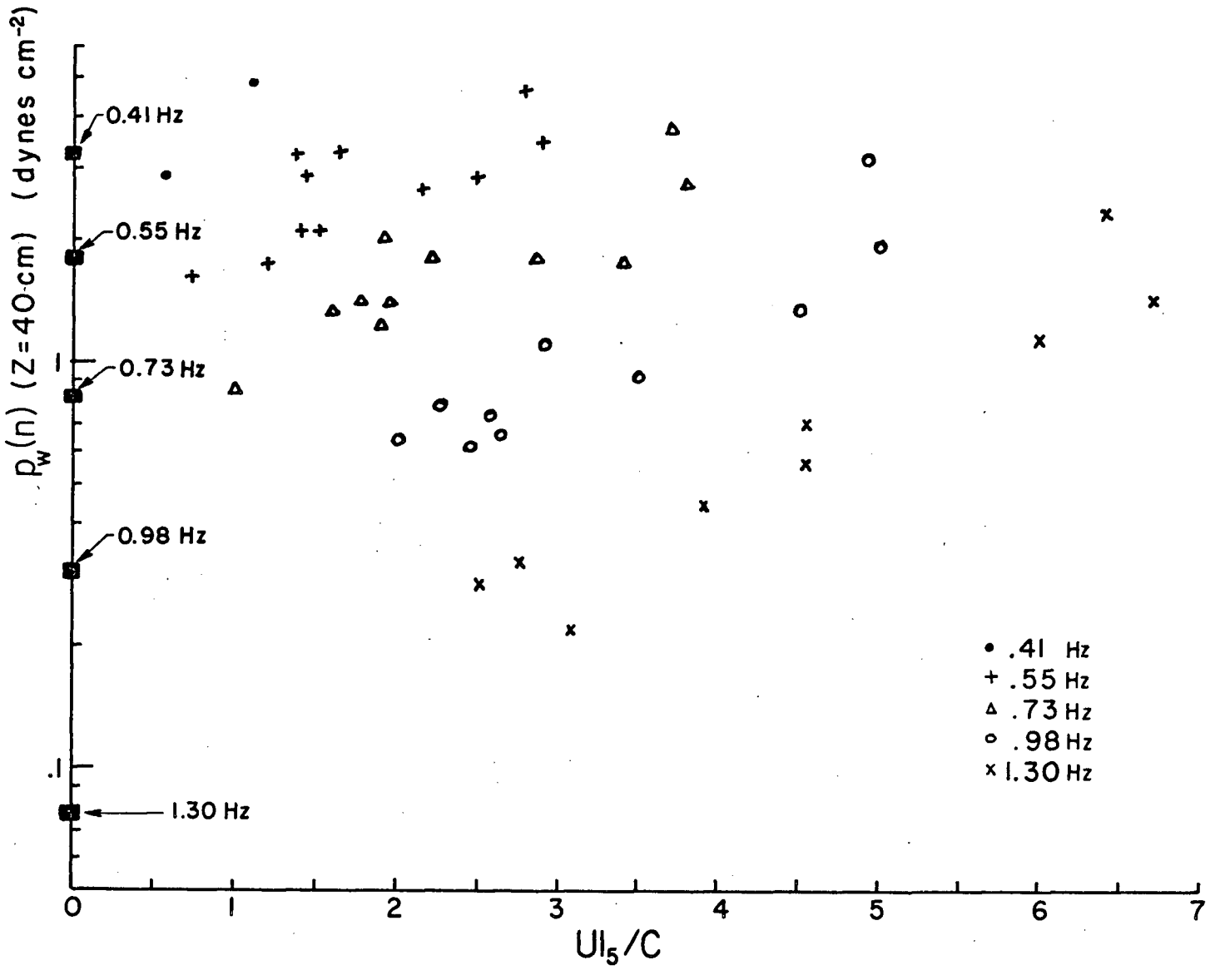

Figure 72. $p_w(n)$ at various constant frequencies for different values of $U|_5/C$. The values plotted at $U|_5/C = 0$ are for the potential flow solution.

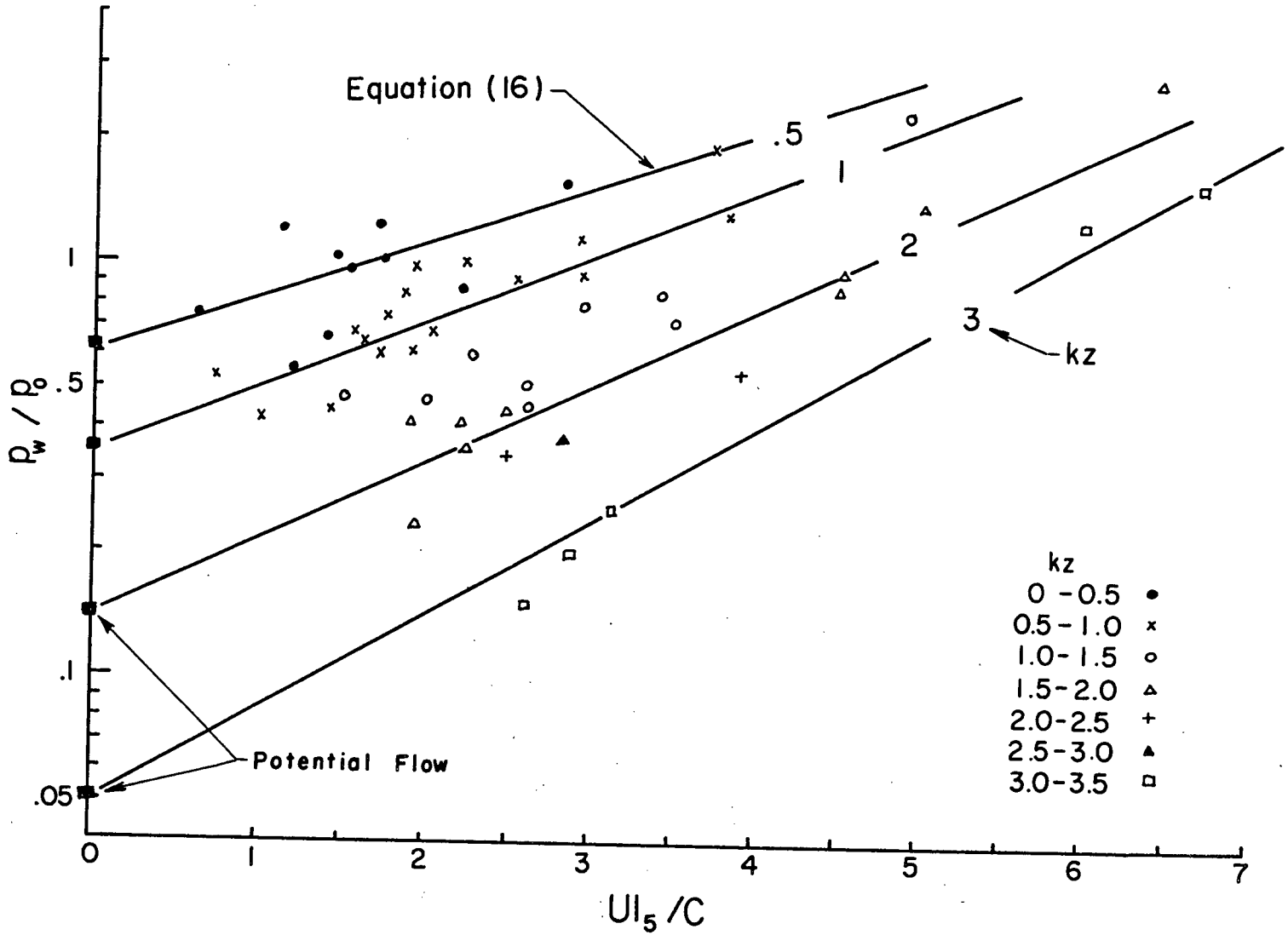

Figure 73. P_w/P_o for different $U|_5/C$ at constant kz

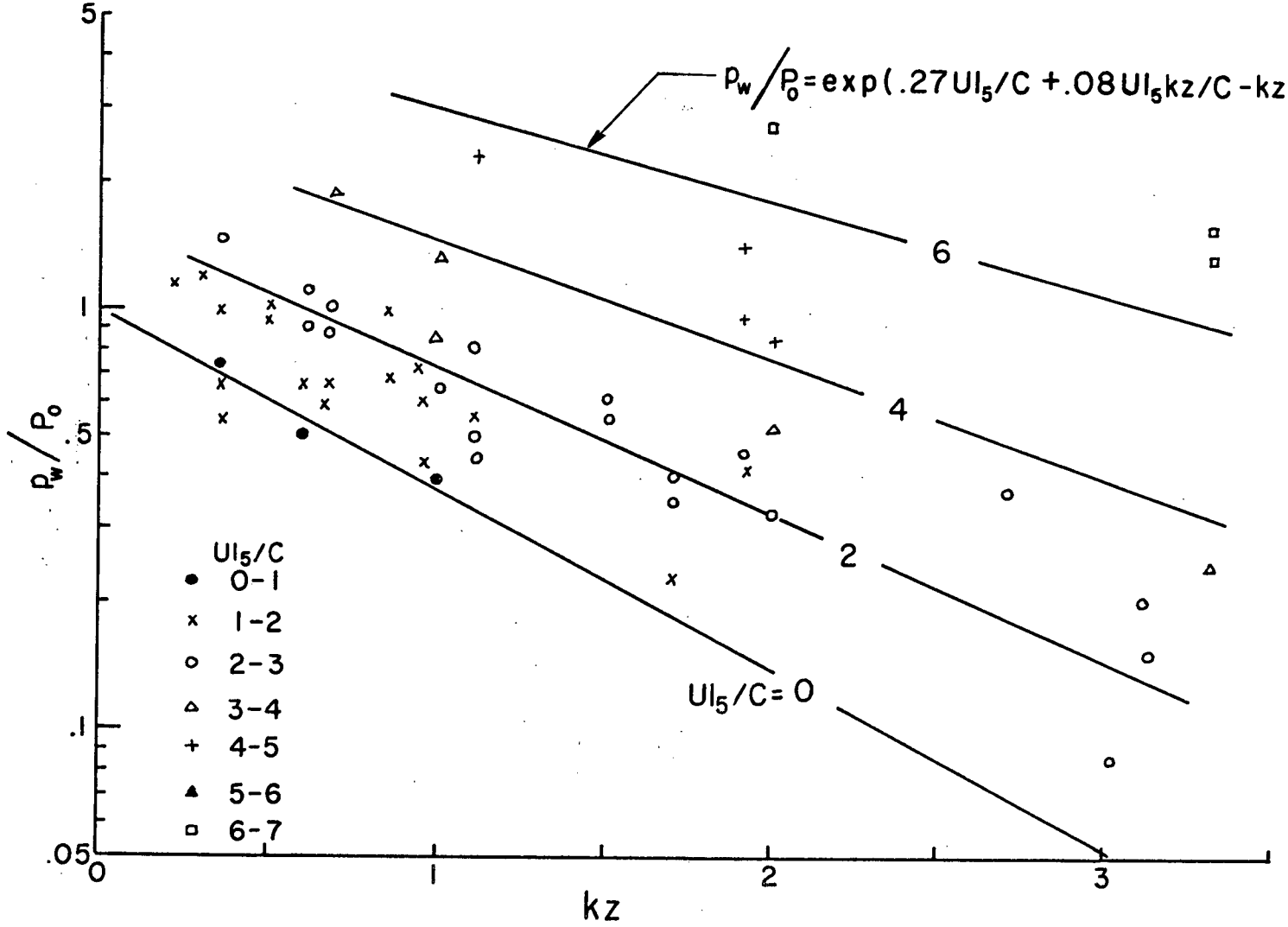

Figure 74. p_w/p_o for different kz at constant $U|_5/C$

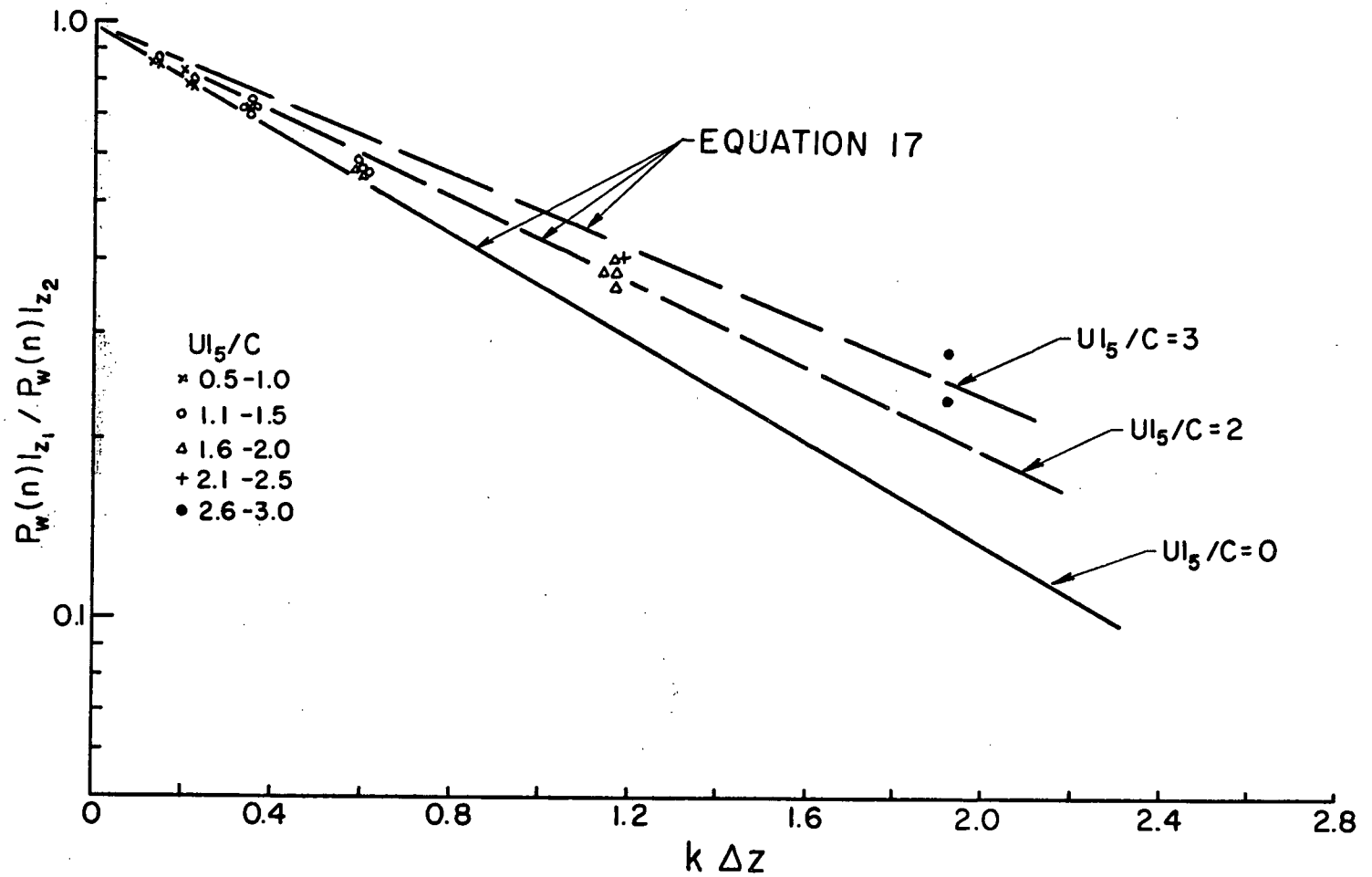

Figure 75. Ratio of the p_w measured at two levels. The lines drawn are the predicted ratio from equation 17.

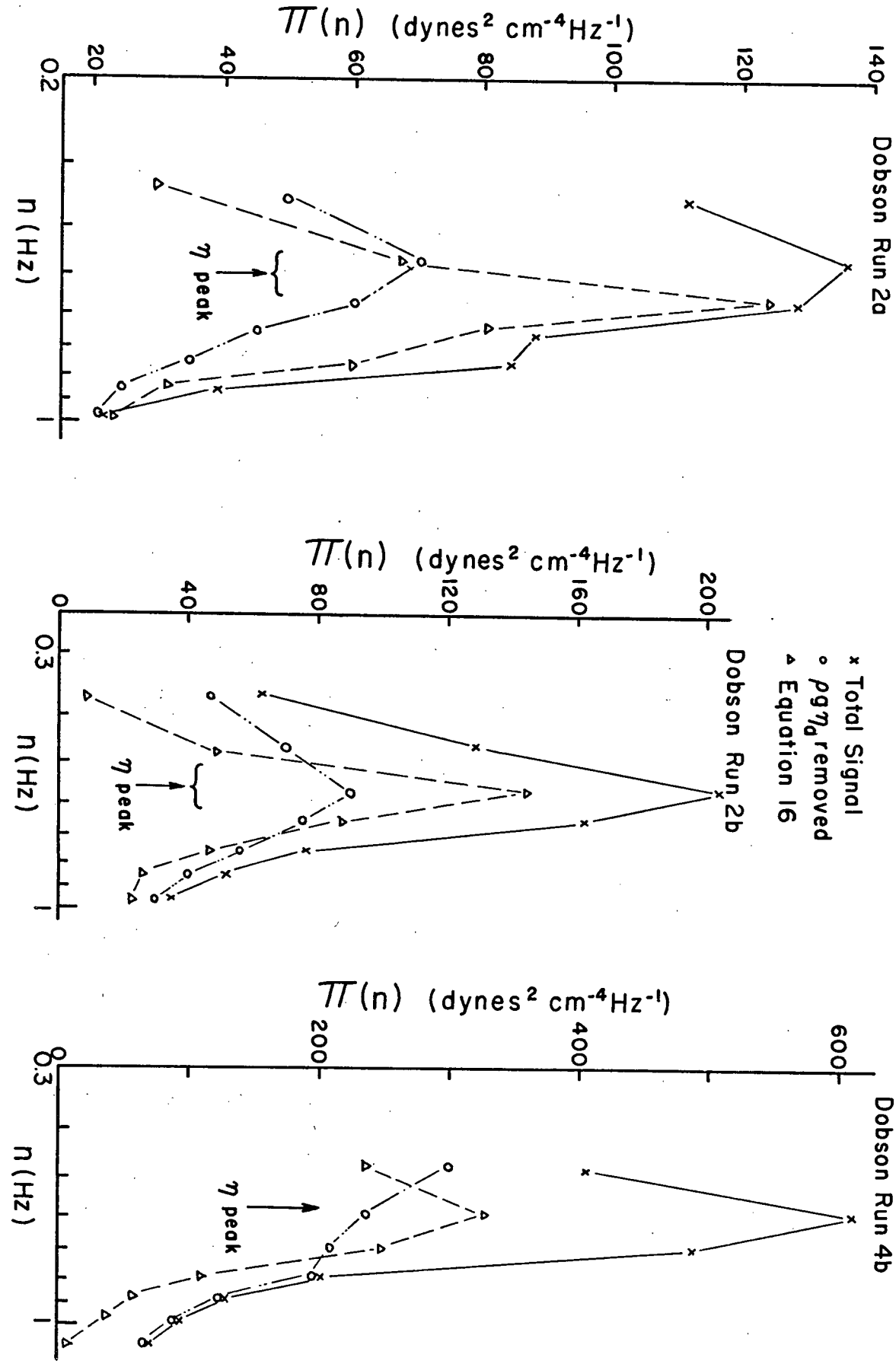

Figure 76. Comparison between equation 16 and Dobson (1969)

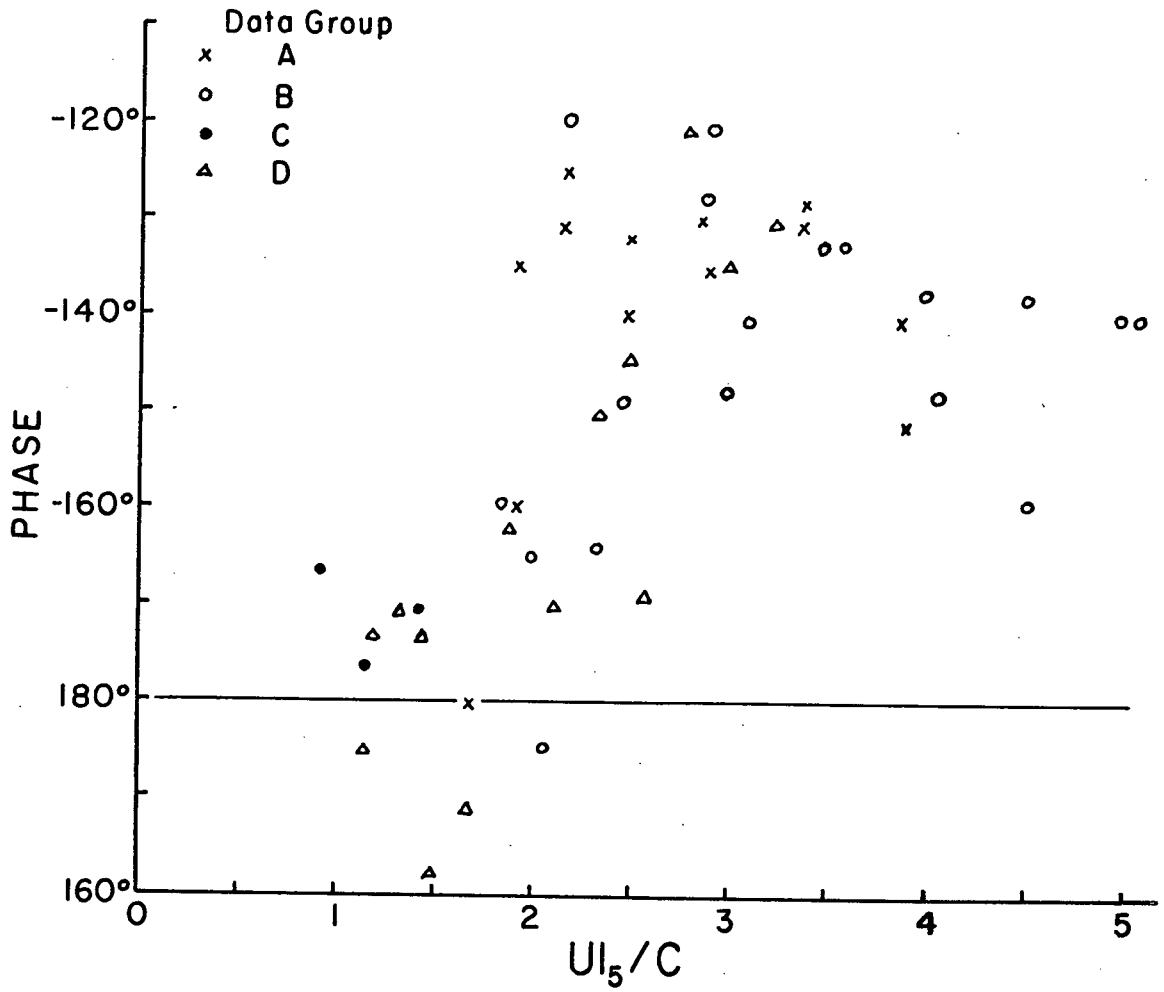

Figure 77. Phase shift between pressure and waves at various values of $U|_5/C$
Phase positive means pressure leads waves.

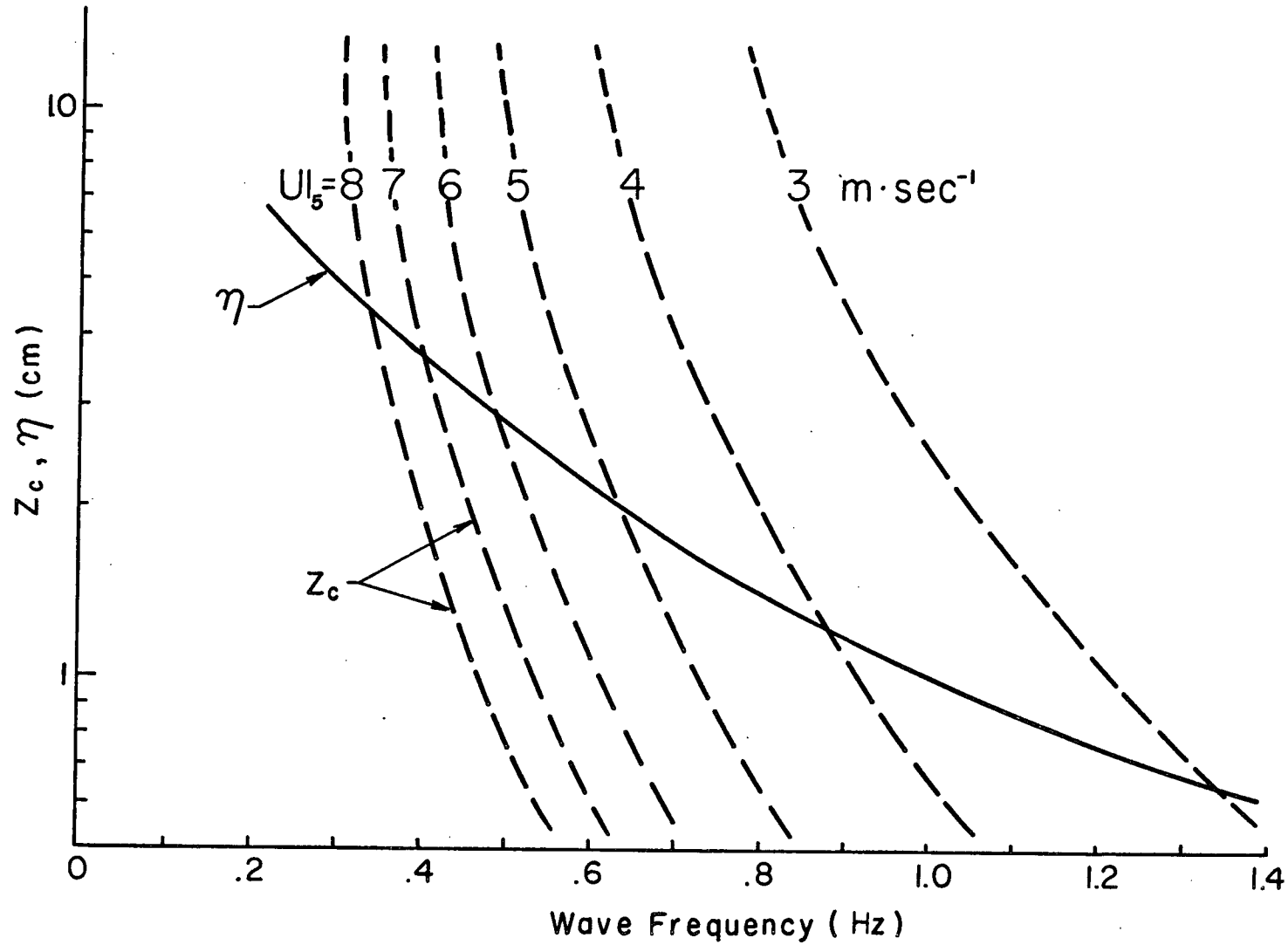

Figure 78. Wave amplitude and critical height for constant $U|_5$ plotted for different wave frequencies

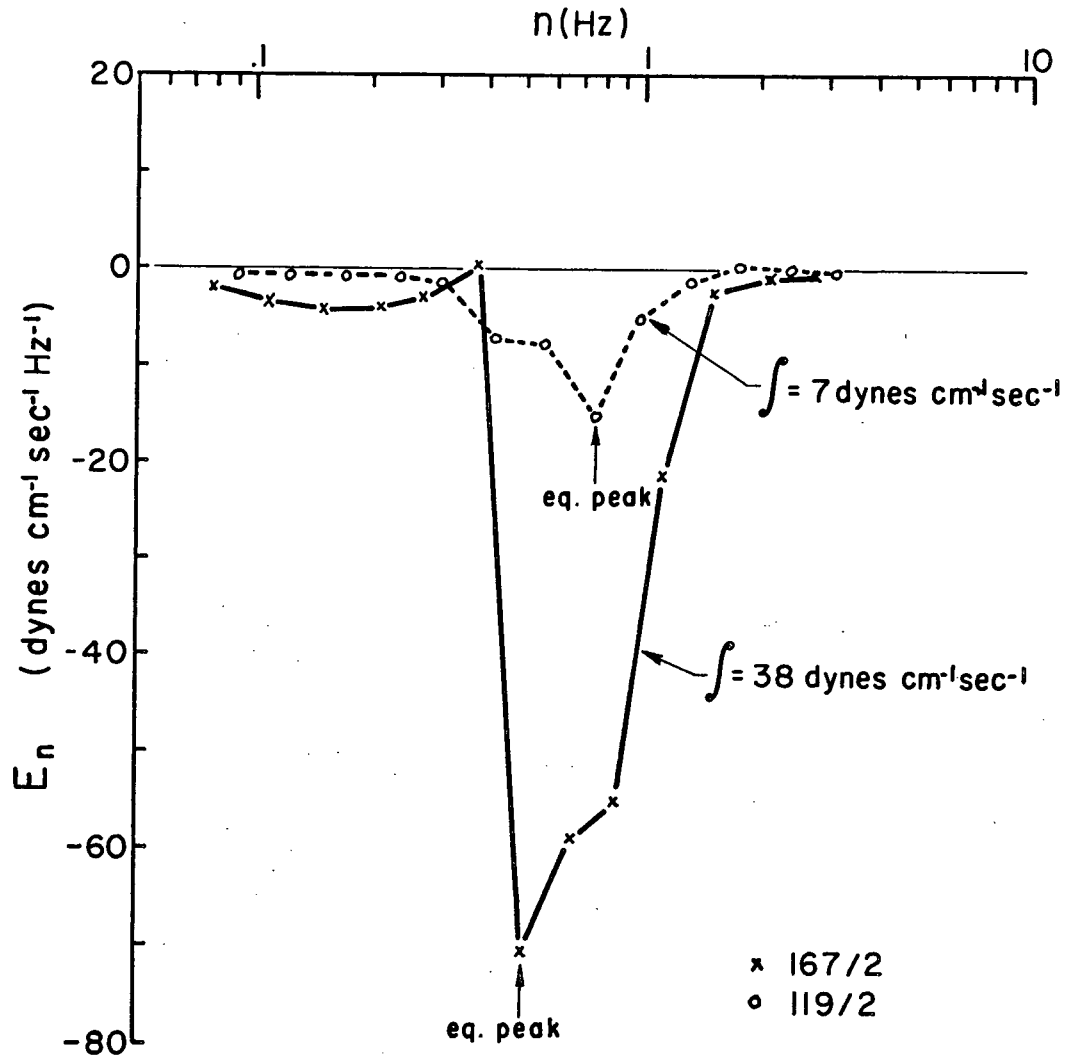

Figure 79. Spectral distribution of the approximate energy flux to the waves, calculated using the pressure measured above the wave crests.

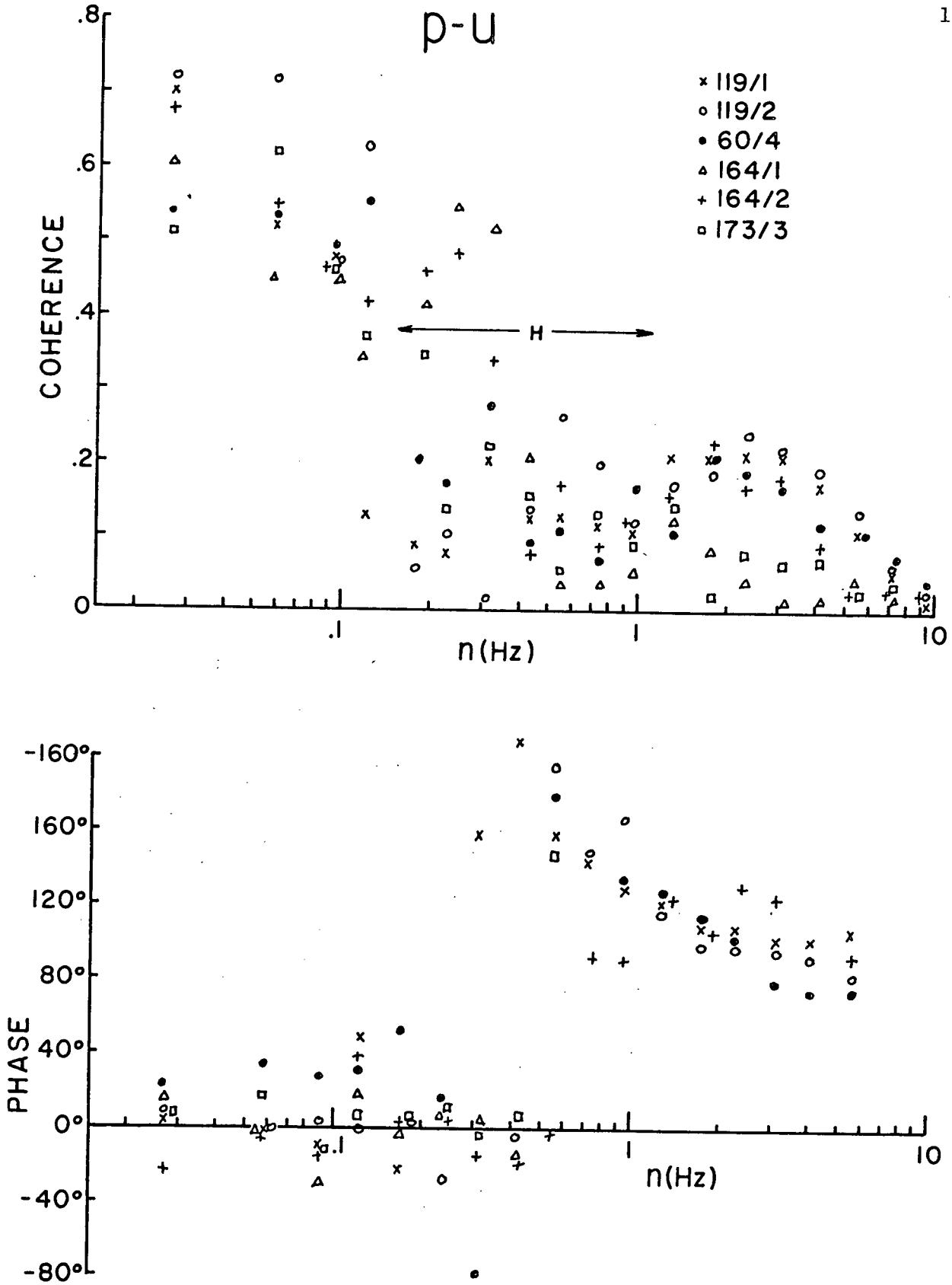

Figure 80. Coherence and phase between pressure and u velocity measured near waves. Phase positive means pressure leads velocity.

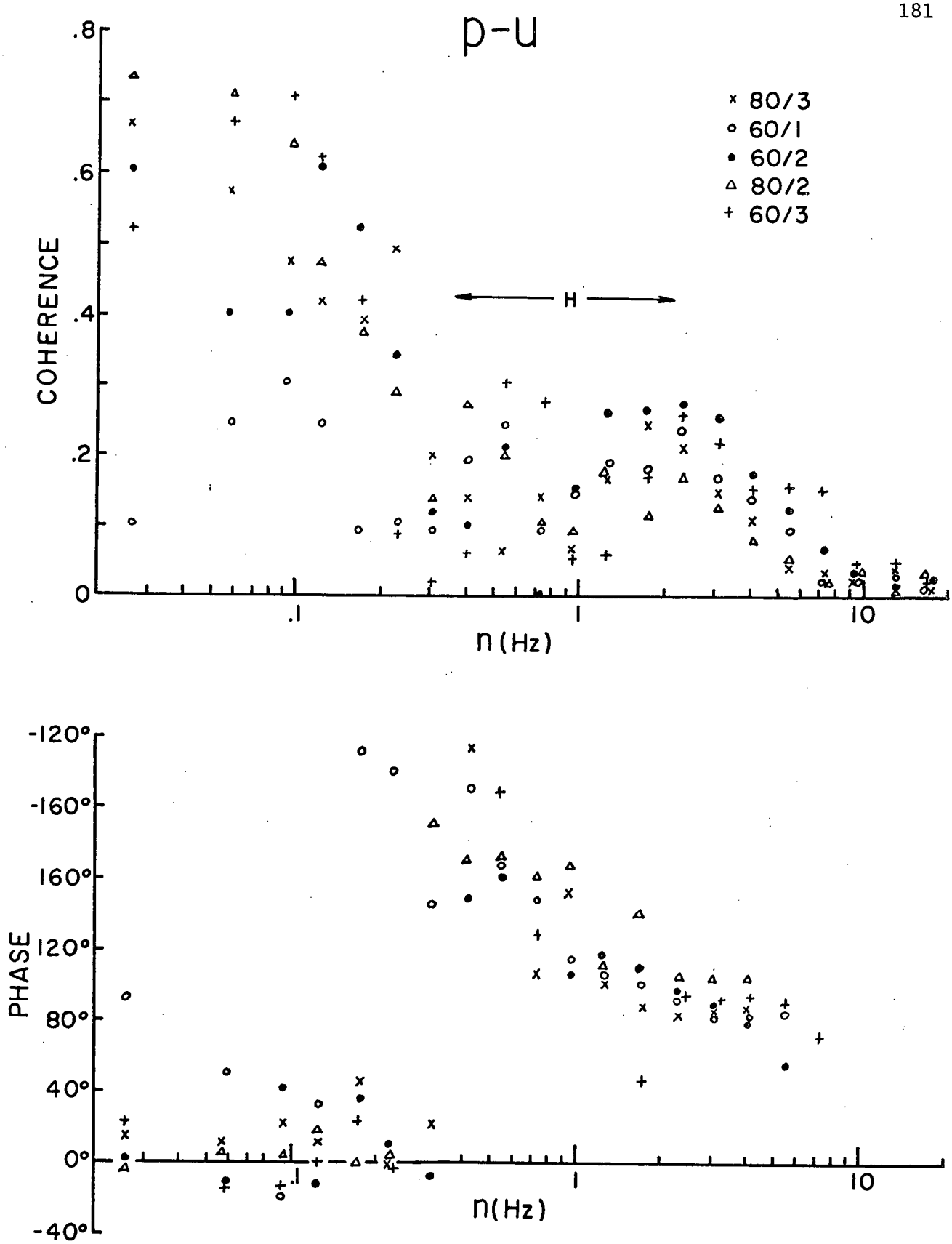

Figure 81. Coherence and phase between pressure and u velocity measured near waves. Phase positive means pressure leads velocity.

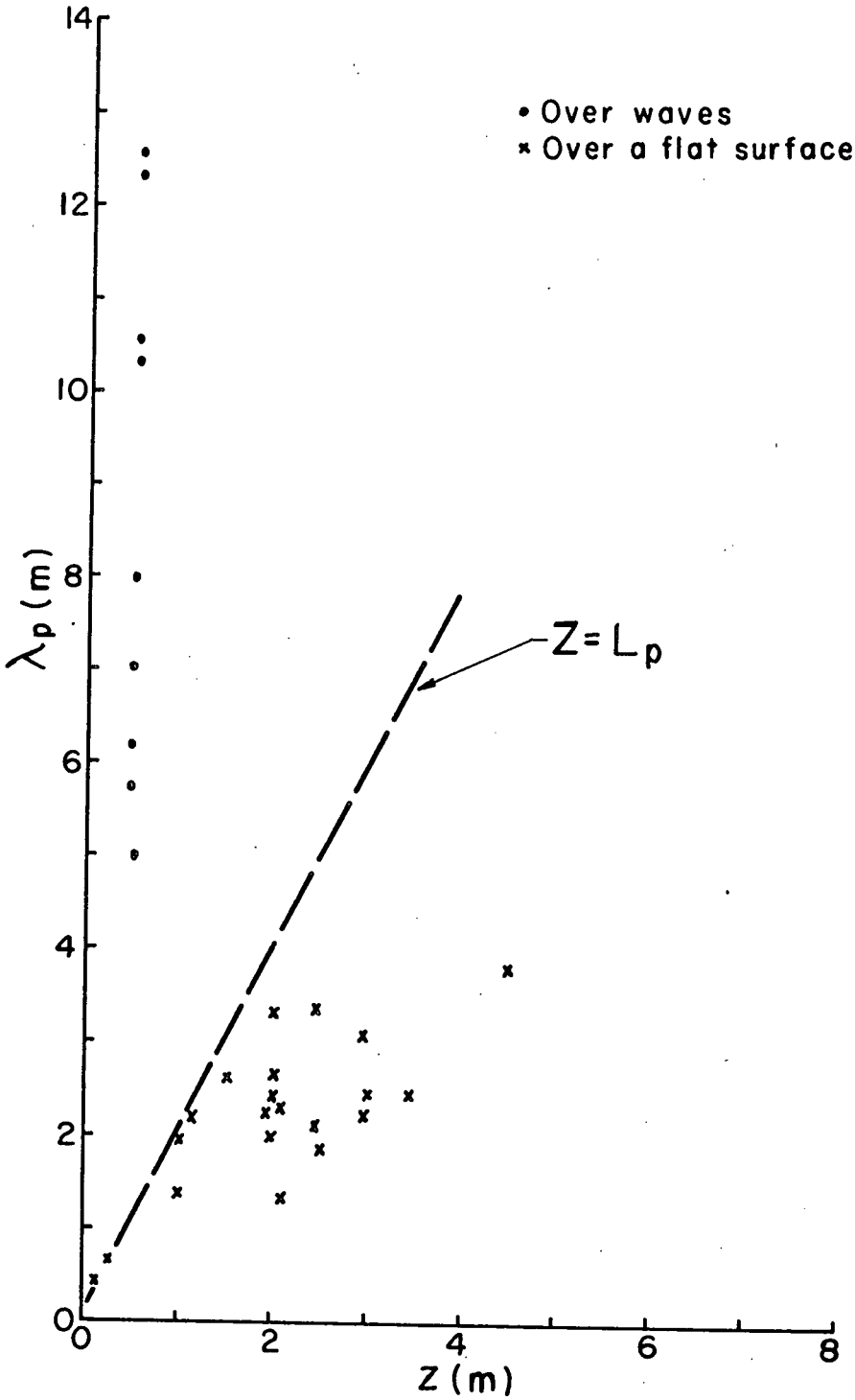

Figure 82. Wavelength associated with the p-u phase transition

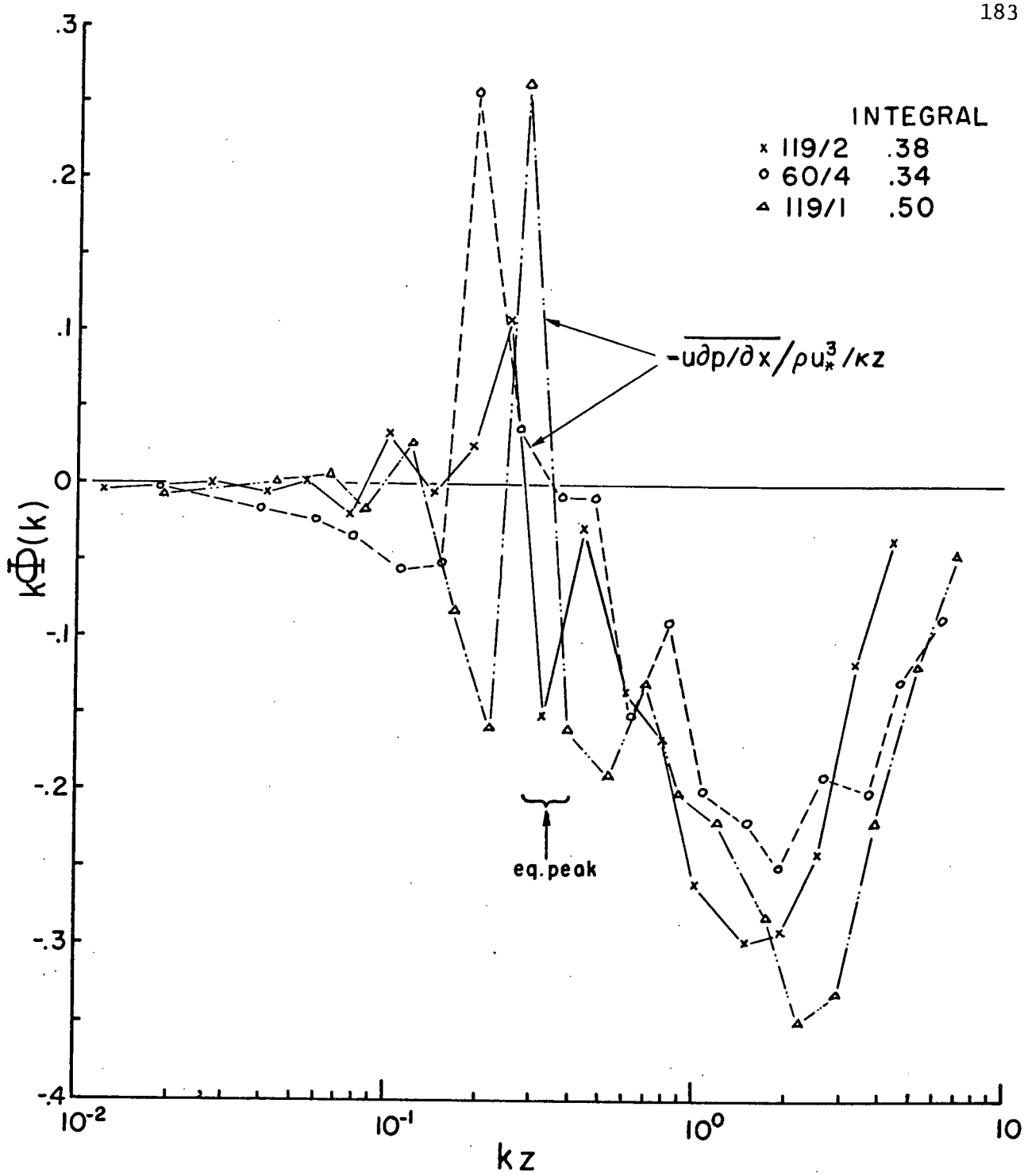

Figure 83. Nondimensional energy flux from the u velocity component, measured near waves.

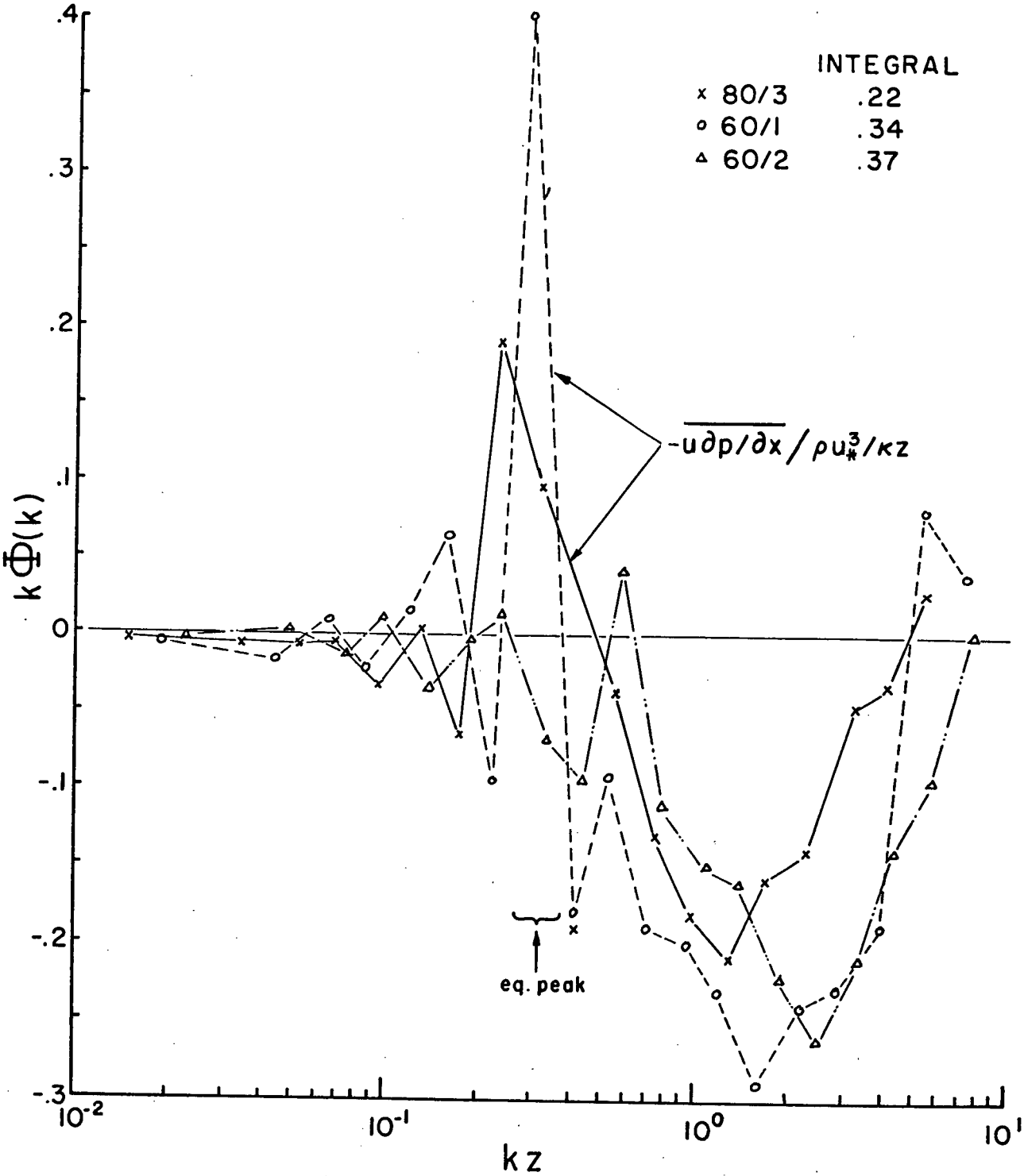

Figure 84. Nondimensional energy flux from the u velocity component, measured near waves.

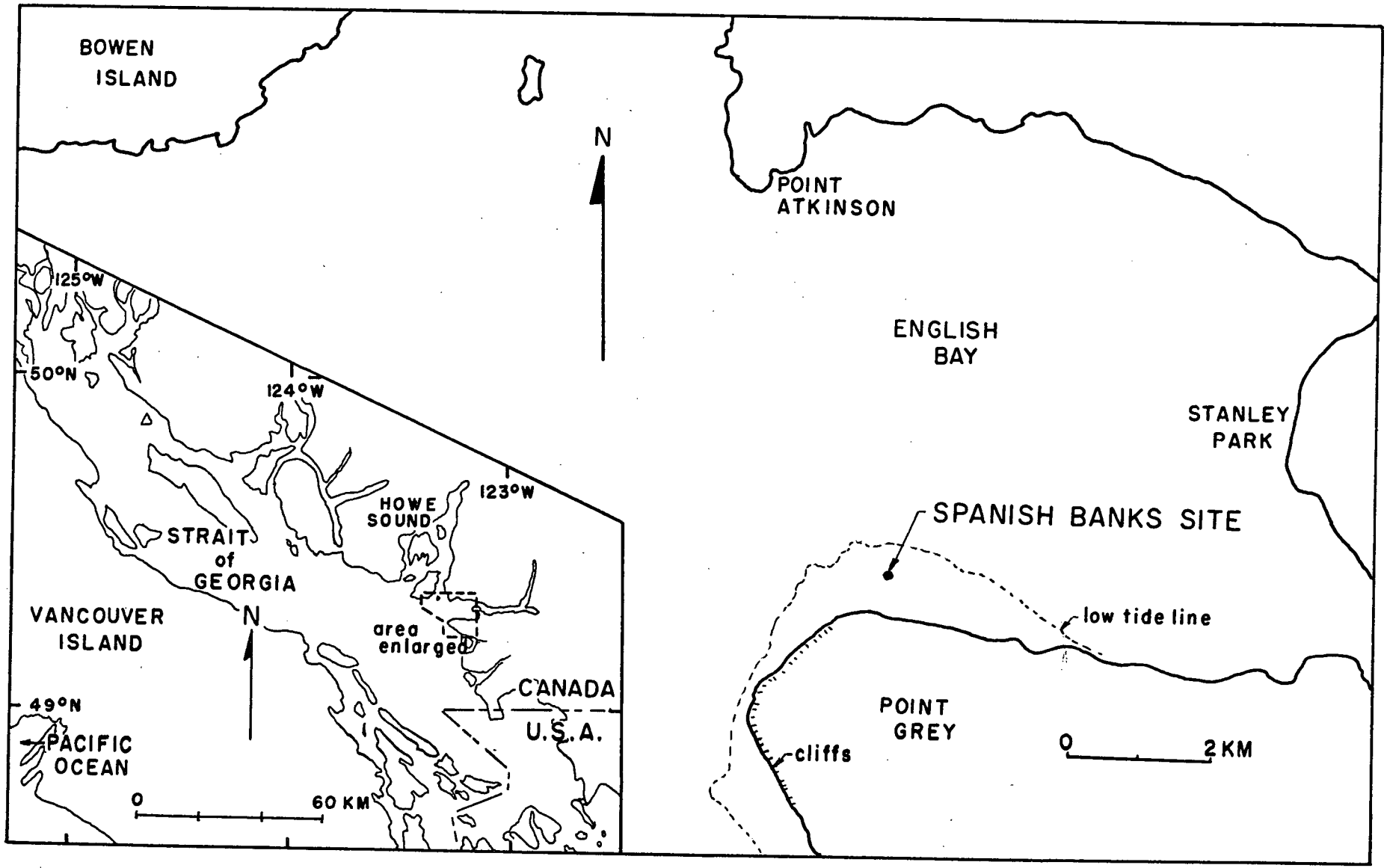

Figure 85. Map of the Spanish Banks site

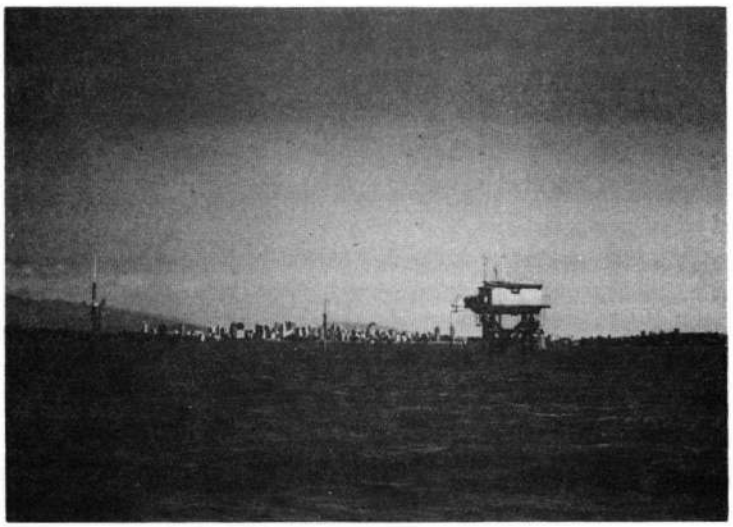

(a)

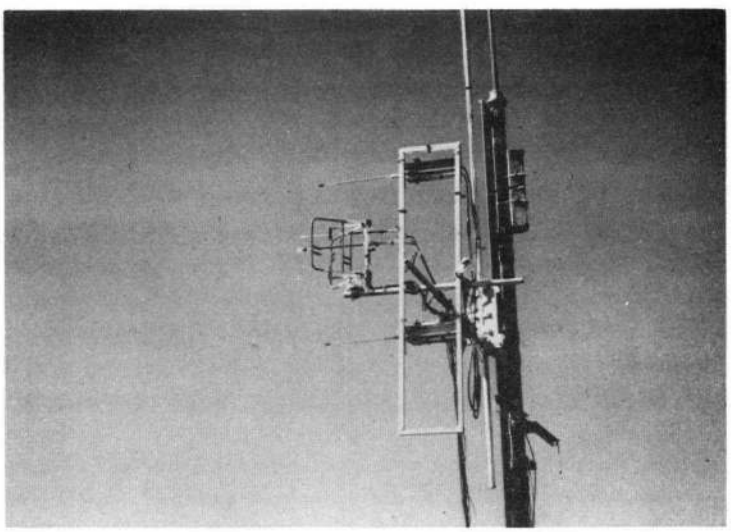

(b)

Figure 86. Platform and instrument masts at the Spanish Banks site
(a) platform and masts looking east
(b) instrumented mast

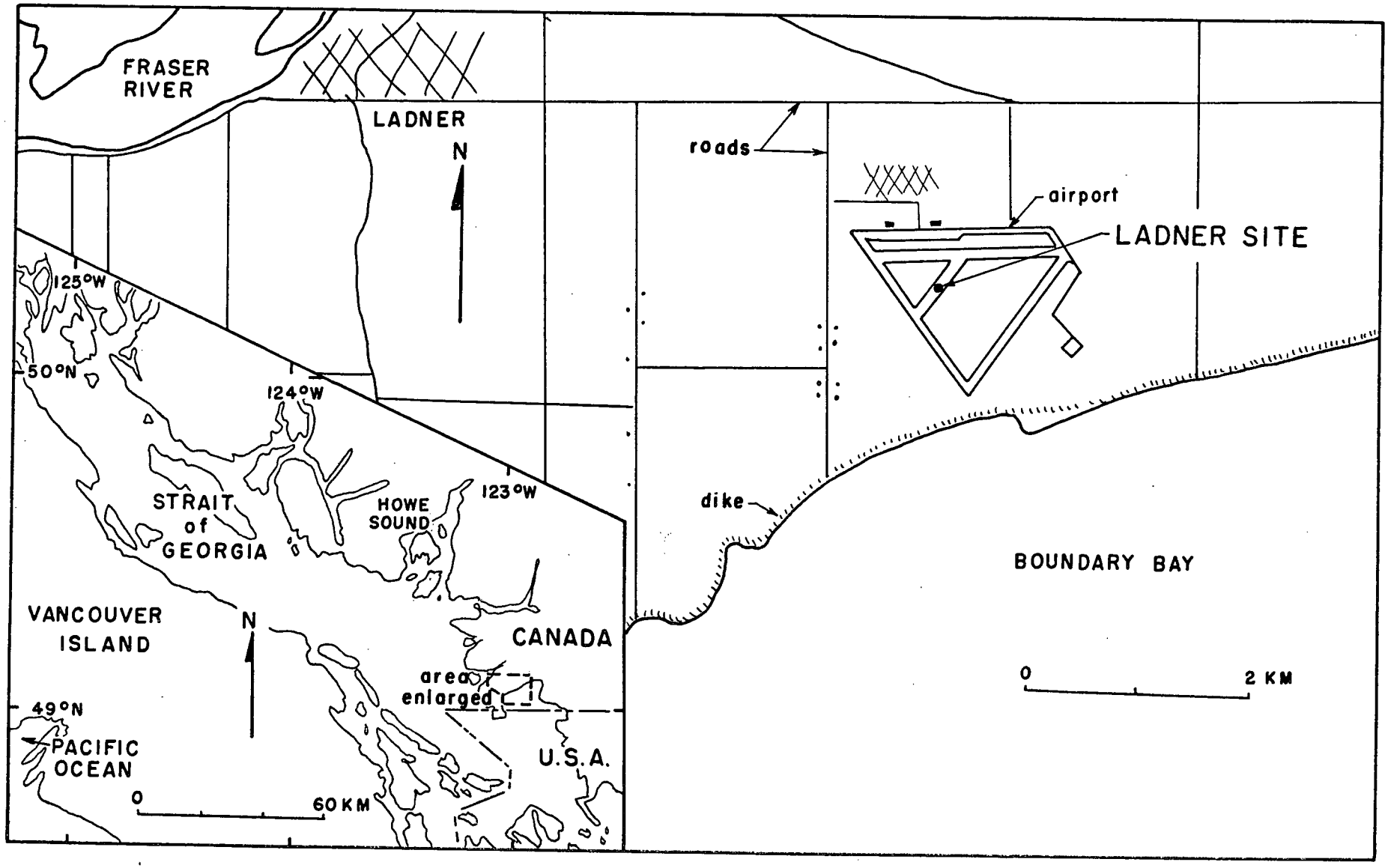

Figure 87. Map of the Ladner site

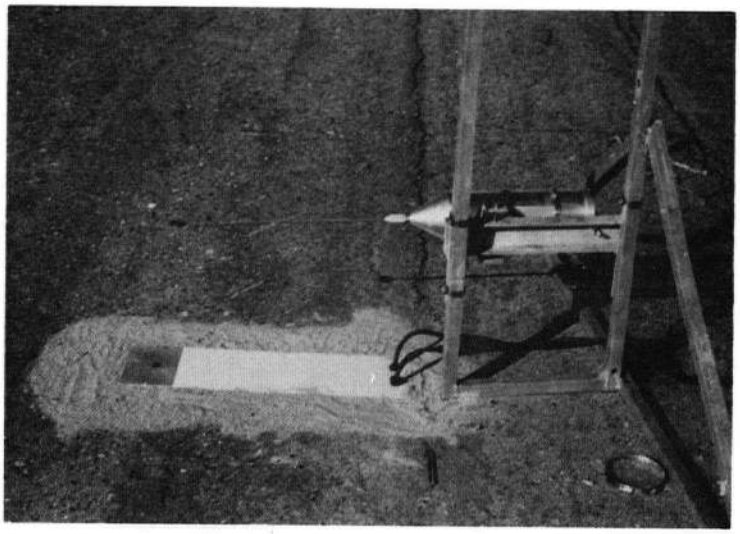

Figure 88. Box in position for surface pressure measurement (Ladner site)

Figure 89. Instruments set up at the Ladner site, looking NNE

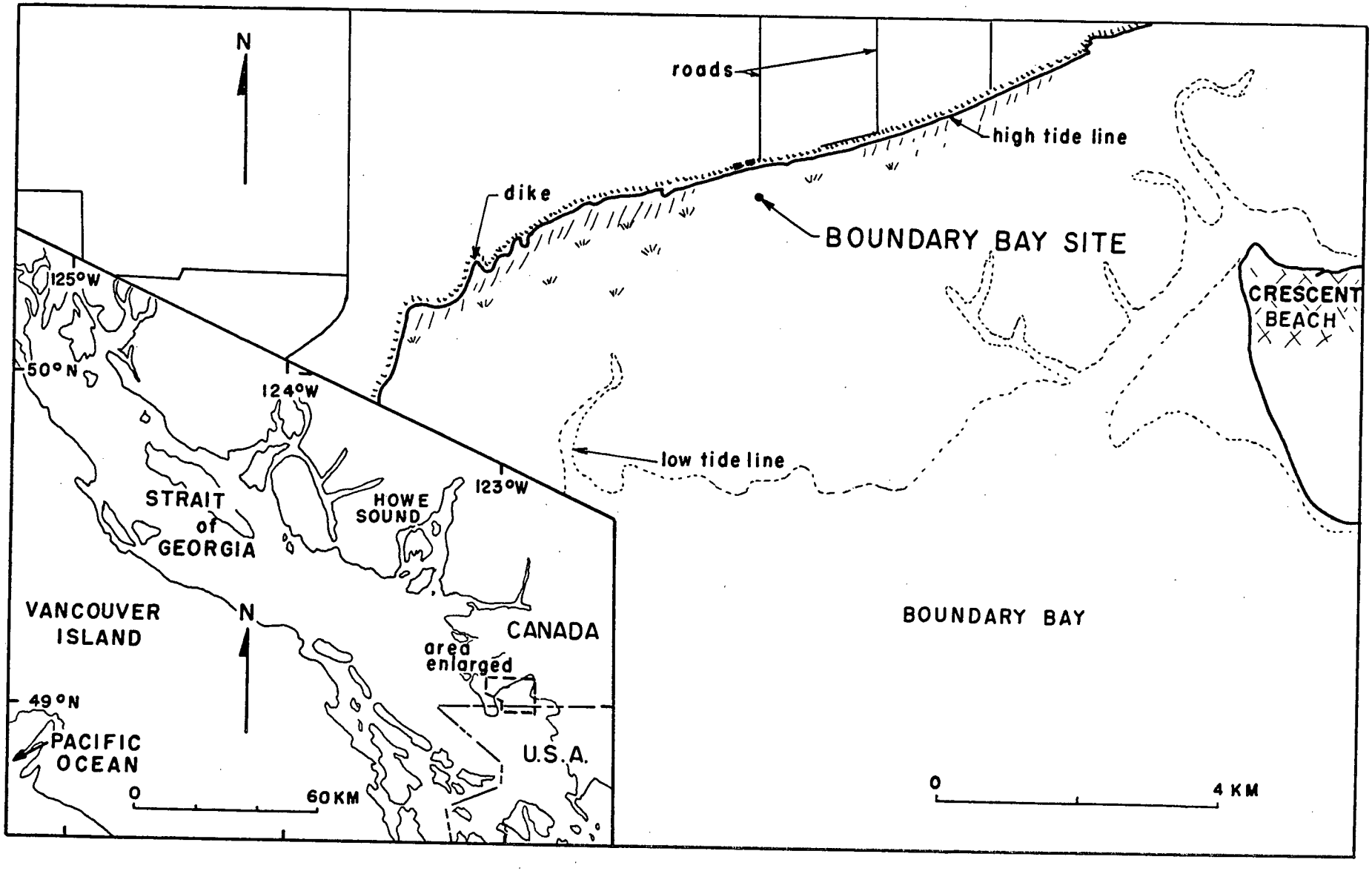

Figure 90. Map of the Boundary Bay site

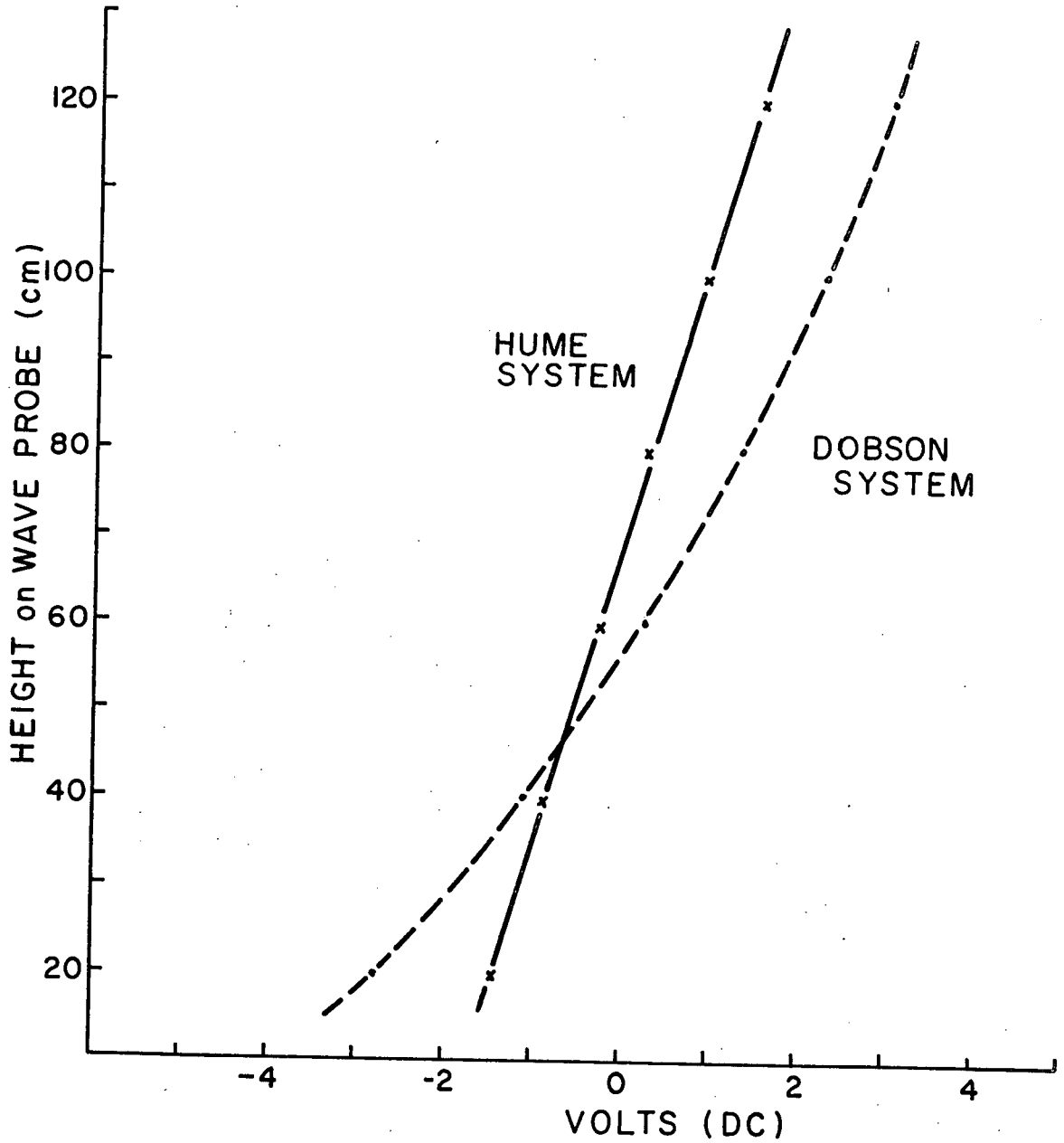

Figure 91. Typical wave probe calibrations

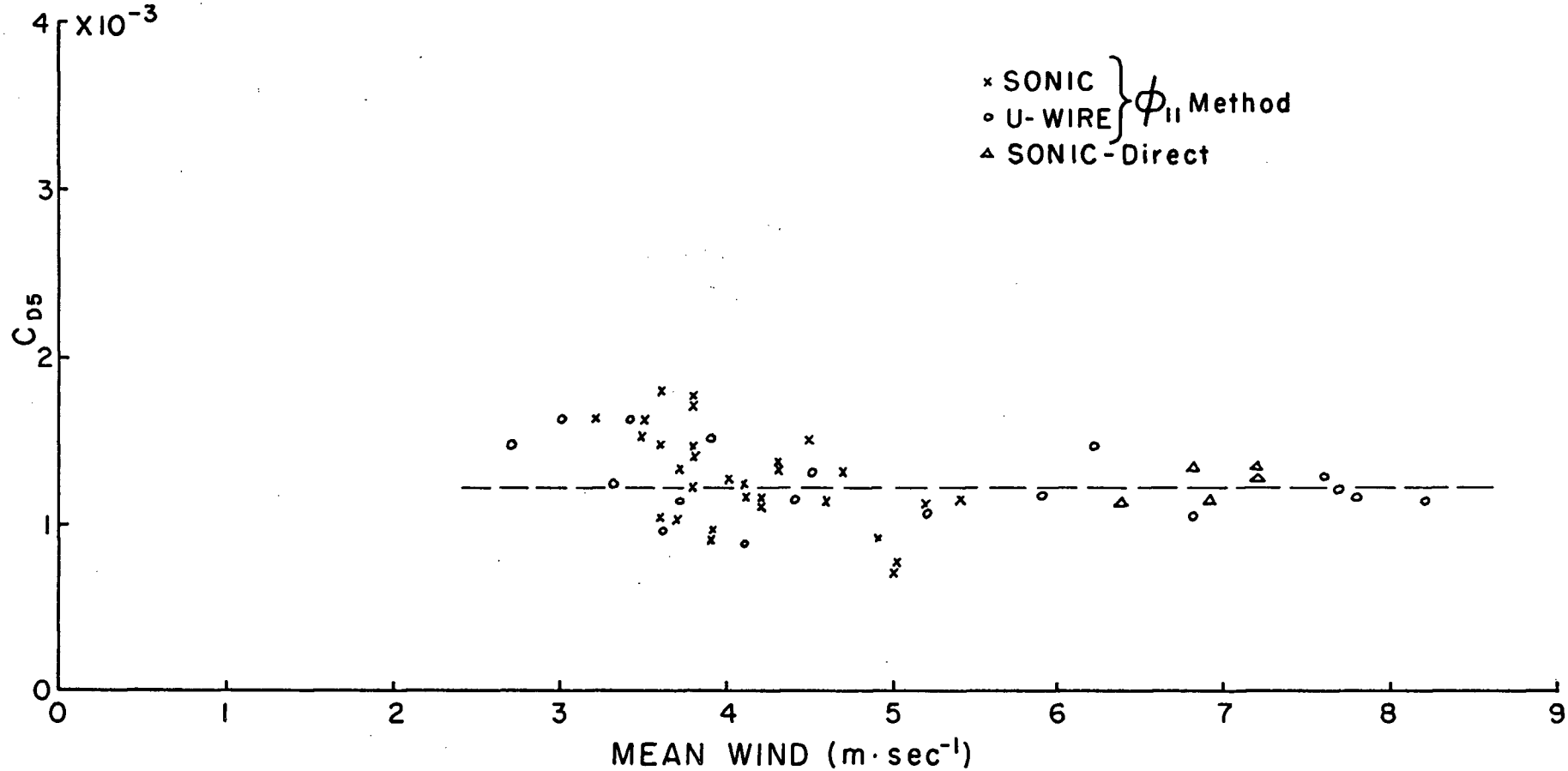

Figure 92. C_{D5} evaluated from the direct and Φ_{11} estimate of the surface stress.

SYMBOL TABLE

A_{rm}	real part of the complex Fourier coefficient C_{rm}
a	radius
B_{rm}	imaginary part of the complex Fourier coefficient C_{rm}
B.W.	bandwidth
b	as a subscript denotes a particular frequency band
C	phase speed of the waves
C_D	drag coefficient
C_{D5}	drag coefficient related to wind at 5 meters
Co	cospectrum
Co_{12}	cospectrum for data channels 1 and 2
Coh_{12}	coherence for data channels 1 and 2
C_{rm}	complex Fourier coefficient for the r^{th} harmonic in the m^{th} block
D	downwind separation of instruments
E	east
En	energy flux into the waves
e	e = 2.72
e_{sa}	saturation vapour pressure
f	nondimensional frequency
g	gravitational constant
H	denotes the hump, associated with waves, in the pressure spectrum
h	water depth
h_{re}	relative humidity
h_{sp}	specific humidity
K'	Kolmogoroff constant
K_p	Obukhov's universal pressure constant
k	wave number

k_p a pressure wave number, $k_p = \omega/U|_5$

L_p scale size of pressure fluctuations

L_v scale size of velocity fluctuations

M number of data blocks per Run

m block number

N number of data points per channel per block

n frequency in cycles per second

Δn bandwidth

n_b geometric mean of the end frequencies in a bandwidth

n_f folding frequency

P total pressure

P_s stagnation pressure

p fluctuating pressure

p_w fluctuating pressure associated with the waves

p_p fluctuating pressure predicted by the potential flow solution

Qu quadrature spectrum

Qu_{12} quadrature spectrum for data channels 1 and 2

q $q^2 = u^2 + v^2 + w^2$

R ratio of work done by the pressure force to work done by the Reynolds stress

Re Reynolds number

Ri_G gradient Richardson number

R_D ratio of measured dynamic pressure to calculated stagnation pressure

r denotes the r^{th} harmonic

r_1, r_2 the harmonics at the ends of a frequency band

S spectral energy density

T temperature

T_A air temperature

$T|_z$ air temperature at height z

T_w water temperature

t time

U mean velocity in the downwind direction

$U|_z$ mean velocity in the downwind direction at height z

U_i mean velocity in the i^{th} direction

U_p pressure propagation velocity

U_w mean water velocity

u velocity fluctuations in the downwind direction

u_i velocity fluctuations in the i^{th} direction

u_* $u_*^2 = -\overline{uw}$

V volume

v crossstream velocity fluctuations in the horizontal

W west

w vertical velocity fluctuations

x downstream coordinate

x_i i^{th} coordinate

y crossstream coordinate

z height above the surface

z_c critical height

z_o surface roughness

z_1 lower level where turbulent energy transfer goes to zero

γ $d\gamma$ incremental volume

ε rate of viscous energy dissipation

η fluctuating water elevation resulting from waves

η_a wave amplitude

θ phase between two data channels

θ	virtual temperature
θ_z	virtual temperature at height z
κ	von Karman's constant
λ	wavelength
λ_p	wavelength of pressure fluctuations
λ_v	wavelength of velocity fluctuations
λ_w	wavelength of the waves
ν	kinematic viscosity
Π	pressure spectrum
Π_{12}	cospectrum between two pressure signals 1 and 2
π	$\pi = 3.14...$
ρ	density of air
σ_p^2	variance of pressure signal
τ	surface stress
Φ_{ij}	cospectrum between i and j velocity components
Φ_{pw}	cospectrum between p and w
Φ_u	u spectrum
Φ_w	w spectrum
Φ_η	wave spectrum
χ	$\chi = x' - x$
ω	frequency in radians/sec
ω_m	measured wave frequency in radians/sec
ω_o	nonharmonic frequency in radians/sec
ω_r	harmonic frequency in radians/sec
ω_η	wave frequency in radians/sec